Design, Fabrication, Packaging, and Characterization of Nano Inertial and FET Sensors

by

Ahmet Gulsaran

A thesis
presented to the University of Waterloo
in fulfillment of the
thesis requirement for the degree of
Doctor of Philosophy
in
Mechanical and Mechatronics Engineering (Nanotechnology)

Waterloo, Ontario, Canada, 2025

© Ahmet Gulsaran 2025

Examining Committee Membership

The following served on the Examining Committee for this thesis. The decision of the Examining Committee is by majority vote.

External Examiner:	George Knopf Professor, Dept. of Mechanical and Materials Engineering Western University
Supervisor(s):	Mustafa Yavuz Professor, Dept. of Mechanical and Mechatronics Engineering University of Waterloo
	Eihab Abdel-Rahman Professor, Dept. of Systems Design Engineering University of Waterloo
Internal Member:	Yimin Wu Assistant Professor, Dept. of Mechanical and Mechatronics Engineering University of Waterloo
Internal Member:	Sushanta Mitra Professor, Dept. of Mechanical and Mechatronics Engineering University of Waterloo
Internal-External Member:	Michal Bajcsy Associate Professor, Dept. of Electrical and Computer Engineering University of Waterloo

Author's Declaration

This thesis consists of material all of which I authored or co-authored: see Statement of Contributions included in the thesis. This is a true copy of the thesis, including any required final revisions, as accepted by my examiners.

I understand that my thesis may be made electronically available to the public.

Statement of Contributions

The thesis includes six manuscripts that have already been published. Below are the contributions for each chapter and publication.

Chapter 2: Scaling Down of Inertial Sensors

I am the sole author of the chapter, under the supervision of Dr. Mustafa Yavuz and Dr. Eihab Abdel-Rahman, except for the following publication:

1. **Ahmet Gulsaran**, Bersu Bastug Azer, Resul Saritas, Samed Kocer, Yasser S. Shaba, Sasan Rahmanian, Hamza Mouharrar, Rana Abdelrahman, Eihab Abdel-Rahman, and Mustafa Yavuz. High sensitivity, thermal noise-driven aluminum-based resonant MEMS humidity sensor. *Sensors and Actuators A: Physical*, 378:115844, 2024.

I am the first and corresponding author of this publication. I was responsible for writing the original draft, review and editing, visualization, validation, supervision, software development, project administration, methodology, investigation, formal analysis, data curation, and conceptualization.

- Bersu Bastug Azer: Contributed to writing the original draft, software development, methodology, investigation, and formal analysis.
- Resul Saritas, Samed Kocer, Yasser S. Shama, Sasan Rahmanian, Hamza Mouharrar, and Rana Abdelrahman: Contributed to validation.
- Eihab Abdel-Rahman: Contributed to review and editing, validation, supervision, resource provision, and investigation.
- Mustafa Yavuz: Contributed to supervision, validation, resource provision, project administration, and funding acquisition.

Chapter 3: Packaging of Miniaturized Sensors

I am the sole author of the chapter, under the supervision of Dr. Mustafa Yavuz and Dr. Eihab Abdel-Rahman, except for the following two publications:

2. **Ahmet Gulsaran**, Bersu Bastug Azer, Samed Kocer, Sasan Rahmanian, Resul Saritas, Eihab M. Abdel-Rahman, and Mustafa Yavuz. Built-In Packaging for Single Terminal Devices. *Sensors*, 22(14):5264, 2022.

   I am the first and corresponding author of this publication. I was responsible for conceptualization, methodology, software development, validation, formal analysis, investigation, data curation, writing the original draft, review, and editing, visualization, project administration

   original draft writing, reviewing and editing, visualization, validation, software development, project administration, methodology, investigation, formal analysis, data curation, and conceptualization.

   Here are the contributions of my co-authors:

   - Bersu Bastug Azer: Contributed to software development, validation, review and editing, investigation and formal analysis.
   - Samed Kocer: Contributed to software development and validation.
   - Sasan Rahmanian: Contributed to software development, validation, and review and editing.
   - Resul Saritas: Contributed to validation.
   - Eihab Abdel-Rahman: Contributed to supervision, validation, resources, supervision, and funding acquisition.
   - Mustafa Yavuz: Contributed to conceptualization, validation, resources, supervision, and funding acquisition.

3. **Ahmet Gulsaran**, Bersu Bastug Azer, Dogu Ozyigit, Resul Saritas, Samed Kocer, Eihab Abdel-Rahman, and Mustafa Yavuz. Built-In Packaging for Two-Terminal Devices. *Micromachines*, 14(7):1473, 2023.

   I am the first and corresponding author of this publication. I was responsible for conceptualization, methodology, software development, validation, formal analysis, investigation, data curation, writing the original draft, review and editing, visualization, and project administration.

   Here are the contributions of my co-authors:

- Bersu Bastug Azer: Contributed to validation, writing the original draft, and review and editing.
- Dogu Ozyigit: Contributed to software, validation, and data curation.
- Samed Kocer and Resul Saritas: Contributed to validation.
- Eihab Abdel-Rahman: Contributed to validation, resources, review and editing, supervision, and funding acquisition.
- Mustafa Yavuz: Contributed to validation, resources, supervision, and funding acquisition.

Chapter 4: Interface Engineering of Semiconductor Nanoparticles

All semiconductor nanoparticles (quantum dots) used in this chapter were synthesized by the Sargent Group at the University of Toronto including the ligand exchange and coating processes. Therefore, I acknowledge their collaboration and support in providing the quantum dots, as well as the necessary equipment and resources for characterization including nitrogen glovebox, electrical instruments, and laboratory space.

I am the sole author of the chapter, under the supervision of Dr. Mustafa Yavuz, except for the following three publications:

4. Ozan Atan, Joao M. Pina, Darshan H. Parmar, Pan Xia, Yangning Zhang, **Ahmet Gulsaran**, Eui Dae Jung, Dongsun Choi, Muhammad Imran, Mustafa Yavuz, Sjoerd Hoogl, and Edward H. Sargent. Control over Charge Carrier Mobility in the Hole Transport Layer Enables Fast Colloidal Quantum Dot Infrared Photodetectors. *Nano letters*, 23(10):4298-4303, 2023.

5. Pan Xia, Sasa Wang, Yiqing Chen, **Ahmet Gulsaran**, Yangning Zhang, Maral Vafaie, Muhammad Imran, Amin Morteza Najarian, Yanjiang Liu, Hyeongwoo Ban, Laxmi Kishore Sagar, Mustafa Yavuz, and Edward H. Sargent. Improved Facet and Edge Passivation in Near-Infrared III-V Colloidal Quantum Dot Photodetectors. *Advanced Materials*, 37(18):2419020, 2025.

6. Yangning Zhang, Muhammad Imran, Pan Xia, Yiqing Chen, **Ahmet Gulsaran**, Yanjiang Liu, Ehsan Nikbin, Benjamin Rehl, Lizhou Fan, Filip Dinic, Da Bin Kim, Lewei Zeng, Mustafa Yavuz, Sjoerd Hoogland, and Edward H. Sargent. Nucleophilic Covalent Ligands Enable Simultaneous Surface Reconstruction and Passivation of Colloidal InSb Quantum Dots for Stable Short-Wave Infrared Photodetectors. *Angewandte Chemie International Edition*, e202505179, 2025.

The manuscripts of these three publications were prepared by the team from the Sargent Group at the University of Toronto. I was responsible for all aspects related to the field effect transistor (FET) work, including the design, fabrication, mobility measurements, data analysis, charge carrier mobility estimation, and plotting.

Abstract

Miniaturization is necessary and unavoidable for the advancement of sensor technology. This thesis explores the effect of miniaturization on performance and proposes solutions to addressed challenges through the development of a novel packaging solution and engineering device interfaces.

First, a theoretical model is developed to understand the impact of miniaturization on sensor properties such as sensitivity and signal-to-noise ratio for nano and micro electro mechanical systems-based (N/MEMS-based) gas sensing applications. Then, these theoretical predictions are experimentally verified through the experimental comparison of NEMS and MEMS-based humidity sensors. The experiments confirm that miniaturization enhances the sensitivity of inertial gas sensors. However, it also introduces challenges such as lower signal-to-noise ratio (SNR) due to attenuated output signals that are more susceptible to noise, thereby motivating the development of improved packaging and interface solutions.

To minimize the noise sources, a novel packaging technique, called built-in packaging, is proposed and performance of MEMS resonators and metal-insulator-metal (MIM) diodes are compared with the conventional techniques such as wire bonding and probing. Experimental results show that built-in packaging methods enhance output signal levels by 12% while preserving overall performance.

Finally, to implement novel materials into sensing technologies, interface engineering is studied for development of colloidal quantum dot based field effect transistors (CQD-based FETs). These devices can quantify the electrical properties of novel CQDs and highlights the importance of interface engineering. The quantified results accelerates the development of improved CQDs, leading to better photodetector performance in infrared (IR) detection.

Overall, this thesis presents a detailed analysis of the trade-offs in sensor miniaturization and provides critical insight for the advancement of compact and high-performance sensors.

Acknowledgements

The list is long but I'd like to start by acknowledging my supervisor, Dr. Mustafa Yavuz. Thank you for all the trust, freedom, and support you gave me through this journey. Looking back at these tough five years, it was a pleasure to work with you, and I'm glad that you were my supervisor. To my co-supervisor Dr. Eihab Abdel-Rahman, thank you for your technical support and guidance. May the nonlinearity be with you. To my committee member, Dr. Yimin Wu, Dr. Sushanta Mitra, Dr. Michal Bajcsy, and Dr. George Knopf, thank you for serving on my dissertation committee and your valuable feedback. To our industrial collaborator, Robert Menegotto, thank you for trusting us and sponsoring our research.

To my group mates, Dr. Resul Saritas, Dogu Ozyigit, Samed Kocer, Nizamettin Tanacar, I would like thank you for your collaboration and friendship inside and outside of the lab. To my colleagues from Toronto, thank you Ozan Atan for introducing me into your group and your friendship, Dr. Pan Xia for introducing me into your lab and collaboration, Dr. Yangning Zhang and Dr. Benjamin Rehl for your collaboration, and Dr. Ted Sargent for letting me in to your lab and giving us a chance to collaborate.

To the champs of my rowing family, Leon Domagalski, Connor Wideman, Meghan Harris, Ceilidh Aho, Natasha Hansford, Jonathan Wong, Natasha Melli, Benjamin Wiebe, and Edward Wilp, thank you for your friendship on and off the water. Also to my rowing coaches Pearl Schachter and Siobhan Crean, thank you for your great coaching in rowing and beyond.

Also, I wouldn't be here without the support of my teammates from my homeclub, Kaan Yaramis, Metin Kurt, Burhan Ozcanli, Cavit Can Ozcan, Burak Can Sahin, Duygu Keser, and Ayca Arisoy, and my close friends Dr. Canberk Guvendik, Deniz Baskurt, and Oguzhan Kocak. Thank you all for your intercontinental support.

Last but not least, to best office mate ever, partner-in-research, and big sister, Dr. Bersu Bastug Azer, we shared this journey together, and I couldn't be any luckier.

Dedication

Aileme (To my family)...

Table of Contents

Examining Committee Membership ii

Author's Declaration iii

Statement of Contributions iv

Abstract viii

Acknowledgements ix

Dedication x

List of Figures xv

List of Tables xxi

List of Abbreviations xxii

List of Symbols xxv

1 Introduction 1

1.1 Motivation 1

1.2 Chapter Synopses 4

2 Scaling Down of Inertial Gas Sensors **6**
2.1 Introduction . . . 7
2.2 Partial Differential Equation . . . 9
2.2.1 Displacement Field . . . 9
2.2.2 Static Equilibrium . . . 11
2.2.3 Equation of Motion . . . 16
2.2.4 External Forces . . . 18
2.3 Eigenvalue Analysis . . . 19
2.4 Reduced Order Model . . . 23
2.5 Sensor Metrics . . . 28
2.5.1 SNR . . . 32
2.5.2 Sensitivity . . . 36
2.6 Experimental Investigation . . . 41
2.6.1 Fabrication and Design . . . 41
2.6.2 Experimental Setup . . . 47
2.7 Results and Discussion . . . 50
2.8 Conclusions . . . 53

3 Built-in Packaging for Miniaturized Sensors **55**
3.1 MEMS resonator . . . 55
3.1.1 Introduction . . . 56
3.1.2 Actuator Design . . . 58
3.1.3 Fabrication . . . 62
3.1.4 Packaging . . . 63
3.1.5 Characterization . . . 66
3.1.6 Results and Discussion . . . 68
3.1.7 Conclusions . . . 72
3.2 MIM diode . . . 73

3.2.1 Introduction . . . 74
3.2.2 Materials and Methods . . . 75
3.2.3 Results and Discussion . . . 80
3.2.4 Conclusions . . . 83

4 Interface Engineering of Semiconductor Nanoparticles 85
4.1 Introduction . . . 85
4.2 Working Principle . . . 90
4.2.1 Qualitative . . . 91
4.2.2 Quantitative . . . 93
4.3 Interface Engineering . . . 96
4.3.1 CQD-CQD Interface . . . 97
4.3.2 CQD-Dielectric Interface . . . 98
4.3.3 CQD-Electrode Interface . . . 100
4.3.4 CQD-Environment Interface . . . 102
4.4 Fabrication . . . 103
4.4.1 Bottom Electrodes . . . 106
4.4.2 Gate Dielectric . . . 107
4.4.3 Top Electrodes . . . 107
4.4.4 Packaging and Surface Treatment . . . 108
4.5 Electrode Design . . . 108
4.5.1 Conventional . . . 109
4.5.2 IDE . . . 110
4.5.3 Local Gate . . . 110
4.5.4 Chip Layout . . . 110
4.6 Results and Discussion . . . 112
4.6.1 Initial Results without Interface Engineering . . . 112
4.6.2 Initial Results with Interface Engineering . . . 115

4.6.3 Layout Testing . . . 117
4.6.4 Dielectric Interface Testing . . . 117
4.6.5 InAs Measurements . . . 118
4.6.6 InSb Measurements . . . 119
4.7 Conclusion . . . 121

5 Conclusions and Future Work **123**
5.1 Conclusions . . . 123
5.2 Future Works . . . 125

References **126**

APPENDICES **153**

A Fabrication of N/MEMS Resonators **154**

B Python Code for Extracting Diode Performance Parameters **155**

C Preleminary Results from Dielectric Interface Testing **159**

List of Figures

1.1 Sensing scheme in three stages: (1) Monitoring, highlighted in magenta, where sensors detect physical quantities from the environment and output data; (2) Control, highlighted in green, where the sensed data is processed by algorithms to maintain desired states; and (3) Intelligence, highlighted in blue, where internet-connected control loops enable IoT, ML, and AI for communication, self-training, and real-time adaptation. 1

1.2 Chapter outlines. 4

2.1 Schematics of the fixed-fixed beam: (a) 3D view, (b) 2D side view, (c) 2D cross-sectional view, and (d) 3D cross-sectional side view. 9

2.2 Graphical solution of the characteristic equation, $\cos(\lambda_i)\cosh(\lambda_i) = 1$. . . . 21

2.3 The first ten normalized mode shapes of a fixed–fixed beam $\phi_i(x)$ as functions of the nondimensional position x/l. 24

2.4 The normalized damped frequency as a function of the quality factor. . . . 31

2.5 PSDs of (a) the thermomechanical force and (b) the displacement it induces. 34

2.6 Detection methods based on frequency-shift, magnitude modulation, and area under PSD curves. Reproduced with permission from Nature [177]. . 38

2.7 Fabrication process and elemental analysis. (a-c) represent the sequential fabrication steps: (a) deposition of the photoresist sacrificial layer (in yellow), (b) patterning of the metal structure (in red), and (c) sacrificial layer release. (d) Colorized SEM image of the final structure, highlighting metal in red and photoresist in yellow. (e) XPS spectrum displaying an 8 nm oxide thickness for the structure. Reproduced with permission from Elsevier [72]. 43

2.8 XRD analysis of the resonator. The peak corresponds to the (111) plane of FCC structured Al. Reproduced with permission from Elsevier [72]. . . . 45

2.9 Frequency responses of the fabricated resonators with widths of 2µm (blue), 3µm (red), 4µm (green), and 5µm (brown). 46

2.10 The image of the experimental setup shows the testing chamber with optical window, gas inlets and outlets, vibrometer microscope, and tested die. Reproduced with permission from Elsevier [72]. 48

2.11 Experimental setup. (a) Schematic representation of the experimental setup, including the dry air (N_2) source, two MFCs, bubbler, vibrometer, test chamber, and probe station. (b) Schematics of the resonator with the laser beam focused on its center. (c) Atomic cross-sectional view of the structure, with aluminum (blue), oxygen (red), and hydrogen (gray). (d) Frequency response of an example resonator under various humidity levels, illustrating response to adsorption and desorption of water vapor. Reproduced with permission from Elsevier [72]. 49

2.12 The PSDs of displacement in inertial sensors under thermomechanical S_{qq}^{th} (green curves) and electrostatic S_{qq}^{es} (blue curves) excitation as functions of frequency and (a) length, (b) width, and (c) thickness. The red curve represents the PSD of measurement noise S_{qq}^{V}. 50

2.13 Comparison of the MEMS and NEMS sensors' u(a) resonance frequency ω_0, (b) quality factor Q, (c) absolute sensitivity M_f, and (d) relative sensitivity S_f as functions of relative humidity $\%RH$. 54

3.1 Packaging methods: (a) no packaging, (b) wire bonding, (c) flip-chip bonding, (d) tape-automated bonding, and (e) built-in packaging. Reproduced with permission from MDPI [73]. 56

3.2 Schematics of the (a) actuation, and (b) characterization strategies. The red color indicates the focus of this study while the bold text indicates elements fabricated in the scope of this work. LDV stands for laser Doppler vibrometer. Reproduced with permission from MDPI [73]. 57

3.3 Simulation plots of the (a) first natural frequency vs. axial stress and (b) deflection and stress with respect to the actuation signal. Reproduced with permission from MDPI [73]. 61

3.4 Device fabrication: (a) Actuation electrode patterning, (b) Sacrificial layer deposition, (c) Structure patterning, and (d) Releasing the resonator. (Yellow: Actuation electrode; Brown: Ground electrode and resonator; Gray: Substrate; Green: Sacrificial layer.) Reproduced with permission from MDPI [73]. 63

3.5 Fabricated resonator images from the following: (a) 100× optical microscope, (b) 50× optical microscope of the LDV with the laser spot, (c) 2000× SEM, and (d) 8000× SEM zoomed showing the purple area circled in (c). (Yellow: Actuation electrode; Brown: Ground electrode; Red: Resonator; Gray: Substrate). Reproduced with permission from MDPI [73]. 64

3.6 (a) The fabricated die without packaging, with wire bonding packaging, and with built-in packaging, from left to right. The resonator location is circled with yellow. The experimental setup comprises (b) reference measurements, (c) wire bonding packaging measurements, and (d) built-in packaging measurements. Reproduced with permission from MDPI [73]. 65

3.7 Experimental setup of (a) frequency sweep, and (b) pulse response analysis shown with blue and red backgrounds, respectively. Equipment configuration in frequency sweep analysis, (a), is 1: Oscilloscope, 2: Vibrometer, 3: F.G. (Function Generator), 4: Microscope, and 5: Resonator, while in pulse response analysis, (b), the configuration is 1: LDV software, 2: LDV, 3: Amplifier, 4: F.G., 5: Microscope, and 6: Resonator. Optical, velocity, actuation, ground, and trigger signals are shown with blue, green, yellow, brown, and red, respectively. Reproduced with permission from MDPI [73]. 67

3.8 Frequency sweep measurement: (a) oscilloscope data, and (b) processes data. Reproduced with permission from MDPI [73]. 68

3.9 Pulse response measurement: (a) velocity data, and (b) vacuum data. Reproduced with permission from MDPI [73]. 69

3.10 The results of frequency sweep measurements for (a) built-in and (b) wire bonding chips. Reproduced with permission from MDPI [73]. 70

3.11 The plots of pulse response measurements performed in (a) in air, and (b) under vacuum conditions. Reproduced with permission from MDPI [73]. . 71

3.12 The first theoretical and experimental mode shapes. Reproduced with permission from MDPI [73]. 72

3.13 (a) Energy diagram for the Pt-TiO_2-Al metal-insulator-metal (MIM) diode, and microscope images of the device before (b) and after (c) the top electrode deposition (the inset shows the cross-sectional view). Reproduced with permission from MDPI [74]. 76

3.14 Experimental setup and electrical schematics of (a) probing, (b) wire-bonding, and (c) built-in packaging. Reproduced with permission from MDPI [74]. 79

3.15 Electrical characteristics of the fabricated diode using three different interconnection methods: (a) linear and (b) logarithmic scale IV-curves. The diode resistance is shown on logarithmic scale in (c). The inset depicts the ratio of resistance between conventional methods and built-in packaging. The diode's asymmetry, nonlinearity, and responsivity are shown in (d–f), respectively. Reproduced with permission from MDPI [74]. 81

4.1 Quantum confinement on QD materials. Quantum confinement, leading to size-dependent optical and electrical properties that are distinct from those of parental bulk solids, occurs when the spatial extent of electronic wave functions is smaller than the Bohr exciton diameter. Reprinted with permission from AAAS [64]. 86

4.2 Comparison of the process flow for integrated hybrid II-VI and III-V compound semiconductor arrays (a) and colloidal quantum dot monolithic arrays (b). The smallest pixel pitch of hybrid arrays is 5 µm. (c) shows the cross-sectional view on monolithic array structure based on colloidal quantum dot (CQD)s with potentially pixel pitch below 1 µm. Reproduced with permission from Springer Nature [185]. 88

4.3 Schematics of an FET structure in the saturation region. Reproduced with permission from Springer Nature [214]. 90

4.4 Discrete energy levels in the channel under (a) zero, (b) negative, and (c) positive gate biases. 91

4.5 Combined energy bands coupled with the source, drain, and gate electrodes under (a) zero, (b) negative, and (c) positive drain biases. 92

4.6 Example transfer curves from the literature showing the FET mobility extraction using (a-b) linear region, and (c-d) saturation region. Reproduced with permissions from the MRS [174] and Elsevier [148]. 94

4.7 FET defect interfaces. Reproduced with permission from ACS [50]. 97

4.8 Schematics of the experimental setup. 102

4.9 Common FET device architectures: (a) staggered, top-gate; (b) coplanar, top-gate; (c) staggered, bottom-gate; and, (d) coplanar, bottom-gate. . . . 104

4.10 FET fabrication. 105

4.11 FET designs: (a) Conventional global gated design, (b) Cconventional local gated design, (c) IDE with global gated design, and (d) IDE with local gated design. 109

4.12 FET layout of the (a) gate electrode, (b) source and drain electrodes, and (c) combined layers. 111

4.13 Figure S4 Microscope images of the channels. (a) Microscope image of the FET channels (source and drain). The length of the channel is measured as 1000 µm and width as 30 µm. SiOx thickness is 100 nm. (b-c) Microscope image of the substrate channels used in conductivity study. Channel dimensions are 35 µm in length and 1000 µm in width. SiOx thickness is 300 nm. Reproduced with permission from ACS [10]. 113

4.14 FET substrates measurement setup using Keithley 4200 parameter analyzer. Samples are measured with three contact probes inside a Faraday cage. Reproduced with permission from ACS [10]. 113

4.15 Transfer (VGS vs IDS) and b) Output (VDS vs IDS) curves for EDT FET devices. Arrows show the sweeping direction. The low-conductivity material demonstrated high hysteresis under large bias, similar to previous reports [1]. Due to the relatively small W/L ratio and low-conductivity material, the ambipolar characteristics of the EDT-PbS are shadowed. Negatively charged carrier dominated current readings are below the noise floor of the measurement system. However, a strong signal is obtained where positively charged carriers dominate the current. Hole mobility is obtained from these clear curvatures in the reverse sweep. The measurement is repeated under different biasing conditions. Reproduced with permission from ACS [10]. . 114

4.16 Image of the FET device fabricated for testing mixed-halide passivated PbS CQDs. 115

4.17 Output and transfer curves of the tested mixed-halide passivated PbS CQDs. 116

4.18 Extracted hole mobilities from FETs with different channel W/L ratios, all based on identical mixed-halide passivated PbS CQDs. 117

4.19 Transfer and output characteristics of InAs CQD FETs passivated with different halide ligands: (a,b) Br, (c,d) Br/Cl mixture, and (e,f) Cl. The inset shows a schematic of the IDE-based FET structure. Reproduced with permission from Wiley [231]. 119

4.20 Field-effect characterization of InSb CQD films. (a) Schematic of the FET device structure. (b) Microscope image of the channel region. Transfer characteristics of (c) ME-InSb and (d) MTG-InSb CQDs, with arrows indicating the sweep directions. Output characteristics of (e) ME-InSb and (f) MTG-InSb CQDs. The applied gate-source voltages (V_{GS}) are indicated in the legends. For both samples, the drain-source current (I_{DS}) increases with decreasing V_{GS}, consistent with p-type behavior of the CQDs. Reproduced with permission from Wiley [247]. 120

A.1 The surface profile of Al obtained from mechanical surface profilometer. Reproduced with permission from Elsevier [72]. 154

C.1 FET performance with Al_2O_3 dielectric interface. 159

C.2 FET performance with HfO_2 dielectric interface. 160

C.3 FET performance with SiO_2 dielectric interface. 160

C.4 FET performance with ZrO_2 dielectric interface. 161

List of Tables

2.1 Dimensions of the resonators. 46

2.2 Comparison of the analytical expressions and scale relationships of key performance metrics for resonant gas sensors of the inertial type. 52

3.1 Device fabrication. Reproduced with permission from MDPI [73]. 62

3.2 The results of frequency sweep measurements. Reproduced with permission from MDPI [73]. 70

3.3 The results of pulse response measurements. Reproduced with permission from MDPI [73]. 71

3.4 Fabrication steps for MIM diode. Reproduced with permission from MDPI [74]. 76

3.5 Performance comparison of the MIM diodes with the literature. Reproduced with permission from MDPI [74]. 83

4.1 Properties of gate dielectrics from the literature. 99

4.2 The electronic properties of the electrode materials. For the metals, the workfunction, resistivity, and electronegativity values are referenced from [155], [81], and [29], respectively. 101

4.3 Device fabrication. 105

4.4 The precursors and temperatures of the ALD of each film. 107

4.5 Pin mapping of the transistors. (LG: Local Gate, GG: Global Gate) 112

List of Abbreviations

AI artificial intelligence 2, 74

ALD atomic layer deposition 77

CMOS complementary metal-oxide-semiconductor 8

CMUT capacitive micromachined ultrasonic transducers 7

CQD colloidal quantum dot xviii, 5, 85–90, 95–98, 100–103, 108, 110–115, 117–122, 124, 125

CQD-FET colloidal quantum dot based field effect transistor 5, 89, 91, 93, 96, 116–118, 121

DOS density of states 91

EBL electron beam lithography 45

FBAR film bulk acoustic resonator 7

FCC face-centered cubic 44

FEM finite element model 9, 60

FET field effect transistor 57, 89, 90, 95, 96, 98, 99, 103–106, 108–110, 112, 113, 115, 117–122, 124, 125

FFT fast Fourier transform 68

HVAC heating, ventilation, and air conditioning 2

IC integrated circuit 74

ICP inductively coupled plasma 42, 62

IoT internet of things 2, 7, 74

LDV laser Doppler vibrometer 46, 47, 58–60, 66, 68

MEMS micro electro mechanical systems 4–6, 8, 9, 15, 41, 42, 44–47, 52, 53, 55, 56, 59, 73, 123–125

MFC mass flow controller 47, 48

MIM metal-insulator-metal xvii, xxi, 5, 8, 55, 74–76, 78, 82, 124

ML machine learning 2

MLA maskless lithography aligner 42, 62, 77, 106

N/MEMS nano and micro electro mechanical systems 6–8, 18

NEMS nano electro mechanical systems 4, 6, 8, 9, 15, 41, 42, 44–47, 52, 53, 56, 59, 73, 123

ODE ordinary differential equation 9, 20, 23, 25, 53

PCB printed circuit board 55, 63, 64, 73, 78, 79, 124

PDE partial differential equation 9, 18, 23–25, 53

PR photoresist 42, 45, 62, 77, 106

PSD power spectral density 32–35, 37, 50, 51

QCM quartz crystal microbalance 7

QNFCF Quantum-Nano Fabrication and Characterization Facility 42, 101, 106, 108

RIE reactive ion etching 42, 62

ROM reduced order model 9, 53, 60

SAW surface acoustic wave 7

SCLC space-charge-limited current 89, 119, 120

SEM scanning electron microscope 43, 62

SMA SubMiniature version A 64, 77, 80

SMU source measure unit 80

SNR signal-to-noise ratio 32, 36, 50, 51, 53, 123, 124

XPS X-ray photoelectron spectroscopy 43, 44

XRD X-ray diffraction 43, 44

List of Symbols

C_i Capacitance per unit area 94

C Concentration 37

D^* Detectivity 81

$\mathbf{D}$ Displacement vector 10

E Elastic modulus of the beam 12

$I_{\mathbf{D}}$ Drain current 93

I_{yy} Second moment of inertia of the cross-sectional beam element normal to the lateral direcition 16

I Current 80

J Current density 80

L Channel length 94

$M_a^{\mathbf{es}}$ The absolute sensitivity of the resonant peak magnitude under electrostatic actuation with respect to the gas concentration 40

$M_a^{\mathbf{th}}$ The absolute sensitivity of the resonant peak magnitude under thermomechanical actuation with respect to the gas concentration 40

S_f The absolute sensitivity of the frequency with respect to the gas concentration 39

$M_{\mathbf{rm}}^{\mathbf{es}}$ The absolute sensitivity of the mean square displacement under electrostatic actuation with respect to the gas concentration 41

$M_{\mathbf{rm}}^{\mathbf{th}}$ The absolute sensitivity of the mean square displacement under thermomechanical actuation with respect to the gas concentration 41

M Moment 11

N_0 Initial axial load 15

NA Numerical aperture 58

N Axial load 11

P Pressure 37

Q Quality factor 29

$\mathcal{R}$ Optical reflectance 59

R Resistance 35

$S_a^{\mathbf{es}}$ The relative sensitivity of the resonant peak magnitude under electrostatic actuation with respect to the gas concentration 40

$S_a^{\mathbf{th}}$ The relative sensitivity of the resonant peak magnitude under thermomechanical actuation with respect to the gas concentration 39

S_f The relative sensitivity of the frequency with respect to the gas concentration 39

$S_{\mathbf{rm}}^{\mathbf{es}}$ The relative sensitivity of the mean square displacement under electrostatic actuation with respect to the gas concentration 40

$S_{\mathbf{rm}}^{\mathbf{th}}$ The relative sensitivity of the mean square displacement under thermomechanical actuation with respect to the gas concentration 41

T Temperature 33

$V_{\mathbf{D}}$ Drain voltage 90, 92

$V_{\mathbf{G}}$ Gate voltage 90, 93

V_s Shear force 11

V Voltage 18

W Channel width 94

b Beam width 9

$c_n^{\mathbf{es}}$ Electrostatic force coefficients 27

$\hat{c}$ Viscous damping coefficient per unit area 18

$c_{i,n}^{\mathbf{m}}$ Membrane stiffness coefficients 27

c Damping coefficient 26

$\delta\omega$ Bandwidth 32

d Gap between the unactuated beam and the stationary electrode 18

ϵ Permittivity 18

$f_{\mathbf{b}}$ Bending stiffness of the cross-sectional beam element 14, 24

f_c Cut-off frequency 81

$f_{\mathbf{d}}$ Distributed damping force 18, 24

$f_{\mathbf{es}}$ Distributed electrostatic force 18, 24

$f_{\mathbf{in}}$ Distributed inertial force 24

$f_{\mathbf{m}}$ Membrane stiffness of the cross-sectional beam element 15, 24

$f_{\mathbf{th}}$ Distributed thermomechanical force 18, 24

f Distributed transverse load 11

h Beam thickness 9

k_B Boltzmann constant 33

κ Dielectric constant 98

$k_n^{\mathbf{b}}$ Bending stiffness of the n^{th} mode 26

$\lambda_{\mathbf{o}}$ Optical wavelength 58

λ Wavenumber 20

l Beam length 9

$m_{\mathbf{lin}}$ Transconductance in the linear region 93

$\mu_{\mathbf{C}}$ Electrochemical potential of the channel 92

$\mu_{\mathbf{D}}$ Electrochemical potential of the drain 91

$\mu_{\mathbf{S}}$ Electrochemical potential of the source 91

$\mu_{\mathbf{f}}$ Viscosity 59

μ Charge carrier mobility 94

m Mass of the beam 25

ω_0 Resonance frequency 31

ω_d Damped frequency 29

ω_n Natural frequency 28

ω Angular frequency 19

ϕ Mode shape of the beam 19

q_e Charge of an electron 92

q Modal coordinate 23

ρ Density of the beam 16

$\mathbf{r}$ Position vector 10

σ Axial stress 12

t Time 10

u Axial displacement 10

ε Mechanical strain 10

ς Electrical conductivity 59

v Lateral displacement 10

w Transverse displacement 10

$\xi_{\mathbf{th}}$ Thermomechanical force 27

x Axial coordinate 10

y Lateral coordinate 10

ζ Damping ratio 28

z Transverse coordinate 10

Chapter 1

Introduction

1.1 Motivation

Sensors are the bridge between the physical and digital worlds. They act as the eyes and ears of machines and play a huge role in our society. From its technical definition, a sensor produces an output signal for detecting a physical phenomenon, as shown in Figure 1.1.

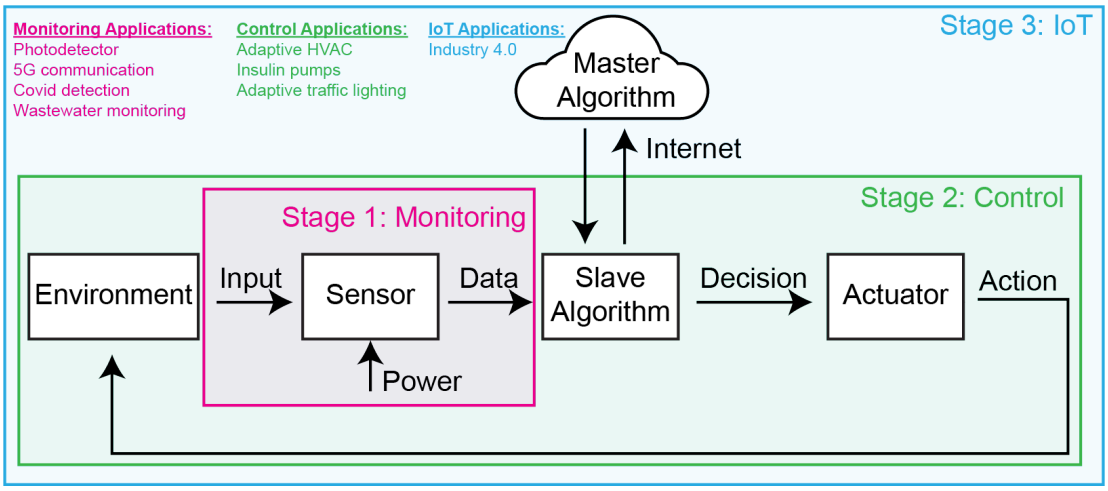


Figure 1.1: Sensing scheme in three stages: (1) Monitoring, highlighted in magenta, where sensors detect physical quantities from the environment and output data; (2) Control, highlighted in green, where the sensed data is processed by algorithms to maintain desired states; and (3) Intelligence, highlighted in blue, where internet-connected control loops enable IoT, ML, and AI for communication, self-training, and real-time adaptation.

From an application perspective, sensing systems can be classified into three distinct stages:

1. **Monitoring:** In this initial stage, the sensor interacts directly with the environment, detecting physical quantities (input) such as light, chemical concentration, or motion. The sensor converts this input into a measurable electrical signal (data) while receiving power for operation. As highlighted in the pink section of the figure, Stage 1 focuses purely on observation and data acquisition, without influencing the environment. Example monitoring applications include photodetectors, 5G communication receivers, COVID-19 detection kits, and wastewater monitoring systems.

2. **Control:** In the second stage, shown in green, the sensor output is processed by a slave algorithm that makes a decision, which is then executed by an actuator to produce an action. This closed-loop process allows systems to maintain or adjust operational states automatically. Representative examples include adaptive heating, ventilation, and air conditioning (HVAC) systems, insulin pumps, and adaptive traffic lighting. Here, sensing is directly coupled with actuation to form responsive control systems.

3. **Intelligence:** The final stage integrates internet of things (IoT) connectivity with machine learning (ML) and artificial intelligence (AI). As highlighted blue in the figure, the slave algorithm can communicate with a master algorithm over the internet, enabling coordination between distributed sensors, data sharing, and AI model refinement. This stage allows sensors not only to inform their own control loops but also to learn from global datasets and adapt over time. Applications include self-driving vehicles, smart factories in Industry 4.0, and large-scale environmental monitoring networks.

Overall, the figure emphasizes that sensors form the foundation of all stages from simple monitoring (Stage 1) to advanced, interconnected intelligence (Stage 3). Regardless of how sophisticated algorithms, connectivity, or automation become, each system relies on accurate, reliable, and responsive sensors to provide the essential data that drives decision-making. With the expansion of AI applications, sensor technology will be in greater demand as sensors fuel AI systems with data. Wherever AI is deployed, robust sensors are needed to train these systems and enhance their accuracy and efficiency. To meet this growing need, one promising approach is to enhance sensor performance through miniaturization.

Miniaturization has several advantages on sensor performance. First, surface interactions play a crucial role in defining the sensitivity. As the sensor size decreases, the

surface-to-volume ratio increases and leads to improved sensitivity and limit of detection. Second, reduced sensor size enables higher array density, allowing noise reduction via signal averaging, increased resolution through more pixels, and multiplexed detection of multiple physical phenomenon simultaneously. Third, miniaturization reduces required sample volumes which is critical for analyzing biological or rare samples. Furthermore, at nanoscales, quantum phenomena such as discretization of energy levels or quantum entanglement and enables nonclassical sensing methods for quantum sensors.

On the other hand, these improvements come with challenges that must be addressed. Firstly, smaller sensors often requires complex fabrication techniques therefore simple there's a need for simple nanofabrication techniques. Moreover, the signal-to-noise ratio can drop as smaller sensors produce weaker signals and negligible noise sources at larger scales can be more significant. Weaker signals need be countered with high-sensitive nano materials and noise has to be surpassed by optimizing materials interface and advancing sensor packaging. Last but not least, increased sensitivity reduces selectivity as the sensor becomes more susceptible to interference from undesired stimula which can lead to false positives. To overcome this, robust environmental isolation is critical, particularly during development and calibration.

Moore's Law suggests that the number of transistors in an integrated circuit doubles about every two years and this trend extends naturally to sensor technology [159]. Given the rising application areas, high expectations, addressable challenges, and the relevant guide of Moore's Law, the main objective of this research is the miniaturization of sensors. Although primarily focused on sensors, this research also benefits energy harvester technology, as both systems operate on the same principle. Sensors convert input signals into information, while harvesters discard that information to extract energy as shown in Figure 1.1. Therefore, innovations in sensor technology drive advancements in energy harvesting.

1.2 Chapter Synopses

An overview of the chapter structure is presented in Figure 1.2.

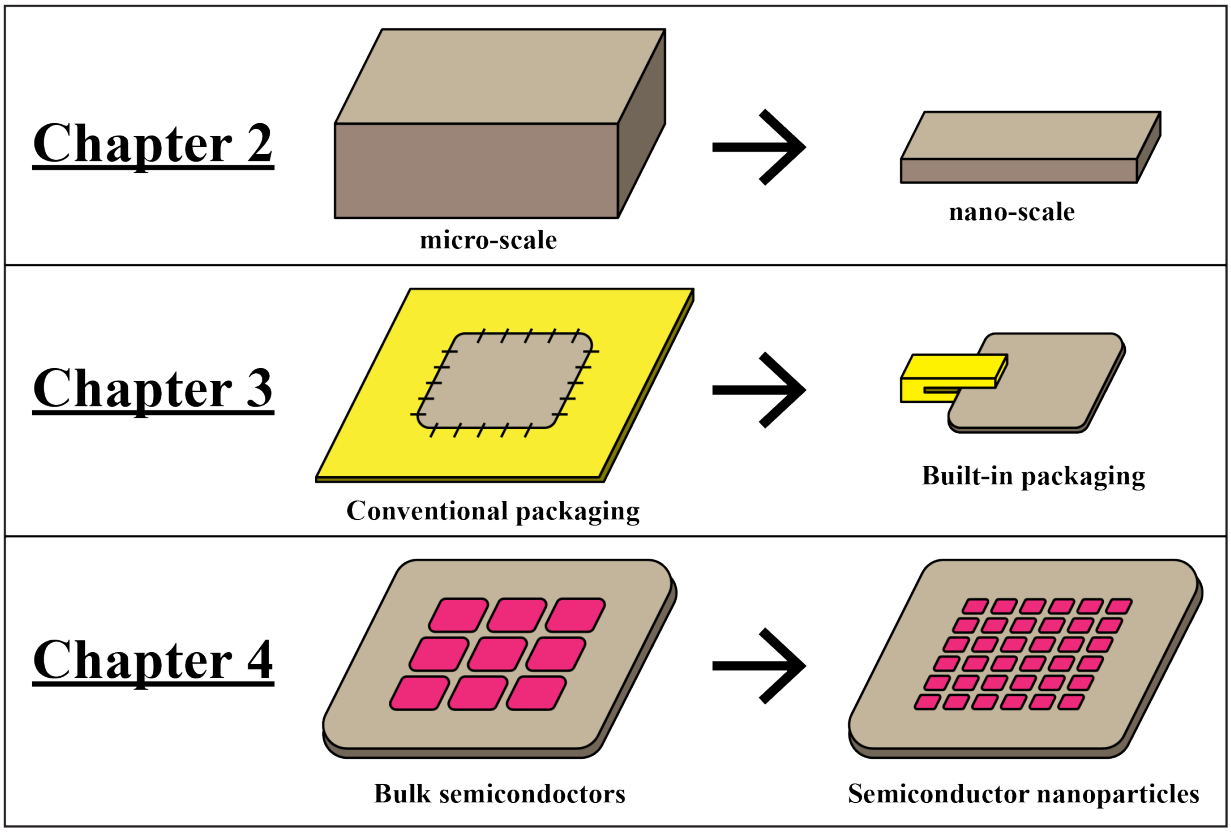


Figure 1.2: Chapter outlines.

Chapter 2: Scaling Down of Inertial Sensors

As sensors scale down, their intrinsic characteristics and performance evolve. This chapter develops a theoretical model to predict these trends and validates the findings through experimental demonstrations, focusing on micro electro mechanical systems (MEMS) and nano electro mechanical systems (NEMS) resonators for gas sensing applications.

Chapter 3: Packaging of Miniaturized Sensors

Sensor miniaturization require parallel developments in packaging and interconnection techniques. This chapter introduces built-in packaging as an innovative alternative to traditional methods such as wire bonding, probing, and flip-chip bonding, with a focus on its application in MEMS resonators and MIM diodes.

Chapter 4: Interface Engineering of Semiconductor Nanoparticles

The transition from bulk materials to nano materials is essential for sensor miniaturization. This chapter focuses on the miniaturization of photodetector pixels by replacing conventional bulk active materials with semiconductor nanoparticles, more specifically CQDs, by optimizing the device-material interface in colloidal quantum dot based field effect transistor (CQD-FET)s.

Chapter 5: Conclusions

This chapter concludes the thesis by summarizing key findings and highlighting potential directions for future research.

Chapter 2

Scaling Down of Inertial Gas Sensors

As sensors continue to scale down from micro to nanoscale, their characteristics, such as sensitivity, signal-to-noise ratio, and resonant frequency or characteristic time, evolve. Understanding these changes is critical for designing high-performance sensing platforms at the micro/nano interface. This chapter focuses on modeling and experimentally validating the performance evolution of miniaturized resonators, particularly MEMS and NEMS beam resonators, for gas sensing applications.

To get a better understanding of the effects of miniaturization on sensor performance, I first present a comprehensive theoretical framework describing the mechanics of nano and micro electro mechanical systems (N/MEMS) resonators. The governing equations of motion are derived including nonlinearities that become significant at nanoscales. From this theoretical basis, we analytically derive formulas for their key performance metrics, such as sensitivity, limit of detection, and dynamic range, as functions of beam dimensions and operating conditions.

The theoretical formulation is followed by experimental demonstration. NEMS and MEMS resonator-based gas sensors are designed and fabricated, and an experimental setup is developed to evaluate their humidity sensing performance. By comparing performance of MEMS and NEMS sensors under the same test conditions, we extract quantitative insights into how miniaturization affects resonator behavior and sensing capabilities.

The final section of this chapter compares theoretical and experimental results, emphasizing both consistent trends and notable deviations. Miniaturization typically improves sensing performance by increasing sensitivity, however it also introduces new challenges, such as reduced signal output. These challenges are addressed in the subsequent chapters through improved packaging and interconnects and interface engineering.

2.1 Introduction

The integration of connected devices and the IoT is transforming our lives with the dawn of Industry 4.0. In this digital revolution, sensors play a critical role by providing feedback for automation. Among these sensors, humidity sensors play a critical role in various applications such as respiration and wound monitoring [134], noncontact human-machine interfaces [137], fuel cell performance [165], and electronic circuit failure [30]. Humidity sensors can be classified into several types based on their working principles, including capacitive, resistive, optical, and gravimetric sensors. Although electronic humidity sensors based on capacitance, resistance, or impedance change dominate the market, frequency shift- or gravimetric-based sensing is a promising, yet undervalued method due to complicated fabrication and operation processes, high cost, and nonlinear characteristics [119].

Gravimetric sensors operate by measuring changes in mass due to moisture adsorption, offering high sensitivity and reliability. Gravimetric platforms can be classified into five main types, including surface acoustic wave (SAW) resonators, quartz crystal microbalance (QCM), capacitive micromachined ultrasonic transducers (CMUT), film bulk acoustic resonator (FBAR), and N/MEMS resonators. Regardless of the type, they all consist of three essential elements: the structure layer that ensures mechanical stability, the electrical layer that carries input and output signals, and the receptor layer that selectively identifies target molecules.

The main performance parameter, sensitivity, depends on the inertia of the bound sensed molecules compared to that of the sensor. To enhance the sensitivity, either more chemical gas should be bound, or the inertia of the sensor should be decreased. This can be accomplished by improving the receptor layer with nanoengineered materials such as zero-dimensional (0D) quantum dots [176], one-dimensional (1D) nanorods [232], two-dimensional (2D) materials [124], three-dimensional (3D) architecture materials [208], or micropatterned surfaces [13] to maximize active surface area. Recent explorations into resistance/impedance-type humidity sensors, as highlighted in studies by Wang et al. [229] and Li et al. [130], underscore the importance of various sensing mechanisms for a more comprehensive understanding and practical application. While resistance/impedance-type sensors have their merits, the limitations imposed by conventional platforms, such as the need for input activation voltage and the performance reaching a plateau, pose challenges. Therefore, the exploration of advanced platforms, like N/MEMS resonators, coupled with nanoengineered materials, is crucial to push the boundaries of sensor technology.

To get a better understanding of the effects of miniaturization on sensor performance, a comprehensive theoretical framework is presented to describe the mechanics of N/MEMS

resonators. The governing equations of motion are derived by including nonlinearities that become significant at nanoscales. From this theoretical basis, we analytically derive the sensing principles on beam resonators, followed by the formulation of key performance metrics, such as sensitivity, limit of detection, and dynamic range, as functions of beam dimensions and operating conditions.

In this work, MEMS and NEMS resonators were fabricated from 100 and 220 nm Al thin film, respectively. This layer serves as structural, electrical, and receptor layers to demonstrate consistency and reproducibility. Al is a suitable structural layer due to its lightweight and rigid characteristics, demonstrating promising sensor performance when fabricated with an industrial 0.35 µm complementary metal-oxide-semiconductor (CMOS) technology [93, 224]. It is also a good conductor layer and widely used in the wire bonding industry and as an electrical layer in N/MEMS-based humidity sensors [61, 157, 124, 71, 128, 93, 224]. Finally, the nature oxide formed on the surface acts as a receptor layer due to its hydrophilic properties. The concept of combining a metal with its oxide was previously employed in early MIM diodes to create an ultra-thin quantum barrier between two Al contacts, promoting electron tunneling in a specific direction [58]. In this context, we employ a similar idea where the thin oxide layer formed on the surface binds the water molecules, while the metal layer contributes mechanical strength and electrical stability. The integrated nature of these layers within the sensor minimizes inertia, leading to outstanding sensitivity values.

Unlike conventional MEMS resonators actuated by electrostatic forces or the piezoelectric effect, the developed sensors are self-driven by intrinsic thermomechanical noise at room temperature and do not require an external power source due to their ultra high length-to-thickness aspect ratio (40×0.22µm). In 2010, Hiebert et al.[84] experimentally demonstrated the use of thermomechanical noise to characterize the resonance properties of N/MEMS resonators with high aspect ratios (20×0.5µm) at room temperature under vacuum, achieving results comparable to those obtained through electrostatic actuation. Although the aspect ratio was high, the experiments were conducted under vacuum conditions. The source of this thermomechanical noise is the Brownian motion whose rate can be quantified as $1/2k_BT$ according to the equipartition theorem [84]. In 2013, Hauer et al.[80] developed a theoretical framework and general procedure for calibrating N/MEMS resonators using thermomechanical noise. Building on this, in 2022, Mistry et al.[157] applied this method to a N/MEMS resonator with a higher aspect ratio (20×0.25µm) at room temperature and atmospheric pressure to actuate a highly sensitive humidity sensor. Most recently, in 2024, Qiao et al.[177] generalized the concept of thermal noise-based resonant sensors and demonstrated that this approach could be employed for sensing using three methods: shifts in resonance frequency, resonance amplitude, and the area of the

resonance curve.

This study presents thermal noise-driven, aluminum-based MEMS and NEMS resonators for humidity sensing by correlating humidity with the resonance frequency of the developed devices. Our work explores a unique fabrication process that uses aluminum as a multifunctional layer that serves as the structural support, electrical channel, and receptor layer for humidity detection. Moreover, the noise-driven nature of the sensors presents a new opportunity for practical NEMS sensors that operate at room temperature and ambient pressure, for cheaper, simpler, and low-power-consumption solutions.

2.2 Partial Differential Equation

First, the partial differential equation (PDE) describing the motions of a fixed-fixed beam is derived. Then, using the reduced order model (ROM), the PDE is transformed into a set of ordinary differential equation (ODE)s, one for each bending mode. Alternatively, PDE could also be solved via finite element model (FEM) however FEMs don't give insight enough to understand miniaturization trends or conduct parametric analysis.

2.2.1 Displacement Field

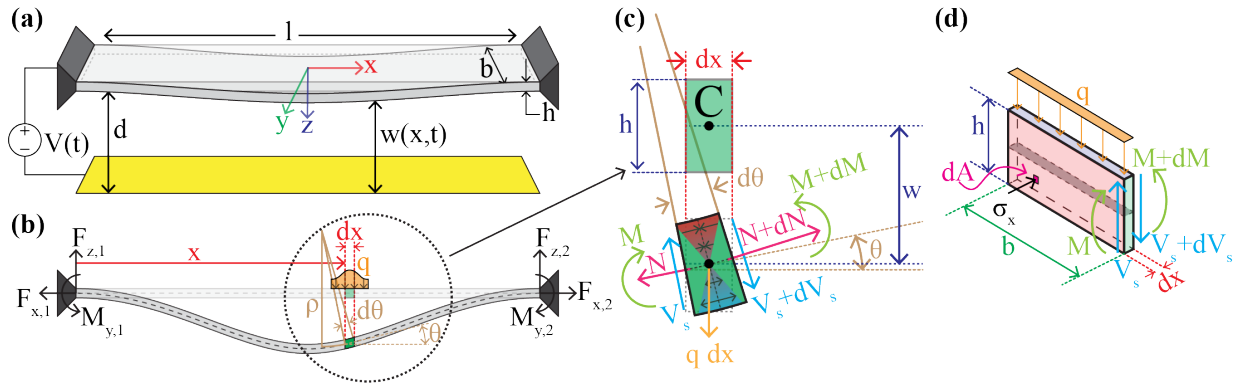


Figure 2.1: Schematics of the fixed-fixed beam: (a) 3D view, (b) 2D side view, (c) 2D cross-sectional view, and (d) 3D cross-sectional side view.

A 3D schematic of the fixed–fixed beam is shown in Figure 2.1(a), where l, b, and h denote the length, width, and thickness of the beam, respectively. The origin of the inertial

frame is located at the center of the undeflected beam along the neutral axis, where the position vector $\mathbf{r}$ is defined as

$$\mathbf{r} \equiv x\,\hat{\mathbf{i}} + y\,\hat{\mathbf{j}} + z\,\hat{\mathbf{k}} \tag{2.1}$$

The displacement field $\mathbf{D} = \mathbf{D}(x, y, z, t)$ at any point (x,y,z) and time t on the undeflected beam is defined over the stationary domain $-l/2 < x < l/2$, $-b/2 < y < b/2$, and $-h/2 < z < h/2$ and can be expressed as

$$\mathbf{D}(x, y, z, t) \equiv u\,\hat{\mathbf{i}} + v\,\hat{\mathbf{j}} + w\,\hat{\mathbf{k}} \tag{2.2}$$

where the displacement vectors u, v, and w are also functions of the spatial coordinates and time, i.e., $u(x, y, z, t)$, $v(x, y, z, t)$, and $w(x, y, z, t)$. Given the aspect ratio of the beam, deflections can be assumed to occur primarily in the transverse (out-of-plane) direction. Restricting my interest to transverse loads that vary uniformly along the beam width, I can ignore displacement along that direction and set

$$v(x, y, z, t) = 0 \tag{2.3}$$

Furthermore, the motion of the beam along the axial direction can be restricted as the external loads are applied along the transverse direction and the axial displacement can be set to zero as a constrain as,

$$u(x, y, z, t) = 0 \tag{2.4}$$

Under these conditions, the displacement field simplifies to,

$$\mathbf{D}(x, y, z, t) \equiv w(x, y, z, t)\,\hat{\mathbf{k}} \tag{2.5}$$

By neglecting the twisting motion, the displacement field reduces to

$$\mathbf{D}(x, z, t) \equiv w(x, z, t)\,\hat{\mathbf{k}} \tag{2.6}$$

and neglecting deformation in the transverse (z) direction, thus setting strain ε in the transverse direction equal to zero, $\varepsilon_z = 0$, the displacement field becomes,

$$\mathbf{D}(x, t) \equiv w(x, t)\,\hat{\mathbf{k}} \tag{2.7}$$

as illustrated in Figure 2.1(b).

The fixed boundary conditions at both ends can be represented in equation form as,

$$\begin{aligned} w(-l/2,t) = 0\ , \qquad & w'(-l/2,t) = 0 \\ w(l/2,t) = 0\ , \qquad & w'(l/2,t) = 0 \end{aligned} \tag{2.8}$$

where $w'(x_0) = \frac{\partial w}{\partial t}\big|_{x=x_0}$ denotes the first derivative with respect to axial position at position x_0 and time t_0.

2.2.2 Static Equilibrium

The static force balance in the transverse direction, $\sum F_z = 0$, yields

$$\frac{\mathrm{d}}{\mathrm{d}x}\left(V_s \cos\theta - N \sin\theta\right) = f \tag{2.9}$$

where $V_s = (x,t)$, $M = M(x,t)$, and $N = N(x,t)$ are the shear force, moment, and axial load, respectively, acting on the section-face of an infinitesimal element at position x and time t. The term $f = f(x,t)$ represents the distributed transverse load. Similarly, the force balance in the axial direction, $\sum F_x = 0$, yields

$$\frac{\mathrm{d}}{\mathrm{d}x}\left(V_s \sin\theta - N \cos\theta\right) = 0 \tag{2.10}$$

The moment balance around the perpendicular axis, $\sum M_y = 0$, yields

$$\begin{aligned} -M - V_s\frac{\mathrm{d}s}{2}\cos(\mathrm{d}\theta/2) + N\frac{\mathrm{d}s}{2}\sin(\mathrm{d}\theta/2) + (M + \mathrm{d}M) \\ - (V_s + \mathrm{d}V_s)\frac{ds}{2}\cos(\mathrm{d}\theta/2) - (N + dN)\frac{\mathrm{d}s}{2}\sin(\mathrm{d}\theta/2) = 0 \end{aligned} \tag{2.11}$$

The trigonometric terms can be expanded as

$$\cos(\mathrm{d}\theta/2) = 1 - \frac{(\mathrm{d}\theta)^2}{8} + \frac{(\mathrm{d}\theta)^4}{384} + \cdots \approx 1$$

and

$$\sin(\mathrm{d}\theta/2) = \frac{\mathrm{d}\theta}{2} - \frac{(\mathrm{d}\theta)^3}{48} + \cdots \approx \frac{\mathrm{d}\theta}{2}$$

Therefore, the moment balance can be simplified into

$$\mathrm{d}M = V_s \mathrm{d}s + \mathrm{d}V_s \frac{\mathrm{d}s}{2} + dN \frac{\mathrm{d}s}{2} \frac{\mathrm{d}\theta}{2} \tag{2.12}$$

yielding the linear term,

$$\mathrm{d}M = V_s \mathrm{d}s \tag{2.13}$$

From the geometry, we can write

$$\begin{aligned} \mathrm{d}s &= \sqrt{1 + w'^2}\mathrm{d}x, \quad w' = \tan\theta, \qquad \rho = \frac{(1 + w'^2)^{3/2}}{w''} \\ \sin\theta &= \frac{w'}{\sqrt{1 + w'^2}}, \quad \cos\theta = \frac{1}{\sqrt{1 + w'^2}}, \quad \mathrm{d}\theta = \frac{w''}{1 + w'^2}\mathrm{d}x \end{aligned} \tag{2.14}$$

Using the effort balance relationships, Eqs. (2.10) and (2.13), and the geometric relationships of Eq. (2.14) to eliminate V_s and θ in Eq. (2.9), we can write the transverse force balance for a beam element $\mathrm{d}x$ as

$$f = \underbrace{\frac{1}{1 + w'^2} M'' - 2\frac{w''w'}{(1 + w'^2)^2} M'}_{\text{Bending stiffness, } f_\mathrm{b}} + \underbrace{\frac{w''}{(1 + w'^2)^{3/2}} N - \frac{w'}{\sqrt{1 + w'^2}} N'}_{\text{Membrane stiffness, } f_\mathrm{m}} \tag{2.15}$$

The bending moment on the section face around the neutral axis, M, can be calculated by integrating the normal stress due to bending moment over the section area A

$$M = \int z\, \sigma_x \, \mathrm{d}A \tag{2.16}$$

The stress σ in the axial direction $\sigma_x(x, z, t)$, under elastic deformation is given by

$$\sigma_x = E\, \varepsilon_x \tag{2.17}$$

where $\varepsilon_x(x, z, t)$ is the axial strain, and E is the elastic modulus of the beam. This linear relationship is valid within the elastic regime of interest. Inserting this equation into the moment equation, we obtain

$$M = E \int_{-h/2}^{h/2} \int_{-b/2}^{b/2} z\varepsilon_x \, \mathrm{d}y \, \mathrm{d}z$$

Carrying out the integration over the beam width, we obtain

$$M = Eb \int_{-h/2}^{h/2} z\, \varepsilon_x \, \mathrm{d}z \tag{2.18}$$

The true elastic strain can be written as:

$$\varepsilon_x = \ln\Big(\frac{ds(z)}{ds(0)}\Big) \tag{2.19}$$

Expanding the logarithmic function around unity, we obtain

$$\begin{aligned}\varepsilon_x = \frac{ds(z)-ds(0)}{ds(0)} - \frac{1}{2}\Big(\frac{ds(z)-ds(0)}{ds(0)}\Big)^2 + \frac{1}{3}\Big(\frac{ds(z)-ds(0)}{ds(0)}\Big)^3 \\ - \frac{1}{4}\Big(\frac{ds(z)-ds(0)}{ds(0)}\Big)^4 + O(\epsilon^5)\end{aligned} \tag{2.20}$$

where ϵ is a small bookeeping parameter. Noting that,

$$\begin{aligned}\frac{ds(z)-ds(0)}{ds(0)} &= \frac{(\rho+z)d\theta - \rho d\theta}{\rho d\theta} \\ &= \frac{z}{\rho}\end{aligned}$$

we can drop terms of order $O(\epsilon^5)$ and higher and rewrite the strain as

$$\varepsilon_x = \frac{z}{\rho} - \frac{1}{2}\Big(\frac{z}{\rho}\Big)^2 + \frac{1}{3}\Big(\frac{z}{\rho}\Big)^3 - \frac{1}{4}\Big(\frac{z}{\rho}\Big)^4 \tag{2.21}$$

Substituting it into the moment equation,

$$\begin{aligned}M = \frac{Eb}{\rho}\int_{-h/2}^{h/2} z^2 \, \mathrm{d}z - \frac{1}{2}\frac{Eb}{\rho^2}\int_{-h/2}^{h/2} z^3 \, \mathrm{d}z + \frac{1}{3}\frac{Eb}{\rho^3}\int_{-h/2}^{h/2} z^4 \, \mathrm{d}z \\ - \frac{1}{4}\frac{Eb}{\rho^4}\int_{-h/2}^{h/2} z^5 \, \mathrm{d}z + \cdots\end{aligned} \tag{2.22}$$

For symmetric sections, integrals of odd powers of z vanish identically and the moment

equation reduces to

$$\begin{aligned} M &= \frac{Eb}{\rho}\int_{-h/2}^{h/2} z^2\,\mathrm{d}z + \frac{1}{3}\frac{Eb}{\rho^3}\int_{-h/2}^{h/2} z^4\,\mathrm{d}z + \cdots \\ &= \frac{Eb}{12\rho}h^3 + \frac{Eb}{240\rho^3}h^5 + \cdots \end{aligned} \tag{2.23}$$

Using equation (2.14) to substitute for ρ, we obtain

$$M = \frac{Eb}{12}h^3\Big(\frac{w''}{(1+w'^2)^{3/2}}\Big) + \frac{Eb}{240}h^5\Big(\frac{w''}{(1+w'^2)^{3/2}}\Big)^3 + \cdots \tag{2.24}$$

Therefore, as long as h and w'' are of order $O(\epsilon)$, we can drop the second (higher order) term and the moment can be written as,

$$M = \frac{Ebh^3}{12}\frac{w''}{(1+w'^2)^{3/2}} \tag{2.25}$$

This is the same result obtained traditionally using the engineering strain definition of ε_x.

We can use this expression to evaluate the bending stiffness of the beam f_b, the first two terms in Eq. (2.15), as

$$f_\mathrm{b} = \frac{Ebh^3}{12}\left(\frac{1}{1+w'^2}\frac{\mathrm{d}^2}{\mathrm{d}x^2}\Big(\frac{w''}{(1+w'^2)^{3/2}}\Big) - \frac{2w''w'}{(1+w'^2)^2}\frac{\mathrm{d}}{\mathrm{d}x}\Big(\frac{w''}{(1+w'^2)^{3/2}}\Big)\right) \tag{2.26}$$

Carrying out the differentiation with respect to x and expanding the denominators around $w' = 0$ as,

$$\begin{aligned} f_\mathrm{b} = \frac{Ebh^3}{12}\Big(& w^{iv} + (-\frac{5}{2}w^{iv}w'^2 - 9w'''w''w' - 3w''^3) \\ &+ (\frac{35}{8}w^{iv}w'^4 + \frac{63}{2}w'''w''w'^3 + \frac{51}{2}w''^3w'^2) \\ &- 2w'''w''w' + (6w''^3w'^2 + 7w'''w''w'^3)\Big) + \cdots \end{aligned} \tag{2.27}$$

where $w^{iv} \equiv w''''$ is the forth derivative of the transverse deflection with respect to the axial coordinate. We scale the thickness h, transverse deflection w, and slope w' at $O(\epsilon)$ to indicate their smallness. Considering the upscaling of the derivative terms with the mode, we scale the curvature and shear terms w'' and w''' at $O(1)$ and the bending term w^{iv} at

$O(1/\epsilon)$. Dropping terms of order $O(\epsilon^4)$ and higher, the bending stiffness reduces to

$$f_{\mathrm{b}} = \frac{Ebh^3}{12}\left(w^{iv} - \frac{5}{2}w^{iv}w'^2 - 11w'''w''w' - 3w''^3\right) \tag{2.28}$$

A further simplification can be made by assuming a uniform axial load $N(t)$ along the beam. The fundamental axial resonance frequency of a fixed-fixed beam scales as $f_{\mathrm{axial}} \propto \frac{1}{l}\sqrt{\frac{E}{\rho}}$ while the fundamental transverse frequency scales as $f_{\mathrm{trans}} \propto \frac{h}{l^2}\sqrt{\frac{E}{\rho}}$ yielding a frequency ratio of $\frac{f_{\mathrm{axial}}}{f_{\mathrm{trans}}} \propto \frac{l}{h}$. In MEMS and NEMS resonators studied in this work, $(l \gg h)$ with this ratio ranging from 200 to 1000 which indicates that the axial response reaches equilibrium much faster than the transverse response. Therefore, during transverse motion, the axial load can be considered quasi-static and spatially uniform, $N(x,t) \approx N(t)$, and the force balance can be reduced to,

$$f = \frac{1}{1+w'^2}M'' - 2\frac{w''w'}{(1+w'^2)^2}M' + \frac{w''}{(1+w'^2)^{3/2}}N \tag{2.29}$$

The axial load is the sum of an initial (preload) force N_0 and stretching forces applied by the fixed-fixed boundary conditions to elongate the neutral axis as it deflects away from the straight configuration. It can be expressed as

$$N = N_0 + \frac{Ebh}{l}\int_{-l/2}^{l/2}(\sqrt{1+w'^2} - 1)\,\mathrm{d}x \tag{2.30}$$

I note that the latter is purely geometric in origin resulting from nonlinear curvature effects.

Membrane stiffness of the beam f_{m} can, then, be obtained by substituting the axial load into Eq. (2.29) as

$$f_{\mathrm{m}} = \frac{w''}{(1+w'^2)^{3/2}}\left(N_0 + \frac{Ebh}{l}\int_{-l/2}^{l/2}(\sqrt{1+w'^2} - 1)\,\mathrm{d}x\right) \tag{2.31}$$

Expanding the denominator and integrand around $w' = 0$ and dropping terms of order $O(\epsilon^4)$ and higher, we can write it as

$$f_{\mathrm{m}} = N_0\left(w'' - \frac{3}{2}w''w'^2\right) + \frac{Ebh}{2l}w''\int_{-l/2}^{l/2}w'^2\,\mathrm{d}x \tag{2.32}$$

The static equilibrium equation can, therefore be written as

$$f = \frac{Ebh^3}{12}\left(w^{iv} - \frac{5}{2}w^{iv}w'^2 - 11w'''w''w' - 3w''^3\right) + N_0\left(w'' - \frac{3}{2}w''w'^2\right) + \frac{Ebh}{2l}w''\int_{-l/2}^{l/2} w'^2\,\mathrm{d}x \tag{2.33}$$

For comparison, the traditional form of the weekly nonlinear equilibrium equation is [241]

$$f = \frac{Ebh^3}{12}w^{iv} + N_0w'' + \frac{Ebh}{l}\frac{1}{2}w''\int_{-l/2}^{l/2} w'^2\,\mathrm{d}x \tag{2.34}$$

and the linear equation is

$$f = \frac{Ebh^3}{12}w^{iv} \tag{2.35}$$

2.2.3 Equation of Motion

Using Newton's 2nd law, the dynamic force balance in the transverse direction, $\sum F_z = m\ddot{w}$, yields

$$f - \frac{\mathrm{d}}{\mathrm{d}x}\left(V_s\cos\theta - N\sin\theta\right) = \rho bh\ddot{w} \tag{2.36}$$

where ρ is the density of the beam. As $u = 0$, the force balance in the axial direction, $\sum F_x = 0$, yields

$$\frac{\mathrm{d}}{\mathrm{d}x}\left(V_s\sin\theta - N\cos\theta\right) = 0 \tag{2.37}$$

Finally, the moment balance around the perpendicular axis, $\sum M_y = I_{yy}\ddot{\theta}$, yields

$$\frac{\mathrm{d}M}{\mathrm{d}x} - V_s\frac{\mathrm{d}s}{\mathrm{d}x} = \rho\frac{bh^3}{12}\ddot{\theta} \tag{2.38}$$

where the second moment of inertia of the cross-sectional beam element I_{yy} is

$$I_{yy} = \int z^2 dm = \int z^2(\rho\, b\,\mathrm{d}x)\mathrm{d}z = \frac{1}{12}\rho\, b\, h^3\mathrm{d}x$$

Using the effort balance relationships, Eqs. (2.37), (2.38), and the geometric relationships of Eq. (2.14) to eliminate V_s and θ in Eqs. (2.36), we can write the equation of motion

of the beam element $\mathrm{d}x$ in the transverse direction as

$$\begin{aligned} f+\rho bh\ddot{w}+\frac{\rho bh^3}{12}\Big(\frac{\ddot{w}''}{(1+w'^2)^2}-2\frac{w''\dot{w}'^2}{(1+w'^2)^4}-2\frac{w'w''\ddot{w}'}{(1+w'^2)^3}-4\frac{w'\dot{w}'\dot{w}''}{(1+w'^2)^3}\Big) \\ =\frac{1}{1+w'^2}M''-2\frac{w''w'}{(1+w'^2)^2}M'+\frac{w''}{(1+w'^2)^{3/2}}N-\frac{w'}{\sqrt{1+w'^2}}N' \end{aligned} \tag{2.39}$$

Substituting with the moment expression from Eq. (2.25) and the axial force expression from Eq.(2.30) ino this equation, we obtain

$$\begin{aligned} f+\rho bh\ddot{w}+\frac{\rho bh^3}{12}\Big(\frac{\ddot{w}''}{(1+w'^2)^2}-2\frac{w''\dot{w}'^2}{(1+w'^2)^4}-2\frac{w'w''\ddot{w}'}{(1+w'^2)^3}-4\frac{w'\dot{w}'\dot{w}''}{(1+w'^2)^3}\Big) \\ =\frac{Ebh^3}{12}\big(w^{iv}-\frac{5}{2}w^{iv}w'^2-11w'''w''w'-3w''^3\big) \\ +N_0\big(w''-\frac{3}{2}w''w'^2\big)+\frac{Ebh}{2l}w''\int_{-l/2}^{l/2}w'^2\,\mathrm{d}x \end{aligned} \tag{2.40}$$

Expanding the denominators in the equation around $w'=0$ and retaining terms up to order $O(\epsilon^4)$, we can rewrite the equation as

$$\begin{aligned} f+\rho bh\ddot{w}+\frac{\rho bh^3}{12}\ddot{w}''=&\frac{Ebh^3}{12}\big(w^{iv}-\frac{5}{2}w^{iv}w'^2-11w'''w''w'-3w''^3\big) \\ &+N_0\big(w''-\frac{3}{2}w''w'^2\big)+\frac{Ebh}{2l}w''\int_{-l/2}^{l/2}w'^2\,\mathrm{d}x \end{aligned} \tag{2.41}$$

For comparison, the traditional form of the weekly nonlinear equation of motion is [241]

$$f+\rho bh\ddot{w}=\frac{Ebh^3}{12}w^{iv}+N_0w''+\frac{Ebh}{2l}w''\int_{-l/2}^{l/2}w'^2\,\mathrm{d}x \tag{2.42}$$

For comparison, the simplest form of the beam equation of motion occurs in absence of axial forces and nonlinearity as

$$f+\rho bh\ddot{w}=\frac{Ebh^3}{12}w^{iv} \tag{2.43}$$

2.2.4 External Forces

The distributed external loads f acting on the beam along the transverse direction include distributed damping f_{d}, electrostatic f_{es}, and thermomechanical f_{th} forces.

$$f(x,t) = f_{\mathrm{d}} + f_{\mathrm{es}} + f_{\mathrm{th}} \tag{2.44}$$

In continuum mechanics, viscous damping is used to represent energy loss phenomena, in which the damping force is proportional to the element velocity through a fluid. Also, this damping force increases with the width of the element, as a wider surface interacts more strongly with the surrounding fluid. Therefore, the relationship for a beam element can be written as,

$$f_{\mathrm{d}}\,\mathrm{d}x = \hat{c}\,b\,\dot{w}\,\mathrm{d}x \tag{2.45}$$

where $\hat{c}$ is the viscous damping coefficient per unit area.

In classical statistical mechanics, the equipartition theorem relates the temperature of a system to its average energies. The theorem states that at thermal equilibrium, energy is distributed equally among all degrees of freedom. As these degrees of freedom will be preseted in a later section, for the construction of PDE, the thermomechnical noise will be presented as a stochastic force that can be represented over a beam element by

$$f_{\mathrm{th}}\,\mathrm{d}x = \hat{\xi}_{\mathrm{th}}(t)\,\mathrm{d}x \tag{2.46}$$

where $\hat{\xi}_{\mathrm{th}}(t)$ represents a uniformly distributed stochastic process (white-noise in frequency domain) without any phase. The details will be discussed in the following sections. This thermomechanical noise represent an external force acting on the beam. Thermomechanical noise keeps the beam in thermal equilibrium with its environment by supplying back energy lost into the environment via damping , such that the beam will not cool down spontaneously below the thermal bath temperature.

While several actuation mechanisms are applicable to micro and nano beams, electrostatic actuation is the most common mechanism in N/MEMS. The electrostatic force acting on the beam element can be represented by

$$f_{\mathrm{es}}\,\mathrm{d}x = \frac{1}{2}\frac{\epsilon b\,\mathrm{d}x}{(d-w)^2}V^2 \tag{2.47}$$

where $V = V(t)$ is the voltage difference between the beam and the actuation electrode, d is the gap between the unactuated beam and the electrode, and ϵ is the permittivity of the medium between the beam and electrode.

Using Eqs. (2.45)– (2.47) in Eq. (2.41), we can write the equation of motion as

$$\begin{aligned}\rho bh(\ddot{w}+\frac{h^2}{12}\ddot{w}'')+\hat{c}b\dot{w}+\frac{Ebh^3}{12}\big(w^{iv}-\frac{5}{2}w^{iv}w'^2-11w'''w''w'-3w''^3\big)\\ +N_0\big(w''-\frac{3}{2}w''w'^2\big)+\frac{Ebh}{2l}w''\int_{-l/2}^{l/2}w'^2\,\mathrm{d}x=\frac{1}{2}\frac{\epsilon b}{(d-w)^2}V^2+\hat{\xi}_{\mathrm{th}}(t)\end{aligned} \tag{2.48}$$

For comparison, the traditional form of the weekly nonlinear equation of motion is [241]

$$\rho bh\ddot{w}+\hat{c}b\dot{w}+\frac{Ebh^3}{12}w^{iv}+N_0w''+\frac{Ebh}{2l}w''\int_{-l/2}^{l/2}w'^2\,\mathrm{d}x=\frac{1}{2}\frac{\epsilon b}{(d-w)^2}V^2 \tag{2.49}$$

To derive the linear companion equation of motion, we expand the electrostatic force expression around $w=0$ as,

$$\frac{1}{2}\frac{\epsilon b}{(d-w)^2}V^2=\frac{1}{2}\epsilon bV^2\Big(\frac{1}{d^2}+\frac{2w}{d^3}+\frac{3w^2}{d^4}+\frac{4w^3}{d^5}+\cdots\Big) \tag{2.50}$$

Therefore, the linear form of the equation of motion can be written as

$$\rho bh\ddot{w}+\hat{c}b\dot{w}+\frac{Ebh^3}{12}w^{iv}+N_0w''=\frac{1}{2}\epsilon bV^2\big(\frac{1}{d^2}+\frac{2w}{d^3}\big)+\hat{\xi}_{\mathrm{th}}(t) \tag{2.51}$$

2.3 Eigenvalue Analysis

Dropping damping, axial load, forcing, and nonlinearity, reduces the equation of motion to,

$$\rho bh\ddot{w}+\frac{Ebh^3}{12}w^{iv}=0 \tag{2.52}$$

This equation can be solved by separation of variables, assuming the solution form

$$w(x,t)=\phi(x)\,e^{i\omega t} \tag{2.53}$$

where $\phi=\phi(x)$ is a mode shape of the straight undamped fixed-fixed beam and the exponential term represents a harmonic time-dependent response with an eigenfrequency of ω.

Substituting this solution form into boundary conditions of the beam:

$$\begin{aligned} w(-l/2,t) = \phi_i(-l/2)\, e^{i\omega t} = 0 \quad &, \quad w(l/2,t) = \phi_i(l/2)\, e^{i\omega t} = 0 \\ w'(-l/2,t) = \phi_i'(-l/2)\, e^{i\omega t} = 0 \quad &, \quad w'(l/2,t) = \phi_i'(l/2)\, e^{i\omega t} = 0 \end{aligned} \tag{2.54}$$

we find that a non-trivial solution requires elimination of the time-dependent term $e^{i\omega t}$, thereby reducing the boundary conditions to:

$$\begin{aligned} \phi_i(-l/2) = 0 \quad &, \quad \phi_i'(-l/2) = 0 \\ \phi_i(l/2) = 0 \quad &, \quad \phi_i'(l/2) = 0 \end{aligned} \tag{2.55}$$

Inserting the solution form of Eq. (2.53) into Eq. (2.52) results in,

$$\phi^{iv} = \frac{12\rho}{Eh^2}\omega^2\phi \tag{2.56}$$

The solution of this ODE is of the form,

$$\phi(x) = C_1 \cos\left(\lambda\frac{x}{l}\right) + C_2 \sin\left(\lambda\frac{x}{l}\right) + C_3 \cosh\left(\lambda\frac{x}{l}\right) + C_4 \sinh\left(\lambda\frac{x}{l}\right) \tag{2.57}$$

where the wavenumber λ/l is related to the eigenfrequency (natural frequency) by,

$$\omega = \lambda^2 \sqrt{\frac{E}{12\rho}} \frac{h}{l^2} \tag{2.58}$$

To solve for the coefficients C_i, and λ, I substitute the modal form into the boundary conditions, Eqs. (2.55), yielding a homogeneous system of equations, which can be written in matrix form as:

$$\begin{bmatrix} \cos(\lambda/2) & -\sin(\lambda/2) & \cosh(\lambda/2) & -\sinh(\lambda/2) \\ \frac{\lambda}{l}\sin(\lambda/2) & \frac{\lambda}{l}\cos(\lambda/2) & -\frac{\lambda}{l}\sinh(\lambda/2) & \frac{\lambda}{l}\cosh(\lambda/2) \\ \cos(\lambda/2) & \sin(\lambda/2) & \cosh(\lambda/2) & \sinh(\lambda/2) \\ -\frac{\lambda}{l}\sin(\lambda/2) & \frac{\lambda}{l}\cos(\lambda/2) & \frac{\lambda}{l}\sinh(\lambda/2) & \frac{\lambda}{l}\cosh(\lambda/2) \end{bmatrix} \begin{bmatrix} C_1 \\ C_2 \\ C_3 \\ C_4 \end{bmatrix} = \begin{bmatrix} 0 \\ 0 \\ 0 \\ 0 \end{bmatrix} \tag{2.59}$$

For a nontrivial solution, the determinant of the coefficient matrix must be equal to zero. Therefore, the corresponding characteristic equation can be written as

$$\cos(\lambda)\cosh(\lambda) = 1 \tag{2.60}$$

where the trivial solution $\lambda = 0$ has been eliminated.

The solutions of the characteristic equation can be visualized by observing the intersections of the functions $y = \cos(\lambda)\cosh(\lambda)$ and $y = 1$. Each of these solutions corresponds to a mode shape $\phi_i(x)$ and its natural frequency ω_i. Those solutions are approximately $\lambda_i \approx \frac{(2i+1)\pi}{2}$ with the error of the approximation diminishing as the mode number i increase.

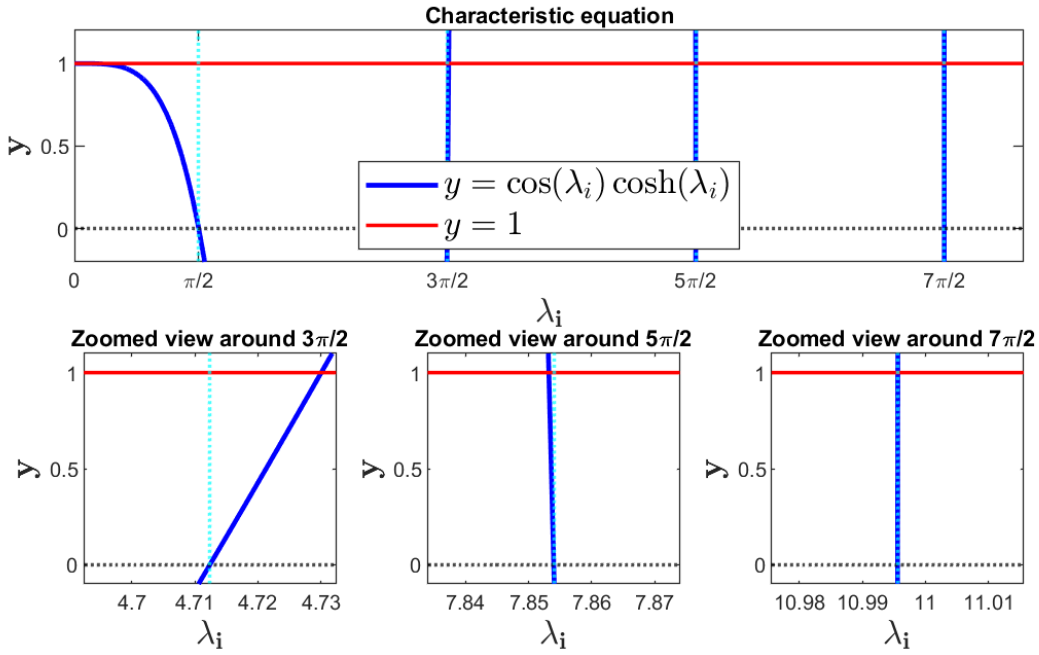


Figure 2.2: Graphical solution of the characteristic equation, $\cos(\lambda_i)\cosh(\lambda_i) = 1$.

For non-repeating roots λ_i, substituting λ_i into Eq. (2.59) results in a linear system matrix rank-deficient by one. It can only be solved for three out of the four constants in the mode shape expression in terms of the fourth constant. The reduced linear system for the first mode shape can be written by substituting for $\lambda_1 = 4.730$ into Eq. (2.59) and eliminating the row corresponding to the boundary condition $\phi_1'(l/2) = 0$ to obtain:

$$\begin{bmatrix} 0.9825 & -7.527 & 7.395 \\ -1.018 & -7.527 & 7.661 \\ -0.9825 & -7.527 & -7.395 \end{bmatrix} \begin{bmatrix} C_{1,2} \\ C_{1,3} \\ C_{1,4} \end{bmatrix} = \begin{bmatrix} C_{1,1} \\ C_{1,1} \\ C_{1,1} \end{bmatrix} \tag{2.61}$$

Solving this system gives:

$$\begin{bmatrix} C_{1,2} \\ C_{1,3} \\ C_{1,4} \end{bmatrix} = \begin{bmatrix} 0 \\ -0.1329\, C_{1,1} \\ 0 \end{bmatrix} \tag{2.62}$$

Therefore, the first mode shape is:

$$\phi_1(x) = C_{1,1}\big(\cos\big(4.73\frac{x}{l}\big) - 0.1329\cosh\big(4.73\frac{x}{l}\big)\big) \tag{2.63}$$

I set the $C_{1,1}$ to enforce orthonormality of the mode shapes,

$$\int_{-l/2}^{l/2} \phi_i \phi_j \,\mathrm{d}x = l\delta_{ij} \tag{2.64}$$

where δ_{ij} is Kronecker delta. In nondimensional terms, this equation can be written as

$$\int_{-1/2}^{1/2} \phi_i \phi_j \,\mathrm{d}\hat{x} = \delta_{ij} \tag{2.65}$$

where $\hat{x} = x/l$. The constant $C_{1,1}$, can therefore be evaluated by substituting with $\phi_1(x)$ inot this equation to obtain:

$$C_{1,1}^2 \int_{-1/2}^{1/2} \big(\cos\big(4.73\hat{x}\big) - 0.1329\cosh\big(4.7\hat{x}\big)\big)^2 d\hat{x} = 1 \tag{2.66}$$

Numerically evaluating the integral yields:

$$C_{1,1} = 1.4019 \tag{2.67}$$

Thus, the normalized first mode shape is:

$$\phi_1(x) = 1.4019\cos\big(4.7300\frac{x}{l}\big) - 0.1863\cosh\big(4.7300\frac{x}{l}\big) \tag{2.68}$$

The same procedure can be applied to compute other mode shapes. However, even numbered modes are written in terms of $C_{i,2}$ instead of $C_{i,1}$. This choice reflects the dominant coefficient in each mode shape. Following this procedure, the first ten modes

shapes can be written as:

$$\begin{bmatrix} C_{1,1} & C_{1,2} & C_{1,3} & C_{1,4} & \lambda_1 \\ C_{2,1} & C_{2,2} & C_{2,3} & C_{2,4} & \lambda_2 \\ C_{3,1} & C_{3,2} & C_{3,3} & C_{3,4} & \lambda_3 \\ C_{4,1} & C_{4,2} & C_{4,3} & C_{4,4} & \lambda_4 \\ C_{5,1} & C_{5,2} & C_{5,3} & C_{5,4} & \lambda_5 \\ C_{6,1} & C_{6,2} & C_{6,3} & C_{6,4} & \lambda_6 \\ C_{7,1} & C_{7,2} & C_{7,3} & C_{7,4} & \lambda_7 \\ C_{8,1} & C_{8,2} & C_{8,3} & C_{8,4} & \lambda_8 \\ C_{9,1} & C_{9,2} & C_{9,3} & C_{9,4} & \lambda_9 \\ C_{10,1} & C_{10,2} & C_{10,3} & C_{10,4} & \lambda_{10} \end{bmatrix} = \begin{bmatrix} 1.4019 & 0 & 1.8625 \times 10^{-1} & 0 & 4.7300 \\ 0 & 1.4148 & 0 & 3.9436 \times 10^{-2} & 7.8532 \\ -1.4142 & 0 & 8.1914 \times 10^{-3} & 0 & 10.9956 \\ 0 & -1.4142 & 0 & 1.7029 \times 10^{-3} & 14.1372 \\ 1.4142 & 0 & 3.5399 \times 10^{-4} & 0 & 17.2788 \\ 0 & 1.4142 & 0 & 7.3588 \times 10^{-5} & 20.4204 \\ -1.4142 & 0 & 1.5297 \times 10^{-5} & 0 & 23.5619 \\ 0 & -1.4142 & 0 & 3.1800 \times 10^{-6} & 26.7035 \\ 1.4142 & 0 & 6.6106 \times 10^{-7} & 0 & 29.8451 \\ 0 & 1.4142 & 0 & 1.3742 \times 10^{-7} & 32.9867 \end{bmatrix} \tag{2.69}$$

Inspecting the mode shapes, we note that they take either a symmetric or anti-symmetric form depending on whether the mode number is odd or even, respectively,

$$\phi_i(x) = \begin{cases} C_{i,1} \sin(\dfrac{\lambda_i x}{l}) + C_{i,2} \sinh(\dfrac{\lambda_i x}{l}) & ;\ i = 1, 3, 5, \dots \\ C_{i,3} \cos(\dfrac{\lambda_i x}{l}) + C_{i,4} \cosh(\dfrac{\lambda_i x}{l}) & ;\ i = 2, 4, 6, \dots \end{cases} \tag{2.70}$$

The first ten mode shapes are plotted in Figure 2.3. We note that enforcing the slope boundary conditions at both ends results in packing up of the alternating curvatures domain away from the boundaries $x = \pm l/2$. Those mode shapes will be used to expand the beam deflection $w(x,t)$ following the Galerkin method, in order to project the spatial variation of the equation of motion onto a modal basis, thus converting the PDE into a set of time-dependent ODEs.

2.4 Reduced Order Model

Towards that end, I express the transverse deflection of the beam as the infinite sum:

$$w(x,t) = \sum_{i=1}^{\infty} \phi_i(x)\, q_i(t) \tag{2.71}$$

where $\phi_i(x)$ are the normalized mode shapes of a straight fixed-fixed beam and $q_i(t)$ are the corresponding time-dependent modal coordinates.

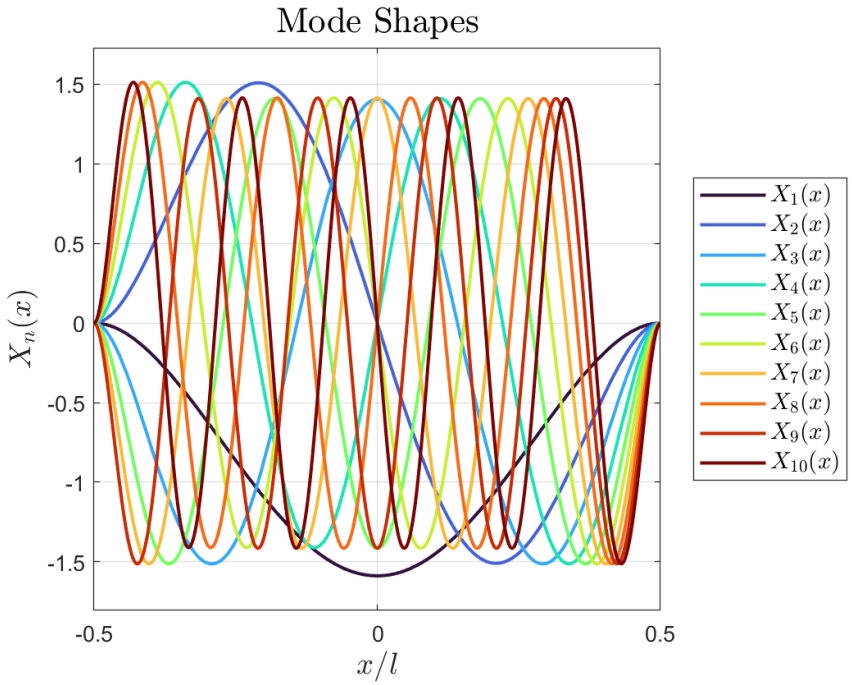


Figure 2.3: The first ten normalized mode shapes of a fixed–fixed beam $\phi_i(x)$ as functions of the nondimensional position x/l.

The PDE, Eq. (2.51) can be rewritten as the force balance,

$$\underbrace{\rho bh\ddot{w}}_{f_{\text{in}}} + \underbrace{c\dot{w}}_{f_{\text{d}}} + \underbrace{\frac{Ebh^3}{12}w^{iv}}_{f_{\text{b}}} + \underbrace{N_0 w''}_{f_{\text{m}}} = \underbrace{\frac{1}{2}\epsilon bV^2\left(\frac{1}{d^2} + \frac{2w}{d^3}\right)}_{f_{\text{es}}} + \underbrace{\hat{\xi}_{\text{th}}(t)}_{f_{\text{th}}} \tag{2.72}$$

which includes the distributed inertial force f_{in}, damping force f_{d}, bending stiffness f_{b}, membrane stiffness f_{m}, electrostatic force f_{es}, and thermomechanical force f_{th}.

The Galerkin method posits that the integral:

$$\int_{-l/2}^{l/2} (\text{PDE})\, \phi_n \, \mathrm{d}x = 0 \tag{2.73}$$

must vanish. For given mode shape ϕ_n, carrying out the integration over the beam domain,

eliminates the PDE's dependence on the spatial variable x and reduces it to the ODE,

$$\int_{-l/2}^{l/2} \big(f_{\text{in}} + f_{\text{d}} + f_{\text{b}} + f_{\text{m}}\big)\phi_n \,\mathrm{d}x = \int_{-l/2}^{l/2} \big(f_{\text{es}} + f_{\text{th}}\big)\phi_n \,\mathrm{d}x \tag{2.74}$$

$$F_{\text{in}} + F_{\text{d}} + F_{\text{b}} + F_{\text{m}} = F_{\text{es}} + F_{\text{th}} \tag{2.75}$$

Inertial force

The distributed inertial force can be projected onto the mode shape as,

$$F_{\text{in}} = \int_{-l/2}^{l/2} \rho b h \ddot{w} \phi_n \,\mathrm{d}x \tag{2.76}$$

Using $\ddot{w} = \sum_{i=1}^{\infty} \phi_i \ddot{q}_i$ in the integrand, reduces it to,

$$F_{\text{in}} = \rho b h \sum_{i=1}^{\infty} \ddot{q}_i \int_{-l/2}^{l/2} \phi_i \phi_n \,\mathrm{d}x \tag{2.77}$$

Using the orthonormality condition, Eq. (2.64), we can write the inertial force projected onto ϕ_n as,

$$F_{\text{in}} = m\, \ddot{q}_n \tag{2.78}$$

where $m = \rho b h l$.

Damping force

The distributed damping force can be projected onto the mode shape as,

$$F_{\text{d}} = \int_{-l/2}^{l/2} \hat{c} b \dot{w} \phi_n \,\mathrm{d}x \tag{2.79}$$

Using $\dot{w} = \sum_{i=1}^{\infty} \phi_i \dot{q}_i$, in the integrand, reduces it to,

$$F_{\text{d}} = \hat{c} b \sum_{i=1}^{\infty} \dot{q}_i \int_{-l/2}^{l/2} \phi_i \phi_n \,\mathrm{d}x \tag{2.80}$$

Using the orthonormality condition, we can write the damping force projected onto ϕ_n as,

$$F_{\mathrm{d}} = c\,\dot{q}_n \tag{2.81}$$

where $c = \hat{c}bl$.

Bending stiffness

Bending stiffness and can be projected onto the mode shape as,

$$F_{\mathrm{b}} = \int_{-l/2}^{l/2} \frac{Ebh^3}{12} w^{iv} \phi_n \,\mathrm{d}x \tag{2.82}$$

Recalling Eq. (2.70), we write that

$$w^{iv} = \sum_{i=1}^{\infty} \frac{\lambda_i^4}{l^4} \phi_i \, q_i$$

Substituting with this equation into the integrand, reduces it to

$$F_{\mathrm{b}} = \frac{Ebh^3}{12l^4} \sum_{i=1}^{\infty} q_i \lambda_i^4 \int_{-l/2}^{l/2} \phi_i \phi_n \,\mathrm{d}x \tag{2.83}$$

Using the orthonormality condition, we can write the bending stiffness project onto ϕ_n as,

$$F_{\mathrm{b}} = k_n^{\mathrm{b}} \, q_n \tag{2.84}$$

where $k_n^{\mathrm{b}} = \frac{Ebh^3}{12l^3} \lambda_n^4$.

Membrane stiffness

Membrane stiffness and can be projected onto the mode shape as,

$$F_{\mathrm{m}} = \int_{-l/2}^{l/2} N_0 w'' \phi_n \,\mathrm{d}x \tag{2.85}$$

Using Eq. (2.71) in the integrand, yields

$$F_{\mathrm{m}} = N_0 \sum_{i=1}^{\infty} q_i \int_{-l/2}^{l/2} \phi_i'' \phi_n \, \mathrm{d}x \tag{2.86}$$

$$= \frac{N_0}{l} \sum_{i=1}^{\infty} c_{i,n}^{\mathrm{m}} \, q_i \tag{2.87}$$

where $c_{i,n}^{\mathrm{m}} = l \int_{-l/2}^{l/2} \phi_i'' \phi_n \, \mathrm{d}x$ is a nondimensional coefficient.

Electrostatic force

The distributed electrostatic force can be projected onto the mode shape as,

$$F_{\mathrm{es}} = \int_{-l/2}^{l/2} \frac{1}{2} \epsilon b V^2 \big(\frac{1}{d^2} + \frac{2w}{d^3} \big) \phi_n \, \mathrm{d}x \tag{2.88}$$

$$= \frac{\epsilon b V^2}{2d^2} \int_{-l/2}^{l/2} \phi_n \, \mathrm{d}x + \frac{\epsilon b V^2}{d^3} \sum_{i=1}^{\infty} q_i \int_{-l/2}^{l/2} \phi_i \phi_n \, \mathrm{d}x \tag{2.89}$$

Using the orthonormality condition, we can write the electrostatic force project onto ϕ_n as,

$$F_{\mathrm{es}} = \frac{\epsilon b l V^2}{d^2} \Big(\frac{c_n^{\mathrm{es}}}{2} + \frac{1}{d} q_n \Big) \tag{2.90}$$

where $c_n^{\mathrm{es}} = \frac{1}{l} \int_{-l/2}^{l/2} \phi_n \, \mathrm{d}x$ is a nondimensional coefficient.

Thermomechanical force

The distributed thermomechanical force can be projected onto the mode shape as,

$$\xi_{\mathrm{th}}(t) = \int_{-l/2}^{l/2} \hat{\xi}_{\mathrm{th}}(t) \phi_n \, \mathrm{d}x \tag{2.91}$$

where is the ξ_{th} is the projected thermomechanical force acting on the beam.

Equation of Motion

Combining force contributions, the equation of motion becomes,

$$m\ddot{q}_n + c\dot{q}_n + k_n^{\mathrm{b}} q_n + \frac{N_0}{l}\sum_{i=1}^{\infty} c_{i,n}^{\mathrm{m}}\, q_i = \frac{\epsilon b l V^2}{d^2}\left(\frac{c_n^{\mathrm{es}}}{2} + \frac{1}{d} q_n\right) + \xi_{\mathrm{th}}(t) \tag{2.92}$$

which can be rewritten as,

$$m\ddot{q}_n + c\dot{q}_n + \underbrace{\left(k_n^{\mathrm{b}} + c_{n,n}^{\mathrm{m}}\frac{N_0}{l} - \frac{\epsilon b l V^2}{d^3}\right)}_{k_n} q_n + \frac{N_0}{l}\sum_{\substack{i=1 \\ i\neq n}}^{\infty} c_{i,n}^{\mathrm{m}}\, q_i = \frac{\epsilon c_n^{\mathrm{es}} b l V^2}{2d^2} + \xi_{\mathrm{th}}(t) \tag{2.93}$$

where $k_n = k_n^{\mathrm{b}} + c_{n,n}^{\mathrm{m}}\frac{N_0}{l} - \frac{\epsilon b l V^2}{d^3}$ is the effective stiffness of the n^{th} mode composed of bending stiffness, membrane stiffness, and electrostatic softening, respectively. Assuming that the linear coupling terms introduced by membrane stiffness are negligible, the equation of motion reduces to,

$$m\ddot{q}_n + c\dot{q}_n + k_n q_n = \frac{\epsilon b l V^2}{2d^2} c_n^{\mathrm{es}} + \xi_{\mathrm{th}}(t) \tag{2.94}$$

2.5 Sensor Metrics

I study in this section the performance metrics of an inertial sensor designed to exploit the resonance of the n^{th} mode. For the sake of simplicity, the subscript indicating the modal index n will be omitted hereafter. In the absence of disturbances, the modal equation of motion

$$m\ddot{q} + c\dot{q} + kq = 0 \tag{2.95}$$

has the solution

$$q(t) = (A_1 e^{i\omega_n\sqrt{1-\zeta^2}t} + A_2 e^{-i\omega_n\sqrt{1-\zeta^2}t})e^{-\zeta\omega_n t} \tag{2.96}$$

where the natural frequency ω_n is defined as

$$\omega_n \equiv \sqrt{\frac{k}{m}}$$

the damping ratio ζ is defined as

$$\zeta \equiv \frac{c}{2\sqrt{km}}$$

and A_1 and A_2 are real constants. For an underdamped response ($\zeta < 1$), it can be written as,

$$q(t) = B\cos(\omega_d t + \varphi)e^{-\zeta\omega_n t} \tag{2.97}$$

where B is a real constant, the damped natural frequency ω_d is

$$\omega_d \equiv \omega_n\sqrt{1-\zeta^2}$$

and φ is the phase of the response.

Quality Factor

The quality factor Q relates the energy stored in the system $\langle E\rangle$ to the energy lost per oscillation cycle ΔE,

$$Q \equiv 2\pi\frac{\langle E\rangle}{\Delta E} \tag{2.98}$$

The total mechanical energy can be written as the summation of potential and kinetic energies as,

$$E = \frac{1}{2}kq^2 + \frac{1}{2}m\dot{q}^2 \tag{2.99}$$

and from Eq. (2.96), it can be written as,

$$\begin{aligned} E = \frac{B^2}{2}k\cos^2(\omega_d t+\varphi)e^{-2\zeta\omega_n t} + \frac{B^2}{4}m\omega_n^2 e^{-2\zeta\omega_n t}\big(1-(1-2\zeta^2)\cos(2\omega_d t+2\varphi) \\ + 2\zeta\sqrt{1-\zeta^2}\sin(2\omega_d t+2\varphi)\big) \end{aligned} \tag{2.100}$$

and using $\langle\cos^2(\omega_d t+\varphi)\rangle = \frac{1}{2}$, $\langle\cos\big(2(\omega_d t+\varphi)\rangle = 0$, and $\langle\sin\big(2(\omega_d^2 t+\varphi)\big)\rangle = 0$, the expectation value of energy over a period $\frac{\omega_d}{2\pi}$ can be written as,

$$\langle \mathrm{E}\rangle = \frac{B^2}{2}ke^{-2\zeta\omega_n t} \tag{2.101}$$

The dissipated power is,

$$c\dot{q}^2 = \frac{B^2}{2}c\,\omega_n^2 e^{-2\zeta\omega_n t}\big(1-(1-2\zeta^2)\cos(2\omega_d t+2\varphi) + 2\zeta\sqrt{1-\zeta^2}\sin(2\omega_d t+2\varphi)\big) \tag{2.102}$$

and averaging over one cycle yields

$$\langle c\dot{q}^2 \rangle = \frac{B^2}{2} c\,\omega_n^2 e^{-2\zeta\omega_n t} \tag{2.103}$$

Therefore, energy lost per period is,

$$\Delta E = B^2 \pi c \frac{\omega_n^2}{\omega_d} e^{-2\zeta\omega_n t} \tag{2.104}$$

Substituting Eqs. (2.101) and (2.104) into Eq. (2.98),

$$Q = 2\pi \frac{\frac{B^2}{2} k}{B^2 \pi c\, \omega_n^2/\omega_d} \tag{2.105}$$

$$= \frac{m\,\omega_d}{c} \tag{2.106}$$

Lightly damped resonators with $\zeta \leq 0.2$ are typically used in resonant sensing. Therefore, for a typically resonator $\omega_n \geq \omega_d \geq 0.98\omega_n$ and we can assume that $\omega_n \approx \omega_d$ and write,

$$Q = \frac{\sqrt{mk}}{c}$$

$$= \frac{1}{2\zeta} \tag{2.107}$$

I plot in Figure 2.4 the relationship between the quality factor and the ratio of the damped frequency to the natural frequency. It illustrates the closeness of the two frequencies for typical resonant sensors where $Q \geq 2.5$. Neglecting membrane stiffness and electrostatic softening and using this expression for the quality factor, it can be related to the sensors's dimensions by,

$$Q = \frac{\lambda^2}{2\sqrt{3}} \sqrt{\frac{E\rho}{\hat{c}}} \frac{h^2}{l^2} \propto \frac{h^2}{l^2} \tag{2.108}$$

Resonance Frequency

Even though the resonator oscillates with the damped frequency ω_d, the natural frequency ω_n has a much simpler form and as they are numerically similar as visualized in Figure

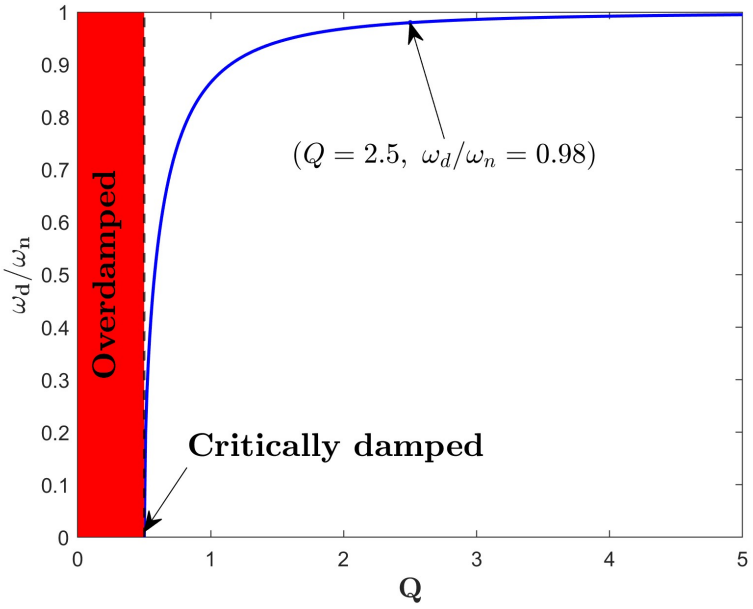


Figure 2.4: The normalized damped frequency as a function of the quality factor.

2.4, the resonance frequency ω_0 can be defined as,

$$\omega_0 \equiv \sqrt{\frac{k}{m}} \tag{2.109}$$

Neglecting membrane stiffness and electrostatic softening, it reduces to,

$$\omega_0 \approx \sqrt{\frac{k^{\mathrm{b}}}{m}} \tag{2.110}$$

inserting the definitions of k^{b} and m yields,

$$\omega_0 = \frac{\lambda^2}{2\sqrt{3}}\sqrt{\frac{E}{\rho}}\frac{h}{l^2} \propto \frac{h}{l^2} \tag{2.111}$$

2.5.1 SNR

The signal-to-noise ratio (SNR) quantifies the relative strength of the measured signal compared to noise (uncertainty in the signal). It is defined as the ratio of the signal $S^s_{qq}(\omega)$ to noise $S^n_{qq}(\omega)$ power spectral density (PSD)s evaluated over the measurement bandwidth $\delta\omega$,

$$\text{SNR} = \frac{\int_{\delta\omega} S^s_{qq}(\omega)\,\mathrm{d}\omega}{\int_{\delta\omega} S^n_{qq}(\omega)\,\mathrm{d}\omega} \tag{2.112}$$

For a small bandwidth $\delta\omega$, the PSDs can be assumed constant simplifying the integration to,

$$\int_{\delta\omega} S_{qq}(\omega)\,\mathrm{d}\omega \approx S_{qq}(\omega)\delta\omega \tag{2.113}$$

and the measured SNR on resonance to,

$$\text{SNR} = \frac{S^s_{qq}(\omega_0)}{S^n_{qq}(\omega_0)} \tag{2.114}$$

To find the sensor's displacement PSD under thermomechanical forcing, its equation of motion

$$m\ddot{q} + c\dot{q} + kq = \xi_{\text{th}}(t) \tag{2.115}$$

is transformed into the frequency-domain using the Fourier transform,

$$(-m\omega^2 + ic\omega + k)Q(\omega) = \Xi_{\text{th}}(\omega) \tag{2.116}$$

where

$$\mathscr{F}\{q(t)\} \equiv Q(\omega) = \int_{-\infty}^{\infty} q(t)e^{-i\omega t}\,\mathrm{d}t \tag{2.117}$$

$$\mathscr{F}\{\xi_{\text{th}}(t)\} \equiv \Xi_{\text{th}}(\omega) = \int_{-\infty}^{\infty} \xi_{\text{th}}(t)e^{-i\omega t}\,\mathrm{d}t \tag{2.118}$$

It can be rewritten as,

$$Q(\omega) = \frac{1}{-m\omega^2 + ic\omega + k}\Xi_{\text{th}}(\omega) \equiv H(\omega)\Xi_{\text{th}}(\omega) \tag{2.119}$$

where $H(\omega)$ is a transfer function. The output PSD is evaluated by obtaining the square

of the magnitude of both sides,

$$S_{qq}^{\text{th}}(\omega) = |H(\omega)|^2 S_{\xi\xi}(\omega) \tag{2.120}$$

The thermomechanical force is stochastic and doesn't have a preferred state. Its PSD can be described as,

$$S_{\xi\xi}(\omega) = \begin{cases} S_{\xi\xi} & ;\omega \geq 0 \\ 0 & ;\omega < 0 \end{cases} \tag{2.121}$$

yielding,

$$S_{qq}^{\text{th}}(\omega) = \begin{cases} \frac{S_{\xi\xi}}{(k-m\omega^2)^2+(c\omega)^2} & ;\omega \geq 0 \\ 0 & ;\omega < 0 \end{cases} \tag{2.122}$$

The mean squared displacement can be found as,

$$\begin{aligned} \langle q^2 \rangle^{\text{th}} = \frac{1}{2\pi}\int_{-\infty}^{\infty} S_{qq}^{\text{th}}\,\mathrm{d}\omega &= \frac{S_{\xi\xi}}{2\pi}\int_{0}^{\infty} \frac{1}{(k-m\omega^2)^2+(c\omega)^2}\,\mathrm{d}\omega \\ &= \frac{S_{\xi\xi}}{2\pi}\frac{\pi}{2kc} \\ &= \frac{S_{\xi\xi}}{4kc} \end{aligned} \tag{2.123}$$

According to the equipartition theorem, at thermal equilibrium the energy of a system is equally distributed among all its degrees of freedom with each degree of freedom possessing an energy of $\frac{1}{2}k_BT$ where k_B is Boltzmann constant and T is temperature. Therefore, we can write that

$$\frac{1}{2}k\langle q^2 \rangle^{\text{th}} = \frac{1}{2}k_BT \tag{2.124}$$

Using Eqs. (2.123) and (2.124), to solve for $S_{\xi\xi}$ we can write that,

$$S_{\xi\xi}(\omega) = \begin{cases} 4k_BTc & ;\ \omega \geq 0 \\ 0 & ;\ \omega < 0 \end{cases} \tag{2.125}$$

and,

$$S_{qq}^{\text{th}}(\omega) = \begin{cases} \frac{4k_BTc}{(k-m\omega^2)^2+(c\omega)^2} & ;\ \omega \geq 0 \\ 0 & ;\ \omega < 0 \end{cases} \tag{2.126}$$

The peak PSD of thermomechanically induced displacement realized at resonance can be

found as,

$$S_{qq}^{\text{th}}(\omega_0) = 4k_B T \frac{m}{kc} \tag{2.127}$$

Ignoring membrane stiffness and electrostatic softening, the effective stiffness reduces to bending stiffness $k = k^{\text{b}}$ and the thermomechanically induced displacement PSD at the resonance can be written as,

$$S_{qq}^{\text{th}}(\omega_0) = \frac{48k_B T}{\lambda^4} \frac{\rho}{E\hat{c}} \frac{l^3}{bh^2} \propto \frac{l^3}{bh^2} \tag{2.128}$$

and the mean squared displacement is,

$$\langle q^2 \rangle^{\text{th}} = \frac{k_B T}{k} = \frac{12k_B T}{\lambda^4} \frac{1}{E} \frac{l^3}{bh^3} \propto \frac{l^3}{bh^3} \tag{2.129}$$

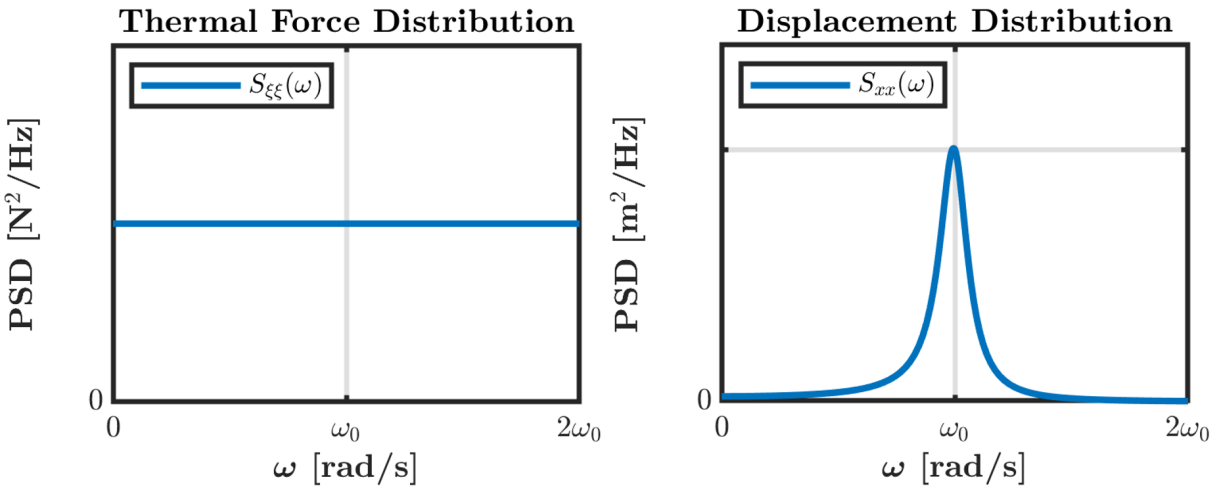


Figure 2.5: PSDs of (a) the thermomechanical force and (b) the displacement it induces.

The PSDs of the thermomechanical force $S_{\xi\xi}(\omega)$ and the displacement it induces $S_{qq}^{\text{th}}(\omega)$ are shown in Figure 2.5. The figures clearly demonstrate that the resonator acts as a filter, transforming the stochastic and white input of thermomechanical noise into a 'colored' displacement response that is concentrated around the resonance frequency.

The peak amplitude of the displacement resulting from a harmonic electrostatic force

with an amplitude of F_{es} is realized at resonance as,

$$\begin{aligned} q^{\text{es}}_{peak} &= Q\frac{F_{\text{es}}}{k} \\ &= \frac{\sqrt{m}}{c\sqrt{k}}F_{\text{es}} \end{aligned} \tag{2.130}$$

The mean squared displacement can be written as,

$$\begin{aligned} \langle q^2\rangle^{\text{es}} &= \frac{1}{2}q^2_{peak} \\ &= \frac{m}{2c^2k}F^2_{\text{es}} \\ &= \frac{3\epsilon^2}{2}\frac{(c^{\text{es}})^2}{\lambda^4}\frac{\rho}{E\hat{c}^2}V^4\frac{l^4}{d^4h^2} \\ &\propto \frac{l^4}{d^4h^2} \end{aligned} \tag{2.131}$$

Assuming a Lorentzian frequency response similar to the thermomechanical response, the displacement PSD can be written as,

$$S^{\text{es}}_{qq}(\omega) = \begin{cases} \frac{2\frac{m}{c}F^2_{\text{es}}}{(k-m\omega^2)^2+(c\omega)^2} & ;\ \omega \geq 0 \\ 0 & ;\ \omega < 0 \end{cases} \tag{2.132}$$

with the peak value of,

$$S^{\text{es}}_{qq}(\omega_0) = \frac{2m^2}{kc^3}F^2_{\text{es}} = \frac{6\epsilon^2}{\lambda^4}\frac{\rho^2}{E\hat{c}^3}(c^{\text{es}})^2V^4\frac{l^4}{d^4h} \propto \frac{l^4}{d^4h} \tag{2.133}$$

Johnson [99] experimentally showed that a stochastic voltage with a PSD of $S_{VV} = 4k_BT_RR$ will appear across the effective resistance R of a circuit placed in a thermal bath at a temperature of T_R. Given that the output voltage $\tilde{V}_R(\omega)$ of the readout circuit can be related to displacement by,

$$\tilde{V}_R(\omega) = G\,Q(\omega) \tag{2.134}$$

where G is a frequency-independent gain, Johnson noise will result in an apparent displacement PSD of,

$$S^V_{qq}(\omega) = \begin{cases} \frac{4k_BT_RR}{G^2} & ;\ \omega \geq 0 \\ 0 & ;\ \omega < 0 \end{cases} \tag{2.135}$$

This indicates that the readout circuit will inject a flat measurement noise floor in the frequency-domain, provided that shot noise and other skirt noise sources are ignored.

Substituting with Eqs. (2.127) and (2.135) into Eq. (2.114), $\mathrm{SNR}^{\mathrm{th}} \equiv \frac{S_{qq}^{\mathrm{th}}(\omega_0)}{S_{qq}^{V}(\omega_0)}$ for a sensor driven exclusively by thermomechanical noise can be written as,

$$\begin{aligned}\mathrm{SNR}^{\mathrm{th}} &= \frac{T}{T_R}\frac{G^2}{R}\frac{m}{kc} \\ &= \frac{12}{\lambda^4}\frac{T}{T_R}\frac{G^2}{R}\frac{\rho}{E\hat{c}}\frac{l^3}{bh^2} \\ &\propto \frac{l^3}{bh^2}\end{aligned} \tag{2.136}$$

This relationship shows that, the SNR for thermomechanically driven sensors improves with decreasing thickness h and width b. In contrast, shortening the sensor length l decreases SNR, therefore, the readout of miniaturized sensors more challenging.

Furthermore, assuming that thermoelectrical noise is negligible compared to thermomechanical noise at resonance $S_{qq}^{V}(\omega_0) \ll S_{qq}^{\mathrm{th}}(\omega_0)$ and substituting with Eqs. (2.127) and (2.133) into Eq. (2.114), the $\mathrm{SNR}^{\mathrm{es}} \equiv \frac{S_{qq}^{\mathrm{es}}(\omega_0)}{S_{qq}^{\mathrm{th}}(\omega_0)}$ for an electrostatically driven sensor can be written as,

$$\begin{aligned}\mathrm{SNR}^{\mathrm{es}} &= \frac{1}{2k_BT}\frac{m}{c^2}F_{\mathrm{es}}^2 \\ &= \frac{\epsilon^2}{8k_B}\frac{\rho}{\hat{c}^2}\frac{(c^{\mathrm{es}})^2V^4}{T}\frac{bhl}{d^4} \\ &\propto \frac{bhl}{d^4}\end{aligned} \tag{2.137}$$

This relationship states that the SNR for electrostatically driven sensors scales down with volume. Highlighting the increasing difficulty of signal extraction in miniaturized electrostatic sensors and the importance of miniaturizing the electrostatic gap d.

2.5.2 Sensitivity

The linear equation of motion, Eq. (2.94), of the sensor shows that a target stimulus that varies its mass m, damping coefficient c, stiffness k, axial load N_0, thermomechanical force ξ_{th} or electrostatic force F_{es} correlated to its response enabling the establishment of a

correlation between the stimulus and the response of an inertial sensor. The scope of this chapter is limited to gas sensing applications, therefore the discussion will limited to those stimuli. However, the same principles can be extended to other sensing applications.

The state of a gas can classically be described by relating pressure P, gas concentration C, and temperature T via the ideal gas law ,

$$P = CRT \tag{2.138}$$

This equation can be applied at the macroscopic level where P, C, and T represent the pressure, concentration, and temperature of the surrounding environment (reservoir) or at the microscopic level using partial pressure, target gas concentration and surrounding environment temperature, assuming a thermal equilibrium. For sensing purposes, pressure and temperature will be treated as macroscopic variables, while concentration will be considered at a microscopic level.

As ambient pressure changes, damping (c) changes in proportion to viscosity and density of the surrounding medium. This change in damping directly affects thermomechanical forcing according to Eq. 2.125. To maintain thermal equilibrium between the sensor and its environment, energy dissipated through damping has to be balanced against energy acquired through thermal noise. If energy dissipated were not to be fully replaced, a net loss of energy would result in the sensor temperature dropping below that of the environment. Thus to maintain thermal equilibrium, the thermomechanical force must scale with both the ambient temperature and rate of energy dissipation. change in temperature can also affect sensor parameters, such as the axial load N_0, via thermal stress, and thus effective stiffness k.

Finally, variations in the concentration of the target gas can lead to mass loading, adsorption or desorption of gas molecules on the beam surface, resulting in a change in the beam's effective mass m and influencing its dynamic behavior. The scope of this chapter is limited to gas sensing, therefore the effects of temperature and pressure variations will not be discussed further. However, the analysis below can be extended to temperature and pressure sensing applications in a similar manner.

The absence of a deterministic phase in noise-driven sensors limits their measurable metric to those observed in the frequency domain. Three of these observables are illustrated in Figure 2.6: the resonance frequency, the resonant (peak) magnitude, and the area under the PSD curve, which corresponds to the mean square displacement. To create a consistent framework, I compare here the sensitivity of noise-driven to that of electrostatically dirven sensors using these metrics only.

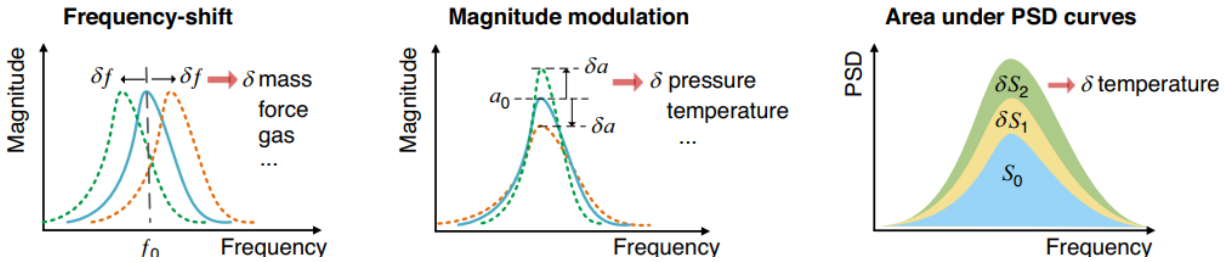


Figure 2.6: Detection methods based on frequency-shift, magnitude modulation, and area under PSD curves. Reproduced with permission from Nature [177].

The resonance frequency is a function of the stiffness and mass of the sensor. Therefore, it can be used to detect stimuli that change stiffness, mass, or both of them. This is true irrespective of the drive force. The peak magnitude can be evaluated using a narrow measurement bandwidth as,

$$a_0 = S_{qq}(\omega_0)\,\delta\omega \tag{2.139}$$

For thermomechanical actuation, I use Eq. (2.127) to evaluate it as,

$$a_0^{\text{th}}(m,k,c,T) = 4k_BT\frac{m}{kc}\delta\omega \tag{2.140}$$

and for electrostatic actuation, I use Eq. (2.133), to evaluate it as,

$$a_0^{\text{es}}(m,k,c,F_{\text{es}}) = \frac{2m^2}{kc^3}F_{\text{es}}^2\delta\omega \tag{2.141}$$

I use Eq. (2.124), to evaluate the mean square displacement under thermomechnaical actuation as,

$$\langle q^2\rangle^{\text{th}}(k,T) = \frac{k_BT}{k} \tag{2.142}$$

and Eq. (2.131) to evaluate the mean square displacement under electrostatic actuation as,

$$\langle q^2\rangle^{\text{es}}(m,k,c,F_{\text{es}}) = \frac{m}{2c^2k}F_{\text{es}}^2 \tag{2.143}$$

The adsorption or desorption of a gas molecules to the surface of a sensor is proportional to its area $A = 2bl$. The change in the sensor mass as a result of the chnage in gas

concentration C can be written as,

$$\frac{dm}{dC} = 2bl\chi \tag{2.144}$$

where χ is measure of the gas affinity to the sensor surface. It should be noted that the affinity of the gas to the sensor surface is a function of gas concentration, $\chi = \chi(C)$, particularly as the surface saturates at higher gas concentrations.

The relative sensitivity S_f of the frequency can be defined as rate of change of the resonant frequency with respect to the gas concentration C as a fraction of the resonant frequency. Assuming that the gas concentration results only in mass loading, we can write it as,

$$\begin{aligned} S_f &\equiv \frac{1}{\omega_0}\frac{\mathrm{d}\omega_0}{\mathrm{d}C} = -\frac{1}{2m}\frac{\mathrm{d}m}{\mathrm{d}C} \\ &= -\frac{\chi}{\rho}\frac{1}{h} \propto \frac{1}{h} \end{aligned} \tag{2.145}$$

The absolute sensitivity S_f can, therefore, be defined as,

$$\begin{aligned} M_f &= \frac{\mathrm{d}\omega_0}{\mathrm{d}C} = -\frac{1}{2}\sqrt{\frac{k}{m^3}}\frac{\mathrm{d}m}{\mathrm{d}C} \\ &= -\frac{\lambda^2}{2\sqrt{3}}\sqrt{\frac{E}{\rho^3}}\,\chi\frac{1}{l^2} \propto \frac{1}{l^2} \end{aligned} \tag{2.146}$$

Here and for the rest of this analysis, membrane stiffness and electrostatic softening were ignored and the effective stiffness was reduced to $k = k^{\mathrm{b}}$. This shows that the absolute sensitivity increases as the length of the sensor shortens.

Similarly, the relative sensitivity of the resonant peak magnitude under thermomechanical actuation S_a^{th} can be written as,

$$\begin{aligned} S_a^{\mathrm{th}} &= \frac{1}{a_0^{\mathrm{th}}}\frac{\mathrm{d}a_0^{\mathrm{th}}}{\mathrm{d}C} = \frac{1}{m}\frac{\mathrm{d}m}{\mathrm{d}C} \\ &= 2\frac{\chi}{\rho}\frac{1}{h} \propto \frac{1}{h} \end{aligned} \tag{2.147}$$

and the corresponding absolute sensitivity M_a^{th} can be written as,

$$\begin{aligned} M_a^{\text{th}} &= \frac{\mathrm{d}a_0^{\text{th}}}{\mathrm{d}C} = 4k_BT\delta\omega\frac{1}{kc}\frac{\mathrm{d}m}{\mathrm{d}C} \\ &= \frac{96k_BT}{\lambda^4}\frac{\chi}{E\hat{c}}\delta\omega\frac{l^3}{bh^3} \propto \frac{l^3}{bh^3} \end{aligned} \tag{2.148}$$

The relative sensitivity of the resonant peak magnitude under electrostatic actuation S_a^{es} can be written as,

$$\begin{aligned} S_a^{\text{es}} &= \frac{1}{a_0^{\text{es}}}\frac{da_0^{\text{es}}}{dC} = \frac{2}{m}\frac{\mathrm{d}m}{\mathrm{d}C} \\ &= 4\frac{\chi}{\rho}\frac{1}{h} \propto \frac{1}{h} \end{aligned} \tag{2.149}$$

and the corresponding absolute sensitivity M_a^{es} can be written as,

$$\begin{aligned} M_a^{\text{es}} &= \frac{\mathrm{d}a_0^{\text{es}}}{\mathrm{d}C} = 4\delta\omega\frac{m}{kc^3}\frac{\mathrm{d}m}{\mathrm{d}C} \\ &= \frac{24\epsilon^2}{\lambda^4}\frac{\rho\chi}{E\hat{c}^3}\delta\omega(c^{\text{es}})^2V^4\frac{l^4}{d^4h^2} \propto \frac{l^4}{d^4h^2} \end{aligned} \tag{2.150}$$

The sensitivity of peak magnitude of both thermomechanical and electrostatical displacement increase as the sensor thickness h decreases while the absolute sensitivities increases with the scaling down of thickness and width but decreases with scaling down of the sensor length. These relations highlight the benefits of miniaturization in the thickness.

The relative sensitivity of mean square displacement under electrostatic actuation $S_{\text{rm}}^{\text{es}}$ can be written as,

$$\begin{aligned} S_{\text{rm}}^{\text{es}} &= \frac{1}{\langle q^2\rangle^{\text{es}}}\frac{\mathrm{d}\langle q^2\rangle^{\text{es}}}{\mathrm{d}C} = \frac{1}{m}\frac{\mathrm{d}m}{\mathrm{d}C} \\ &= 2\frac{\chi}{\rho}\frac{1}{h} \propto \frac{1}{h} \end{aligned} \tag{2.151}$$

and the corresponding absolute sensitivity $M_{\mathrm{rm}}^{\mathrm{es}}$ can be written as,

$$\begin{aligned} M_{\mathrm{rm}}^{\mathrm{es}} &= \frac{\mathrm{d}\langle q^2\rangle^{\mathrm{es}}}{\mathrm{d}C} = \frac{1}{2c^2k} F_{\mathrm{es}}^2 \frac{\mathrm{d}m}{\mathrm{d}C} \\ &= \frac{3\epsilon^2 (c^{\mathrm{es}})^2}{\lambda^4} \frac{\chi}{\hat{c}^2 E} V^4 \frac{l^4}{d^4 h^3} \propto \frac{l^4}{d^4 h^3} \end{aligned} \tag{2.152}$$

The sensitivity of mean square displacement under electrostatic actuation increases for thinner sensors. For the absolute sensitivity, the performance improves as the thickness scales down while decreases as the length miniaturizes.

On the other hand, the mean square displacement of thermomechanically driven sensors are insensitive to gas concentration since the absolute sensitivity $M_{\mathrm{rm}}^{\mathrm{th}}$ evaluates in this case to,

$$M_{\mathrm{rm}}^{\mathrm{th}} = \frac{\mathrm{d}\langle q^2\rangle^{\mathrm{th}}}{\mathrm{d}C} = \frac{\mathrm{d}}{\mathrm{d}C}\left(\frac{k_B T}{k}\right) = 0 \tag{2.153}$$

and thus $S_{\mathrm{rm}}^{\mathrm{th}}$=0.

2.6 Experimental Investigation

In the following section, I investigate the impact of miniaturization into the nano-scale using a class of humidity sensors as a case study as it is scaled down from MEMS to NEMS.

2.6.1 Fabrication and Design

The resonators were not designed entirely based on theoretical equations due to uncertainties in parameters such as the axial stress and material properties. For example, axial stress have a significant affect the resonance behavior yet its magnitude depends on fabrication factors that are dificult to quantify analytically. In addition to the axial stress, uncertainties in material properties such as Young's modulus and density further complicate accurate prediction. These properties can deviate from their bulk values when scaled down to micro and nanoscale dimensions due to factors such as surface effects, grain structures, and process dependent variability. Moreover, practical limitations such as fabrication challenges and readout constraints can prevent a direct translation of the theoretical model into functional devices. Neglecting these factors may results in structures that are difficult to fabricate or incompatible with available measurement tools. As

a result, the final dimensions of the NEMS and MEMS resonators were not pre-set from theory but instead determined using an iterative experimental approach. A series of resonators with varying geometries were fabricated by following the theoretical model as a reference and considering the practical limitations. Their performance was evaluated based on theoretical criteria, fabrication feasibility and readout compatibility. Hence, the final dimensions were selected according to the characterization results of these test structures, taking into account fabrication challenges, signal quality from the readout and the desire to keep resonance frequencies within the measurable range of the system.

The fabrication steps of both NEMS and MEMS resonators are illustrated in Figure 2.7 (a-c). As the starting substrate, a 4" prime grade p-doped silicon wafer with a 50 nm thick thermal oxide layer was chosen due to its low cost, compatibility with Quantum-Nano Fabrication and Characterization Facility (QNFCF) cleanroom tools, and ability to yield multiple devices per fabrication cycle. First, to form the 4 µm thick sacrificial layer, the negative tone photoresist (PR) NLOF-2035 was spin coated at 1000 RPM and hard baked under vacuum for 30 minutes to minimize outgassing as shown in 2.7 (a). Then, for the structure layer, aluminum was deposited using electron-beam evaporator (Amod, Angstrom Engineering) at a rate of 0.3 nm/s to reach 90 nm and 220 nm thick films for NEMS and MEMS resonators, respectively. Aluminum was chosen as the beam material due to its mechanical stability, high optical reflectivity, and electrical conductivity. The thicknesses of the deposited Al films were verified with a mechanical surface profilometer (DektakXT, Bruker), and the corresponding surface profiles are presented in the Appendix A in Figure A.1. To pattern the structure layer, the positive tone PR S1811 was spin coated at 5000 RPM and soft baked at 120 °C for 90 seconds resulting a uniform thickness of 1.3 µm. The coated PR then exposed using maskless lithography aligner (MLA) (MLA 150, Heidelberg Instruments) at a dose of 100 mJ/cm^2 to define the aluminum structural pattern before etching. After the exposure, the PR was developed with MF-319 (Microposit) developer for 60 seconds to obtain openings in the PR layer. These openings were then etched using plasma-based dry reactive ion etching (RIE) (ICP380, Oxford Instruments), employing 120W with an RF generator and 800W with inductively coupled plasma (ICP) in a controlled environment of 5 mTorr with 40 sccm Cl_2 and 10 sccm BCl_3 for 40 seconds, as shown in Figure 2.7 (b). Notably, using shadow mask in the Al deposition can bypass these lithography and etching steps. Then, the beam was released via isotropic dry etch (CV200RFS, Yield Engineering Systems) using 25 sccm of O_2 at 900W RF power and 750 mTorr pressure at room temperature. In order to securely fix the beam from both ends, the anchor width was set at 50 µm, ensuring its stability and preventing unwanted release of the anchors due to the undercut, as illustrated in Figure 2.7 (c). Because the chamber temperature rose during the plasma process, the system was paused every 10 minutes to

cool. This cycle was repeated until the beam was fully released which was visually confirmed by scanning electron microscope (SEM) (JSM-7200F, JEOL USA Inc.), as shown in Figure 2.7(d). The uniformity of the beam reflects the absence of high residual stress during fabrication, which could have caused bending. Although the etching process was considered isotropic, some degree of anisotropy was observed, resulting in a remaining sacrificial layer beneath the beam. However, the resonator was successfully released. Finally, using an automated dicing saw (Disco, DAD3240), the 4" wafer was diced into 8.6×8.6mm dies. Additional process details and design considerations were reported in our previous works for similar structures [73, 74, 72].

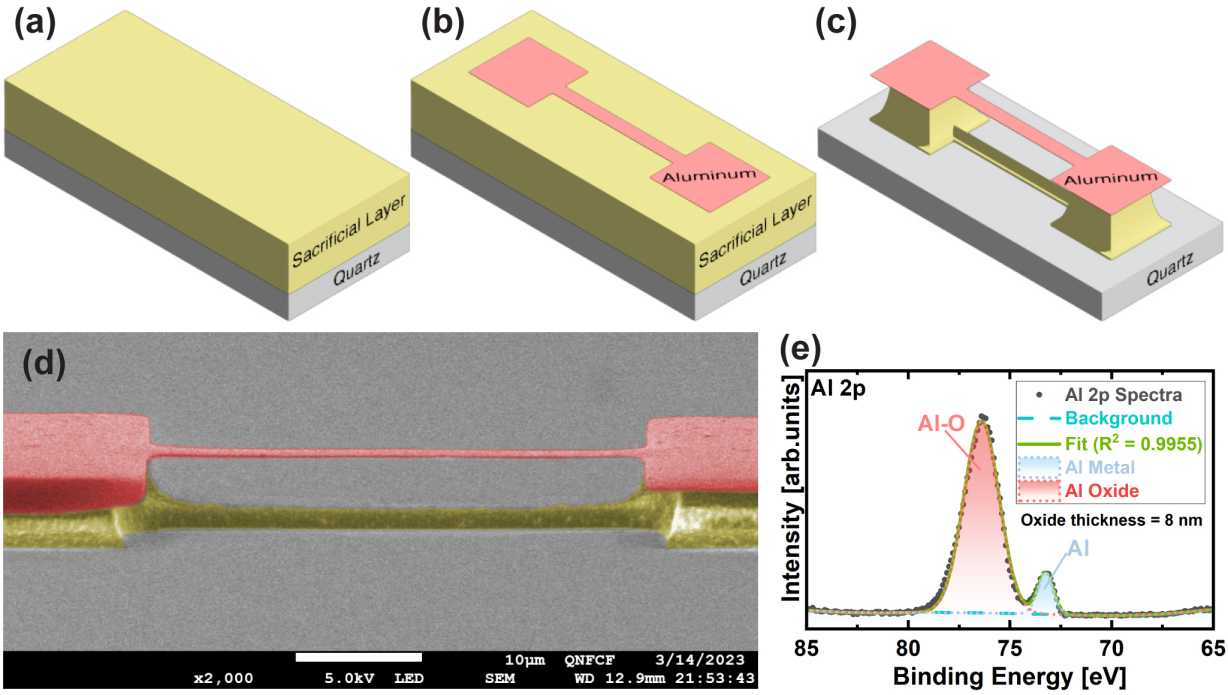


Figure 2.7: Fabrication process and elemental analysis. (a-c) represent the sequential fabrication steps: (a) deposition of the photoresist sacrificial layer (in yellow), (b) patterning of the metal structure (in red), and (c) sacrificial layer release. (d) Colorized SEM image of the final structure, highlighting metal in red and photoresist in yellow. (e) XPS spectrum displaying an 8 nm oxide thickness for the structure. Reproduced with permission from Elsevier [72].

After the fabrication, the elemental composition and crystal morphology were analyzed using X-ray photoelectron spectroscopy (XPS) and X-ray diffraction (XRD) measurements, respectively. Figure 2.7(e) shows the XPS data indicating the formation of an 8 nm thick

Al oxide layer on the surface. The formation of the oxide layer is due to the combined effects of ambient air oxidation and O_2 plasma treatment during the last etching process. This oxide is hydrophilic, allowing the resonator to absorb humidity and function as a sensing layer. The AlO_x film thickness was estimated using the calculations developed by Strohmeier [207] as follows:

$$d_{\text{oxide}} = \lambda_{\text{oxide}} \sin\theta \ln\left(\frac{N_{\text{metal}} + \lambda_{\text{metal}} I_{\text{oxide}}}{N_{\text{oxide}} + \lambda_{\text{oxide}} I_{\text{metal}}} + 1\right) \tag{2.154}$$

where $d_{\text{oxide}} = 28$Å and $d_{\text{metal}} = 26$Å and are the inelastic mean free path of oxide and metal, respectively, $\theta = 90°$ is the photoelectron take-off angle N_{metal} and N_{oxide} are the volume densities of the metal atoms in the metal and oxide, respectively with the relationship of $\frac{N_{\text{metal}}}{N_{\text{oxide}}} = 1.5$, I_{oxide} and I_{metal} are the area percentages of the oxide and metal peaks in Al 2p XPS spectra, respectively, and d_{oxide} is the oxide film thickness in Angstroms. We found the I_{oxide} as 91.1 and I_{metal} 8.9 by calculating the areas under each peak in the Al 2p XPS spectra using OriginPro 2021b using Shirley XPS baseline, and Gaussian fitting corresponding to an 8 nm oxide thickness on the surface.

XRD measurements were performed on a Bruker D8-Focus with Cu-Kα radiation at a wavelength of 1.5406 Å, an acceleration voltage of 40 kV, and an emission current of 40 mA. The diffraction pattern confirmed the presence of a face-centered cubic (FCC) structure with (111) plane of Al. However, no peaks corresponding to aluminum oxide were observed, likely due to the limited thickness of the oxide layer which falls below the effective detection depth of the XRD technique. The XRD spectra is presented in Figure 2.8.

The developed process flow for fabricating the NEMS and MEMS resonators is relatively cheaper, faster, and simpler compared to conventional silicon-based approaches. These improvements were achieved by utilizing aluminum as a multifunctional material, providing structural integrity, optical reflectivity, electrical conductivity, and humidity sensing capabilities. Last but not least, the resonators self-actuate via thermomechanical noise and produce optically detectable signals via thermomechanical noise alone, requiring no external excitation and supporting low-power applications.

After the process flow and some material properties had been defined, the dimensions of the beam can be chosen to experimentally demonstrate the effects of downscaling on sensing performance. As discussed in the theoretical section, maintaining a high length-to-width ratio is crucial for optimal resonator performance. To achieve a high aspect ratio, the beam width needs to be minimized by addressing the limitations in resonator fabrication and signal readout.

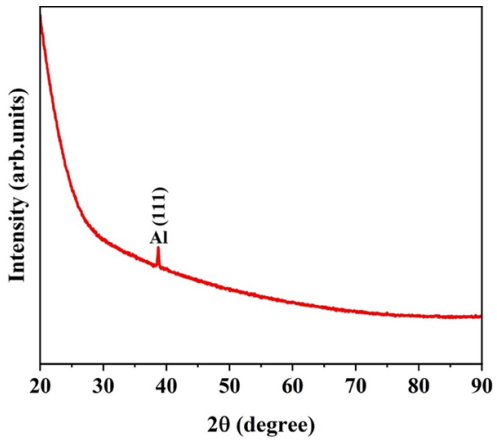


Figure 2.8: XRD analysis of the resonator. The peak corresponds to the (111) plane of FCC structured Al. Reproduced with permission from Elsevier [72].

In terms of the fabrication, there are two main considerations. The first one is the releasing step shown in Figure 2.7(c). A polymer-based sacrificial layer with dry release in oxygen plasma [17] was chosen to prevent the sticking problems due to surface tension forces and usage of aggressive etchants. However, the plasma might struggle to reach underneath the resonator, especially when the width-to-air-gap ratio is high, resulting in incomplete etch. Therefore, a low width-to-air-gap ratio is desired for a smooth release process. For this purpose, a thick PR layer, 4 µm thick, had been selected as the sacrificial material as stated earlier. As narrower beams result lower aspect ratio, they are advantageous for release thereby improving the reliability of the release process which aligns well with the design goal. Another important design factor is feature size. Sub-micrometer require electron beam lithography (EBL) which is more expensive, complex, and time-consuming compared to optical lithography. Achieve features below 2 µm with optical lithography requires additional process optimization, including focus and dose testing, spin coating, baking, and development of the PR. Therefore, to simplify the fabrication process and ensure repeatable results, a minimum feature size of 2 µm was selected.

To determine the minimum optically measurable width, a series of resonators with a fixed length of 40 µm and varying widths from 1 µm to 5 µm were fabricated and characterized optically. All resonators showed similar resonance performance in terms of quality factor and resonance frequency. The results of these measurements are given in the Figure 2.9. Therefore, the widths of 4 and 5 µm were determined to be the optimal choice for NEMS and MEMS resonators, respectively.

As the thicknesses and widths of the NEMS and MEMS resonators were set, the last

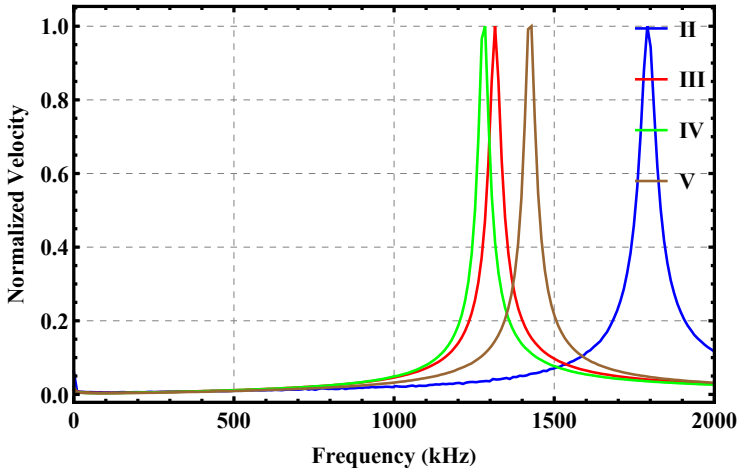


Figure 2.9: Frequency responses of the fabricated resonators with widths of 2µm (blue), 3µm (red), 4µm (green), and 5µm (brown).

step was to determine the length of the beams. The laser Doppler vibrometer (LDV) used for the readout has a low-pass filter at 1.5 MHz, which attenuates signals exceeding this frequency. As described in the theoretical section, the resonance frequency increases as the beam length decreases. Therefore, as the final design rule, the minimum lengths that produce resonance frequencies within the detectable range, below 1.5 MHz, were selected. For the MEMS resonator, only the fundamental resonance frequency was designed to fall in this range. In contrast, for the NEMS resonator, multiple resonance modes were observed therefore the first six modes were designed to lie in the detectable regime. Resonators with varying lengths were fabricated and characterized. Based on their resonance frequencies, lengths of 50 µm and 100 µm were chosen for the NEMS and MEMS resonators, respectively. As a result, the final dimensions for the NEMS and MEMS resonators are given in Table 2.1.

Table 2.1: Dimensions of the resonators.

Resonator	Length [µm]	Width [µm]	Thickness [nm]	# of modes
MEMS	40	5	220	1
NEMS	100	4	100	6

2.6.2 Experimental Setup

The NEMS and MEMS resonators were fabricated through two separate fabrication runs following the procedure described above. The experimental setup for sensor testing is illustrated in Fig. 2.11 (a). A dry air source (99.999% pure Nitrogen) and two mass flow controller (MFC)s are used to control the relative humidity in the environmental chamber. The first MFC supplies dry air directly from the source, whereas the other supplies humid air by passing dry air through water in a bubbler. The total inlet flow was set at 1000 sccm and the humidity inside the test chamber was controlled by adjusting the flow ratio of the two MFC s. All measurements were recorded at room temperature, 24 °C. Relative humidity and temperature were monitored using a commercial environmental sensor (SensorPush HTP.xw) with an error of ±1.5%RH and ±0.1°C, respectively. After the humidity inside the chamber was stabilized, the vibrometer laser beam was focused on the resonators, as demonstrated in Fig. 2.11 (b). An image of the experimental setup is shown in Figure 2.10. It should be noted that no electrical connection was made with the sensor as the sensor was actuated with thermomechanical noise at room temperature and measured optically.

Fig. 2.11 (c) presents the cross-sectional view of the structure. Hydrophilicity of the surface oxide enables the interaction with water vapor and formation of hydrogen bonds with water molecules that has a dipole moment coming from the asymmetric molecular structure of water with the hydrogen bonds forming a 108.25° angle. The core metal maintains its mechanical stability, optical reflectivity and electrical conductivity. Optical reflectivity is required for optical readout via LDV. The electrical conductivity of the resonators was tested in our previous work [73] with several electrical interconnection methods such as wire bonding, probing, and built-in packaging. The resonance frequency of the microbridge, affected by the resulting changes in the microbridge mass and stiffness, varies as the concentration of water vapor varies, as demonstrated in Fig. 2.11 (d).

To reduce measurement noise, the frequency-response of the mid-point velocity was averaged over 500 readings in the frequency-domain. Background (baseline) noise, was constructed in Origin software using asymmetric least squares smoothing with an asymmetric factor of 10^{-4}, a threshold of 10^{-8} and a smoothing factor of 6. The baseline shows a rising trend with frequency up to 1.5 MHz, the velocity encoder's cutoff frequency which acts as a low-pass filter. After subtracting the baseline noise, the measured frequency response was fitted using a Lorentzian fit while ensuring an R^2 value greater than 0.95.

In this study, only the steady-state behavior of the resonators was analyzed, following a similar approach to that outlined in the literature [157]. The chamber was purged with a 1000 sccm N2 flow for approximately 3 hours to achieve the driest condition, 1%

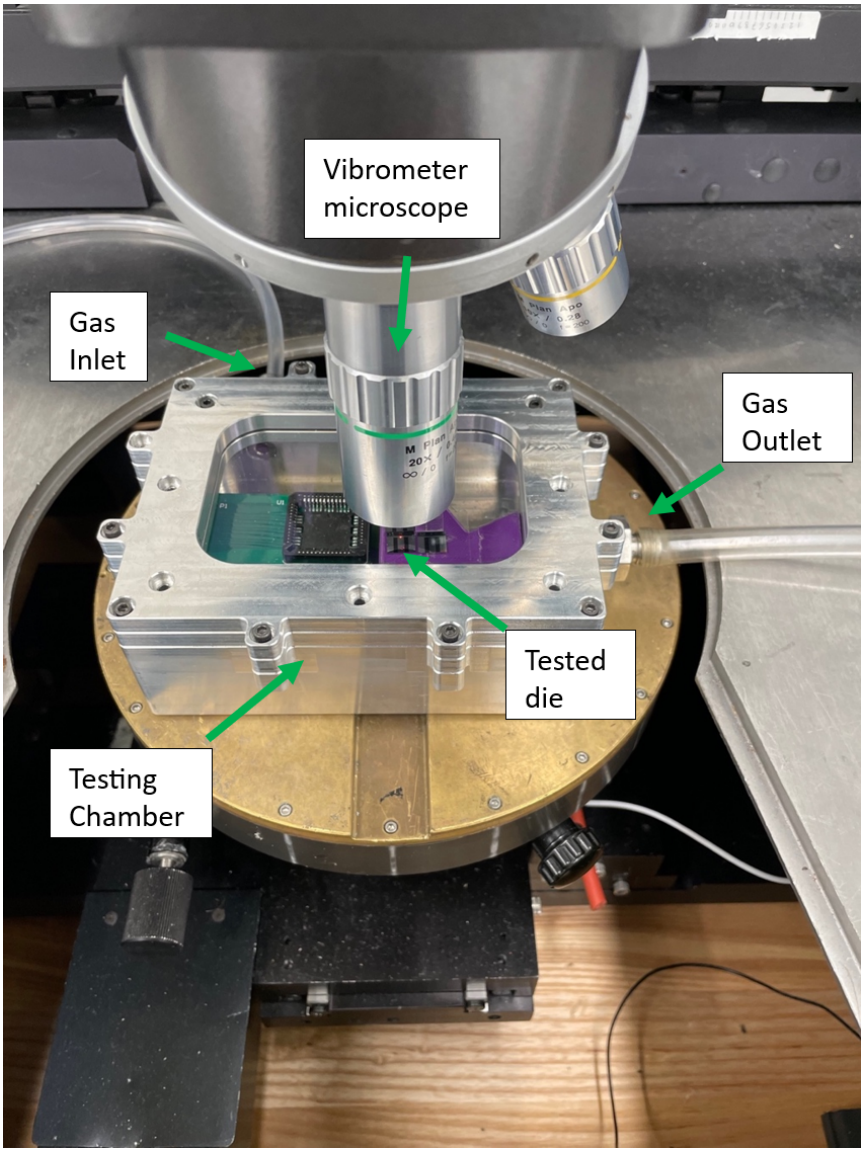


Figure 2.10: The image of the experimental setup shows the testing chamber with optical window, gas inlets and outlets, vibrometer microscope, and tested die. Reproduced with permission from Elsevier [72].

RH. Subsequently, the wet flow increased in increments of 50 sccm while maintaining a constant total flow of 1000 sccm. Once the MFC s were configured, the conditions were kept constant for an hour to ensure steady-state behavior. This process was repeated 11

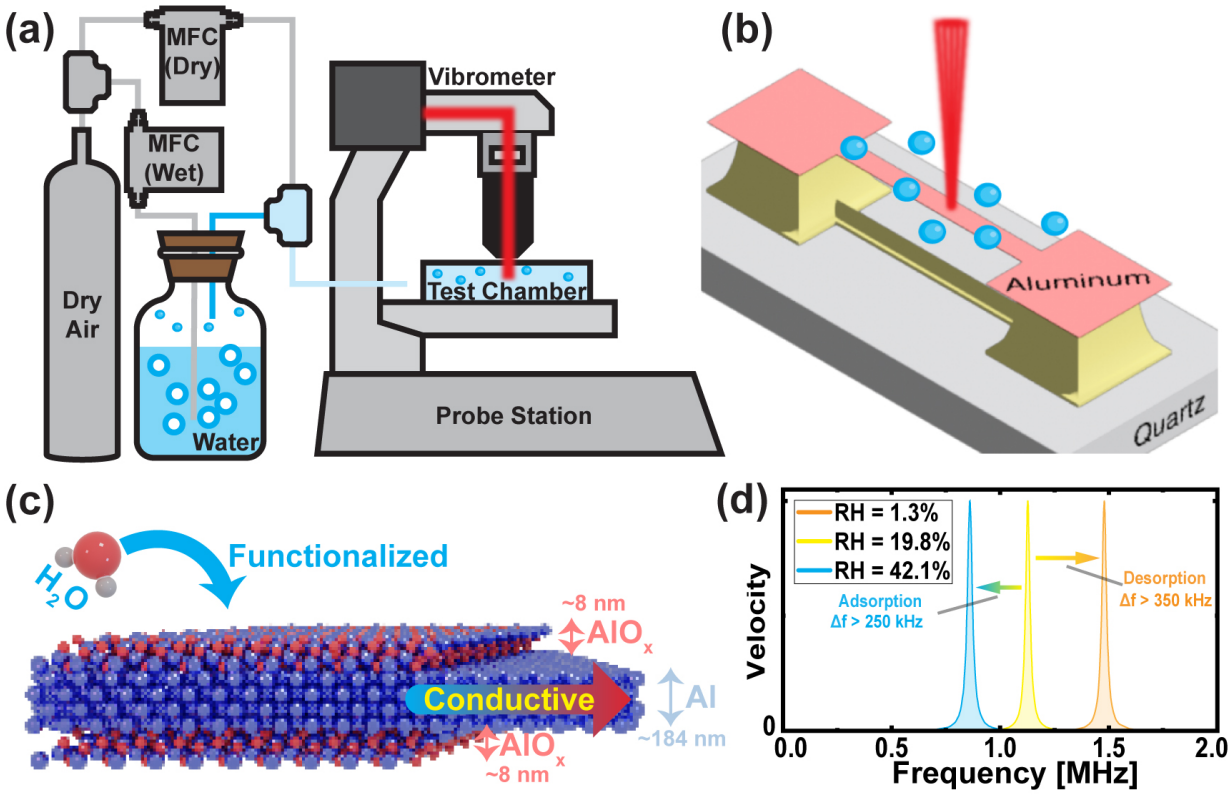


Figure 2.11: Experimental setup. (a) Schematic representation of the experimental setup, including the dry air (N_2) source, two MFCs, bubbler, vibrometer, test chamber, and probe station. (b) Schematics of the resonator with the laser beam focused on its center. (c) Atomic cross-sectional view of the structure, with aluminum (blue), oxygen (red), and hydrogen (gray). (d) Frequency response of an example resonator under various humidity levels, illustrating response to adsorption and desorption of water vapor. Reproduced with permission from Elsevier [72].

times for each resonator, at 19 different levels of relative humidity from 1% RH to 75% RH. RH values beyond this range could not be reached with the experimental setup. The resulting resonance frequencies and quality factors were averaged and plotted with respect to relative humidity.

2.7 Results and Discussion

I compare in Figure 2.12 the PSD of thermomechanical noise-driven to electrostatically driven inertial sensors as their dimensions scale down. The noise floor, originating from the readout circuit, S_{qq}^{V} does not scale down with the sensor dimensions. It is spectrally flat, affecting all frequencies and geometries equally as shown by the red background surface in the figure.

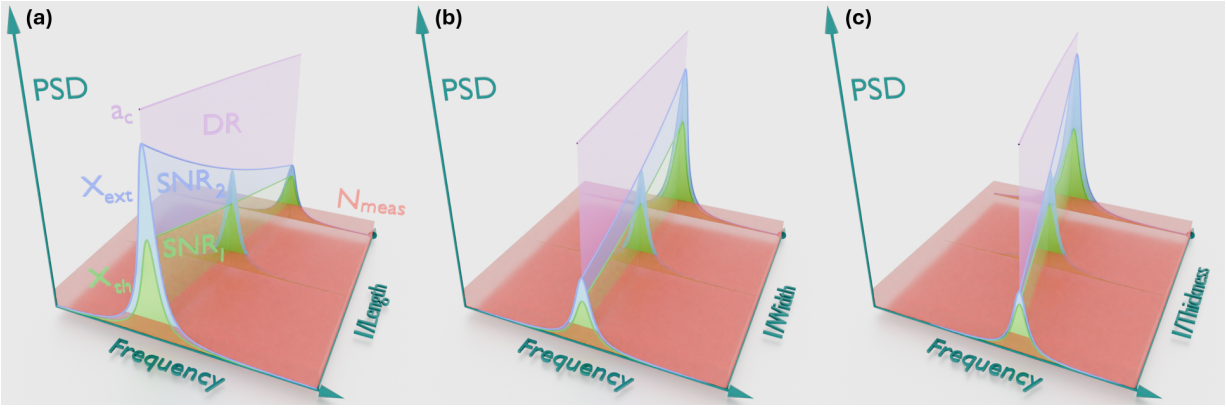


Figure 2.12: The PSDs of displacement in inertial sensors under thermomechanical S_{qq}^{th} (green curves) and electrostatic S_{qq}^{es} (blue curves) excitation as functions of frequency and (a) length, (b) width, and (c) thickness. The red curve represents the PSD of measurement noise S_{qq}^{V}.

In contrast, the PSDs of displacement for thermomechanically S_{qq}^{th} (green) and electrostatically S_{qq}^{es} (blue) driven sensors peak at the resonance highlighting resonant sensors' function as frequency-selective filters. In particular, thermomechanically driven sensors exploit that to transform white noise input power into a colored output signal by accepting and amplifying components near resonance while rejecting and attenuating those away from it. The change in the characteristics of this 'color' due to a stimulus is the detection signal used to sense (quantify) the stimulus. The function of the readout circuit is to amplify the sensor response (blue or green curves) over the noise floor.

Scaling down the sensor length, Figure 2.12(a), degrades the PSD and SNR of thermomechanically driven sensors quickly at l^3, Table 2.2. It also degrades the PSD of electrostatically driven sensors at an even faster rate pf l^4 resulting in their SNR scaling down like l. As a result, at very short lengths, the PSDs of thermomechanically and electrostatically driven sensors are barely distinguishable. This makes it challenging to extract useful infor-

mation as the sensor shortens, and emphasizes the need to employ countervailing factors to improve the SNR.

The absolute sensitivity of frequency shift sensors M_f, Table 2.2, scales up like $1/l^2$ as length scales down due to the scaling up of the resonance frequency at the same rate. As a result, the corresponding relative sensitivity S_f is unchanged with length. On the other hand, frequency stability, which proportional to $\sqrt{\omega_0 Q}$ [177], scales up like $1/l^2$ like M_f. Therefore, it can be seen frequency shift is a robust sensing metric as length scales down. While the sensitivity of the peak magnitude and mean square displacement metrics is not impacted by length changes, the corresponding absolute sensitivities degrade quickly as length scales down at the rates of l^3 and l^4, respectively. These conclusions indicate that frequency shift should be adopted as a metric for shorter sensors at the 'deep' nano-scale and beyond dimensions.

Reducing the sensor width, increases the PSD and SNR of thermomechanically driven sensors like $1/b$, Figure 2.12(b), but does not impact the PSD of electrostatically driven sensors. This results in a linear degradation of the SNR for electrostatically driven sensors, Table 2.2, as width scales down. The only impact it has on sensitivity is that it increases the absolution sensitivity of the peak magnitude metric for thermomechanically driven sensors like $1/b$.

As sensors become thinner, the PSDs of thermomechanically driven sensors scale up faster than than those of electrostatically driven sensors, Figure 2.12(c), at $1/h^2$ compared to $1/h$. As a result, while the SNR of thermomechanically driven sensors scales up like $1/h^2$, the SNR of electrostatically driven sensors scales down like h resulting in a similar challenge for very thin sensors with the PSDs of thermomechanically and electrostatically driven sensors being barely distinguishable.

Scaling down thickness also reduces the frequency stability of inertial sensors like $\sqrt{h^3}$, Table 2.2, because it scales down the natural frequency and quality factor like h and h^2, respectively. However it improves, the sensitivity of all sensing metrics except for the absolute sensitivity of frequency shift sensors and the mean square of thermomechanically driven sensors. In contrast to length, the preferred metric for thinner sensors is peak magnitude for thermomechanically driven sensors and mean square displacement for electrostatically driven sensors. The absolute sensitivity of both of them scale up like $1/h^3$ while being impervious to concomitant degradation in frequency stability.

One method to counteract the degradation in the SNR of electrostatically driven sensors with miniaturization is to scale down the electrostatic gap d. The fact that this SNR scales up like $1/d^4$ means that the gap alone can overpower the scaling down of all mass dimensions bhl, Table 2.2. In tandem with scaling down of thickness, the two factors can

improve the absolute sensitivity of the peak magnitude and means square displacement metrics of electrostatically driven sensors to overcome degradation due to scaling down of length.

Table 2.2: Comparison of the analytical expressions and scale relationships of key performance metrics for resonant gas sensors of the inertial type.

Parameter	Exact	Simplified	Scaling
ω_0	$\sqrt{k/m}$	$\frac{\lambda^2}{2\sqrt{3}}\sqrt{\frac{E}{\rho}}\frac{h}{l^2}$	$\frac{h}{l^2}$
Q	$\frac{\sqrt{mk}}{c}$	$\frac{\lambda^2}{2\sqrt{3}}\sqrt{\frac{E\rho}{\hat{c}}}\frac{h^2}{l^2}$	$\frac{h^2}{l^2}$
$\mathrm{SNR}^{\mathrm{th}}$	$\frac{T}{T_R}\frac{G^2}{R}\frac{m}{kc}$	$\frac{12}{\lambda^4}\frac{T}{T_R}\frac{G^2}{R}\frac{\rho}{E\hat{c}}\frac{l^3}{bh^2}$	$\frac{l^3}{bh^2}$
$\mathrm{SNR}^{\mathrm{es}}$	$\frac{1}{2k_BT}\frac{m}{c^2}F_{\mathrm{es}}^2$	$\frac{\epsilon^2}{8k_B}\frac{\rho}{\hat{c}^2}\frac{(c^{\mathrm{es}})^2V^4}{T}\frac{bhl}{d^4}$	$\frac{bhl}{d^4}$
S_f	$-\frac{1}{2m}\frac{\mathrm{d}m}{\mathrm{d}C}$	$-\frac{\chi}{\rho}\frac{1}{h}$	$\frac{1}{h}$
M_f	$-\frac{1}{2}\sqrt{\frac{k}{m^3}}\frac{\mathrm{d}m}{\mathrm{d}C}$	$-\frac{\lambda^2}{4\sqrt{3}\,\pi}\sqrt{\frac{E}{\rho^3}}\chi\frac{1}{l^2}$	$\frac{1}{l^2}$
S_a^{th}	$\frac{1}{m}\frac{\mathrm{d}m}{\mathrm{d}C}$	$2\frac{\chi}{\rho}\frac{1}{h}$	$\frac{1}{h}$
M_a^{th}	$4k_BT\delta\omega\frac{1}{kc}\frac{\mathrm{d}m}{\mathrm{d}C}$	$\frac{96k_BT}{\lambda^4}\frac{\chi}{E\hat{c}}\delta\omega\frac{l^3}{bh^3}$	$\frac{l^3}{bh^3}$
S_a^{es}	$\frac{2}{m}\frac{\mathrm{d}m}{\mathrm{d}C}$	$4\frac{\chi}{\rho}\frac{1}{h}$	$\frac{1}{h}$
M_a^{es}	$4\delta\omega\frac{m}{kc^3}\frac{\mathrm{d}m}{\mathrm{d}C}$	$\frac{24\epsilon^2}{\lambda^4}\frac{\rho\chi}{E\hat{c}^3}\delta\omega(c^{\mathrm{es}})^2V^4\frac{l^4}{d^4h^2}$	$\frac{l^4}{d^4h^2}$
$S_{\mathrm{rm}}^{\mathrm{th}}$	0	0	N.A.
$M_{\mathrm{rm}}^{\mathrm{th}}$	0	0	N.A.
$S_{\mathrm{rm}}^{\mathrm{es}}$	$\frac{1}{m}\frac{\mathrm{d}m}{\mathrm{d}C}$	$2\frac{\chi}{\rho}\frac{1}{h}$	$\frac{1}{h}$
$M_{\mathrm{rm}}^{\mathrm{es}}$	$\frac{1}{2}\frac{1}{c^2k}\frac{\mathrm{d}m}{\mathrm{d}C}$	$\frac{3\epsilon^2(c^{\mathrm{es}})^2}{\lambda^4}\frac{\chi}{\hat{c}^2E}V^4\frac{l^4}{d^4h^3}$	$\frac{l^4}{d^4h^3}$

The measured resonance frequencies and quality factors of the NEMS and MEMS sensors are shown in Figures 2.13(a) and (b), respectively, as functions of relative humidity levels in the range of $[1\%, 78\%]$. The absolute and relative sensitivities of the frequency

shift metric for those sensors were calculated using Eqs. (2.146) and (2.145), respectively, and are shown in Figures 2.13(c) and (d), respectively. As expected from Table 2.2, the NEMS sensor's resonance frequency is significantly lower than that of the MEMS given that scaling down process, Table 2.1, results in the ratio $(h_n/l_n^2)/(h_m/l_m^2) \approx 0.07$. The quality factor of the NEMS sensor is also significantly lower than that of the MEMS sensor due to a scaling down ratio of $(h_n^2/l_n^2)/(h_m^2/l_m^2) \approx 0.034$.

The absolute sensitivity of the MEMS sensor was found to outperform that of the NEMS sensor, Figure 2.13(c), since it is shorter and M_f scales like $1/l^2$. This is noteworthy given that the NEMS sensor is smaller in the other dimensions. In contrast, the relative sensitivity of the NEMS sensor is better than that of the MEMS sensor, Figure 2.13(d), since S_f scales as $1/h$ and the NEMS sensor is thinner than the MEMS sensor.

These experimental results closely agree with the theoretical scaling relationships I developed and confirm my hypothesis that miniaturization improves sensor sensitivity. However, this improvement occurs at different rates depending on the dimension being scaled down and the actuation method. While the potential for miniaturization is obvious, the pitfalls of miniaturizing all dimensions systematically without paying attention to those tradeoffs are also obvious. The complexity of those relationships also makes the typical trial-and-error approach to sensor development foolhardy. A more deliberate, analytically informed, approach is imperative to the success of miniaturization process. Those tradeoffs motivate the need for improved signal amplification and noise minimization, which are addressed in subsequent chapters through packaging and interface optimization.

2.8 Conclusions

In this chapter, a theoretical model was developed to analyze the effects of sensor miniaturization. PDE governing the resonator dynamics was first derived and then reduced to ODEs using a ROM method. These ODEs were used to define key performance parameters such as resonance frequency, quality factor, SNR, and sensitivities to formulate their dependence on device geometry. To validate the model, MEMS and NEMS humidity sensors were fabricated and tested under identical conditions. The experimental results aligned closely with theoretical predictions, confirming that miniaturization enhances sensing performance. However, this improvement comes at the cost of reduced output signal amplitudes and increased susceptibility to noise, motivating the need for advanced packaging and interface engineering, which are addressed in following chapters.

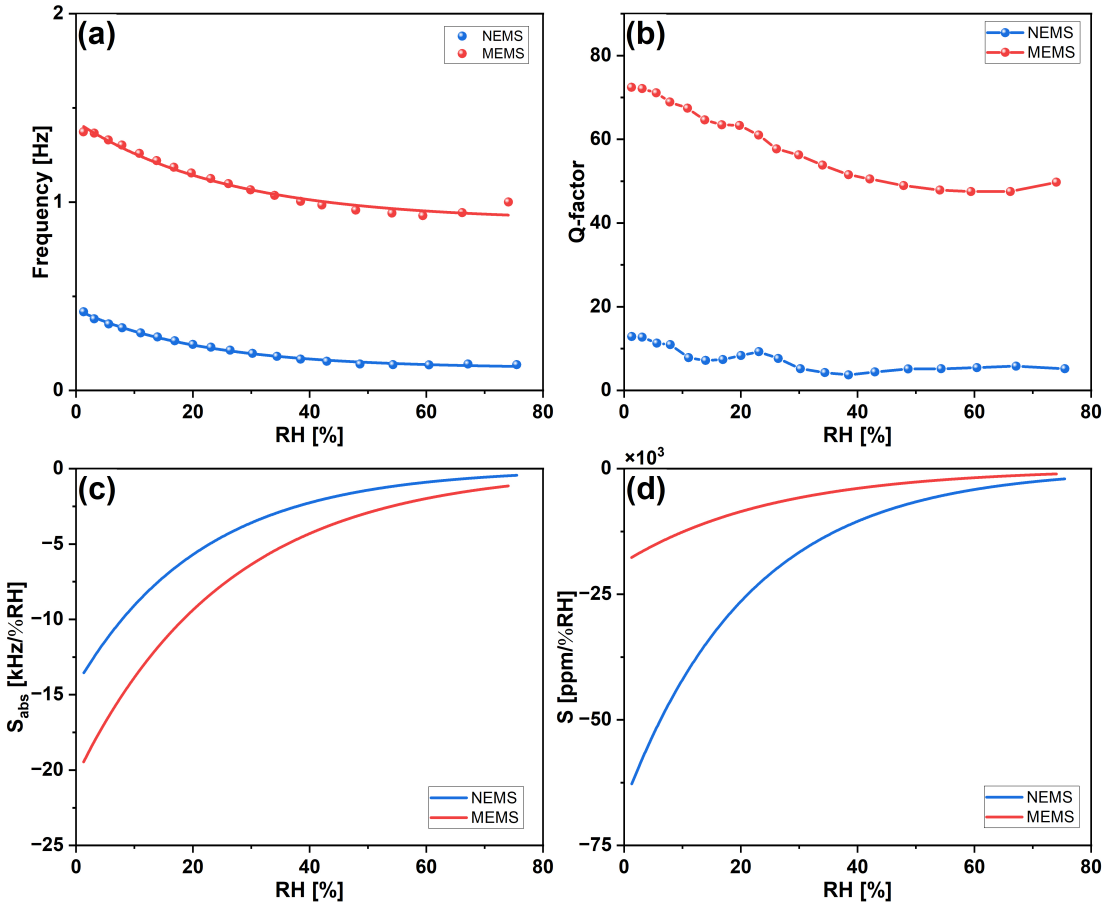


Figure 2.13: Comparison of the MEMS and NEMS sensors' u(a) resonance frequency ω_0, (b) quality factor Q, (c) absolute sensitivity M_f, and (d) relative sensitivity S_f as functions of relative humidity $\%RH$.

Chapter 3

Built-in Packaging for Miniaturized Sensors

As the sensors miniaturize, their signal output also shrinks. Therefore, the signals might be lost under the noise due to the conventional packaging and interconnections. As a result, the sensor miniaturization require paralllel developments in packaging and interconnection techniques. In this chapter, a novel packaging technique, called built-in packaging, is introduced and demonstrated for MEMS resonator and MIM diode applications with the comparisons of the conventional packaging methods such as wire bonding, and probing. The first section focuses on the MEMS resonator applications while the second section focuses on MIM diode applications.

3.1 MEMS resonator

An alternative packaging method, termed built-in packaging, is proposed for single terminal devices, and demonstrated with an actuator application. Built-in packaging removes the requirements of wire bonding, chip carrier, printed circuit board (PCB), probe station, interconnection elements, and even wires to drive single terminal devices. Reducing these needs simplifies operation and eliminates possible noise sources. A micro resonator device is fabricated and built-in packaged for demonstration with electrostatic actuation and optical measurement. Identical actuation performances are achieved with the most conventional packaging method, wire bonding. The proposed method offers a compact and cheap packaging for industrial and academic applications.

3.1.1 Introduction

The typical working principle of a sensor is two-fold. First, the system is set into the sensing state that is sensitive to the target input. Generally, an external signal is required for this activation, except for self-actuated structures [233]. Second, the output signal containing detection information is translated into the proper form. The majority of the sensor research focuses between these two feedthroughs where detection interaction happens by exploring state-of-the-art sensing concepts [180], functionalizing high-performance materials [160], and expanding fabrication limits [65]. Developments in these areas enabled a better understanding of the universe by measuring quantized unit of electrical conductance [222] and mass of Higgs boson [37] or resulted in detecting more practical targets such as the mass of a single proton [36] or energy of a single photon [116] under ideal conditions. As sensitivity increases, the signal levels decrease, and feedthrough losses of these tiny messages start to play a more significant role. Therefore, developments in the sensing state need to be followed by the ones in feedthrough for keeping the sensing state precisely and reading the output signal with minimal losses.

Principally, a package is required for interfacing the chip with actuation and readout circuits, and there are three popular methods for bonding a chip on top of a carrier board. In wire bonding, the chip is attached to the package with welded fine wire leads, as shown in Fig. 3.1b. In flip-chip bonding, the top layer of the chip is soldered with the carrier, as illustrated in Fig. 3.1c. In tape-automated bonding, a thin conductor tape is attached on top of the metal pads of the device, as demonstrated in Fig. 3.1d. Each of these techniques introduces design restrictions for compatibility. Although all the components and processes are well standardized, they introduce additional feedthrough loss, complexity, size, and cost. In addition, it is known that feedthrough noises and losses play a significant role in the electrical actuation and measurements of MEMS and NEMS [168, 194, 236, 103]. In addition modeling of the parasitic effects of these noise sources was attempted, to minimize the damage [147].

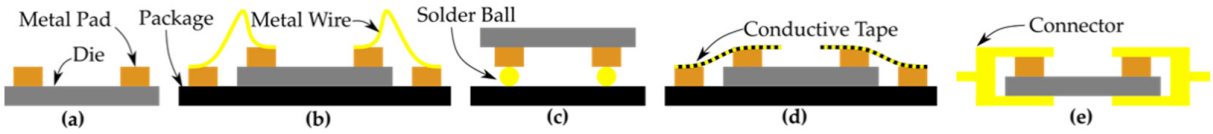


Figure 3.1: Packaging methods: (a) no packaging, (b) wire bonding, (c) flip-chip bonding, (d) tape-automated bonding, and (e) built-in packaging. Reproduced with permission from MDPI [73].

Instead of putting up with these problems, it is aimed to eliminate the source directly

by proposing a new concept called built-in packaging. Unlike all conventional methods, in the proposed method, the built-in packaging, a connector is directly attached to the die without any package or carrier board, as illustrated in Fig. 3.1e. The main goal of this work is to eliminate all the interconnection components, even wires, and facilitate the device into a plug-and-play operation.

The proposed concept is demonstrated using a single-terminal device where a resonator is designed, modeled, fabricated, packaged, and characterized. The one and only electrical terminal is used on the actuation side, and the mechanical motion is detected optically. Therefore, the actuation performance of the proposed method is compared with the most conventional method, the wire bonding, to inspect the packaging performance. The actuation and readout schemes are illustrated in Fig. 3.2. To examine the performance of the operation, the results are compared with the most conventional method, wire bonding.

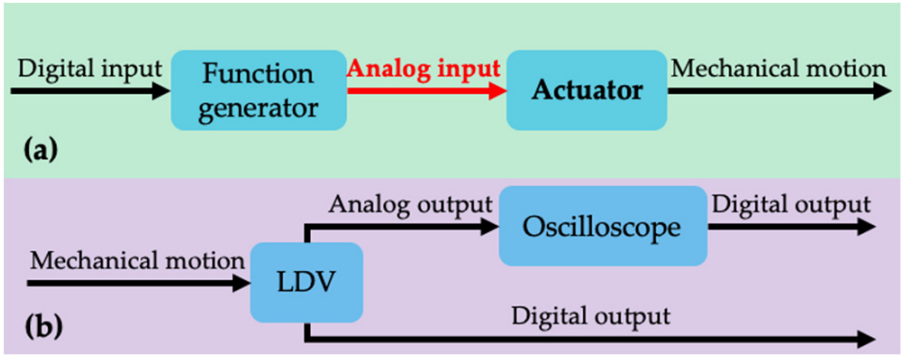


Figure 3.2: Schematics of the (a) actuation, and (b) characterization strategies. The red color indicates the focus of this study while the bold text indicates elements fabricated in the scope of this work. LDV stands for laser Doppler vibrometer. Reproduced with permission from MDPI [73].

Though only a single-terminal actuator application is illustrated in this work, the proposed concept is valid for sensor applications (accelerometer [188], gyroscope [9], mass sensor [153], humidity sensor [158], temperature sensor [27], pressure sensor [79], gas sensor [3], magnetometers [151], photoacoustic sensors [40], field effect transistor (FET)-biosensor [162], and permittivity sensor [55]), optical and photonic applications (micromirror [101][114], microswitch [239], LiDAR [246], beam steering [32], bolometer [115], photon detector [10], and PeCOD [11]), RF applications (diode [166], transistor [92], antennas [83], switch [235], phase shifter [201], filter [203], and tunable capacitor [181]), microfluidics (mi-

cropump [154], microdroplet generator [195], and microvalve [131]), and other applications (energy harvester [189], rectenna [4], gripper [54], etc.).

3.1.2 Actuator Design

To illustrate the proposed packaging method for an actuator application, a microresonator needed to be designed, and this design should be compatible with the actuation and characterization setups, and easy to fabricate and package. First, the important criteria were specified and then associated with geometrical and material properties, and finally, a complete design satisfying these criteria was developed. In addition, a mathematical model was built and numerically solved for optimization and verification. Detailed equipment information is provided in the supplementary information of my recent publication [73].

Compatibility

While it is possible to make in-plane motion measurements with LDV [7], out-of-plane motion is easier to catch. In addition, the lowest eigenmode offers the highest deformation and results in a larger output signal from the LDV. Thus, the main operation mode of the resonator was chosen as the first out-of-plane mode. Both cantilever and fixed–fixed structures are appropriate for this purpose and fixed–fixed boundary conditions were preferred to minimize the curvature.

LDV converts motion into an electrical signal from the Doppler shift in the reflected laser beam frequency due to the movement of the surface. The laser spot has a finite diameter, called airy disk, and should fully cover the top surface of the resonator, otherwise the laser beam might also reflect from stationary parts, causing the output signal to decay. This can especially affect the calibration between motion and electrical signals and might cause imprecise results. To eliminate all these complications, the minimum width of the resonator, b_{min}, should be larger than the spot size of the beam. The spot size of the beam is defined as the Airy disk diameter, d_{airy}, in Eq. (3.1) [198].

$$d_{\text{airy}} = 1.22\frac{\lambda_{\text{o}}}{\text{NA}} \tag{3.1}$$

λ_{o} and NA are the wavelength of the laser beam and numerical aperture of the objective lens, respectively. Smaller spots can be achieved by using an objective lens with higher NA or a laser beam with a lower wavelength. In our setup, $\lambda_{\text{o}} = 633$ nm and $\text{NA} = 0.42$ yield a theoretical limit of $d_{\text{airy}} = 1.8$ µm . On the other hand, imperfect calibration introduces

optical aberration, and the practical spot diameter is around $d_{\text{airy}} \cong 4$ µm; hence, the width of the resonator should be wider than 4 µm.

Electrical conductance is required to both transmit voltage and generate electrostatic force. Moreover, it is desired to have high reflectance on the resonator surface to obtain a high output from the LDV. The relationship between optical reflectance, $\mathcal{R}$, and electrical conductivity, ς, for conductive materials is well-defined with Hagen–Rubens formula in Eq. (3.2) [78].

$$\mathcal{R} \approx 1 - 4\sqrt{\frac{\pi\epsilon_0}{\varsigma\lambda_{\text{o}}}} \tag{3.2}$$

ϵ_0 is the vacuum permittivity. This relation shows that materials with high electrical conductivity also have high optical reflectivity. Therefore, a conductor material is preferred for the resonating medium. In terms of fabrication, it should be easy to etch for patterning, compatible with Al wire bonding, and cheap to deposit. Hence, Al was selected as the structure layer after considering all these concerns.

Larger actuation force produces a larger output signal and increases the signal-to-noise ratio. Recalling from the Eq. (2.47), the electrostatic force per unit length applying on the undeflected structure, f_{es}, can be written as,

$$f_{\text{es}} = \frac{\epsilon b V^2}{2d^2} \tag{3.3}$$

ϵ, V, and d are the dielectric constant of the gap medium, actuation voltage, and gap width, respectively. The actuation voltage is limited by the function generator. Although decreasing the air gap between the resonator and actuation electrode increases the electrostatic force, it could introduce additional squeezed film damping, c_{sf}, in Eq. (3.4) [145].

$$c_{\text{sf}} = f_{b/l}\frac{\mu_{\text{f}} l^4}{d^3} \tag{3.4}$$

$f_{b/l}$, l, and μ_{f} are a geometrical factor, the length of the resonator and the viscosity of the gap medium, respectively. Moreover, decreasing the air gap width can also produce an underetch issue, discussed in Section 3.1.2. As a result, the stiffness of the beam needs to be as weak as possible to convert limited electrostatic force into the greatest deflection. From a geometrical point of view, this can be achieved by having a large length-to-thickness ratio (>100), and the exact ratio was calculated as 160 using the simulations.

The dimensions in MEMS and NEMS tend to scale down, and natural frequencies increase according to the scaling law [33]. Therefore, it is desired to push the limits of

frequency while designing the actuator to demonstrate the proposed method for the most updated and future applications. Furthermore, a higher frequency regime offers better quality factors. Nevertheless, the digital velocity output of our LDV starts decaying after 1.5 MHz, and the natural frequency should exceed this threshold for equivalent measurement. Since the geometrical properties, material properties, and residual stress affect the natural frequency, mathematical models were simulated, and the length and thickness were determined as 40 µm and 250 nm, respectively.

Producibility

Standard optical lithography techniques allow patterning of the resonator with the desired length, and width [163]. The releasing step is critical when etching the sacrificial layer underneath the resonator because of aggressive etchants and sticking problems due to surface tension forces. To eliminate these problems, a polymer-based sacrificial layer was chosen with dry release in oxygen plasma [17]. However, plasma might struggle to reach underneath the resonator, especially if the width-to-air-gap ratio is high and can cause saturated underetch. Therefore, a low width-to-air-gap ratio is desired for a smooth release process. The width was chosen as 4 µm, $b_{\min}$, and an air gap of 4 µm was chosen to obtain a unity ratio.

Simulation

The three main aims of running simulations are (i) to identify the design parameters by calculating the natural frequency of the beam under the presence of residual stress, (ii) to perform a failure analysis to define the working regime, and (iii) to obtain the mode shape to compare with the experimental results. An FEM was constructed using COMSOL® by following the AC/DC and Structural Mechanics Modules User's Guide [47, 48]. In addition to that, a ROM was built [1], and the details are provided in the Supplementary Materials. In the numerical calculations, Young's modulus, density, Poisson ratio, and tensile strength of Al are taken as 69 GPa, 2.71 g/cm^3, 0.33, and 90 MPa, respectively [28].

The residual stress gets affected by so many parameters such as growth temperature and rate [215], material, deposition method, thickness [35], epitaxial mismatch [91], surface roughness, and contact angle [193]. Therefore, it is not feasible to make an accurate prediction by a simple calculation. Instead, a reasonable range, ±20 MPa, was defined based on the literature data [118, 170, 59], and the simulations were run in this region. The length and thickness were determined by keeping the first natural frequency below 1.5

MHz. The relationship between the residual stress and the first natural frequency of the finalized design is shown in Fig. 3.3a. It should be noted that compressive stress larger than 10 MPa might cause buckling during the release step, which is not desired. Additionally, buckling stress determines the thermal budget to calculate temperature limits. Fortunately, the first natural frequency of the fabricated structure is obtained at 1.4 MHz, corresponding to tensile stress around 17 MPa.

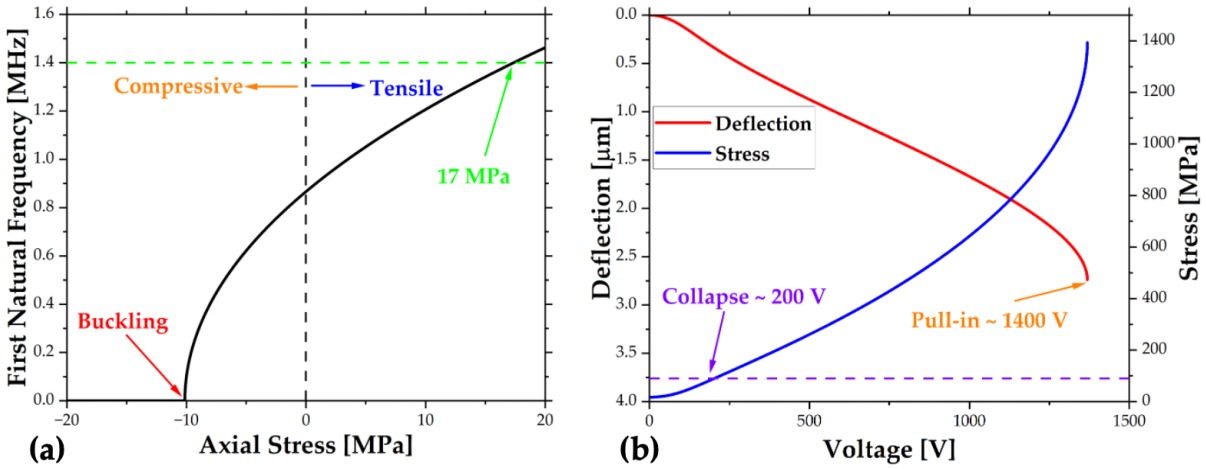


Figure 3.3: Simulation plots of the (a) first natural frequency vs. axial stress and (b) deflection and stress with respect to the actuation signal. Reproduced with permission from MDPI [73].

Secondly, failure analyses were run to determine the maximum actuation voltage limit. While there have been several failure mechanisms that worked in the literature, only two main mechanisms were considered in this analysis [221]. As the actuation voltage increases, the beam deflects more, and after some critical deflection, the beam can stick to the stationary electrode or collapse due to tensile stress. The former phenomenon is called pull-in and can be either static [241] or dynamic [161]. The dynamic pull-in analysis requires specific initial conditions and extra effort to generalize. For the sake of simplicity, only the static case was considered in this analysis. Alternatively, the beam might collapse if von Mises stress exceeds ultimate tensile stress. The variation of deflection and von Mises stress with respect to the actuation voltage is shown in Fig. 3.3b. When both failure mechanisms are considered, collapse happens earlier at a voltage level of around 200 V. To prevent failure, the maximum pulse voltage, 60 V, was set away from this value.

Finally, mode shape analyses were conducted to verify the experimental results and are

illustrated in Section 3.1.6.

3.1.3 Fabrication

The schematics of the fabrication process are shown in Fig. 3.4 and Table 3.1 and 4" prime grade p-doped Silicon wafer with a 50 nm-thick thermal oxide was chosen as the starting substrate.

Table 3.1: Device fabrication. Reproduced with permission from MDPI [73].

Layer	**Step 1**	**Step 2**	**Step 3**	**Step 4**
Actuation electrode	PR coating	Lithography	Metal deposition	Liftoff
Sacrificial layer	PR coating	-	-	-
Structure	Metal deposition	PR coating	Lithography	Dry etch
Dicing and Release	Dicing	Dry etch	-	-

A local actuator electrode was preferred for having a better electrical contact in packaging and eliminating excessive parasitic capacitance. It is patterned with a simple bilayer lift-off process, as shown in Fig. 3.4a [150]. First, HMDS treatment was performed to promote the adhesion between the substrate and PR layer. The underlayer (PMGI SF7) and positive-tone UV-PR (Shipley S1805) were spin-coated and soft-baked, sequentially. The pattern was exposed to 405 nm wavelength light with MLA and developed in MF-319. Then, 150 nm-thick Al film was deposited with e-beam (electron beam) deposition, and the excessive metal was lifted off.

The sacrificial layer, Fig. 3.4b, was built by spin-coating a negative-tone PR (AZ nLOF 2035) to reach 4 µm thickness and hard-baking under vacuum to prevent outgassing.

To construct the structure layer illustrated in Fig. 3.4c, firstly, 250 nm-thick Al film was deposited with e-beam deposition. Then, a positive-tone UV-PR (Shipley S1805) was spin-coated and soft-baked, and the design was exposed to 405 nm wavelength light with MLA and developed in MF-319. Excessive Al was dry etched with ICP-RIE.

The wafer was diced into smaller pieces with an automatic dicing. Finally, the structure was released by etching the sacrificial layer with a PR stripper, as shown in Fig. 3.4d.

Optical microscope and SEM images of the fabricated resonator are shown in Fig. 3.5. The laser spot almost covers the resonator as expected, as shown in Fig. 3.5b.

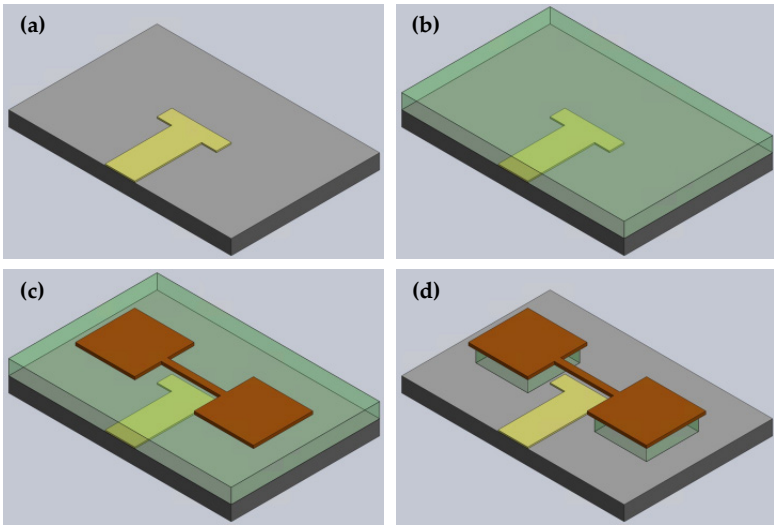


Figure 3.4: Device fabrication: (a) Actuation electrode patterning, (b) Sacrificial layer deposition, (c) Structure patterning, and (d) Releasing the resonator. (Yellow: Actuation electrode; Brown: Ground electrode and resonator; Gray: Substrate; Green: Sacrificial layer.) Reproduced with permission from MDPI [73].

3.1.4 Packaging

The images of the die with and without packaging are shown in Fig. 3.6a. The middle electrode of the die is the actuation electrode, while the rest is the ground electrode. The experimental setup for the reference measurements with a probing technique from the die without packaging is shown in Fig. 3.6b. To obtain electrical contact with the chip, a probe station, micromanipulators, and a relatively larger space are required.

Wire Bonding

The die was fixed to the chip carrier with double-sided tape and wire-bonded with 25 µm Al wire using a semi-automatic wedge–wedge bonder (Westbond 4546E), as shown in the middle of Fig. 3.6a. Then, the chip carrier was mounted on a custom PCB connecting the chip carrier to the testing equipment, and an image from the experimental setup is shown in Fig. 3.6c.

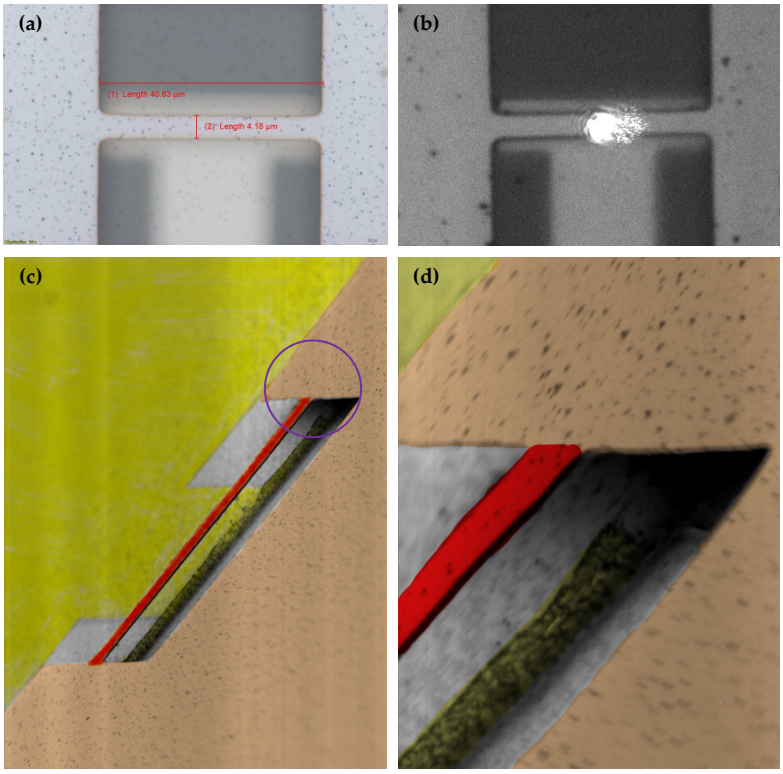


Figure 3.5: Fabricated resonator images from the following: (a) 100× optical microscope, (b) 50× optical microscope of the LDV with the laser spot, (c) 2000× SEM, and (d) 8000× SEM zoomed showing the purple area circled in (c). (Yellow: Actuation electrode; Brown: Ground electrode; Red: Resonator; Gray: Substrate). Reproduced with permission from MDPI [73].

Built-In

Unlike wire bonding, there is no equipment required for built-in packaging, and the die can be simply attached to the SubMiniature version A (SMA) connector jack, as shown in the right side of Fig. 3.6a. A foam tape was placed under the die to tolerate the thickness difference between the die and connector and encourage assembly. An image from the experimental setup is shown in Fig. 3.6d, and in contrast with wire bonding, the built-in package does not require any testing PCB and is ready for connection to the testing equipment. It also allows temporarily packaging, and the die can be easily dismounted from the SMA connector jack if required. In this work, the connector was removed after

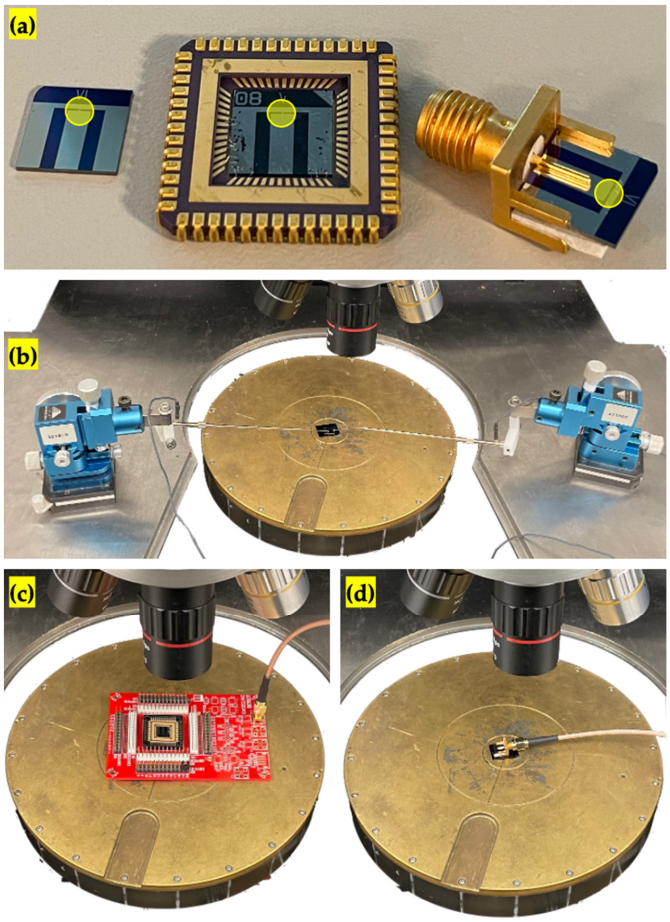


Figure 3.6: (a) The fabricated die without packaging, with wire bonding packaging, and with built-in packaging, from left to right. The resonator location is circled with yellow. The experimental setup comprises (b) reference measurements, (c) wire bonding packaging measurements, and (d) built-in packaging measurements. Reproduced with permission from MDPI [73].

testing, and the die was stored in its carrier, separately. For long-term applications where permanent packaging is necessary, the assembly can be promoted with glue or soldering.

3.1.5 Characterization

Purpose

The main aim of characterization is to compare the proposed packaging idea, built-in, with the conventional one, wire bonding, in terms of actuating performance. It is desired to test the same die with both types of packaging to prevent any variation. Although built-in offers temporary packaging and is suitable for this idea, it is destructive and tedious to remove and package back wire bonding, due to destructing contact pads and wire-bonder tool requirements. Therefore, two similar dies were packaged separately with each method and characterized simultaneously. To overcome the slight variation between dies, both were also characterized under a probe station with micromanipulators as a reference, and the performance comparison was conducted with respect to this reference.

Initially, frequency sweep measurements were performed for AC analyses. Then, DC analyses were completed with pulse response measurements. In addition, to demonstrate the applications inside an isolated chamber, pulse response measurements under vacuum conditions were prepared. Finally, mode shapes were measured and compared with the theoretical ones to associate the experimental results with the theory.

The methodology mentioned in Fig. 3.2 was followed for building the experimental setup for both measurements shown in Fig. 3.7.

Frequency Sweep

The frequency sweep measurement setup is illustrated in Fig. 3.7a. As there are two different chips, each one was measured with and without micromanipulators. The actuation signal was applied directly from the function generator in a linearly sweeping form at 20 V peak to peak and recorded through oscilloscope. The electrostatic force was related to the square of the actuation signal, so the mid frequency was chosen near half of the resonance frequency. For sensitive measurements over a wide range, three different sweeps were performed with 300 kHz, 150 kHz, and 25 kHz spans with 1 ms sweeping time. The laser beam of the LDV was focused on the center of the beam, and the analog velocity output signal of the LDV was measured from the oscilloscope in the time domain. To synchronize the phase of the input signal with the response, a trigger signal with the sweeping time was applied to perform a direct transformation from the time domain to the frequency domain.

The data read from the oscilloscope is shown in Fig. 3.8a. Both the actuation and velocity signals were in the time domain and, firstly, transformed into the frequency domain.

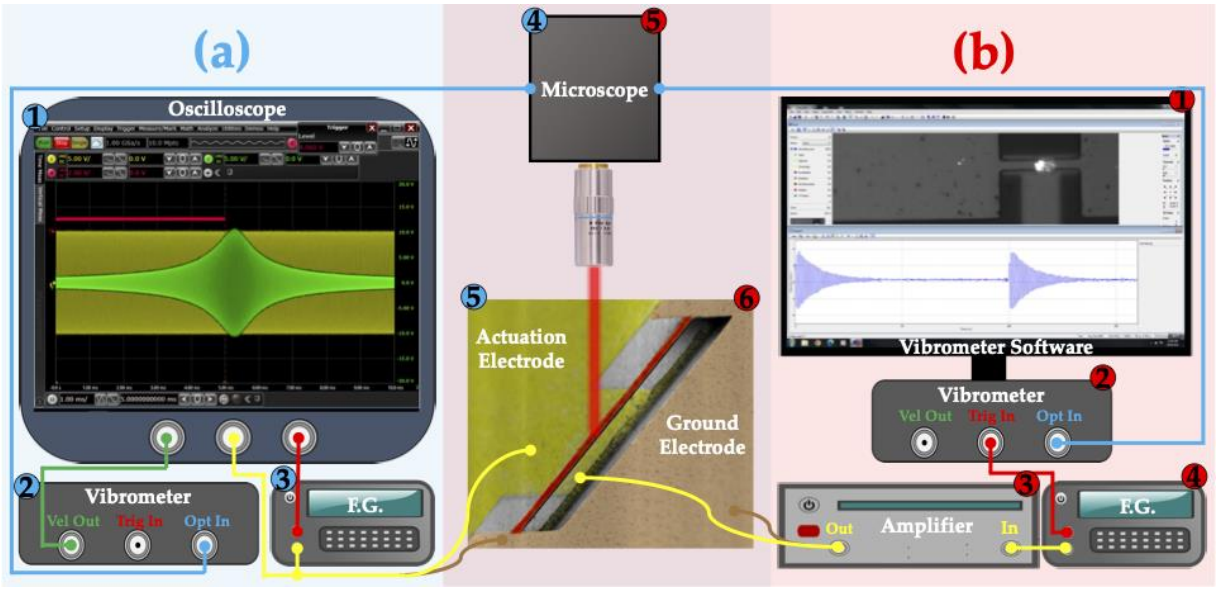


Figure 3.7: Experimental setup of (a) frequency sweep, and (b) pulse response analysis shown with blue and red backgrounds, respectively. Equipment configuration in frequency sweep analysis, (a), is 1: Oscilloscope, 2: Vibrometer, 3: F.G. (Function Generator), 4: Microscope, and 5: Resonator, while in pulse response analysis, (b), the configuration is 1: LDV software, 2: LDV, 3: Amplifier, 4: F.G., 5: Microscope, and 6: Resonator. Optical, velocity, actuation, ground, and trigger signals are shown with blue, green, yellow, brown, and red, respectively. Reproduced with permission from MDPI [73].

Then, the root mean square of the velocity with respect to the actuation frequency was obtained and plotted in the following section to obtain the quality factor, Q, and resonance frequencies. Finally, the phase difference between the force and velocity was obtained in the frequency domain to phase behavior and obtain the Q. The phase difference in the time domain is shown in Fig. 3.8b. The calculations related to this part are illustrated in the Supplementary Materials of my recent publication [73].

Pulse Response

In the pulse response tests, a 4 V peak-to-peak pulse signal with 15× amplification was applied from the function generator at 0.1% pulse width. Again, the laser beam was focused on the middle of the resonator, and the digital velocity signal was read from the vibrometer software in the time domain. The input signal was synchronized with a trigger

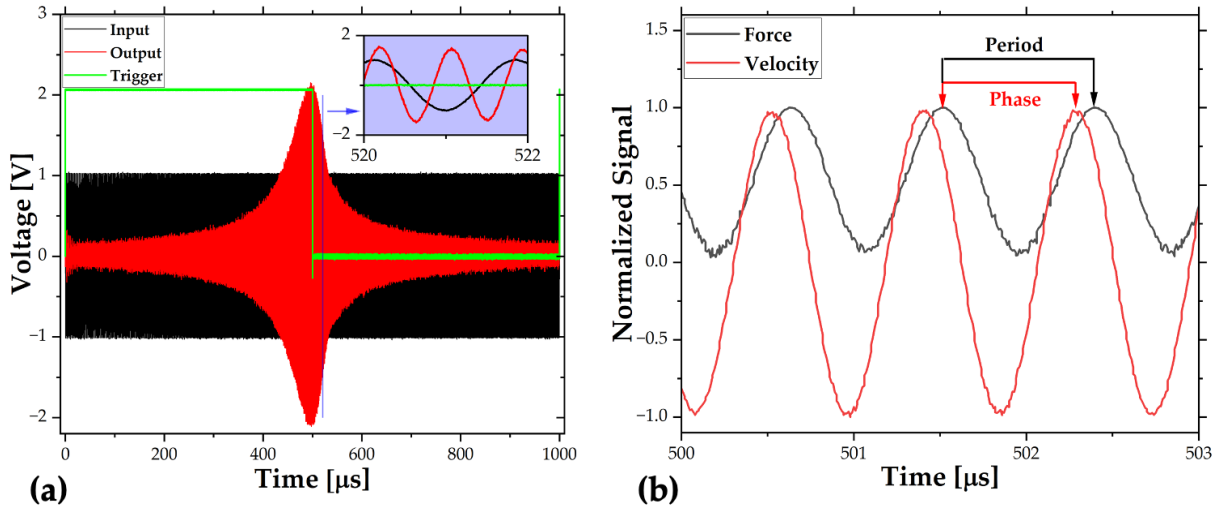


Figure 3.8: Frequency sweep measurement: (a) oscilloscope data, and (b) processes data. Reproduced with permission from MDPI [73].

signal, and the measured velocity is averaged 500 times to reduce noise.

In the vacuum tests, the vacuum level was around 7 mTorr. Unfortunately, the laser beam struggled to focus on the beam, due to additional watch glass between the microscope and the resonator. Although the relative velocity in the time domain was stable, the magnitude was dependent significantly on the focus; therefore, it was normalized to prevent any calibration error.

The data read from the LDV software is shown in Fig. 3.9. Then, the fast Fourier transform (FFT) was applied in MATLAB® to transform the data into the frequency domain.

Mode Shape

The mode shape of the built-in chip was measured with resonance actuation to compare the results with the models.

3.1.6 Results and Discussion

The results of the measurements described in Section 3.1.5 are presented and discussed in this section.

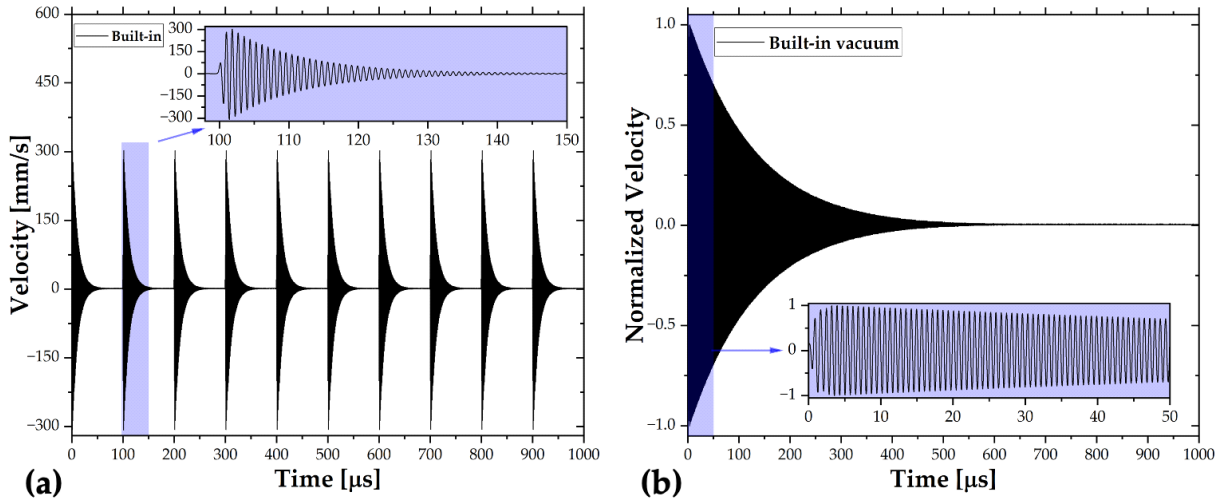


Figure 3.9: Pulse response measurement: (a) velocity data, and (b) vacuum data. Reproduced with permission from MDPI [73].

Frequency Sweep

The results of the frequency sweep are plotted in Fig. 3.10. The Lorentzian-like distributions in both plots represent the rms velocity, while the rest represent phase behavior. The horizontal axis is the actuation frequency domain, while the vertical axis for Gaussian-like behavior curves is velocity and the other is the phase axis. The resonance frequencies, f_0, are determined from the peaks of rms velocity curves. Then, the quality factor from rms velocity, $Q_{\delta f}$, is found by the bandwidth, δf. Finally, the quality factor from phase slope, Q_φ, is calculated by the phase slope at the resonance frequency, $\frac{\mathrm{d}\varphi}{\mathrm{d}f}|_{f_0}$. The exact relationships are given in Eq. (3.5).

$$Q_{\delta f} = \frac{f_0}{\delta f} \ , \ Q_\varphi = \frac{f_0}{2}\frac{\mathrm{d}\varphi}{\mathrm{d}f}|_{f_0} \tag{3.5}$$

The terms shown in Equation (5) for each measurement are listed in Table 3.2.

The resonance frequencies, bandwidths, phase slopes, quality factor calculated from bandwidth, and quality factor calculated from phase slop are in great agreement with the reference measurement of each chip. In fact, the similarity between different devices shows the repeatability of the fabrication, while the high-quality factors point out minimal support and air damping losses with successful fabrication. These measurements clearly

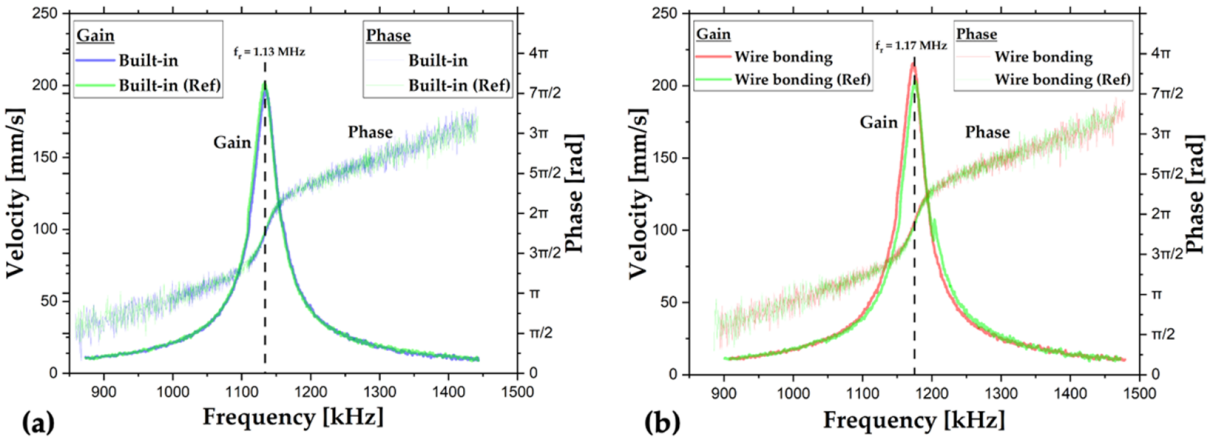


Figure 3.10: The results of frequency sweep measurements for (a) built-in and (b) wire bonding chips. Reproduced with permission from MDPI [73].

Table 3.2: The results of frequency sweep measurements. Reproduced with permission from MDPI [73].

Device	f_0 **[MHz]**	δf **[kHz]**	$\frac{\mathrm{d}\varphi}{\mathrm{d}f}\|_{f_0}$ **rad/MHz**	$Q_{\delta f}$	Q_{φ}
Built-in	1.13	29.8	67.0	38.0	38.0
Built-in (Ref)	1.13	30.0	66.9	37.8	38.0
Wire bonding	1.17	30.1	67.4	38.9	39.6
Wire bonding (Ref)	1.17	28.9	67.8	40.6	39.9

indicate the independency of the interconnection method on the results. Therefore, the built-in packaging offers the equivalent actuation performance as the wire bonding packaging and reference measurements with micromanipulators.

At resonance, the power supplied by the driving force (i.e., the product of the electrostatic force and velocity) is always positive, and hence, the system response (i.e., the amplitude of the velocity) is maximal.

Pulse Response

The pulse response results are shown in Fig. 3.11a. Again, the horizontal axis is the actuation frequency domain, while the vertical axis represents the rms velocity. The resonance

frequencies, f_0, are determined from the peaks of rms velocity curves. Then, the quality factor from rms velocity, $Q_{\delta f}$, is found by the bandwidth, δf, as illustrated in Equation (5).

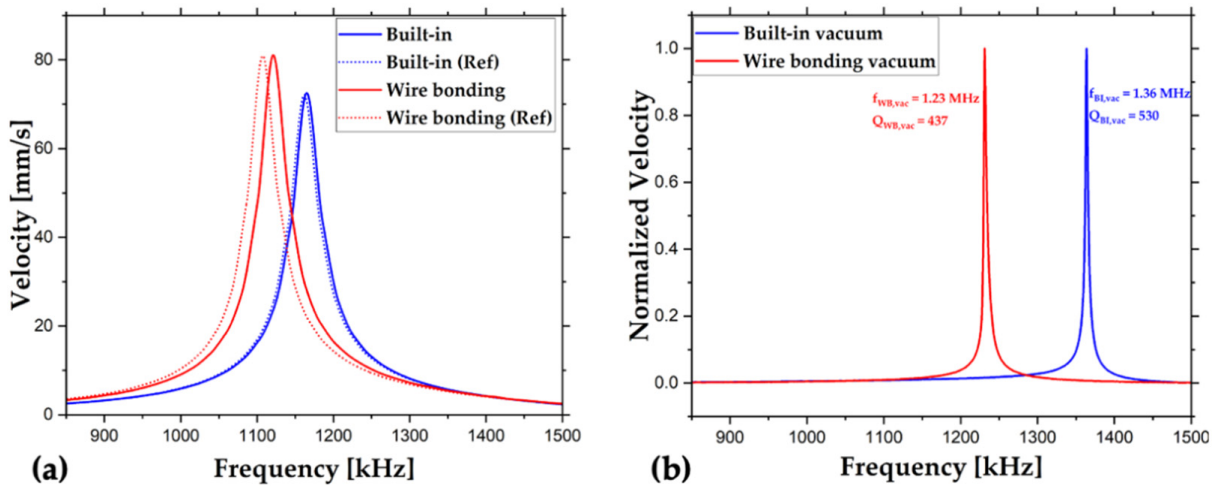


Figure 3.11: The plots of pulse response measurements performed in (a) in air, and (b) under vacuum conditions. Reproduced with permission from MDPI [73].

The resonance frequency, bandwidth, and quality factor obtained from the bandwidth of each measurement are listed in Table 3.3.

Table 3.3: The results of pulse response measurements. Reproduced with permission from MDPI [73].

Device	f_0 **[MHz]**	δf **[kHz]**	$Q_{\delta f}$
Built-in	1.17	30.1	38.7
Built-in (Ref)	1.16	30.2	38.4
Built-in (Vacuum)	1.36	2.58	529
Wire bonding	1.12	30.3	37.0
Wire bonding (Ref)	1.11	30.4	36.4
Wire bonding (Vacuum)	1.23	2.82	436

The outcomes of pulse response match with the frequency sweep measurements. In addition to air tests, very high-quality factors obtained under vacuum conditions indicate

very low structural losses. It should be noted that the vacuum resonance frequencies and quality factors tended to increase with time. Unfortunately, the wire bonding chip stayed under the vacuum for a shorter time, causing lower resonance frequency and quality factor. Therefore, it is not fair to compare the vacuum performances of devices. The main purpose of the vacuum test is to illustrate the application of built-in packaging inside isolated environments, and that was achieved by calculating the vacuum quality factor.

Mode Shape

The experimental mode shape obtained with built-in packaging is shown in Fig. 3.12, as well as the theoretical mode shape.

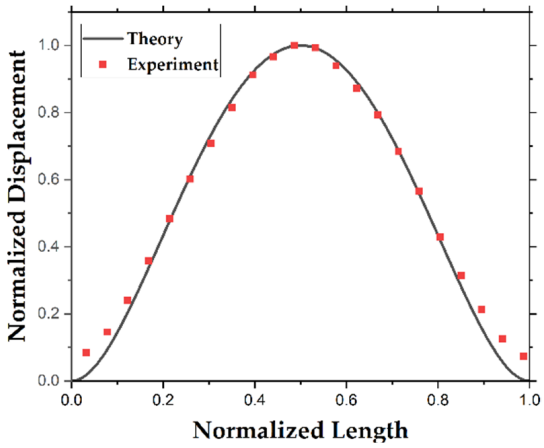


Figure 3.12: The first theoretical and experimental mode shapes. Reproduced with permission from MDPI [73].

The matching mode shapes demonstrate the similarity between the experiment and models. The slight variation between the theory and experiment around the edges could be sourced from the finite spot size of the laser beam causing an average measurement instead of a point measurement.

3.1.7 Conclusions

The main aim of this work is to propose the built-in packaging idea by illustrating its application on a single terminal device. Thus, a single-terminal actuator is designed, fabricated, packaged, and characterized with a detailed procedure.

To compare the performance of the proposed package, an actuator was designed, and a set was fabricated. Two structures were modeled with different mathematical models, FEM and ROM, for design purposes and failure analysis. Afterward, two similar actuators were packaged with the proposed method and a conventional method, wire bonding. The slight variation between devices was removed with reference measurements using micromanipulators. First, frequency sweep analysis was conducted with each device to characterize frequency response and phase behavior. Then, to consolidate the results, pulse response behavior in the frequency domain was analyzed. Outcomes of both measurements offer identical actuation performance between built-in and wire bonding packaging types. The matching results and high-quality factors obtained under air and vacuum verify the repeatability and success of the fabrication. Additionally, the compatibility of built-in packaging for operations inside an isolated chamber was demonstrated with vacuum tests. Finally, a mode shape measurement was executed using built-in packaging to justify the mathematical models. Consequently, the built-in packaging can be considered an alternative method in single-terminal device applications.

The main advantage of built-in packaging is simplicity. Primarily, no necessity for packaging equipment makes the process easy, cheap, and accessible. In addition, no chip carrier requirement gives freedom in chip design and offers immediate characterization after fabrication. Furthermore, it is a standalone packaging allowing connection to testing equipment without any PCB or cable. In addition, built-in packaging can revolutionize regular chips into plug-and-play devices. When all these benchmarks are considered, the proposed conception can catch industrial and academic attention.

Feedthrough losses and noises have a noteworthy role in the electrical actuation and measurements of MEMS and NEMS. These can be minimized by eliminating all possible interconnection elements and wires. The continuation of this work will be followed by the demonstration of single or multiple terminals to show equivalent or improved device performances.

3.2 MIM diode

Conventional packaging and interconnection methods for two-terminal devices, e.g., diodes often involve expensive and bulky equipment, introduce parasitic effects and have reliability issues. In this study, we propose a built-in packaging method and evaluate its performance compared to probing and wire bonding methods. The built-in packaging approach offers a larger overlap area, improved contact resistance, and direct connection to testing equipment. The experimental results demonstrate a 12% increase in current, an 11% reduction in

resistance, and improved performance of the diode. The proposed method is promising for enhancing sensing applications, wireless power transmission, energy harvesting, and solar rectennas. Overall, the built-in packaging method offers a simpler, cheaper, more compact and more reliable packaging solution, paving the way for more efficient and advanced technologies in these domains.

3.2.1 Introduction

In the era of the IoT and AI, there has been an increasing demand for devices that are not only smarter but also more efficient. Diodes, essential components in this digital revolution, play a significant role in our increasingly interconnected world. Their asymmetric conductance underpins the integrated circuit (IC) industry, enabling the formation of electronic logic. Their ability to allow electrical current to flow predominantly in one direction while obstructing the reverse direction makes them a versatile tool in a diverse range of applications, including power applications such as rectifying antennas (rectennas), high-frequency applications in communication and imaging, and a broad spectrum of sensing technologies.

However, the journey to optimal diodes brings significant challenges. Among these, diode resistance is a crucial factor that impacts detectivity limits and needs to be minimized for superior sensing applications [220]. Power applications, in particular, require efficient rectennas characterized by high responsivity, low resistance, and high asymmetry. Furthermore, low diode resistance is critical for high-frequency applications to maximize efficiency [6]. Balancing these conflicting requirements often presents complex design challenges when crafting ideal diodes [70].

The rising popularity of MIM diodes in areas such as energy harvesting [106], solar and infrared rectennas [70, 213], wireless power transmission [22], and sensing applications [135, 104] is due to their notable advantages. These advantages include a high-frequency response, low power consumption, small size, and cost-effective production [200]. The need for improved current density, resistivity, and signal-to-noise ratio is especially critical in sensing, where enhanced sensitivity, accuracy, and reliability can lead to detecting and measuring weaker signals with greater precision [38]. These advancements in MIM diode characteristics can significantly influence the development of more efficient and innovative techniques.

Building on our recent pioneering work on the built-in packaging of single-terminal devices [73], this study represents a significant advancement in two-terminal device packaging

methodologies, explicitly focusing on MIM diodes and directly addressing the above challenges. We introduce an innovative approach to enhance diode performance and reliability that bypasses the limitations associated with traditional packaging. The proposed built-in packaging technique eliminates the need for conventional packaging or a carrier board, thus addressing well-known reliability challenges such as mechanical failure and corrosion associated with wire bonding [225, 96, 66, 63, 62, 133, 230]. By reducing the parasitic resistance arising from conventional packaging and interconnections, we increase current density by 12%, without compromising other essential performance parameters such as asymmetry, nonlinearity, or responsivity.

This novel technique promises significant benefits for high-frequency applications, subdivided into communication and imaging applications [200]. Higher cutoff frequencies facilitate faster data transfer, thereby enhancing communication [15]. Simultaneously, increased detectivity contributes to improved imaging in the terahertz (THz) regime, particularly beneficial for biosensing and astrophysics applications [210, 76]. Therefore, our approach to MIM diodes holds the promise for advancing next-generation 6G communication, astrophysics, logic boards, and bioimaging.

In conclusion, our research highlights the potential of integrated packaging in two-terminal devices, presenting opportunities to enhance the efficiency, reliability, and cost-effectiveness of numerous applications. Our successful demonstration of the built-in packaging concept on both single-terminal [73], and two-terminal devices serve as a catalyst for further exploration of its applicability across diverse areas, including sensors, optics, RF, microfluidics, and other related applications.

3.2.2 Materials and Methods

Fabrication

The self-aligned stepped MIM diode configuration was chosen for its precise layer alignment during fabrication, which facilitates efficient electron tunneling through the thin insulator layer. The device area was designed to be 1 µm^2 (1 × 1 µm) in order to minimize fabrication costs, which can be achieved by using standard photolithography instead of electron-beam lithography. The Pt-Al electrode combination was selected due to its exceptional work function difference of 1.37 eV, which is one of the highest reported in the existing literature [5], although a difference that exceeds approximately 300 meV may also be considered acceptable [173]. Pt was chosen as the bottom electrode due to its noble metal behavior, exhibiting high oxidation resistance that effectively prevents undesired oxide interference

between the bottom and top electrodes, apart from the desired insulator layer. TiO_2 was chosen as the insulator layer due to its wide range of applications [11] and promising results in MIM configurations with a thickness of 60 nm except for a low current density [6]. To enhance the current density, the thickness of TiO_2 was reduced to 6 nm, following a recent study. In particular, a 6 nm thick layer of Al_2O_3 has demonstrated encouraging results in rectenna applications [5]. The energy diagram, microscope images, and process flow of the fabricated MIM diode are presented in Figure 3.13 and Table 3.4, respectively.

Table 3.4: Fabrication steps for MIM diode. Reproduced with permission from MDPI [74].

Device	**Step 1**	**Step 2**	**Step 2**	**Step 3**
Bottom electrode	PR coating	Lithography	Deposition	Liftoff
Insulator	Deposition	PR coating	Lithography	Wet etch
Top electrode	PR coating	Lithography	Deposition	Liftoff

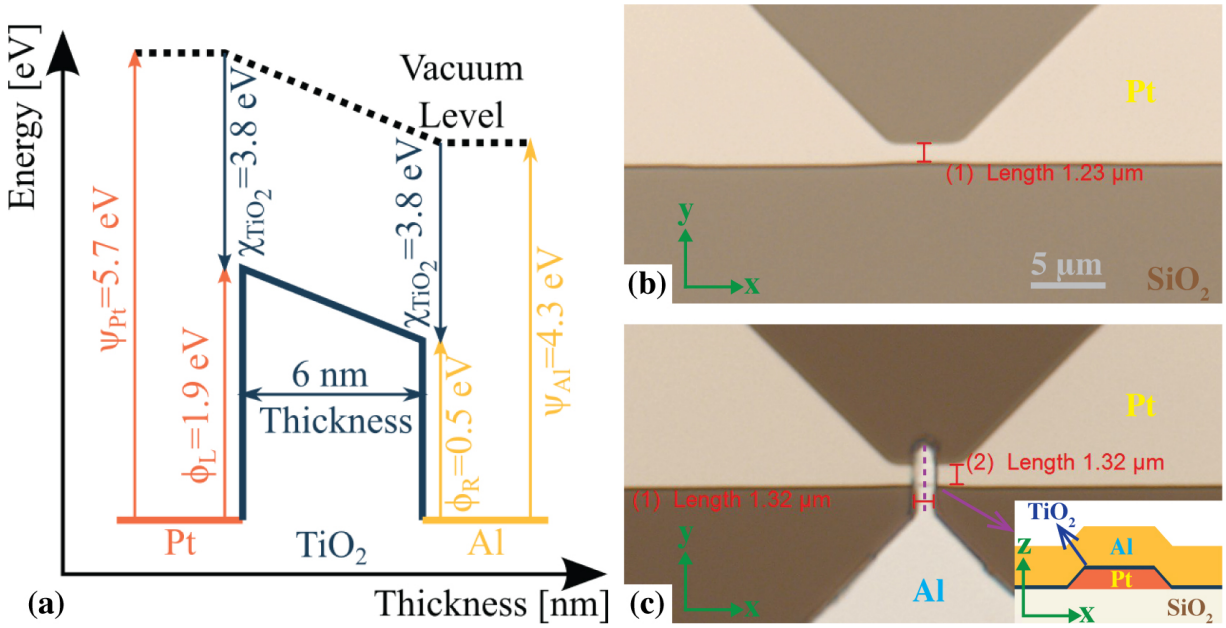


Figure 3.13: (a) Energy diagram for the Pt-TiO_2-Al MIM diode, and microscope images of the device before (b) and after (c) the top electrode deposition (the inset shows the cross-sectional view). Reproduced with permission from MDPI [74].

A 4-inch prime-grade p-doped silicon wafer with a 50 nm thick thermal oxide layer was

selected to serve as the initial substrate. A simple bilayer liftoff technique was employed for the metal electrode patterning process. Initially, the substrate underwent HMDS treatment to enhance adhesion between the substrate and the PR layer. Subsequently, the underlayer (PMGI SF7) was spin coated at a rate of 5000 RPM and subjected to a soft bake at 180 °C for 5 min. The positive tone UV-PR (Shipley S1805) was then spin-coated at 5000 RPM and soft baked at 120 °C for 90 s. Using MLA with a laser wavelength of 405 nm and a dose of 80 mJ/cm^2, the bottom electrode pattern was exposed. The exposed PR was then developed in MF-319 for one minute and rinsed with deionized water. Subsequently, a 100 nm thick Pt film was deposited onto the wafer at room temperature using the electron beam evaporation technique, with a deposition rate of 0.3 nm/s. To uniformly remove the excess metal, the wafer was immersed in a Remover PG solution overnight, rinsing with acetone and isopropyl alcohol (IPA), and finally dried using a nitrogen gun. The microscope image of the bottom electrode can be seen in Figure 3.13b.

To create the insulator layer, a 6 nm thick TiO_2 film was deposited using the atomic layer deposition (ALD) technique, following the standard recipe described in a recent study [6]. In order to establish electrical contact with the bottom electrode, it was necessary to remove the insulator layer from the contact pads. The process began with HMDS treatment. Later, the positive-tone UV-PR (Shipley S1811) was spin-coated at 5000 RPM and subjected to a soft baking at 120 °C for 90 s. Using MLA with a laser wavelength of 405 nm and a dose of 100 mJ/cm^2, the pattern for the insulator layer was exposed. The exposed PR was then developed in MF-319 for one minute and rinsed with deionized water. The wafer was then immersed in a buffered HF solution to perform a wet etching process, effectively removing excessive TiO_2 from the surface.

The top electrode layer was patterned using a single-layer liftoff. The process began by applying HMDS. After that, a positive tone UV resist, Shipley S1805, was spread evenly using spin-coating at a speed of 5000 RPM. The coated PR was then subjected to a soft bake at 120 °C for 90 s. The same MLA parameters as those used for the bottom electrode pattern were applied to define the pattern for the top electrode. Subsequently, the PR exposed to the pattern was developed in MF-319 for one minute, followed by rinsing with deionized water. Then an aluminum film layer with a thickness of 200 nm was deposited onto the wafer at room temperature using electron beam evaporation. The deposition rate was 0.3 nm/s. To remove any excess metal uniformly, the wafer was soaked overnight in a Remover PG solution, then rinsed with acetone and IPA, and finally dried using a nitrogen gun.

Finally, the 4″ wafer was diced into smaller dies (8.6 × 8.6 mm) to match the dimensions of a standard SMA connector jack and a standard chip carrier in order to attach and test the same chip with both. The microscope images and the cross-sectional view of the

fabricated MIM diode are shown in Figure 3.13c. The overlap area of the MIM diode was measured as 1.74 µm^2 (1.32 × 1.32 µm).

Packaging and Experimental Setup

Following the fabrication of the chip, IV-curve characterization was carried out using a source measure unit (SMU, B2902A) for each interconnection method as shown in Figure 3.14.

To evaluate the effectiveness of the proposed built-in packaging method, the same device was characterized using three different techniques: probing with a probe station, wire bonding, and built-in packaging. While soldering is widely used in semiconductor industry, it is not considered suitable for this purpose due to various limitations and potential risks [87, 125]. Semiconductor devices are highly sensitive to surface contamination, making them vulnerable to the negative effects of solder flux. Furthermore, the application of thermal stress during soldering can damage delicate components and elevated temperatures may not be compatible with sensitive materials. Diffusion and alloying processes during soldering can also alter the performance of the device. Furthermore, the irreversible nature of soldering limits repair options, and the miniaturization trend poses challenges for reliable solder connections. For these reasons, soldering is not considered.

Probing is a widely utilized technique for preliminary electrical characterization of two- to three-terminal devices, such as diodes or transistors. The experimental setup for probing, as well as the chip used, are shown in Figure 3.14a. This method possesses two main drawbacks. Firstly, it requires the use of an expensive and bulky setup comprising a probe station, micromanipulators, and a microscope in order to establish electrical contact with the fabricated chip. Second, the probes utilized are thin needle-shaped structures that resemble antennas, which introduce parasitic resistance and capacitance.

For the wire-bonding measurements, the die, Figure 3.14a, was securely affixed to the chip carrier using double-sided tape. Subsequently, a semi-automatic wedge-wedge bonder (Westbond 4546E) was utilized to wire bond the die using 25 µm Al wire, as shown in the inset of Figure 3.14b. The chip carrier was then mounted onto a custom PCB, enabling the connection between the chip carrier and the testing equipment. An image of the experimental setup is presented in Figure 3.14b. While wire-bonding offers a simpler experimental setup compared to probing, the packaging process requires an expensive equipment and a skilled technician to successfully bond the chip to the carrier. Moreover, it is essential to design the die to fit within standardized chip carriers, which imposes restrictions on the dimensions of the die and metal pads. Additionally, it is necessary

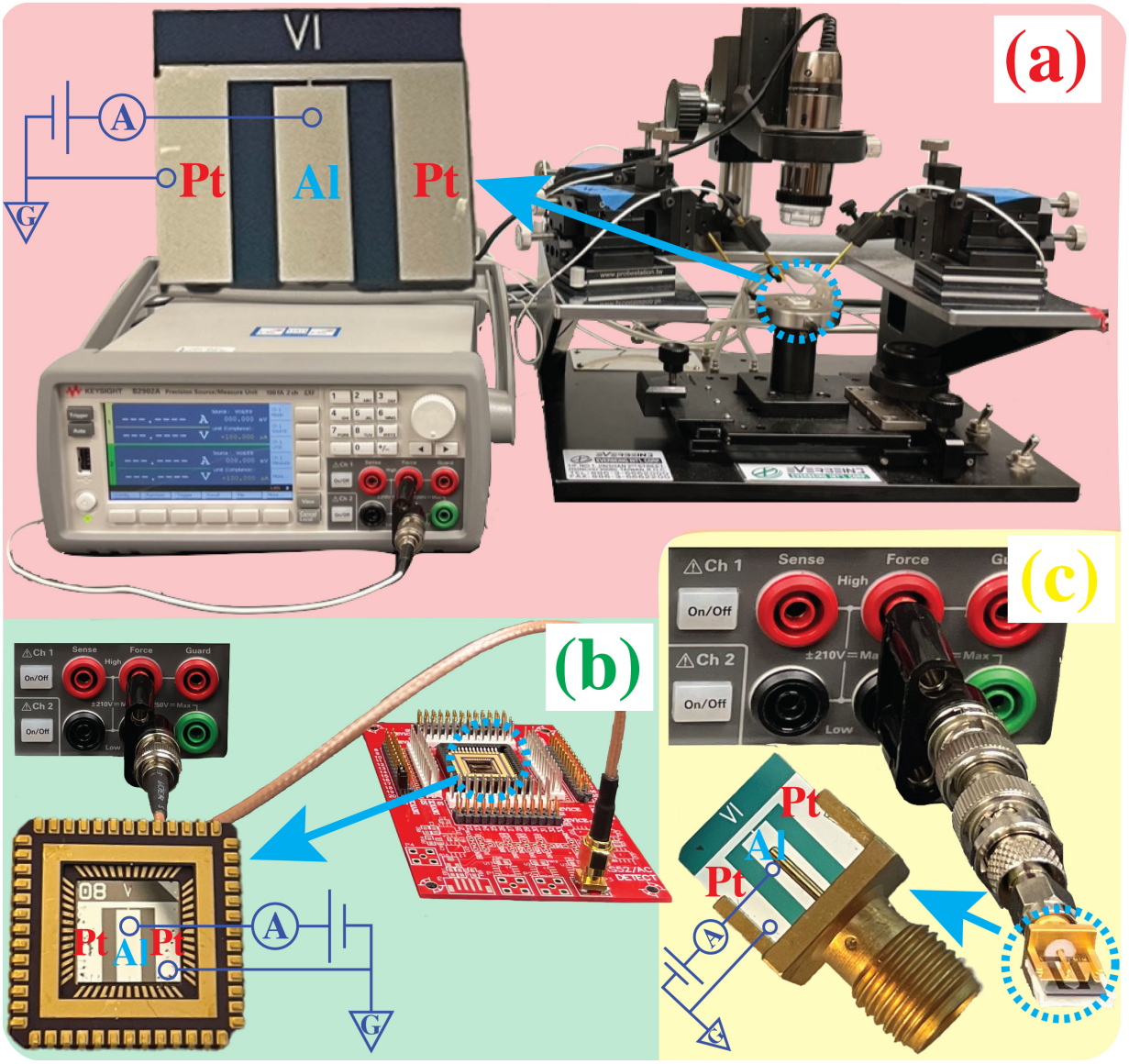


Figure 3.14: Experimental setup and electrical schematics of (a) probing, (b) wire-bonding, and (c) built-in packaging. Reproduced with permission from MDPI [74].

to design and fabricate the corresponding PCB. Similarly to probing, the wires exhibit antenna-like characteristics that give rise to parasitic effects.

The contact pads of the die were specifically designed to align with and cover the pins

of the SMA connector jack. The thickness of the die, 0.5 mm, is slightly smaller than the opening of the SMA connector, therefore the remaining space was fulfilled by placing a foam tape on the backside of the die to provide the necessary support. This approach ensured optimal contact between the connector and the device, allowing reliable connectivity as shown in Figure 3.14c. The proposed approach has a distinct advantage over probing and wire-bonding methods due to its significantly larger overlap area. This is achieved by establishing a wide contact area between the connector and the device, in contrast to the single point of contact utilized in probing and wire-bonding techniques. The expanded contact area not only improves the reliability and stability of the connection but also reduces the contact resistance. This reduction in contact resistance further contributed to the overall performance and efficiency of the connection. Furthermore, this method offered the advantage of a direct connection between the connector jack and testing equipment, such as an source measure unit (SMU), eliminating the need for additional space or components. Consequently, it was highly space-efficient and required minimal setup.

Finally, the diode was detached from the SMA connector jack and subsequently measured using probing techniques to ensure that its electrical characteristics were unchanged before and after each test procedure.

3.2.3 Results and Discussion

For the electrical characterization, voltage was swept with the SMU with a step voltage of 4 mV and the current passing through the diode was measured for each interconnection method as described in Figure 3.14. The measured data were signal processed with the Savitzky-Golay filter [191] in Python to reduce experimental noise and smoothly estimate derivatives of the signal. The plots of the measured IV-curves for each interconnection technique are shown in Figure 3.15a,b.

A uniform increase in the current level of 12% was observed compared to conventional interconnection methods. The maximum current density, denoted as J, reached 1.3×10^5 using conventional methods. However, the proposed method achieved a higher current density of 1.5×10^5, representing an increase of 10%. The resistance of the diode can be found as the slope of the current-voltage curve,

$$R = \frac{\mathrm{d}I}{\mathrm{d}V} \tag{3.6}$$

where I and V are the instantaneous current and voltage, respectively. The calculated values of R for each interconnection method are plotted in Figure 3.15c. The plot clearly

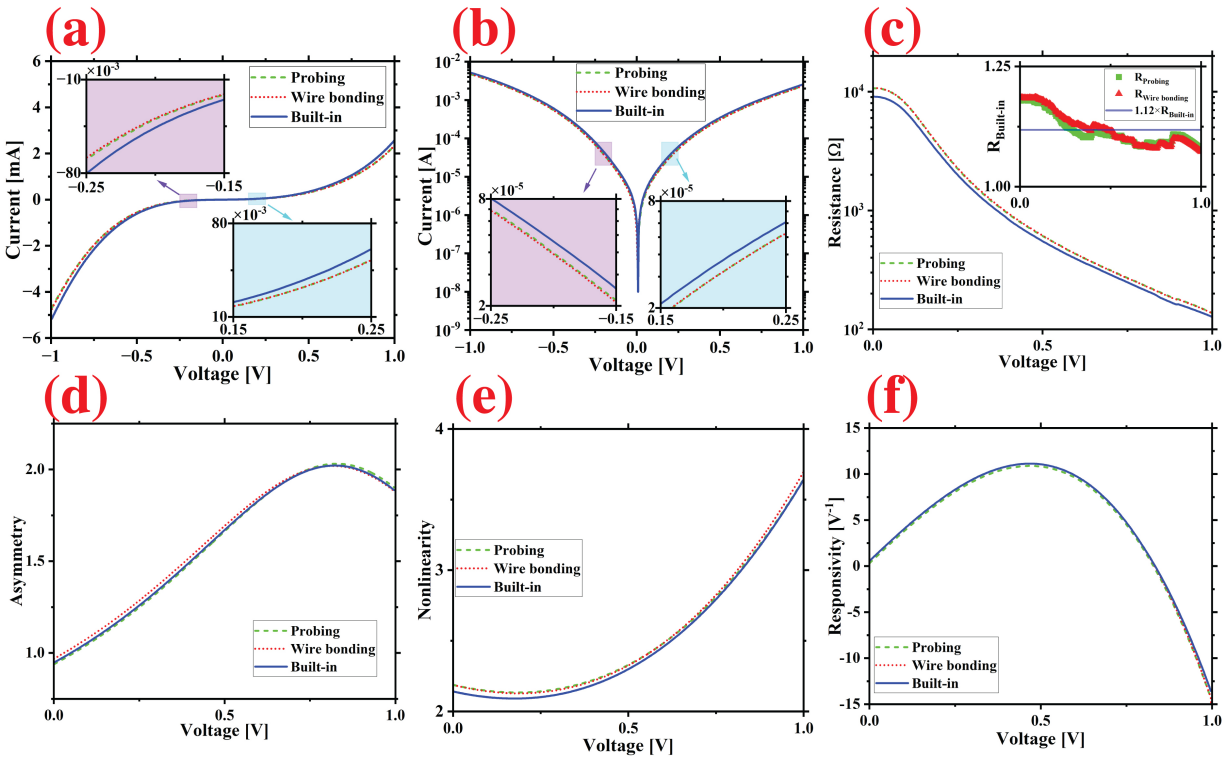


Figure 3.15: Electrical characteristics of the fabricated diode using three different interconnection methods: (a) linear and (b) logarithmic scale IV-curves. The diode resistance is shown on logarithmic scale in (c). The inset depicts the ratio of resistance between conventional methods and built-in packaging. The diode's asymmetry, nonlinearity, and responsivity are shown in (d–f), respectively. Reproduced with permission from MDPI [74].

shows an average reduction in resistance of 11% compared to conventional interconnection methods. In particular, the zero-bias resistance decreased from 10.7 kΩ to 9.0 kΩ, indicating a substantial decrease of 15%. This is highly significant, since resistance directly impacts various diode performance parameters. First, because of their finite resistance R and capacitance C, diodes act as a low-pass filter element limiting their operation range by the cut-off frequency, f_c,

$$f_c = \frac{1}{2\pi RC} \tag{3.7}$$

which suggests that decreasing resistance by 11% corresponds to an increase in the cutoff frequency by 12%. Second, the detectivity of a diode, D^*, is a measure of its sensitivity to

weak signals or its ability to detect low-level signals in the presence of noise. It quantifies the ability of a diode to convert a weak input signal into a detectable electrical output and can be defined as [172]:

$$D^* = \beta_{\text{sys}} \sqrt{A_{\text{abs}}} \sqrt{R/4kT} \tag{3.8}$$

where β_{sys} is the system responsivity, A_{abs} is the absorption area of the detector, k_B is Bolztmann constant, and T is the temperature. As the decreased resistance increases, the signal level, current and detectivity can be increased by 6% by improving the signal-to-noise ratio.

Lastly, for the rectification performances, there are three crucial figures of merit of diodes: asymmetry, nonlinearity, and responsivity. Asymmetry is the ratio between the forward (I_F) and reverse currents (I_R):

$$\text{Asymmetry} = |I_F/I_R| \tag{3.9}$$

which needs to be greater than one for the rectification. As shown in Figure 3.15d, the diode exhibits asymmetric behavior that spans the entire range of 0–1 V, with values exceeding one, demonstrating equivalent responses across the three interconnections. Nonlinearity,

$$\text{Nonlinearity} = \frac{\mathrm{d}I}{\mathrm{d}V} \Big/ \frac{I}{V} \tag{3.10}$$

indicates the sharpness of the transition from the reverse biased (blocking) state to the forward biased (conducting) state. High nonlinearity is essential to achieve significant rectification. The nonlinearity of the three interconnections shows an equivalent response as plotted in Figure 3.15e. Responsivity is the ratio of the output DC current to the input AC power and can be quantified with:

$$\text{Responsivity} = \frac{\mathrm{d}^2 I}{\mathrm{d}V^2} \Big/ \frac{\mathrm{d}I}{2\mathrm{d}V} \tag{3.11}$$

which shows the rectification efficiency of the diode. Figure 3.15f illustrates the identical responsivity behaviors observed for each method. The average values of the zero-bias responsivity were found to be 0.55 V^{-1}, while the maximum responsivity reached 14.3 V^{-1} at 1 V.

The experimental data are provided in the supplementary information. Additionally, the Python code utilized for signal and data processing can be found in the Appendix B. In order to assess the performance of the fabricated diode, a comparison is made in Table 3.5 between its performance parameters and those of the most advanced MIM diodes reported

in recent literature.

The performance of the fabricated and tested diode is similar to those reported in the literature. This suggests that similar improvements can be achieved for state-of-the-art diodes without sacrificing any performance parameters by implementing the two-terminal built-in packaging approach.

Table 3.5: Performance comparison of the MIM diodes with the literature. Reproduced with permission from MDPI [74].

Structure	**Insulator Thickness [nm]**	**Area [µm²]**	**Asym. ≈0.5V**	**Max. Nonlin.**	**Zero-Bias Respon. [V⁻¹]**	**Max. Respon. [V⁻¹]**	**Max. J [A/cm²]**	**Zero-Bias Resistance [Ω]**	**Application**	**Interconnection**	**Ref.**
Al/AlO_x/Ag	0.75	1.76×10^6	1.2	12.5	9	9	3×10^{-10}	27×10^3	Rectenna	Probing	[21]
Al/AlO_x/Pt	0.1–0.2	8×10^{-3}	1	9.9×10^{-6}	-	10^{-3}	43×10^6	1.25×10^2	IR-detector	Probing	[110]
Al/AlO_x/Pt	1–2.5	4×10^{-3}	-	-	-	4.8	5×10^2	312×10^6	IR-detector	Probing/Wire bonding	[20]
Al/AlO_x/Pt	2.5–3.5	4×10^{-3}	1	3×10^{-3}	-	10^{-2}	500×10^3	1.65×10^3	IR-detector	Probing/Wire bonding	[217]
Nb/NbO_x/Pt	15	6.4×10^3	7.7×10^3	4.7	15	16.9	1×10^{-2}	7.8×10^9	-	Probing	[45]
Ni/NiO/Pt	1–2	2.5×10^{-3}	-	9	-	6.5	3.6×10^{-2}	$\approx 10^7$	IR-detector	Probing	[57]
Al/TiO_2/Pt	6	1.74	1.7	3.7	0.55	14.3	1.3×10^5	10.7×10^3	-	Probing	ours
Al/TiO_2/Pt	6	1.74	1.7	3.7	0.55	14.3	1.3×10^5	10.7×10^3	-	Wire bonding	ours
Al/TiO_2/Pt	6	1.74	1.7	3.7	0.55	14.3	1.5×10^5	9.0×10^3	-	Built-in	ours

In sensing applications, achieving an improved signal-to-noise ratio is essential to enhance detectivity and sensitivity. This improvement enables more reliable detection and measurement of weaker signals [86]. Likewise, in wireless power transmission, minimizing power loss during energy transfer is crucial, and this is achieved by reducing resistance. This, in turn, enhances the efficiency of wireless charging systems [199].

In addition, in energy harvesting, increasing the current density plays a significant role in reducing energy loss and improving the efficient conversion of ambient energy sources into usable electrical power [218, 200, 106].

Furthermore, the proposed built-in packaging approach offers several advantages in the test setup. These include simplicity, cost-effectiveness, compact size, and robustness. These advancements open up new possibilities for the development of more efficient technologies in energy harvesting, solar rectennas, wireless power transmission, and sensing applications.

3.2.4 Conclusions

Our study introduces an innovative approach to diode packaging, designed to improve performance and reliability by overcoming traditional limitations. Our proposed built-in packaging method negates the need for conventional packaging or carrier boards, which are known for their susceptibility to mechanical failure and corrosion. The experimental

results reveal the potential of our built-in packaging method. Improvements in current levels, reduction in resistance, and enhanced performance parameters promise substantial advantages for a multitude of applications, notably in sensing, wireless power transmission, energy harvesting, and solar rectennas.

With the rapid advancements in technological sectors, the contribution of our study becomes all the more significant. The built-in packaging method invites simpler, cheaper, and more reliable packaging solutions. This method not only proposes a more efficient approach to existing challenges, but also paves the way for future technological advancements in these domains. However, it is important to note that reliability tests have not been conducted in this work, highlighting the need for further exploration of the reliability of this structure.

In conclusion, our research provides significant progress in the field of two-terminal device packaging, presenting built-in packaging as a viable solution to enhance efficiency, reliability, and cost-effectiveness in numerous applications. It marks a significant contribution to the broader advancements in diode design and packaging techniques, using an innovative approach. The success of the built-in packaging concept in both single-terminal and two-terminal devices paves the way for further exploration of its applicability across a diverse range of areas, including sensors, optics, RF, microfluidics, and more. Thus, the implications of our research extend beyond the current study, stimulating thought and potential future research into improving the efficiency of two-terminal devices and their applications.

Chapter 4

Interface Engineering of Semiconductor Nanoparticles

As the sensors scale down, their output signal shrinks and can become indistinguishable from noise if it drops below the noise floor, thereby imposing a fundamental limitation on miniaturization. Higher responsive sensor active materials materials can push the limits of scaling down by compensating for the reduced signal associated with miniaturization. For smaller photodetector pixel, semiconductor nanoparticles are promising candidates to replace their bulk counterparts due to their enhanced responsiveness. CQDs have tunable and selective optical properties, making them attractive for IR photodetectors with smaller pixel sizes. However, their poor electrical properties prevent the generated signal from efficiently reaching the readout circuit. Improving their electrical performance is essential therefore, there is a need for the robust quantification of their electrical properties.In this chapter, a FET based mobility measurement setup is developed to evaluate the carrier mobility of CQD films. Using this setup, the mobilities of also several types of quantum dots including PbS, InAs, and InSb were measured.

4.1 Introduction

There is a need to develop more sensitive materials to produce equivalent output signals for the miniaturized sensors. For this reason, transition from the conventional bulk materials to novel nanomaterials is essential. Semiconductor based photodetectors have been following this trend and looking for alternatives of Si to achieve higher performances with smaller

pixels. However, bandgap tunability and integration with the readout electronics of the developed material are among the key challenges for photodetector applications. CQDs are solution processed nanosized particles of semiconductors with diameters below 20 nm and they offer several advantages for photodetector applications [142].

First, CQDs absorption and emission wavelengths not only depend on the material but also on the size of the particle through the quantum size effect. As dimensions of semiconductors shrink to the nanometer scale, quantum confinement effects begin to dominate their physical behavior. As a result of the confinement, the energy levels quantize and bandgap increases as shown in Figure 4.1.

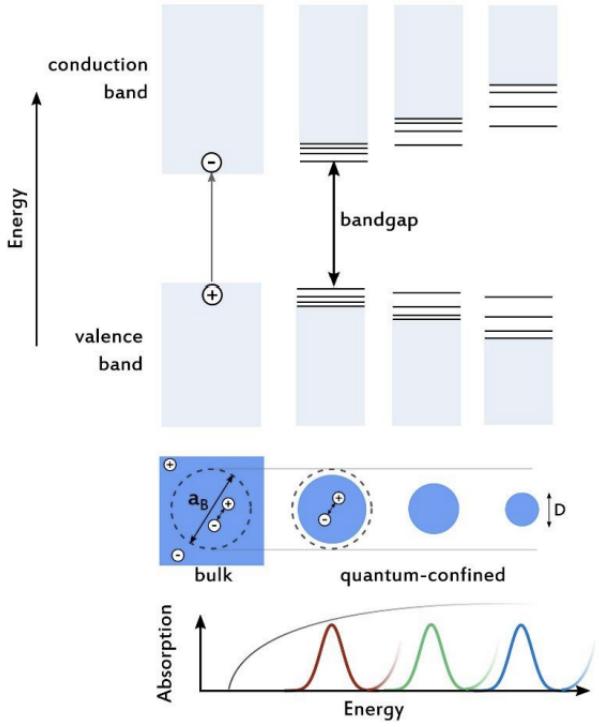


Figure 4.1: Quantum confinement on QD materials. Quantum confinement, leading to size-dependent optical and electrical properties that are distinct from those of parental bulk solids, occurs when the spatial extent of electronic wave functions is smaller than the Bohr exciton diameter. Reprinted with permission from AAAS [64].

For example, PbS is a semiconductor with an energy bandgap around 0.37 eV in the bulk form where its bandgap can be increased up to [156] 2.50 eV at 1.5 nm quantum dot

diameter. Therefore, by tuning the dot size of various semiconductors, they can selectively detect light across a broad infrared (IR) spectrum ranging from near-infrared (NIR, 0.75-1.4 µm) [231], short-wavelength infrared (SWIR, 1.4-3 µm) [247], mid-wavelength infrared (MWIR, 3-8 µm) [25], long-wavelength infrared (LWIR, 8-15 µm) [243], to very long-wavelength infrared (VLWIR, 15-30 µm) [238].

The next step is integration of these optically engineered materials with electronic readout systems. Ideally, these materials should be monolithically integrated with cost-effective CMOS-based readout integrated circuits (ROICs) to reduce the costs and increase the pixel density [117]. Conventional infrared detectors typically require either monolithic fabrication of both optical [140] and electronic components on a single substrate or seperate fabrication followed by a hybridization process [89]. In monolithic integration, both optical and electronic components are co-fabricated on a single CMOS-compatible substrate. Although it seems like a simpler approach, growing the photosensitive layer requires high-temperature processing and vacuum-based deposition, often relying on expensive, specialized equipment. Hybrid integration, in contrast, requires separate fabrication of the detector and ROIC, followed by a hybridization step using flip-chip bonding with relatively large indium bump interconnects [186]. This means the pixel pitch is limited by bump size or flip-chip alignment.

CQDs offer a practical solution to these integration challenges due to their solution-processible nature. They offer low-cost, large-area fabrication using scalable coating techniques such as spin-coating [247], inkjet printing [202], spraying [43], and roll-to-roll (R2R) processing [146]. Therefore, optically engineered CQD nanocrystals can be directly coated onto ROICs, where individual pixels are defined by patterned metal pads on the chip surface. Finally, a transparent electrode completes the device, enabling post-CMOS compatibility and full-area photon detection [117].

The first demonstrations of infrared detections using CQDs were reported in early 2000s, starting with an article in 2004 by the Sargent Group at University of Toronto [152]. Within five years, Siemens reported the first CQD-based infrared image sensor in 2009 [183]. More recently, in the late 2010s and early 2020s, more commercial products have been developed with small pixel size [16] and high resolution [68].

Despite their optical advantages, CMOS compatibility, and successful commercial demonstrations, the performance of CQD-based photodetectors or CQD-based technologies in general remains limited due to their poor electronic properties. CQDs contain a high density of surface trap states and interparticle junctions, which often act as recombination centers and degrade carrier transport and device performance. These interfaces can result in significant loss of photogenerated charge carriers and limit the efficieny of the signal

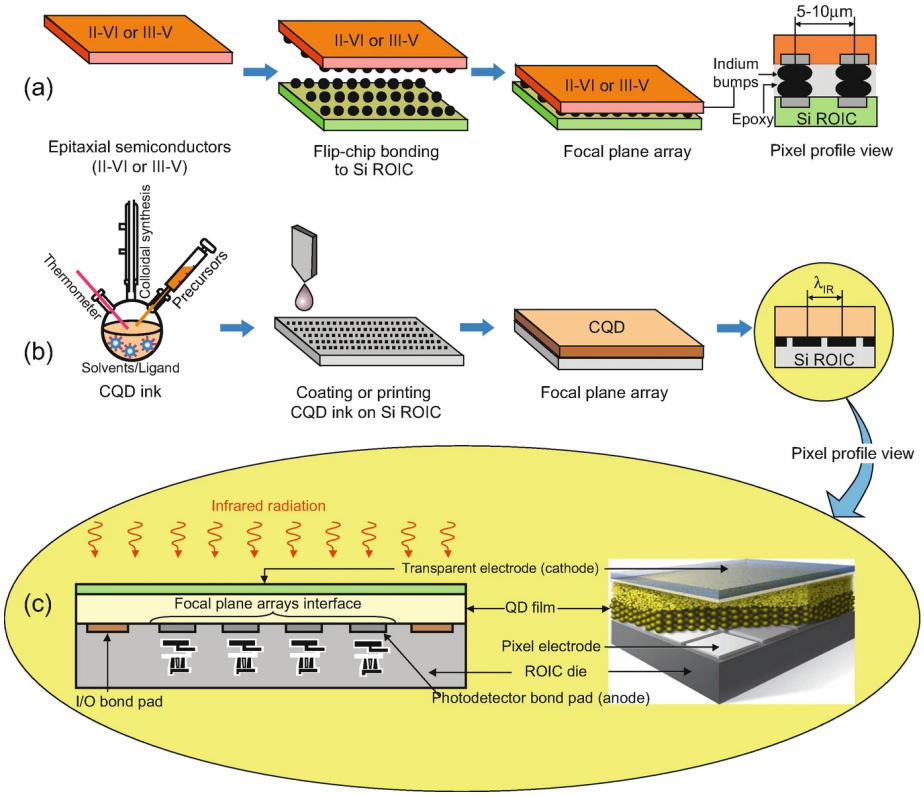


Figure 4.2: Comparison of the process flow for integrated hybrid II-VI and III-V compound semiconductor arrays (a) and colloidal quantum dot monolithic arrays (b). The smallest pixel pitch of hybrid arrays is 5 µm. (c) shows the cross-sectional view on monolithic array structure based on CQDs with potentially pixel pitch below 1 µm. Reproduced with permission from Springer Nature [185].

readout. While such surface "hooks" can be functionalized for chemical [138] or biological [249] sensing to selectively enhance sensitivity, they reduce the performance of photodetector architectures where efficient charge transport is essential. To prevent charge loss through traps, surface passivation is crucial for the signal to reach readout circuit efficiently. Therefore, engineering CQD interfaces through effective passivation strategies is required to develop CQD-based photodetectors [231, 247]. And to enable this engineering, the electrical performance of CQDs must first be quantified.

The main goal of this chapter is to quantify the electrical properties of CQDs in order to provide feedback and guidance to materials engineers for the continued development and optimization of CQD-based photodetectors, with the ultimate goal of pixel size minia-

turization.

Charge carrier mobility is one of the key parameters reflecting the electrical performance of CQDs. It is a measure of how quickly and electron or hole can move through CQDs under electric field, and physically it characterizes how freely charge carriers move. High mobility means faster charge transport, lower resistive losses, and better electrical performance. Surface traps or interdot interfaces slows the transport and results poorer electrical performance. Passivation is the process of chemically treating the CQD surface to remove or neutralize trap states and to enhance coupling between dots and therefore the mobility.

There are three common methods to measure the charge carrier mobilities of CQDs: space-charge-limited current (SCLC) analysis, Hall effect measurements, and FET measurements. Mobility in SCLC method is determined from the current-voltage curve where the charge carriers first occupy trap states and then form a space-charge region. However, this method assumes a uniform film with known thickness and dielectric constant which might lead to inaccurate mobility estimates. Practically, it also requires the fabrication of pinhole-free, uniformly thick films with reliable electrode contacts, which is difficult with solution-processed CQDs. The Hall effect technique measures mobility by detecting the voltage generated from carrier deflection in a magnetic field but the weak Hall signals, need for precise film quality, and poor carrier mobility in CQDs often makes it difficult to obtain reliable measurements.

On the other hand, due to their architecture, FETs operate under conditions similar to photodetectors. FET measurements determine CQD mobility by controlling carrier density at the CQD-FET interface, which in turn affects the channel conductivity. Since the CQD-FET interface strongly affects charge transport, these measurements are highly sensitive to interface traps, contact resistance, and dielectric quality, which may lead to deviations between the measured and the true material value. Although such effects may complicate mobility extraction, the similarity in design between CQD-FETs and photodetectors makes the resulting values more applicable to practical device conditions than the true material value. Moreover, FET fabrication tolerates thinner or less uniform films as mobility is mainly influenced by the CQD-FET interface rather than bulk film uniformity. For these reasons, FETs have become the standard for mobility characterization in CQD research and development. These features makes FETs a powerful tool for research on CQD surface and interface engineering.

In this chapter, CQD-FETs were studied to measure the CQD mobilities. The outcome of this research will be a helpful tool for studying and optimizing electrical properties of CQDs. By measuring the charge carrier mobilities, a correlation can be estimated between

transport behavior and CQD parameters such as semiconductor material, quantum dot size and surface ligands to develop better-performing photodetectors with smaller pixel sizes. Despite their low mobility and high trap density, addressing these challenges could unlock several opportunities, such as the miniaturization of FET to a smaller scale, quantum computing applications to create qubits, and enhancement of sensitivity in sensors. The high surface-to-volume ratio and quantum confinement of CQDs make them suitable for various sensors, including photoconductive and biochemical sensors.

This research benefited from a collaboration with the Sargent Group at the University of Toronto, a leading research team in the CQD field, to standardize procedures and systematically optimize device parameters through expert guidance.

4.2 Working Principle

FET is a three-terminal device with source, drain, and gate electrodes, as shown in Figure 4.3. CQDs form a channel between the source and drain, and the electric field on the channel can be applied from the gate through the dielectric layer.

The resistance of the channel determines the current that flows from the source to the drain when a voltage V_D is applied them. The voltage V_G on the gate is used to control the eelctron density in the channel and hense its resistance. Such a voltage-controlled resistor is the essence of any transistor.

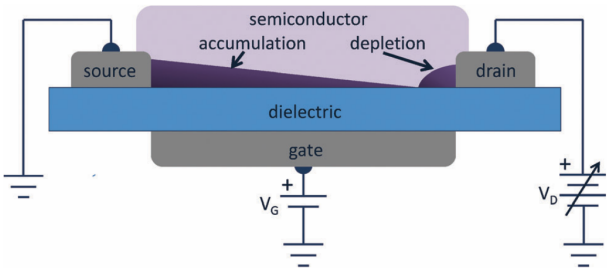


Figure 4.3: Schematics of an FET structure in the saturation region. Reproduced with permission from Springer Nature [214].

4.2.1 Qualitative

The complete physical model of CQD-FETs is inherently complex and requires consideration of several foundational concepts in quantum and statistical mechanics such as density of states (DOS), Fermi-Dirac distribution, work function, and electrochemical potential. These topics are thoroughly and elegantly explained in Prof. Supriyo Datta's foundational book Quantum Transport: Atom to Transistor [49]. Rather than duplicating Prof. Datta's treatment or presenting a full quantitative model, this section aims to provide a simplified conceptual overview of CQD-FET operation. The goal is to qualitatively capture the essence of how charge transport is modulated in these systems, without delving into the full mathematical formalism.

As illustrated in Figure 4.4(a), quantum dots exhibit discrete energy levels due to quantum confinement, while the metallic source and drain contacts have a continuous distribution of states.

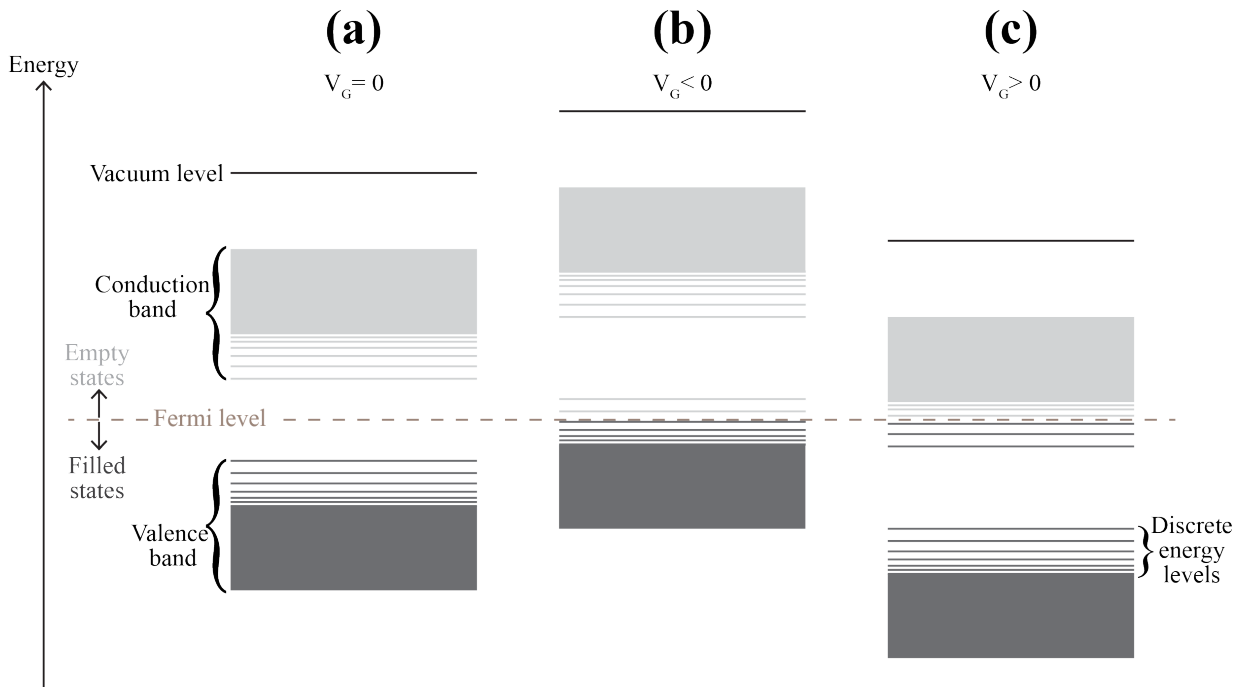


Figure 4.4: Discrete energy levels in the channel under (a) zero, (b) negative, and (c) positive gate biases.

Let the source, drain, and channel terminals have electrochemical potentials of μ_S, μ_D,

and μ_C, respectively. Electrons, being fermions, obey the Pauli exclusion principle and therefore occupy available energy states following the Fermi-Dirac distribution. For conceptual clarity, we consider the zero-temperature approximation, where states below the electrochemical potential are fully occupied and those above are empty. At non-zero temperatures, a smooth transition occurs around Fermi level, though the distribution remains sharply defined.

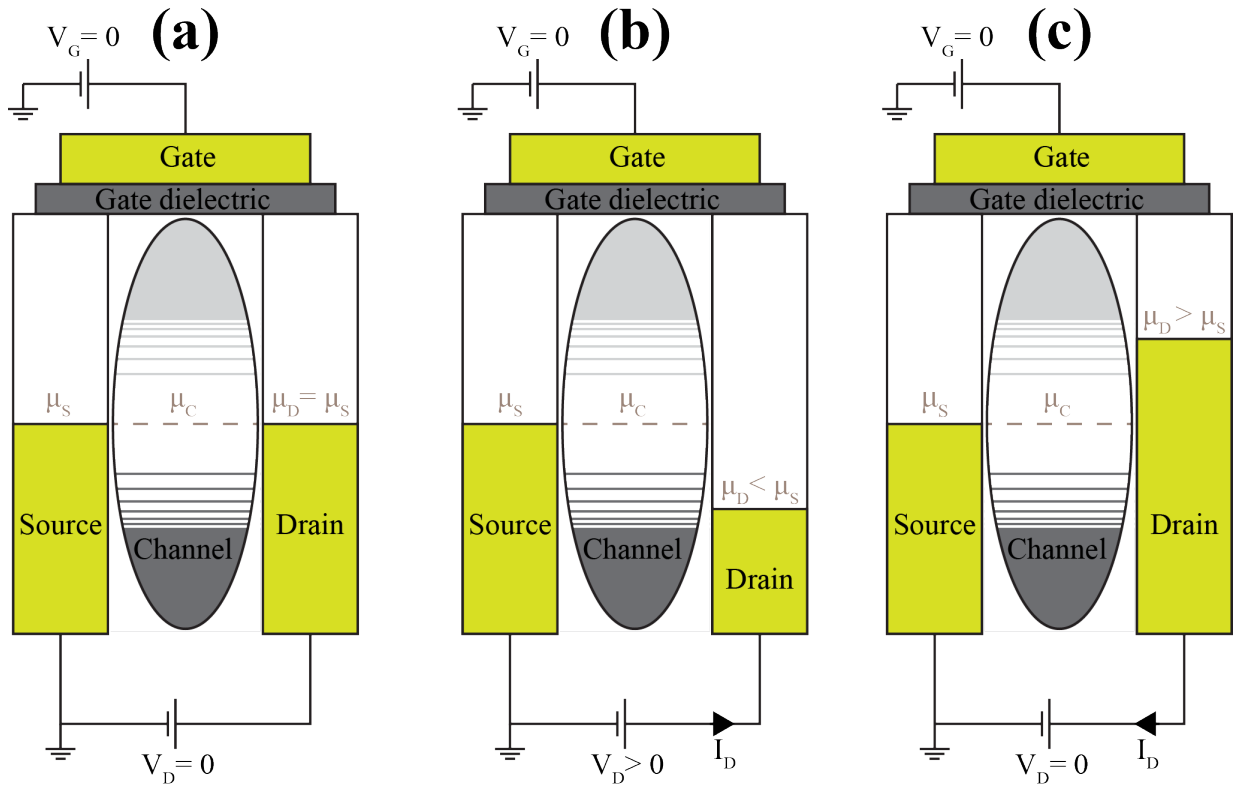


Figure 4.5: Combined energy bands coupled with the source, drain, and gate electrodes under (a) zero, (b) negative, and (c) positive drain biases.

In equilibrium when no applied voltage, all electrochemical potentials are aligned at $\mu_S = \mu_D = \mu_C$ as illustrated in Figure 4.5(a). Applying a drain voltage V_D introduces a potential difference between source and drain as shown in Figure 4.5(b-c), shifting μ_D relative to μ_S by $q_e V_D$:

$$\mu_D = \mu_S + q_e V_D \tag{4.1}$$

where $q_e = -1.602 \times 10^{-19}$ C is the charge of an electron. If available states exist in the

channel between these two potentials, electrons can tunnel from the source to the drain, generating a drain current I_D. As V_D increases, more states fall within this energy window, increasing current flow. On the other hand, apply a gate voltage V_G, as shown in Figure 4.4(b-c), shifts the channel's energy levels as the gate is capacitively coupled to the channel. Assuming the gate has strong capacitive coupling, long-channel approximation states that the channel energy shifts proportionally with V_G while remaining unaffected by V_D. This results in a shift in μ_C, thereby modulating how many of the channel states fall within the μ_S to μ_D window. Hence, gate voltage V_G indirectly controls current by regulating the alignment between channel states and the source-drain bias window.

In simple terms:

1. V_G shifts the energy levels of the channel, modulating the number of available states in the window and thereby changing the channel conductivity.

2. V_D sets the energy window for current to flow. If discrete channel states fall within this window, electrons can tunnel across the channel.

This intuitive picture explains how CQD-FETs function as voltage-controlled switches. The discrete energy levels of the quantum dots lead to sharp on/off transitions, and their alignment with the applied voltages determines the conduction state of the device.

4.2.2 Quantitative

Carrier mobility describes how rapidly a charge carrier, such as an electron or hole, can travel through a channel when subjected to an electric field. The mobilities of the charge carriers can be extracted by analyzing the relationship between the voltage of the input gate and the current of the output drain (transfer curve). This analysis can be conducted through two distinct approaches: linear region measurement and saturation mode measurement. In linear region measurement, the transistor operates within the linear region, characterized by a small drain voltage, V_D, where the drain current, I_D, is approximately proportional to the gate voltage, V_G, with a slope of $m_{lin} \equiv \frac{dI_{D,lin}}{dV_G}$ (also called transconductance) as shown in the following equation:

$$I_{D,lin} = \mu C_i \frac{W}{L} \left((V_G - V_{th}) V_D - \frac{V_D^2}{2} \right) \tag{4.2}$$

where W and L are the width and length of the channel, and C_i represents the gate insulator capacitance per unit area, C_i. Charge carrier mobility, μ, is determined by Equation 4.3:

$$\mu = m_{\text{lin}} \frac{L}{W} \frac{1}{V_{\text{D}}} \frac{1}{C_i} \tag{4.3}$$

As shown in Figure 4.6(a-b), the slope of the output curves in the linear region can be used for determining the mobility and different drain voltages V_{D} results very similar mobilities.

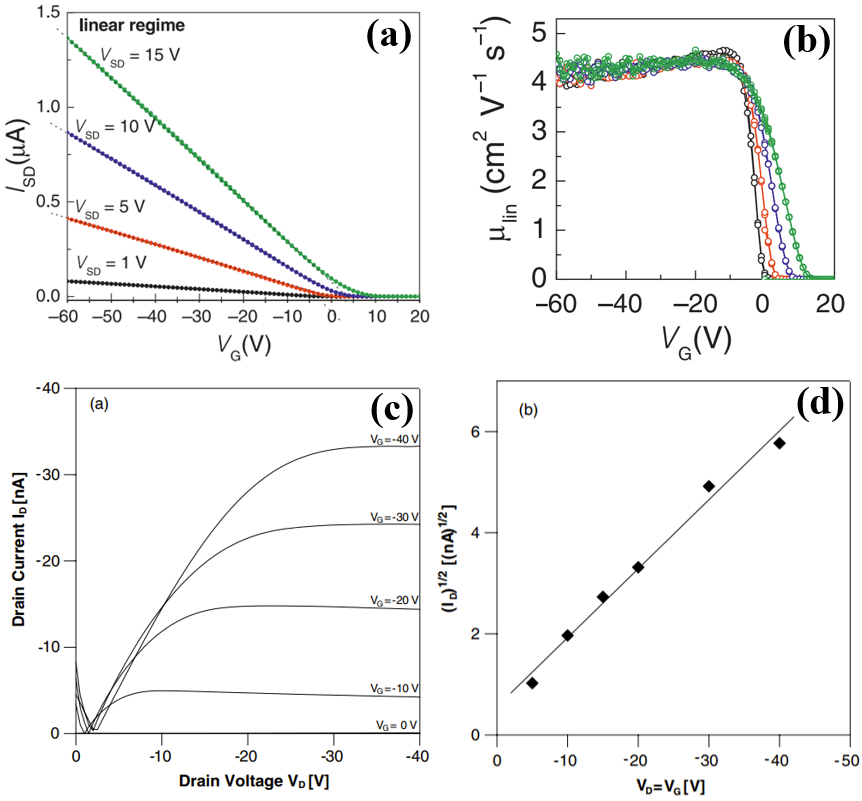


Figure 4.6: Example transfer curves from the literature showing the FET mobility extraction using (a-b) linear region, and (c-d) saturation region. Reproduced with permissions from the MRS [174] and Elsevier [148].

Alternatively, in the measurement of the saturation region, the transistor operates with a fixed gate voltage, and the drain voltage is increased incrementally until the drain current saturates at the threshold voltage, V_{th}. The saturated drain current, $I_{\text{D,sat}}$, at a

given applied gate voltage V_G is given with the following equation,

$$I_{D,sat} = \frac{\mu C_i}{2}\frac{W}{L}(V_G - V_{th})^2 \tag{4.4}$$

The square root of the saturated current is then plotted against the gate voltage, and the slope, m_{sat}, is measured. Mobility in this context is calculated using Equation 4.5:

$$\mu = m_{sat}^2 \frac{2L}{W}\frac{1}{C_i} \tag{4.5}$$

Example illustrations of mobility extraction from the literature are given in Figure 4.6(c-d). These mobility extraction techniques provide valuable insights into the transport properties of carriers within the channel to characterize the electrical performance of CQDs.

In practice, two significant challenges arise in conducting these measurements for CQDs. First, the remarkably low mobilities of CQDs, typically of the order of 10^{-4} $cm^2/(V.s)$, pose a significant challenge due to their minimal responsiveness to electrical fields. Therefore, it is crucial to engineer the transistor structure in a way that allows the production of a strong signal. Maximizing the drain current becomes essential to extract the mobility of CQDs through FET measurement, facilitating less noisy, faster, and more repeatable measurement. The current, as described in Eqs. 4.2 and 4.4, is influenced by three key parameters: mobility (μ), aspect ratio (W/L), and capacitance per unit area (C_i). Mobility, assumed to remain constant through controlled testing environments, is the target parameter for extraction. The geometric aspect ratio (W/L) is a focus of improvement in the Electrode Design section (Section 4.5). Capacitance per unit area (C_i), determined by the dielectric permittivity-to-thickness ratio ($C_i = \varepsilon_r/t$), is influenced by both material and geometric factors, with detailed information available in the Interface Engineering section (Section 4.3). In the context of ideal transistor performance, a key assumption is that all current passes through the channel connecting the source and the drain without leakage. Equations 4.3 and 4.5 are derived on the basis of this assumption, and any current induced by leakage or parasitic capacitance can yield misleading results. Reducing leakage current and parasitic capacitance are discussed in detail in the Electrode Design section (Section 4.5).

Second, the presence of charge traps originating from both the interface and the device can potentially hinder the actual performance of the CQDs. Therefore, it is essential to minimize these traps to assess the mobility of CQDs accurately. Otherwise, electrons excited from the valence band to the conduction band by applying an electric field from the gate may become trapped due to defects or mid energy states originating from charge

traps. Such interference could lead to an underestimate of the actual electrical properties of the CQDs. The electrical performance of CQDs can be affected by exposure to oxygen, humidity, and light. For example, some CQDs or their ligands are chemically not stable in the air, and, their performance can degrade. Alternatively, the current induced by light, i.e. photocurrent, has the potential to excite electrons, causing them to transition from the valence band to the conduction band, consequently boosting the current proportional to light intensity. As a result, it is necessary to use a specialized testing rig to control these parameters during the measurement process to obtain consistent results. The Interface Engineering section (Section 4.3) provides detailed information on the factors to consider when choosing the appropriate electrode and dielectric material, along with surface modification methods and a specialized testing setup to address these concerns. Subsequently, the Fabrication section (Section 4.4) outlines a comprehensive fabrication process to fabricate the proposed devices with minimal traps.

4.3 Interface Engineering

Herbert Kroemer, a Nobel Prize winner, famously highlighted the importance of interfaces in device functionality by stating that "the interface is the device" [120]. He underscored the crucial role that interfaces play in the operation of devices, especially in the realm of thin-film semiconducting devices. These devices have shown impressive advancements in both electronic and photonic uses. In the case of CQD-FETs, the performance of the device is primarily determined by the properties of the materials utilized and the interfaces they create [39].

CQD-FETs consist of three main components: the CQD channel, dielectric, and electrodes. In addition, the surrounding environment of the CQD also plays a significant role. As a result, there are four key interfaces associated with CQDs: the interface within the CQD layers, the interface between the CQDs and the electrodes, the interface between CQDs and the dielectric, and the interface between CQDs and the surrounding environment as shown in Figure 4.7.

The interaction between the dielectric and electrode also affects device performance. Key aspects include charge trapping, where charge carriers can become immobilized at the interface, affecting threshold voltage and carrier mobility. Additionally, interface states, localized electronic states at the interface, can act as traps for charge carriers, impacting device characteristics such as switching speed and stability. Optimizing this interface is essential for improving FET performance, and details are discussed in the Fabrication section 4.4.

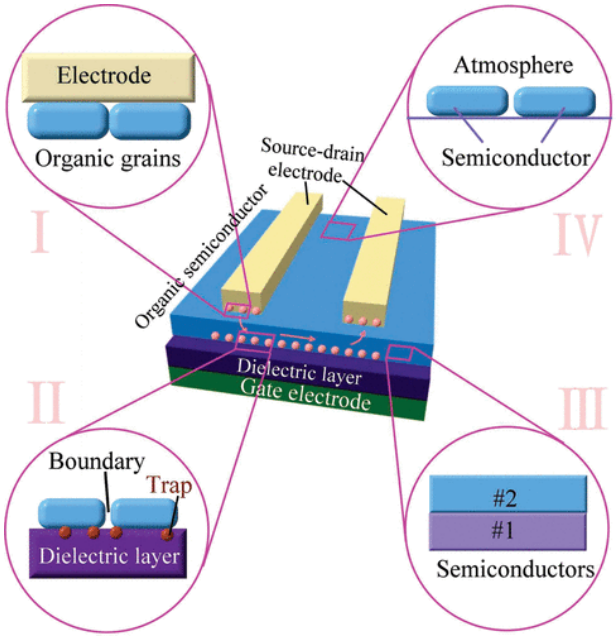


Figure 4.7: FET defect interfaces. Reproduced with permission from ACS [50].

4.3.1 CQD-CQD Interface

The objective of this study is to assess the electrical characteristics of CQDs with minimal interference to evaluate the interface within the CQD layers and establish a practical framework to assist researchers in enhancing this internal interface to improve the electrical properties of CQDs. While the focus of this study is not on the interface within the layers of CQDs, as the same CQDs are utilized in a controlled environment as a benchmark, it is worth briefly mentioning the factors involved.

The interface in the CQDs is influenced by factors such as the size of the ligands, the distribution of the CQD sizes, and the shape and organization of the CQDs. When the quantum dots are connected through ligands with longer chains, the extra length exhibit insulator properties, thereby reducing mobility. On the other hand, short-chain ligands pose challenges in deposition due to their low solvent volatility, attributed to their high zeta potential, causing repulsion and hindering the formation of closely packed films. To address this, adjustments to the pH or the introduction of small ions can be employed to screen charges. Obtaining a more uniform size distribution of CQDs is beneficial because it leads to more similar energy levels and enhances the efficiency of charge transfer at the interface. Additionally, a narrow size distribution can promote controlled self-assembly,

enabling QDs to organize themselves more structuredly. The spherical shape is crucial for the interface within the film, as it promotes uniform packing and reduces surface defects. Finally, an organized arrangement of quantum dots within a film is vital for facilitating efficient and uniform charge transport pathways.

4.3.2 CQD-Dielectric Interface

The interface between CQDs and dielectric plays a crucial role in controlling carrier transport because (i) charge carriers are produced at this interface and (ii) the primary path for electrical current is limited to the initial layers of molecules at the interface. In addition, to get a stronger response from the channel transconductance with the minimum leakage, it is important to provide the strongest field possible to the channel with a high C_i value. The gate dielectric section (Section 4.4.2 presents the details to choose high-κ dielectrics satisfying these conditions where κ is the dielectric constant of the gate insulator. In addition, the surface modification section (Section 4.3.2 presents the a surface modification technique applied to minimize the interface traps.

Gate Dielectric

Ideally, a gate dielectric film should effectively block the passage of electrical current by directing the highest electric field towards the channel in response to the gate voltage applied. However, in practice, there is a certain amount of current, defined as leakage current, flowing through the dielectric; the amount typically depends on the electric field. The applied field is proportional to the capacitance per unit area C_i. Decreasing the dielectric thickness can lead to higher capacitances, but for ultrathin layers, high leakage currents dominate the device performance. As a solution, the high dielectric constant could be used to amplify the capacitance. However, in typical inorganic dielectrics, the dielectric constant is inversely proportional to the band gap; thus, similar to the thickness decrease, high leakage currents could dominate the device performance. Therefore, it is necessary to choose the optimal combination of dielectric materials and thickness.

Moreover, understanding the impact of the gate dielectric on the performance metrics of FET devices requires considering that the key processes occurring in these devices, such as charge accumulation and transport, occur predominantly near the interface between the gate dielectric and the semiconductor layer [164]. This underscores the significance of an optimal dielectric-semiconductor interface for the effective operation of the device. For instance, threshold voltages are typically influenced by the choice of semiconductor

and dielectric materials because of the tendency of impurities and charge-trapping sites to elevate this parameter. It is evident from the equations 4.2 and 4.4 that V_{th} can be easily adjusted by enhancing the capacitance of the dielectric, thereby leading to a higher density of charges at the interface at lower voltages. Several studies have proposed that, by regulating the density of interface states between semiconductor and dielectric, it should be feasible to manipulate the threshold voltages in organic transistors [226].

Unfortunately, finding the optimal combination of dielectric material and thickness is a complex task. As a result, five distinct gate dielectric materials—Al_2O_3, HfO_2, TiO_2, SiO_2, and ZrO_2—have been selected for the construction of various FETs according to the existing literature. The dielectric constant and the bandgap of each insulator are detailed in Table 4.1.

Material	**k-value**	**Bandgap [eV]**
Al_2O_3	~ 7 [69]	~ 7.0 [184]
HfO_2	~ 25 [95]	~ 5.3 [44]
TiO_2	~ 32 (250°C) [100]	~ 3.4 (250°C) [100]
SiO_2	~ 6 [85]	~ 8.8 [111]
SiO_2 (Thermally grown)	~ 4 [85]	~ 8.6 [2]
ZrO_2	~ 32 [141]	~ 5.5 [105]

Table 4.1: Properties of gate dielectrics from the literature.

Another factor to consider is the thickness of the gate dielectric. Various gate thicknesses ranging from a few nanometers to hundreds of nanometers have been investigated for FET applications in the literature. After reviewing the existing literature, a gate dielectric thickness of 30 nm, grown using ALD, is selected for all dielectric materials (Al_2O_3 [108, 167], HfO_2 [209, 196], TiO_2 [149, 167], SiO_2 [126, 129], and ZrO_2 [98, 88]), with the exception of thermally grown SiO_2. For the thermally grown SiO_2, a standard thickness of 285 nm, readily available commercially, is chosen.

Surface Modification

High-κ metal oxides possess distinct characteristics that can adversely affect device performance, including the presence of charge-carrier trap sites on the surface (typically associated with -OH groups), induced ionic polarization due to charge-carrier interactions with the high-κ lattice, and surface roughness [39]. In fact, the surface energy and microstructure of the dielectric interface play a significant role in influencing the local structure of

the semiconductor layer. To address these challenges, surface modification techniques are essential to control the surface properties of high-κ dielectrics.

Modifying this interface using self-assembled monolayers (SAMs) offers a valuable and widely applicable approach to enhancing device performance. Utilizing various SAMs at the interface between the gate dielectric layer and the active chamme; layer enables the manipulation of charge carrier density during channel formation. Implementing SAMs on the gate oxide layer contributes to enhancing the field-effect mobility [144].

Surface modification with organosilanes has long been a common method for preparing SAMs on a wide range of surfaces containing -OH groups, such as silica, aluminum oxide, and zinc oxides. Hexamethyldisilazane (HMDS), among the most commonly used organosilanes, has found extensive application with oxide-based dielectrics [136]. Literature reports indicate that HMDS treatment has been successfully applied to various metal oxides, including Al_2O_3[12], HfO_2[34], TiO_2[12], SiO_2[121], and ZrO_2[82]. Consequently, all samples were coated with HMDS to facilitate surface modification.

4.3.3 CQD-Electrode Interface

The interface between CQDs and electrodes plays a crucial role, as the contact resistance at this junction can negatively impact the device's electrical performance. The contact resistance originates from the mismatch between the Fermi level of the metal electrodes and the energy levels of CQDs corresponding to the highest occupied molecular orbital (HOMO) and lowest unoccupied molecular orbital (LUMO). One approach to improve contact resistance is to incorporate a thin buffer layer, typically a few nanometers thick, at the metal electrode/CQD interfaces known as a charge insertion layer (CIL). However, the thickness of the CIL can influence electron transport, with a thicker CIL potentially reducing mobility due to its insulating properties [107]. Another approach is to coat the surface with a self-assembled monolayer (SAM). SAMs remain firmly attached to metal surfaces even when exposed to different environmental pressures. They can decrease the work function of noble metals such as gold to an extremely low level around $\simeq$3.1 eV [60]. Gold surfaces can be effectively modified to enhance stability under severe conditions [227, 56].

A thorough investigation and complete understanding are crucial for the effective use of CIL and SAM. Moreover, the dynamics of these approaches may vary depending on the specific electrode and semiconductor pairing. Therefore, for a more straightforward solution, the electrodes are selected based on factors such as work function, electrical

resistivity, chemical stability, and cost. Nevertheless, for future research, CIL and SAM treatments could be employed.

A lower work function for the electrode at the CQD-electrode interface is desired for efficient charge injection. It reduces the energy barrier for charge transfer, potentially leading to enhanced device performance in terms of higher current density and improved charge carrier mobility. However, a lower work function typically decreases the chemical stability, thereby increasing the likelihood of chemical reactions or interface degradation. The tendency of metals to undergo oxidation, or their susceptibility to oxidation, is related to the difference in electronegativity between the metal and oxygen. With an electronegativity of 3.44, oxygen ranks as the second highest element after fluorine. Therefore, metals with a higher electronegativity are favored for creating a thinner oxide layer and achieving lower contact resistance at the interface Furthermore, the electrical resistivity plays a crucial role in selecting the electrode material to ensure the efficient transfer of charges.

The table in Table 4.2 presents a range of electrode materials available in the QNFCF cleanroom facility, including their work functions, electrical resistivity, electronegativity, and specifying if thin film deposition for each material has an additional cost.

Table 4.2: The electronic properties of the electrode materials. For the metals, the work-function, resistivity, and electronegativity values are referenced from [155], [81], and [29], respectively.

Material	Work Function [eV]	Resistivity [Ω/m]	Electronegativity	Expensive
Ag	4.3	1.6×10^{-8}	1.9	-
Al	4.3	2.8×10^{-8}	1.5	-
Au	5.1	2.2×10^{-8}	2.4	+
Cr	4.5	13×10^{-8}	1.6	-
Cu	4.7	1.7×10^{-8}	1.9	-
Fe	4.5	10×10^{-8}	1.8	-
Nb	4.3	15×10^{-8}	1.6	-
Pd	5.1	11×10^{-8}	2.2	+
Pt	5.7	11×10^{-8}	2.2	+
Ti	4.3	39×10^{-8}	1.5	-
ITO	4.4 [169]	2×10^{-6} [228]	-	-
AZO	5.0 [67]	3×10^{-4} [228]	-	-

[155] for workfunction [81] for resistivity [29] for electronegativity

Aluminum has the ability to capture certain traps such as residual hydroxyls from water vapor when subjected to forming gas RTP treatment. Research in the literature suggests that a post-metallization anneal with aluminum is more efficient in decreasing the number of defects compared to a post-oxidation anneal [240]. Because of its low work function, high conductivity, moderate chemical stability, and cost-effectiveness, aluminum is selected as the electrode to get good contact with CQDs.

4.3.4 CQD-Environment Interface

The interface between the semiconductor and the environment is significant because external molecules penetrate within the channel, leading to either the doping or trapping of charge carriers. This phenomenon can lead to significant issues such as device instability and irreversibility due to the harmful physical interaction between semiconductors and the environment [14]. To minimize environmental interference, all experiments were carried out within a specialized glovebox, which is an isolated and controlled environment, as shown in Figure 4.8.

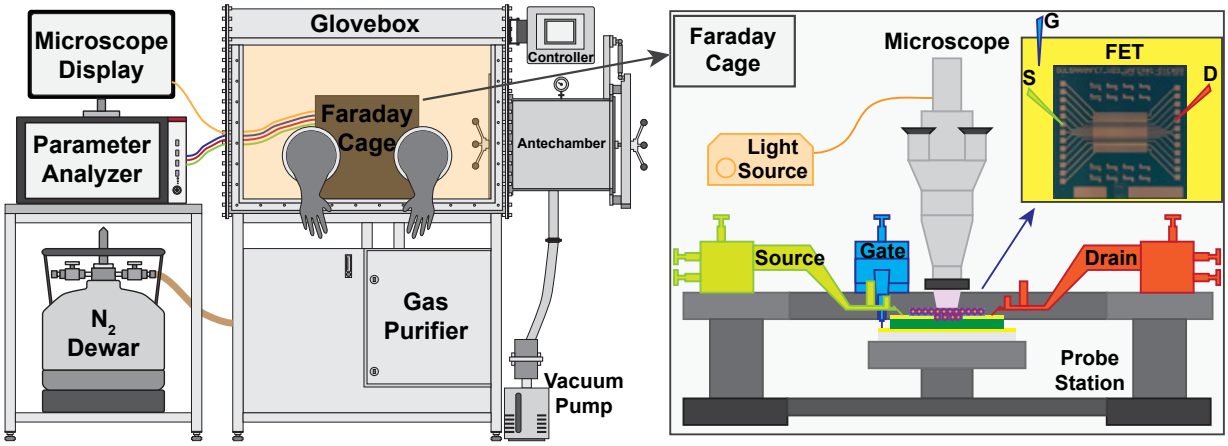


Figure 4.8: Schematics of the experimental setup.

From an air quality perspective, the glovebox is supplied with N2 gas and maintained at positive pressure to prevent the ingress of air into the chamber. Strict control is exercised on oxygen and humidity levels, ensuring that they remain below a predefined threshold. This meticulous regulation is crucial because CQDs are not chemically stable; exposure to oxygen and humidity can alter their properties. Additionally, the air within the glove-

box undergoes filtration to minimize the presence of solvents or contaminants that could compromise the response of the FET.

Optical interference is mitigated by enclosing the setup within a black box, effectively shielding it from ambient light. Given the photoactive nature of CQDs, exposure to light can trigger electron excitations from the valence to the conduction band, inducing a photocurrent. To observe and control this phenomenon, a precisely regulated light source is situated within the black box.

Ensuring accurate measurements requires a focus on electrical factors. Two source measure units (SMUs) (Keithley 4200A-SCS parameter analyzer) were placed outside the glovebox and connected to the probes through triaxial cables and feedthrough. The entire electrical setup is shielded with triaxial shielding to reduce noise and minimize unwanted capacitance without using coaxial or unshilded connections. During the experiment, the chip is positioned precisely on a probe station, and the probes are carefully aligned to make contact with the metal electrodes. A camera placed above the chip assists in the probing process and is connected to the PC for monitoring purposes.

By carefully regulating air quality, optical environment, and electrical links, the experimental configuration is intricately designed to produce consistent measurements, ensuring the dependability and precision of the research results.

4.4 Fabrication

The objective of the fabrication is to minimize the traps introduced during the process while also aiming to increase the chip rate and decrease the overall cost.

The choice of a particular architecture is a critical step in determining the cost and effort of fabrication. To maximize chip rate and minimize cost, different FET architectures from the literature were investigated and the most common four are presented in Figure 4.9.

The position of the gate can be categorized into two main configurations: bottom-gated and top-gated. In the bottom-gated configuration, the gate dielectric separates the gate electrode from the channel, and the channel is coated on top of the gate electrode. This allows wafer-level fabrication without the need for wafer dicing until the channel deposition stage. As a result, multiple sets of chips can be produced simultaneously before the channel coating. Therefore, the bottom-gated FET is preferred over the top-gated counterpart. Additionally, the bottom-gated structure offers versatility, as it can be coated

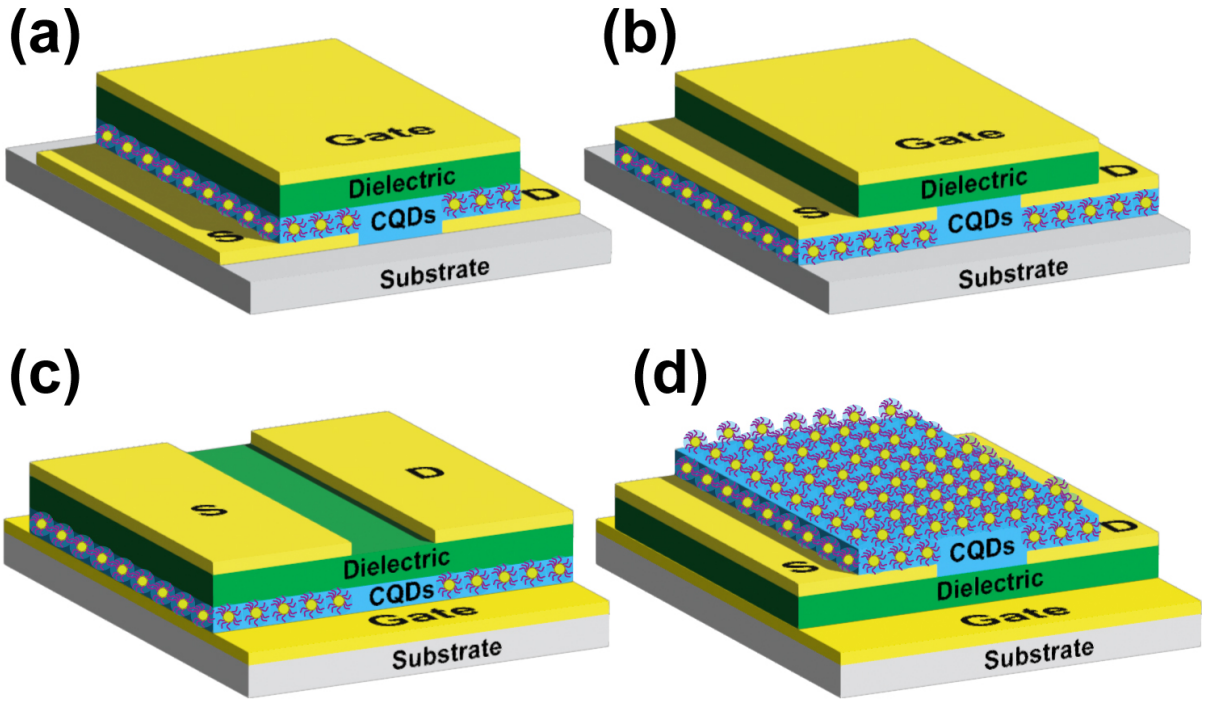


Figure 4.9: Common FET device architectures: (a) staggered, top-gate; (b) coplanar, top-gate; (c) staggered, bottom-gate; and, (d) coplanar, bottom-gate.

with a gate on top after channel coating, resulting in transistors that are gated on both sides separately. Two configurations, namely coplanar and staggered, can be identified by analyzing the source and drain locations in bottom-gated architectures. In the coplanar configuration, the source and drain electrodes are initially deposited on the gate dielectric, followed by a channel coating. Similarly to the bottom-gated architecture, this configuration facilitates wafer-level processing, allowing the wafer to be diced into individual chips electrode fabrication. Therefore, for a more efficient production process and a larger set of transistor chips, the coplanar bottom-gated structure is preferred over the staggered configuration.

A process flow was developed to fabricate the bottom-gated coplanar FETs. The fabrication steps are given in Table 4.3.

There are three chip variations as Si-based global-gated FET, high-κ-based global gated FET and high-κ-based local gated FET. The process flow showing the cross sectional view of these three chips is given in Figure 4.10.

Table 4.3: Device fabrication.

Layer	Step 1	Step 2	Step 3
Gate electrode	Lithography	Metal deposition	Liftoff
Gate dielectric	ALD	Lithography	Ion mill
Source/Drain electrodes	Lithography	Metal deposition	Liftoff
CQDs	Spin-coating	Heat treatment	-

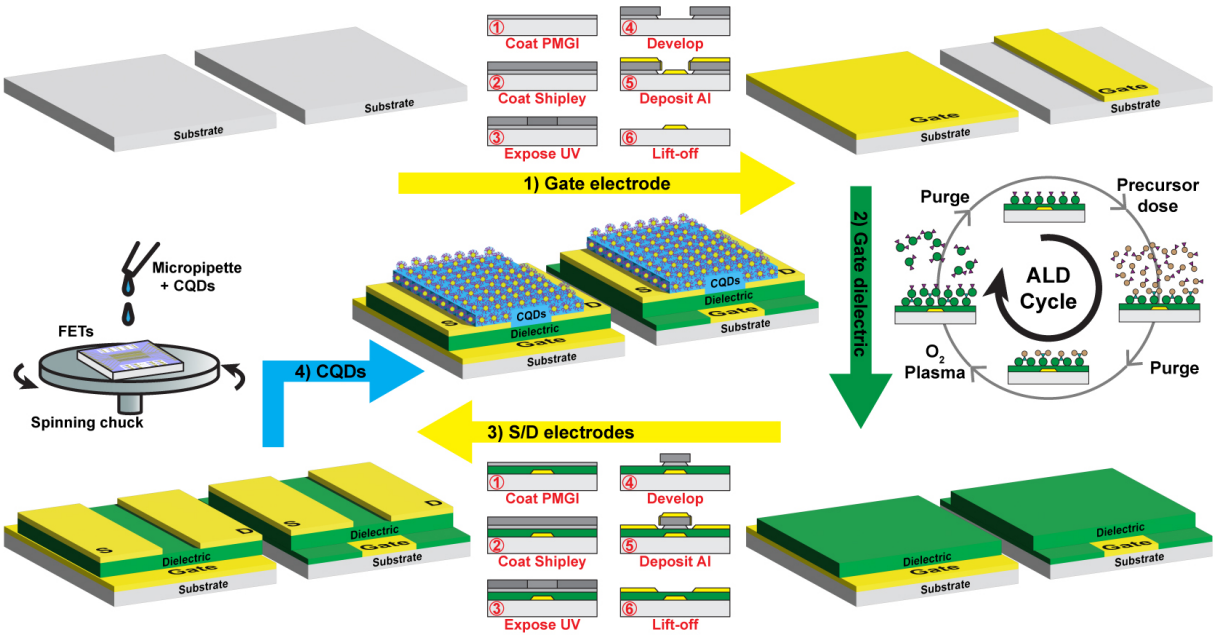


Figure 4.10: FET fabrication.

In order to identify the most suitable equipment and process parameters for these process flows, it is necessary to comprehend the device fabrication traps. The fabrication defects in devices can be categorized into three groups: mobile ions, trapped oxide charges, and fixed oxide charges. Mobile ions refer to positively charged alkali metal impurities that can move and migrate within the oxide layer under the influence of an electric field. These impurities can enter the device either during wafer handling or through contaminated processing equipment. Trapped oxide charges consist of electrons and holes within the oxide layer, generated by ionizing radiation or avalanche injection. On the other hand, fixed oxide charges, which are typically positive in SOI-based FETs near the channel-dielectric inter-

face, may stem from the insulator growth process. During this process, minute amounts of water present in the gases used can become embedded in the oxide, leading to the formation of water impurities that produce hydronium (H3O+) and consequently result in the presence of positive fixed charges [19].

In order to develop a process flow with the minimal introduction of the fabrication traps, a detailed cleanroom procedure is established for the QNFCF at the University of Waterloo. The specific procedures are outlined in the subsequent sections as the Bottom Electrode (Section 4.4.1), Gate Dielectric (Section 4.4.2), Top Electrode (Section 4.4.3), and Packaging and Surface Treatment (Section 4.4.4).

4" Fused Silica wafers (J204001, WaferPro) were selected as the substrate for high-κ gated FETs.

4.4.1 Bottom Electrodes

To pattern the bottom electrodes, a simple bilayer lift-off process is applied. First, HMDS treatment was performed to promote the adhesion between the substrate and PR layer. The underlayer (PMGI SF7) and positive-tone UV-PR (Shipley S1805) were spin-coated at 5000 RPM and soft-baked at 180C for 90 seconds and 120C for 90 seconds, sequentially. The pattern was exposed to 405 nm wavelength light with MLA (Heidelberg MLA 150) with a dose of 70 mJ/cm^2 and developed in MF-319 for 1 minute. It is important to mention that no O2 descum process was implemented after development to reduce the level of fixed oxide charges and interface traps.

The natural oxide grown on the metal electrode might introduce additional charge traps after the gate dielectric deposition due to the metal, natural metal oxide, and high-κ dielectric interface. To minimize that effect, a high electronegativity difference between oxygen is required to minimize the natural oxide growth. As shown in Table 4.2, gold has the maximum electronegativity from the available electrode materials in QNFCF. Also, it has the second most electrical conductivity. Therefore, gold is chosen for the bottom electrode layer. For adhesion, Ti is chosen as the adheision layer.

Hence, Ti/Au films with a thickness of 5/95 nm were deposited with electron beam deposition (Angstrom Amod), and the excessive metal was lifted off. The thickness of the deposited bottom electrode was tested and verified with a stylus surface profiler (Bruker DektakXT).

4.4.2 Gate Dielectric

Atomic layer deposition (ALD) is process known for its superior defect control compared to conventional methods such as thermal oxidation and chemical vapor deposition (CVD). Notably, ALD also minimizes surface roughness, contributing to enhanced device performance. Therefore, the high-κ dielectrics were deposited using ALD (Oxford FlexAL ALD), ensuring uniformity and precision across each wafer, with a targeted thickness of 30 nm. Detailed specifications of the ALD process are outlined in the following table for reference.

Table 4.4: The precursors and temperatures of the ALD of each film.

Material	**Precursor**	**Temperature**
Al_2O_3	TMA	300°C
HfO_2	TEMAH	290°C
TiO_2	TIIP	250°C
SiO_2	BTBAS	300°C

Before ALD coating, each chamber was conditioned to prevent cross-contamination. The thickness and optical properties of the dielectric layers were characterized with a spectroscopic ellipsometer (Woollam M-2000 Model DI).

4.4.3 Top Electrodes

The same lithography procedures as for the bottom electrodes were applied to the top electrodes. Nonetheless, it has been identified that defects may arise from the soft X-ray and UV radiation produced during the e-beam and sputtering processes. Therefore, in order to minimize defects at the interface between the dielectric and electrodes, the samples were shielded from any exposure to soft X-ray and UV radiation. This was achieved by opting for thermal evaporation instead of e-beam evaporation and sputtering, as resistive heating in thermal evaporation causes the source material to evaporate without generating radiation [127]. Furthermore, it is recognized that thermally evaporated aluminum is effective for annealing out defects [31, 19], ensuring minimal defect formation, cost-effectiveness, high electrical conductivity, and good adhesion. Hence, a 40 nm thick layer of aluminum was thermally evaporated for the top electrode.

Subsequently, a post-metallization annealing (PMA) technique using a forming gas mixture (5% H2 in N2) was utilized to reduce the defects caused by the presence of water residues introduced during the dielectric deposition process or absorbed at the oxide surface

before metallization. The water within the oxide layer could be removed by the aluminum contacts during PMA or hot plating after metallization, leading to a notable decrease in defects [31, 19].

4.4.4 Packaging and Surface Treatment

The 4" wafers were cut into 12×12mm individual chips using an automatic dicing saw (Disco DAD3240). Following the wafer dicing process, a HMDS oven (YES 310-TA Vacuum Oven) is employed to treat the surface of the dielectric layer. This oven operates in a heated vacuum setting to eliminate moisture and deposit a monomolecular HMDS coating with an estimated thickness of around 5 Angstroms. To ensure optimal adhesion to the wafer, the surface needs to be moisture-free therefore the process undergoes three dehydration purge cycles at a temperature of 150°C to achieve this state. Subsequently, the HMDS is exposed for 5 minutes at the same temperature under vacuum conditions. Finally, 3 exit loop cycles are performed to conclude the process.

For Si-based FETs, chips were finalized by scribing the bottom of the substrate and applying an Indium-Gallium eutectic alloy (495425-5G, Sigma-Aldrich) to establish ohmic contact with the backside of the Si substrate [205, 187]. The chip was then affixed to a mica or glass sheet using silver paste (16040-30, Ted Pella).

The University of Waterloo's QNFCF facility was used for the fabrication process. Then, the chips were transferred to Sargent Labs of University of Toronto for the functionalization with CQDs. To functionalize the FETs with the CQDs, all chips were spin-coated as previously described [94]. After the coating process, the samples were transferred to the testing glovebox for electrical measurements.

4.5 Electrode Design

The electrode design aims to increase the level of output signal while minimizing leakage and parasitic capacitance by optimizing the device geometry. For this purpose, three different design strategies are applied: conventional design with a pair of parallel electrodes, interdigitated electrode (IDE) design, and local gate design. As shown in Figure 4.7, the first two designs focus on the source and drain electrodes, whereas the latter design focuses on the gate electrode design.

The conventional design (Section 4.5.1) aims to increase the output signal by improving the aspect ratio W/L using single-facing parallel electrodes by designing the source and

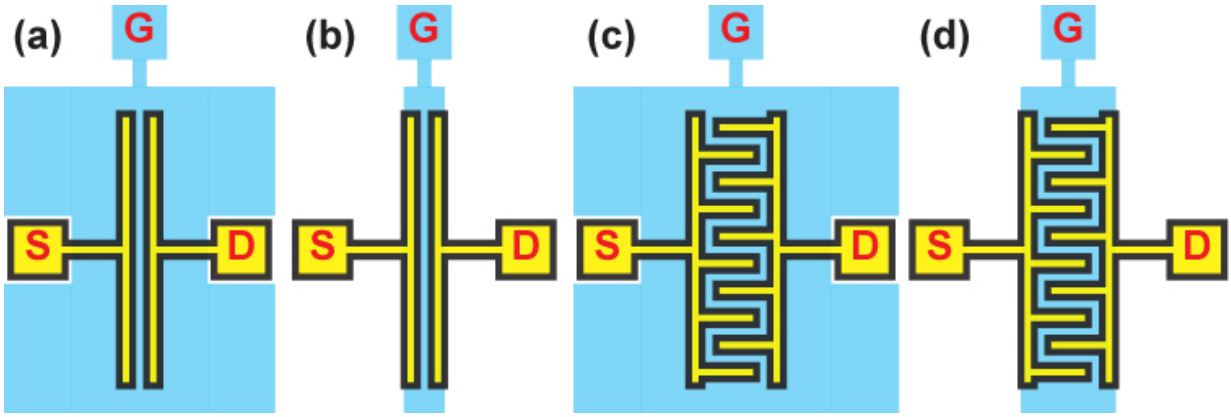


Figure 4.11: FET designs: (a) Conventional global gated design, (b) Cconventional local gated design, (c) IDE with global gated design, and (d) IDE with local gated design.

drain electrodes. In the IDE design (Section 4.5.2), the emphasis is on multiplying the aspect ratio by the increase in the number of electrode faces through the design of the source and drain electrodes. Local gate design (Section 4.5.3) aims to minimize leakage and parasitic capacitance by patterning the gate electrode to minimize the overlap area between the gate electrode and the source and drain electrodes. Finally, the chip layout section (Section 4.5.4) presents the designed layout of the chip.

4.5.1 Conventional

The most common FET structure has parallel electrodes, with a single face having a width of W and separated by a length L, as shown in Figures 4.7 a and b. To increase the aspect ratio W/L, the width should be increased as much as possible. However, the channel width, W, in parallel electrodes is limited by the dimensions of the chip. Additionally, the positioning of FETs is crucial, as the spin-coating process used for the channel material (CQDs) results in a film that is more uniform at the center but becomes less uniform towards the edges. To assess the impact of the aspect ratio W/L and demonstrate the repeatability of the results, four different transistors were inserted into a single chip, limiting the channel width to 5 mm. The channel lengths L, for the four transistors, were selected as 5 µm, 10 µm, 20 µm and 40 µm. Consequently, this resulted in conventionally designed FETs with aspect ratios W/L of 1000, 500, 250, and 125, respectively.

4.5.2 IDE

A common method to improve the ratio W/L is to increase the number of faces of parallel electrodes as shown in Figures 4.7 c and d. Using an IDE structure that allows multiple parallel facing electrodes, the W/L ratio can be multiplied by the number of fingers (n). In this particular configuration, two sets of four designs with a width of 1 mm and lengths of 2 µm, 3 µm, 4 µm, and 5 µm, each with 100 fingers, were incorporated into the remaining areas of the chip. This results in W/L ratios of 50000, 33333, 25000, and 20000.

4.5.3 Local Gate

The gate electrode and the source and drain electrodes act as a parallel plate capacitor separated with the gate dielectric. When the fringing fields are neglected, the parasitic capacitance of a parallel plate capacitor, C_{par}, is equivalent to $C_{\text{par}} = \varepsilon\varepsilon_0 A/d = AC_i$. As capacitance per unit area, C_i, amplifies the output current as shown in Equations 4.2 and 4.4, it should be kept as high as possible as long as the system can compensate. Therefore, the overlap area A between the bottom and top electrodes should be minimized. The most straightforward approach to this problem is to minimize the area of the source and drain electrodes. However, these electrodes still need to be large enough to have electrical conductivity and get contact with a probe station.

To overcome these challenges, the gate electrode can be patterned with a negative pattern of the source and drain electrodes, as shown in Figures 4.7 b and d. To compensate the misalignment coming from the fabrication (±0.5µm for optical lithography), the gate electrode was designed 2 µm wider than the channel length to ensure that the gate electrode fully covers the channel to apply the electric field uniformly. Unfortunately, this local gate design cannot be applied to Si-based FETs, as the whole Si substrate acts as the gate electrode, which cannot be patterned.

4.5.4 Chip Layout

The chip size should be large enough to accommodate numerous individual transistors and be convenient for handling and probing. In contrast, it should be small enough to yield multiple chips from each wafer so that different CQDs could be tested with the same transistors. Moreover, the dimensions should allow for uniform films by spin-coating CQDs. Taking into account all these factors, a chip size of 0.5×0.5 inch has been chosen. The drawings of both chip layout are shown in Figure 4.12.

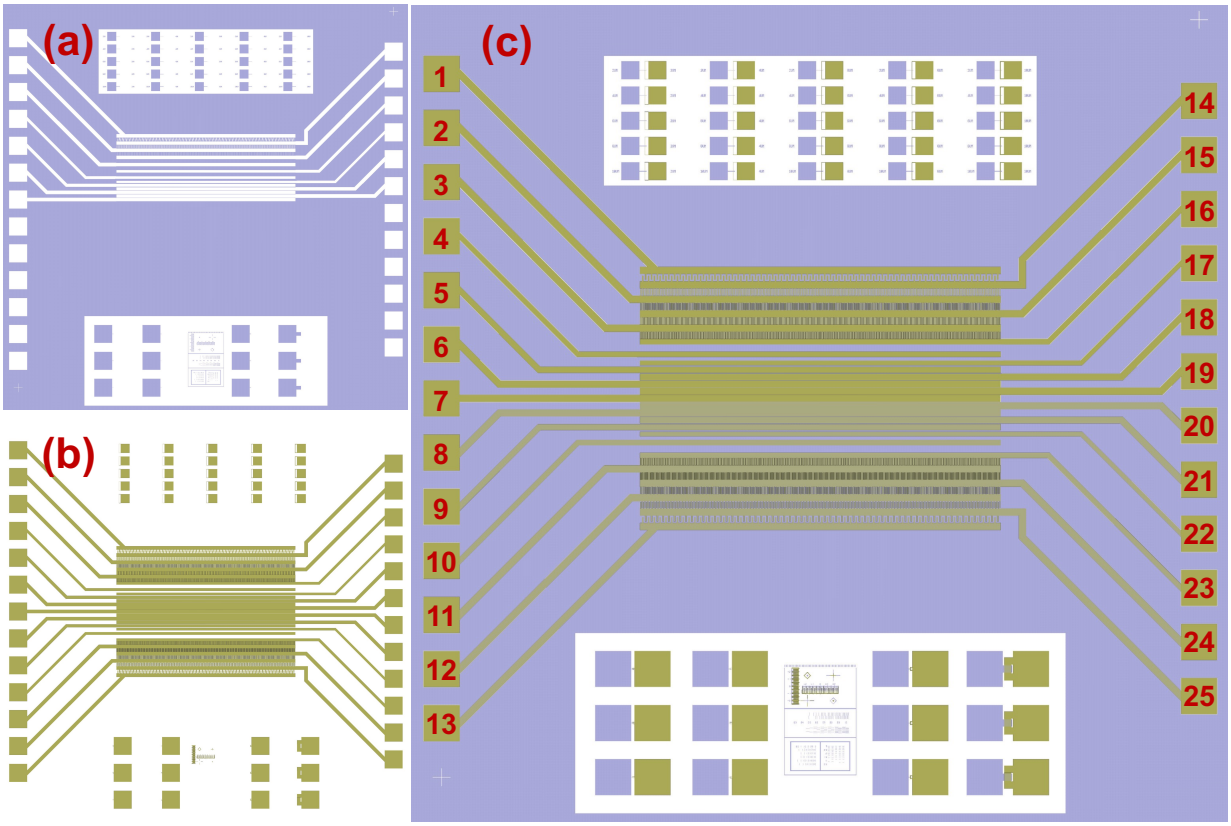


Figure 4.12: FET layout of the (a) gate electrode, (b) source and drain electrodes, and (c) combined layers.

Figure 4.12 (a) shows the layout of the gate electrode. The top part of the chip is the local gated, and the bottom part is the global gated. The contact pads, placed on right and left edges, were negatively patterned to prevent short circuit during probing. In addition, metal-insulator-metal (MIM) diodes were added into the pattern to verify the electrical properties of the gate dielectric by extracting the dielectric constant with CV measurements. Also, alignment marks were included in the layout to measure and verify the quality of the fabrication.

The layout of the source and drain electrodes is shown in Figure 4.12 (b). The same layout was applied for the bottom (global gated) and top (local gated) halves, except the MIMs and alignment marks. The channels of the transistors were placed at the center to obtain a high uniformity of the channels after spin-coating CQDs. The probes were placed at the edges to allow enough space for the probes during the measurements and not

damage the channel during the measurement. The overall chip layout is shown in Figure 4.12 (c). The pin map of the transistors are given in Table 4.5.

Table 4.5: Pin mapping of the transistors. (LG: Local Gate, GG: Global Gate)

Design	L **[µm]**	n	W/L	**Pin # (LG)**	**Pin # (GG)**
	100	1	50	4,16	10,23
	50	1	100	4,17	10,22
	20	1	250	5,17	9,22
Conventional	10	1	500	5,18	9,21
	5	1	1000	6,18	8,21
	2	1	2500	6,19	8,20
	1	1	5000	7,19	7,20
	20	62	615	1, 14	13,25
	10	125	2490	2,14	12,25
IDE	5	250	9980	2,15	12,24
	2	625	62450	3,15	11,24
	1	1250	249900	3,16	11,23

4.6 Results and Discussion

4.6.1 Initial Results without Interface Engineering

In the initial phase of this study, we aimed to quantify the charge carrier mobilities of CQDs using bottom-gate, top-contact FET shown in Figure 4.13.

These early-stage experiments were performed without environmental control (i.e., no glovebox), no optimized gate oxide–CQD interface engineering, and no dedicated electrode design with the experimental setup shown in Figure 4.14. The primary goal was to assess whether measurable transistor characteristics could be observed under these unoptimized conditions and to extract mobility values as a starting benchmark.

Two types of films were tested: NiO_x and EDT-treated PbS CQDs. While NiO_x displayed significantly higher conductivity based on the conductivity measurements by collab-

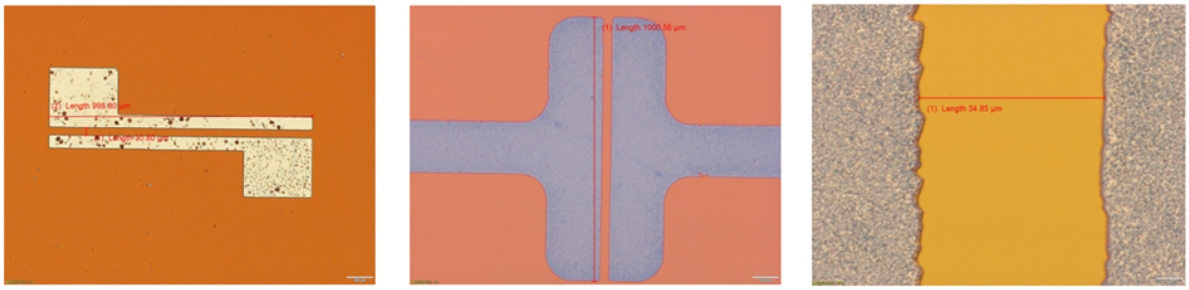


Figure 4.13: Figure S4 Microscope images of the channels. (a) Microscope image of the FET channels (source and drain). The length of the channel is measured as 1000 µm and width as 30 µm. SiOx thickness is 100 nm. (b-c) Microscope image of the substrate channels used in conductivity study. Channel dimensions are 35 µm in length and 1000 µm in width. SiOx thickness is 300 nm. Reproduced with permission from ACS [10].



Figure 4.14: FET substrates measurement setup using Keithley 4200 parameter analyzer. Samples are measured with three contact probes inside a Faraday cage. Reproduced with permission from ACS [10].

orators at the Sargent Lab and consistent with prior reports, it did not exhibit field-effect modulation under the applied gate bias. This suggests that NiO_x either lacks a sufficiently active channel interface or suffers from Fermi level pinning or poor gate coupling, making it unsuitable for mobility extraction in this FET architecture.

In contrast, EDT-treated PbS CQDs demonstrated observable transistor behavior,

though with limitations. As shown in Figure 4.15, the transfer and output characteristics displayed unipolar hole transport with a distinct saturation regime in I_{DS}–V_{DS} curves and an on/off ratio on the order of 10^3–10^4. However, substantial hysteresis and low absolute current levels were observed, likely due to environmental degradation and intrinsic instability of EDT-PbS films when exposed to ambient air.

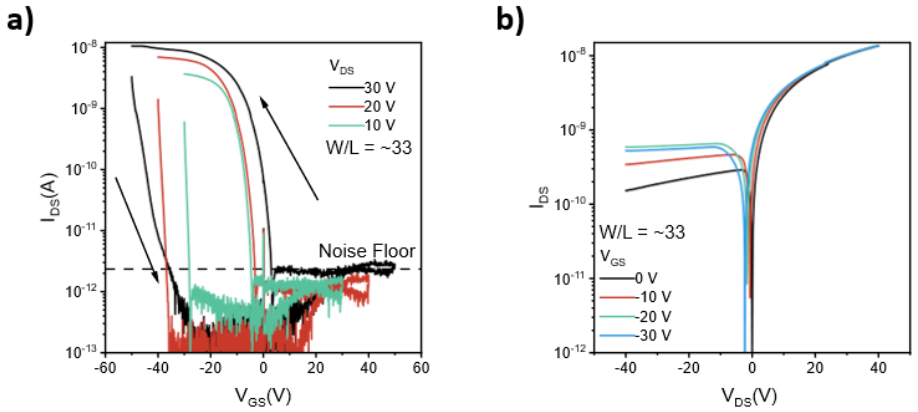


Figure 4.15: Transfer (VGS vs IDS) and b) Output (VDS vs IDS) curves for EDT FET devices. Arrows show the sweeping direction. The low-conductivity material demonstrated high hysteresis under large bias, similar to previous reports [1]. Due to the relatively small W/L ratio and low-conductivity material, the ambipolar characteristics of the EDT-PbS are shadowed. Negatively charged carrier dominated current readings are below the noise floor of the measurement system. However, a strong signal is obtained where positively charged carriers dominate the current. Hole mobility is obtained from these clear curvatures in the reverse sweep. The measurement is repeated under different biasing conditions. Reproduced with permission from ACS [10].

Despite these challenges, we successfully extracted the field-effect mobility using standard analytical models. Using the measured channel dimensions ($W = 30$ μm, $L = 1000$ μm) and gate oxide capacitance ($C_i = 345$ nF/cm^2), a saturation mobility in the range of (2–3) $\times 10^{-5}$ cm^2 V^{-1} s^{-1} was obtained. This value is consistent with previously reported values for EDT-treated PbS CQD films, thereby validating the measurement setup and analysis procedure under ambient conditions.

These results established an initial baseline for CQD mobility measurement but also revealed two major limitations. First, the CQD–environment interface was highly unstable,

necessitating the use of inert atmosphere during both fabrication and testing. Second, the small width-to-length (W/L) ratio of the FETs severely limited the on-state current, thereby suppressing ambipolar behavior and amplifying the impact of noise. As a result, while hole mobility could be estimated, accurate quantification of electron transport was not feasible.

These insights motivated two key directions pursued in subsequent experiments: (i) development of a glovebox-compatible measurement setup to improve CQD stability, and (ii) redesign of the FET layout to achieve higher W/L ratios, enabling more reliable extraction of both hole and electron mobilities.

4.6.2 Initial Results with Interface Engineering

Following the weak transistor behavior observed in the previous section, a custom chamber was designed (Figure 4.8) to enable controlled-environment measurements. In parallel, an improved FET architecture with larger width-to-length ratios was fabricated, as shown in Figure 4.16. This platform enabled testing of PbS CQDs passivated with mixed halide ligands under more stable and representative conditions.

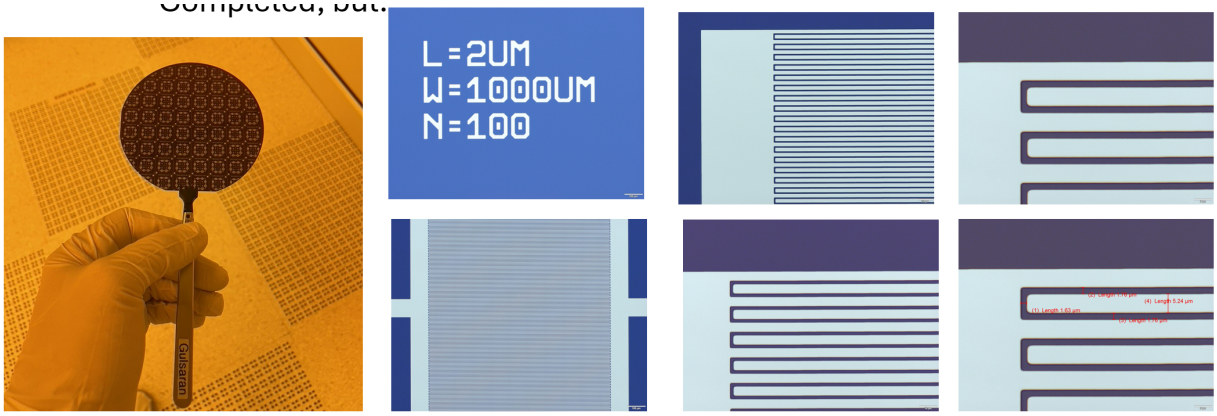


Figure 4.16: Image of the FET device fabricated for testing mixed-halide passivated PbS CQDs.

The electrical characterization was performed using the same parameter analyzer model, and the resulting transfer and output curves are presented in Figure 4.17. Compared to the earlier EDT-passivated devices, the new FETs exhibited clear and well-defined transistor behavior with significantly reduced hysteresis, indicating improved charge transport and environmental stability.

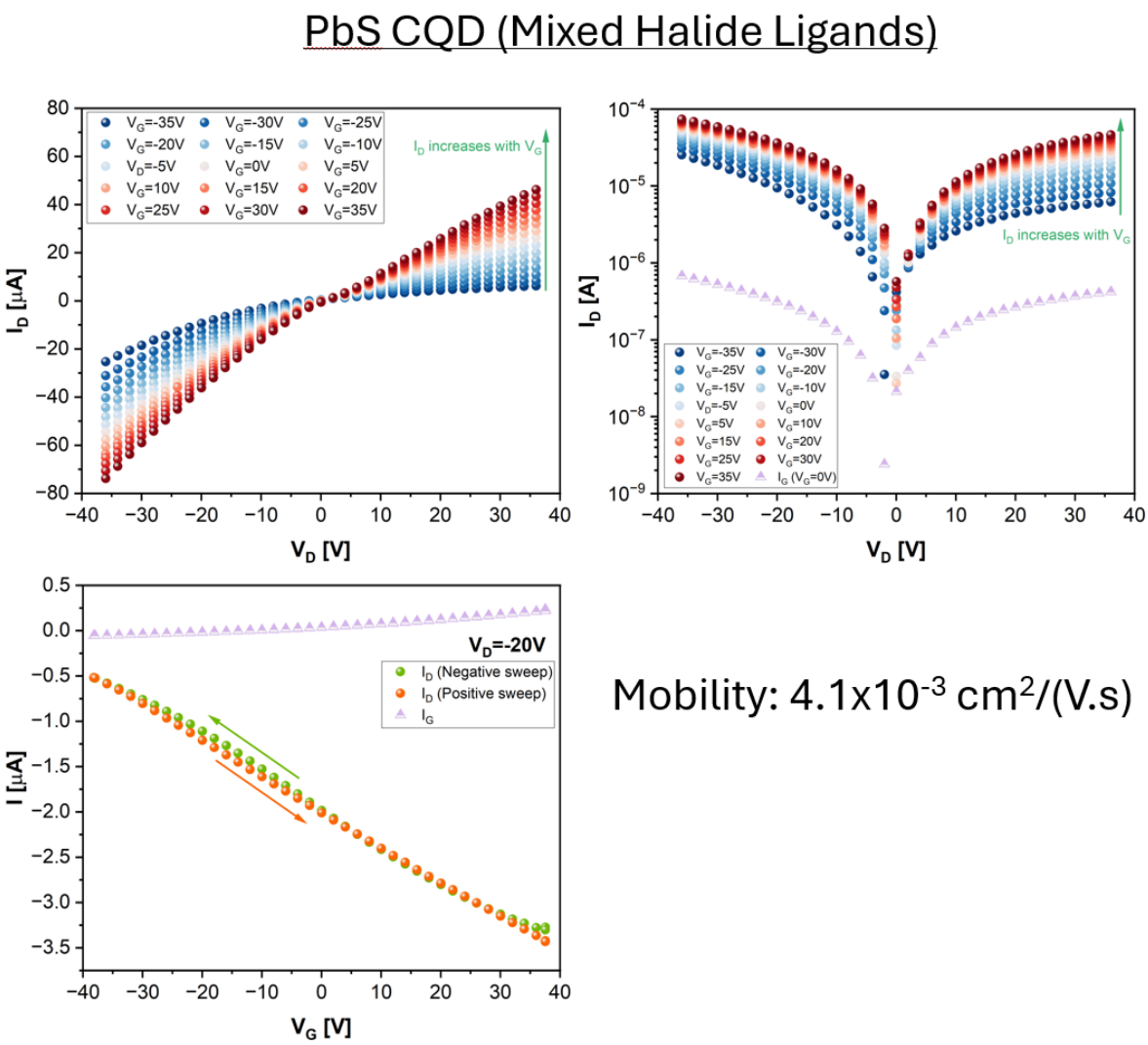


Figure 4.17: Output and transfer curves of the tested mixed-halide passivated PbS CQDs.

Most notably, the extracted field-effect mobility reached 4.1×10^{-3} $\mathrm{cm^2\,V^{-1}\,s^{-1}}$, representing a two-orders-of-magnitude enhancement over EDT-treated samples. This result highlights the critical role of interface engineering in optimizing the electrical performance of CQD-FETs. These improvements establish a more robust platform for accurate carrier mobility quantification for the future measurements.

4.6.3 Layout Testing

As discussed in the initial results, the width-to-length (W/L) ratio of the channel plays a critical role in determining the signal strength and accuracy of extracted mobility values in CQD-FETs. To evaluate this effect, a series of FETs with varying W/L ratios were fabricated using the same batch of mixed-halide passivated PbS CQDs. The extracted field-effect mobilities are summarized in Figure 4.18.

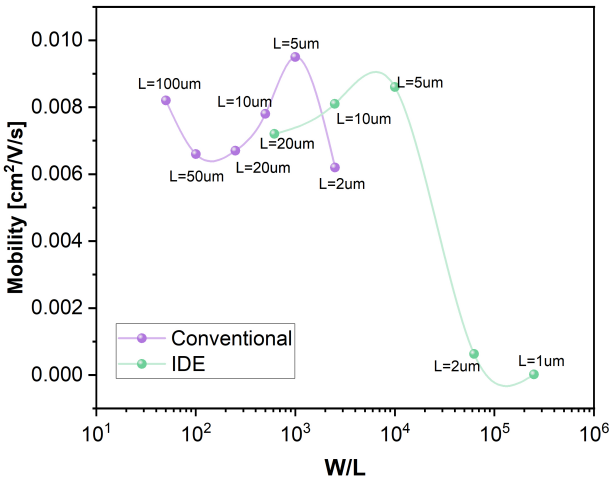


Figure 4.18: Extracted hole mobilities from FETs with different channel W/L ratios, all based on identical mixed-halide passivated PbS CQDs.

The results indicate consistent mobility values across devices with different W/L ratios, suggesting that the channel geometry does not significantly affect the extracted mobility under the tested conditions. However, it was observed that FETs with smaller W/L ratios exhibited lower output current levels. While this did not impact the extracted mobility, it led to poorer signal-to-noise ratios particularly problematic when evaluating low-mobility materials.

Therefore, although the W/L ratio does not bias the mobility extraction, devices with larger W/L ratios are preferred for measuring CQDs with low mobility, as they produce higher drain currents and reduce the effect of instrumental noise.

4.6.4 Dielectric Interface Testing

To investigate the impact of the dielectric–CQD interface on FET performance, devices were fabricated using various thin dielectric surface coatings, including Al_2O_3, HfO_2, SiO_2,

TiO_2, and ZrO_2, each with a nominal thickness of approximately 5 nm. The TiO_2-coated devices exhibited electrical shorting between the source and drain electrodes and were excluded from further analysis. The remaining four interfaces were evaluated using identically prepared InAs CQDs.

The preliminary results of the dielectric interfaces tests are given in Apendix C. Figures C.1–C.4 present the optical images and electrical characteristics (output and transfer curves) of the InAs CQD-FETs fabricated on Al_2O_3, HfO_2, SiO_2, and ZrO_2 surfaces, respectively.

Across all dielectric interfaces, similar field-effect mobility values were extracted, indicating that charge transport in these InAs CQD-FETs is relatively insensitive to the choice of gate dielectric at this thickness. Nonetheless, minor differences were observed in hysteresis behavior and slight shifts in the output characteristics, likely reflecting variations in interfacial trap densities or surface states.

Given the comparable mobility results and the fabrication simplicity, bare SiO_2-based FETs were used in the following measurements throughout this chapter. Nevertheless, dielectric interface engineering remains a promising strategy for reducing hysteresis and enhancing transistor characteristics particularly as a future work.

4.6.5 InAs Measurements

InAs colloidal quantum dots (CQDs) are promising materials for infrared optoelectronic applications; however, their performance remains limited by surface defects and instability under ambient conditions. To address these challenges, we developed a mixed-halide passivation strategy for large-sized InAs CQDs. This approach not only enhances the anti-oxidation resistance by a factor of two but also achieves an operational stability and a high hole mobility of 0.024 $cm^2\,V^{-1}\,s^{-1}$ in photodetectors operating at 1140 nm.

To investigate the effect of different halide ligands, we fabricated FETs passivated with Br, Cl, and a Br/Cl mixture. Devices were patterned using a UV-lithography process on p^{++}-doped silicon substrates with a 291 nm thermally grown SiO_2 dielectric. Each interdigitated electrode (IDE) device had the following specifications: channel width $W = 100\ \mu$m, channel length $L = 2\ \mu$m, number of fingers $n = 625$, resulting in a total effective aspect ratio of $W/L = 62{,}450$. Transfer characteristics were measured at $V_{DS} = +35$ V, and output curves were recorded under various gate voltages V_G as shown in 4.19. Both electron and hole mobilities were extracted from the linear regime of the transfer curves. Hysteresis was quantified using the forward–reverse scan area ratio, serving as an indicator of charge trapping.

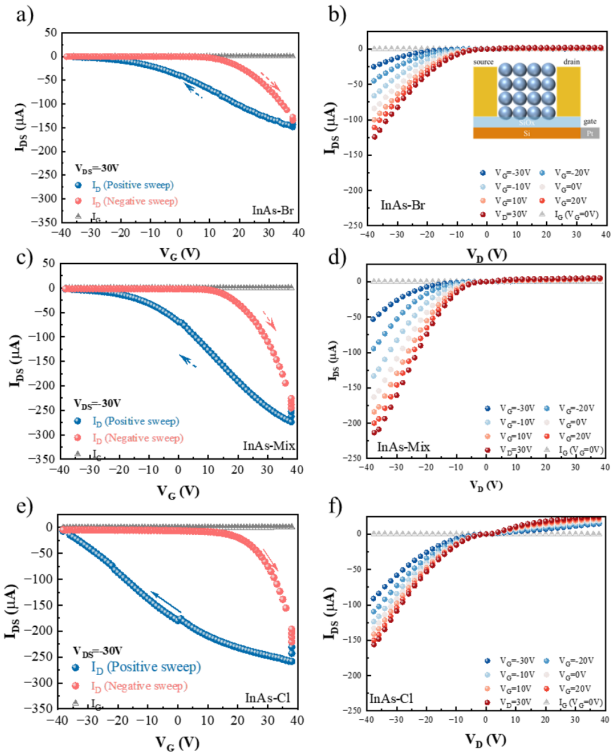


Figure 4.19: Transfer and output characteristics of InAs CQD FETs passivated with different halide ligands: (a,b) Br, (c,d) Br/Cl mixture, and (e,f) Cl. The inset shows a schematic of the IDE-based FET structure. Reproduced with permission from Wiley [231].

To complement the FET measurements, we evaluated the trap density and carrier mobility of the halide-passivated CQD films using hole-only SCLC measurements. The Br/Cl mixed-halide formulation reduced the trap density from 3.2×10^{16} cm^{-3} (Br-passivation) to 5.0×10^{15} cm^{-3}, while improving the hole mobility from 2×10^{-4} to 1×10^{-3} cm^2 V^{-1} s^{-1}. The same trend was validated through FET measurements, with the Br/Cl mixture achieving the highest hole mobility of 0.024 ± 0.009 cm^2 V^{-1} s^{-1} and the lowest hysteresis among the three groups. These findings confirm the effectiveness of mixed-halide surface passivation in reducing trap states and enhancing carrier transport in InAs CQD films.

4.6.6 InSb Measurements

To evaluate the electronic properties of surface-passivated InSb CQDs, we conducted FET and SCLC measurements on CQD films treated with short-chain thiol ligands (ME and

MTG) and metal sulfide ligands (Na_2S). The field-effect transistors were fabricated with an interdigitated electrode (IDE) layout to ensure a high effective width-to-length ratio ($W/L = 62{,}450$), enabling improved current levels for low-mobility films. As shown in Figure 4.20, both ME- and MTG-treated films demonstrated clear p-type behavior, with drain current (I_{DS}) increasing under negative gate bias (V_{GS}). The extracted hole mobilities from transfer curves were 7.8×10^{-4} cm^2 V^{-1} s^{-1} for ME-InSb and 1.1×10^{-4} cm^2 V^{-1} s^{-1} for MTG-InSb, showing a significant improvement compared to Na_2S-passivated films.

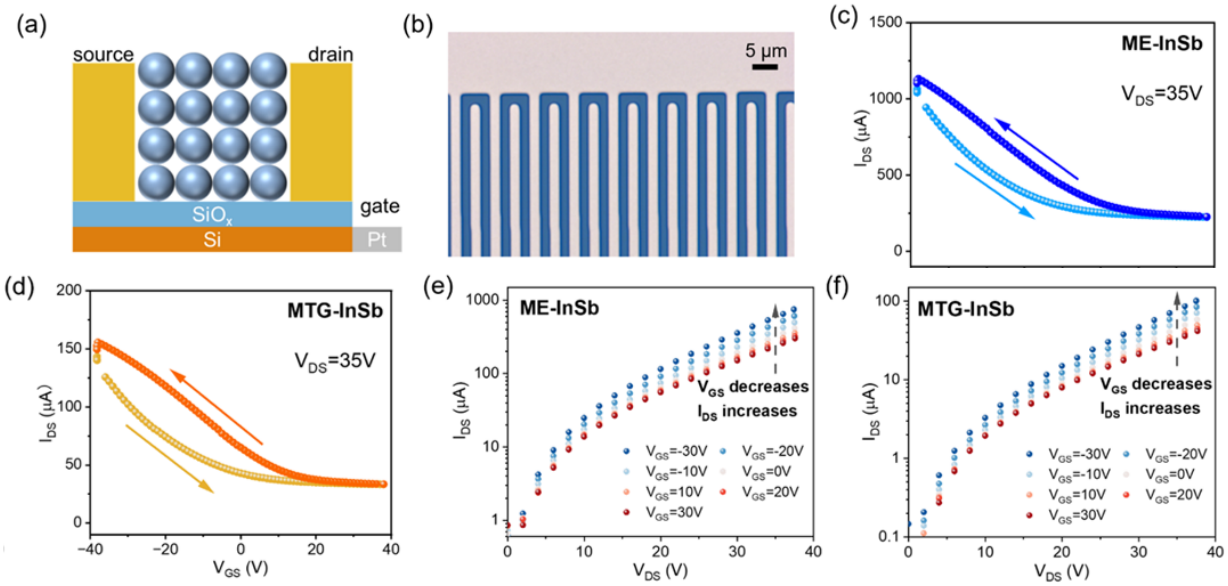


Figure 4.20: Field-effect characterization of InSb CQD films. (a) Schematic of the FET device structure. (b) Microscope image of the channel region. Transfer characteristics of (c) ME-InSb and (d) MTG-InSb CQDs, with arrows indicating the sweep directions. Output characteristics of (e) ME-InSb and (f) MTG-InSb CQDs. The applied gate-source voltages (V_{GS}) are indicated in the legends. For both samples, the drain-source current (I_{DS}) increases with decreasing V_{GS}, consistent with p-type behavior of the CQDs. Reproduced with permission from Wiley [247].

To complement the FET analysis, trap densities and mobilities were also determined via SCLC measurements. ME-passivated CQDs exhibited a tenfold reduction in trap state density (1.86×10^{16} cm^{-3}) compared to Na_2S-passivated CQDs (1.49×10^{17} cm^{-3}), along with a significantly improved hole mobility (1.15×10^{-4} cm^2 V^{-1} s^{-1}). The strong agreement between FET and SCLC mobilities validates the effectiveness of thiol-based surface treatments in removing surface oxides and reducing defect density.

These findings underscore the importance of surface reconstruction in enhancing the optoelectronic quality of InSb CQDs. Short-chain thiol ligands, particularly mercaptoethanol (ME), not only improve carrier mobility and reduce trap density but also maintain colloidal stability for extended periods. Consequently, ME-passivated InSb CQDs enabled SWIR photodetectors with a high external quantum efficiency (EQE) of 28% at 1450 nm and long-term operational stability, retaining 95% performance after 300 hours of biased illumination. Overall, effective oxide removal and ligand engineering prove essential for realizing high-performance and stable infrared CQD devices.

4.7 Conclusion

This chapter investigated the crucial role of how interface quality affects CQD photodetectors built on FET architectures. As sensor dimensions are scaled down, reliable signal performance becomes harder to maintain, emphasizing the importance of well-designed interfaces. Initial studies using basic CQD-FET devices revealed key performance limitations, such as low carrier mobilities, environmental instability, and poor signal-to-noise ratios. These preliminary results addressed the need for advanced interface engineering and optimized experimental setups. Therefore, a specialized measurement chamber was developed to control environmental conditions and provide environmental stability. Simultaneously, FET designs were improved through increased channel aspect ratios (W/L), enhancing the measurable signals and enabling precise mobility extraction. These enhancements significantly increased the measured mobilities and reduced hysteresis, emphasizing the importance of optimized device layouts and environmental control in quantifying CQD performance.

Moreover, the CQD-dielectric interface was systematically studied using various high-κ dielectric materials, including Al_2O_3, HfO_2, SiO_2, TiO_2, and ZrO_2. While mobility values remained relatively consistent across different dielectrics, variations in hysteresis and overall stability were observed. Due to the fabrication simplicity and reliable performance, bare SiO_2 was selected as the dielectric interface though exploring alternative dielectrics remains promising for future investigations.

Significant performance improvements were also demonstrated through surface passivation strategies employing mixed-halide ligands. Specifically, mixed-halide treatments of InAs and InSb CQDs markedly reduced trap densities, increased charge carrier mobilities, and enhanced device operational stability, validating the efficacy of ligand engineering and surface functionalization.

Various electrode designs were tested consistent mobility results were obtained. Due to their high W/L aspect ratios, IDE structures improve the measured signal strength. This optimization enabled more reliable and accurate mobility extraction, particularly beneficial for materials with low carrier mobilities.

Overall, the findings presented in this chapter demonstrate that careful interface engineering such as dielectric optimization, surface treatments, electrode geometry adjustments, and environmental control is essential for maximizing the performance of CQD-based FET devices. These insights contribute significantly to the understanding of CQD interfaces and establish robust methodologies for the continued development of miniaturized, high-performance sensors.

Future work should expand upon these findings by exploring advanced dielectric materials, novel ligand chemistries, and optimized electrode designs. Addressing these interface-related challenges will further enhance CQD-based sensor performance, ultimately enabling smaller pixel sizes, improved sensitivity, and seamless integration into next-generation sensing technologies.

Chapter 5

Conclusions and Future Work

5.1 Conclusions

Miniaturization is not limited to the electronics industry as the principles of Moore's law also applies on the evalution of sensors. For effective miniaturization, well-defined design rules are required rather than relying on trial-and-error approaches. Therefore, there's a need for scaling analyses to quantitatively predict the impact of geometry on sensor performance. These analysis not only provide practical design guidelines but also offer state-of-the-art insights into the future trajectory of sensor development.

This thesis has investigated the effect of sensor miniaturization with associated packaging and interface challenges. By systematically exploring theoretical models, experimental methodologies, and proposing novel packaging and interface engineering strategies, this work advances the understanding of the fundamental mechanisms governing sensor behavior at smaller scales.

First, a theoretical analysis was developed to provide in-depth understanding of the sensing behavior of inertial gas sensors. The developed model correlated the sensor performance with sensor geometry and effectively predicted the trends in sensor performance parameters such as resonance frequency, quality factor, SNR and sensitivities relevant to gas sensing applications. To further support this model, NEMS and MEMS based gas sensors were fabricated by simplified nanofabrication techniques and their resonance and sensor performances were compared under identical sensing conditions. Experimental results showed strong agreement with theoretical predictions, validating the proposed model. Therefore, the established scaling relationships can serve as "design rules" to guide miniaturization while maintaining sufficient signal quality. While it's been theoretically and

experimentally demonstrated that scaling down improves the main performance parameter of the sensors, sensitivity, the output signal power generally scales down with geometry and results weaker SNRs. To counteract this, scaling must be performed by preserving the some key aspect ratios that optimize performance which motivated the need for optimized packaging and interface solutions.

Secondly, a novel packaging technique called built-in packaging was proposed by eliminating packaging and interconnections components such as wire bonding, chip carrier, PCB, probe station, and even wires to minimize parasitic loses and enhance SNR. Comparative studies on conventional packaging and interconnection techniques such as wire bonding and probing versus built-in packaging were conductor for MEMS resonator and MIM diode applications. When tested with the built-in packaging, MIM diodes outputted 12% more electrical current therefore better diode performance compared to the conventional methods, and MEMS resonator showed identical performance with less parasitic components. Hence, the developed built-in packaging method demonstrated improves output signal strength, thereby extending the feasible miniaturization range.

Finally, interface engineering was studied for the integration of novel materials into miniaturized sensor applications. Integration of novel materials into sensor applications is crucial as using more responsive sensing materials can delay miniaturization limits by compensating for signal loss through improved signal generation efficiency.

FET "sensors" were developed to measure the charge carrier mobilities of semiconducting nanocrystals, or more specifically CQDs. A custom testing rig was built by investigating the CQD interfaces including CQD-to-dielectric, CQD-to-electrode, CQD-to-environment, and CQD-to-CQD and device interfaces such as dielectric-to-electrode demonstrated their critical impact on output signal. Through systematic experimentation, surface treatments, optimized fabrication and testing processes, interfaces were engineered and key electrical properties of CQDs such as charge carrier mobility and hysteresis were quantified. The improved electrical performances of CQDs were aligned with their IR detection application and better electrical performance yielded better photosensing properties such as higher EQE and faster pixels. Hence, the developed materials thourgh optimized interfaces support the operation of miniaturized sensors. Improved electrical properties of CQDs aligned well with their application in IR detection, resulted in superior photosensing performance, such as increased EQE and faster pixel response, demonstrating the potential of interface-optimized materials for miniaturized sensors.

In summary, this thesis investigates the key elements of sensor miniaturization thorough exploration of the effects, packaging, and interface engineering challenges associated with sensor miniaturization.

5.2 Future Works

This thesis lay the groundwork for future developments in sensor miniaturization.

For the scaling down of inertial gas sensors, the number of case studies can be increased to further validate the theoretical scaling relationships. In this work, only two devices were compared side-by-side. Expanding the range of geometries would provide a deeper insight into scaling effects. It should also be noted that a linear model was employed which showed strong agreement with the experimental results. Additional case studies could help determine if nonlinear effects become significant at certain scales, and when they should be included in the model.

The novel built-in packaging technique was demonstrated in two case studies. A MEMS resonator was excited using the built-in packaging which simplified the operation. Future work could involve both excitation and sensing of a MEMS resonator with built-in packaging to achieve a complete operation. In fact, its sensing performance can be compared with that of conventional packaging methods. Secondly, a MIM diode was tested where the built-in packaging improved the performance. As a next step, a FET could be packaged using built-in method, and its performance can be compared against conventionally packaged FETs.

In the fourth chapter, carrier mobilities of various CQDs were measured, yielding state-of-the-art values. Future work could expand this testing to other types of CQDs. Moreover, dielectric interface engineering experiments could be carrier out to better understand the interaction between CQD films and the dielectric layer.

References

[1] Eihab M Abdel-Rahman, Mohammad I Younis, and Ali H Nayfeh. Characterization of the mechanical behavior of an electrically actuated microbeam. *Journal of Micromechanics and Microengineering*, 12(6):759, 2002.

[2] Masamichi Akazawa and Yuya Kitawaki. Formation of thermally grown sio2/gan interface. *AIP Advances*, 11(8), 2021.

[3] MS Al-Ghamdi, ME Khater, KME Stewart, Ayman Alneamy, Eihab M Abdel-Rahman, and Alexander Penlidis. Dynamic bifurcation mems gas sensors. *Journal of Micromechanics and Microengineering*, 29(1):015005, 2018.

[4] Martino Aldrigo, Mircea Dragoman, Mircea Modreanu, Ian Povey, Sergiu Iordanescu, Dan Vasilache, Adrian Dinescu, Mazen Shanawani, and Diego Masotti. Harvesting electromagnetic energy in the v -band using a rectenna formed by a bow tie integrated with a 6-nm-thick au/hfo_2/pt metal–insulator–metal diode. *IEEE Transactions on Electron Devices*, 65(7):2973–2980, 2018.

[5] Abdullah H Alshehri, Kissan Mistry, Viet Huong Nguyen, Khaled H Ibrahim, David Muñoz-Rojas, Mustafa Yavuz, and Kevin P Musselman. Quantum-tunneling metal-insulator-metal diodes made by rapid atmospheric pressure chemical vapor deposition. *Advanced Functional Materials*, 29(7):1805533, 2019.

[6] Abdullah H Alshehri, Ahmed Shahin, Kissan Mistry, Khaled H Ibrahim, Mustafa Yavuz, and Kevin P Musselman. Metal-insulator-insulator-metal diodes with responsivities greater than 30 aw- 1 based on nitrogen-doped tiox and alox insulator layers. *Advanced Electronic Materials*, 7(11):2100467, 2021.

[7] Mohamed Arabi, Mary Gopanchuk, Eihab Abdel-Rahman, and Mustafa Yavuz. Measurement of in-plane motions in mems. *Sensors*, 20(12):3594, 2020.

[8] Sajjad Arzemanzadeh, Olivier Pierron, and Ehsan Hosseinian. Understanding compound effect of shear and squeeze-film dissipation in a silicon lateral micro-resonator for mems-based environmental monitoring applications. *Sensors and Actuators A: Physical*, 351:114166, 2023.

[9] Sina Askari, Mohammad H Asadian, and Andrei M Shkel. Performance of quad mass gyroscope in the angular rate mode. *Micromachines*, 12(3):266, 2021.

[10] Ozan Atan, Joao M Pina, Darshan H Parmar, Pan Xia, Yangning Zhang, Ahmet Gulsaran, Eui Dae Jung, Dongsun Choi, Muhammad Imran, Mustafa Yavuz, et al. Control over charge carrier mobility in the hole transport layer enables fast colloidal quantum dot infrared photodetectors. *Nano letters*, 23(10):4298–4303, 2023.

[11] Bersu Bastug Azer, Ahmet Gulsaran, Joel R Pennings, Resul Saritas, Samed Kocer, Jessica L Bennett, Yash Devdas Abhang, Michael A Pope, Eihab Abdel-Rahman, and Mustafa Yavuz. A review: Tio2 based photoelectrocatalytic chemical oxygen demand sensors and their usage in industrial applications. *Journal of Electroanalytical Chemistry*, 918:116466, 2022.

[12] Yonghwa Baek, Sooman Lim, Lae Ho Kim, Seonuk Park, Seung Woo Lee, Tae Hwan Oh, Se Hyun Kim, and Chan Eon Park. Al2o3/tio2 nanolaminate gate dielectric films with enhanced electrical performances for organic field-effect transistors. *Organic Electronics*, 28:139–146, 2016.

[13] S Balasubramanian, SR Polaki, and K Prabakar. Ultrahigh sensitive and ultrafast relative humidity sensing using surface enhanced microcantilevers. *Smart Materials and Structures*, 29(9):095006, 2020.

[14] DM Balazs, MI Nugraha, SZ Bisri, M Sytnyk, W Heiss, and MA Loi. Reducing charge trapping in pbs colloidal quantum dot solids. *Applied Physics Letters*, 104(11), 2014.

[15] Mario Bareiß, Frederik Ante, Daniel Kalblein, Gunther Jegert, Christian Jirauschek, Giuseppe Scarpa, Bernhard Fabel, Edward M Nelson, Gregory Timp, Ute Zschieschang, et al. High-yield transfer printing of metal–insulator–metal nanodiodes. *ACS nano*, 6(3):2853–2859, 2012.

[16] Lionel Barrow, Nikolai Bock, Aurelien Bouvier, Dario Clocchiatti, Jian Feng, Naveen Kolli, Andras Pattantyus, Vitanshu Sharma, Tzi-Hsiung Shu, and Emanuele Mandelli. A quantumfilm based quadvga 1.5 μm pixel image sensor with over 40% qe at 940 nm for actively illuminated applications. *IISW Dig. Tech. Pap*, pages 378–381, 2017.

[17] M Bartek and RF Wolffenbuttel. Dry release of metal structures in oxygen plasma: process characterization and optimization. *Journal of Micromechanics and Microengineering*, 8(2):91, 1998.

[18] Carmen Bartic, Henri Jansen, Andrew Campitelli, and Staf Borghs. Ta2o5 as gate dielectric material for low-voltage organic thin-film transistors. *Organic electronics*, 3(2):65–72, 2002.

[19] Daniel Bauza. Thermal oxidation of silicon and si–sio2 interface morphology, structure, and localized states. *Handbook of surfaces and interfaces of materials*, 1:115–216, 2001.

[20] Jeffrey A Bean, Badri Tiwari, Gary H Bernstein, Patrick Fay, and Wolfgang Porod. Thermal infrared detection using dipole antenna-coupled metal-oxide-metal diodes. *Journal of Vacuum Science & Technology B: Microelectronics and Nanometer Structures Processing, Measurement, and Phenomena*, 27(1):11–14, 2009.

[21] Kapil Bhatt, Sandeep Kumar, and Chandra Charu Tripathi. Highly sensitive al/al2o3/ag mim diode for energy harvesting applications. *AEU-International Journal of Electronics and Communications*, 111:152925, 2019.

[22] Kapil Bhatt and CC Tripathi. Comparative analysis of efficient diode design for terahertz wireless power transmission system. *Indian Journal of Pure & Applied Physics (IJPAP)*, 2015.

[23] M Boukhriss, K Zhani, and R Ghribi. Study of thermophysical properties of a solar desalination system using solar energy. *Desalination and Water Treatment*, 51(4-6):1290–1295, 2013.

[24] Olga Boytsova, Alexey Klimenko, Vasiliy Lebedev, Alexey Lukashin, and Andrey Eliseev. Nanomechanical humidity detection through porous alumina cantilevers. *Beilstein Journal of Nanotechnology*, 6(1):1332–1337, 2015.

[25] Christopher Buurma, Richard E Pimpinella, Anthony J Ciani, Jered S Feldman, Christoph H Grein, and Philippe Guyot-Sionnest. Mwir imaging with low cost colloidal quantum dot films. In *Optical Sensing, Imaging, and Photon Counting: Nanostructured Devices and Applications 2016*, volume 9933, page 993303. SPIE, 2016.

[26] Alberto Cagliani, Valerio Pini, J Tamayo, Montserrat Calleja, and Zachary James Davis. Ultrasensitive thermometer for atmospheric pressure operation based on a micromechanical resonator. *Sensors and Actuators B: Chemical*, 202:339–345, 2014.

[27] Chunhua Cai, Junyan Tan, Di Hua, Ming Qin, and Nianfang Zhu. Piezoresistive temperature sensors fabricated by a surface micromachining cmos mems process. *Scientific reports*, 8(1):17065, 2018.

[28] William D Callister, David G Rethwisch, Aaron Blicblau, Kiara Bruggeman, Michael Cortie, John Long, Judy Hart, Ross Marceau, and Ryan Mitchell. *Materials science and engineering: an introduction*, volume 7. John wiley & sons New York, 2007.

[29] William D Callister Jr and David G Rethwisch. *Materials science and engineering: an introduction*. John wiley & sons, 2020.

[30] Vivien Cartailler. *Study of temperature and moisture impact on water diffusion in materials and on electronic circuits failure mechanisms.* PhD thesis, Université de Bordeaux, 2021.

[31] PL Castro and BE Deal. Low-temperature reduction of fast surface states associated with thermally oxidized silicon. *Journal of the Electrochemical Society*, 118(2):280, 1971.

[32] Charidimos Chaintoutis, Behnam Shariati, Adonis Bogris, Paul V Dijk, Chris GH Roeloffzen, Jerome Bourderionnet, Ioannis Tomkos, and Dimitris Syvridis. Free space intra-datacenter interconnects based on 2d optical beam steering enabled by photonic integrated circuits. In *Photonics*, volume 5, page 21. MDPI, 2018.

[33] Suman Chakraborty. *Mechanics over micro and nano scales*. Springer, 2011.

[34] Kow-Ming Chang, Sung-Hung Huang, and Yi-Wen Tseng. Performance improvement of pentacene-based organic thin-film transistor with hfo2 gate dielectrics treated by cf4 plasma. *ECS Transactions*, 35(19):1, 2011.

[35] Eric Chason and Pradeep R Guduru. Tutorial: Understanding residual stress in polycrystalline thin films through real-time measurements and physical models. *Journal of Applied Physics*, 119(19), 2016.

[36] Julien Chaste, A Eichler, J Moser, G Ceballos, R Rurali, and A Bachtold. A nanomechanical mass sensor with yoctogram resolution. *Nature nanotechnology*, 7(5):301–304, 2012.

[37] Serguei Chatrchyan, Vardan Khachatryan, Albert M Sirunyan, Armen Tumasyan, Wolfgang Adam, Ernest Aguilo, Thomas Bergauer, Marko Dragicevic, Janos Erö, Christian Fabjan, et al. Observation of a new boson at a mass of 125 gev with the cms experiment at the lhc. *Physics Letters B*, 716(1):30–61, 2012.

[38] Chen Chen, Guan Wang, Ziyang Zhang, and Kai Zhang. Dual narrow-band absorber based on metal–insulator–metal configuration for refractive index sensing. *Optics letters*, 43(15):3630–3633, 2018.

[39] Hongliang Chen, Weining Zhang, Mingliang Li, Gen He, and Xuefeng Guo. Interface engineering in organic field-effect transistors: principles, applications, and perspectives. *Chemical reviews*, 120(5):2879–2949, 2020.

[40] Ke Chen, Zhenfeng Gong, and Qingxu Yu. Fiber-amplifier-enhanced resonant photoacoustic sensor for sub-ppb level acetylene detection. *Sensors and Actuators A: Physical*, 274:184–188, 2018.

[41] Qiao Chen, Dong Liu, Xian-He Huang, Yao Yao, and Kun-Lei Mao. Impedance analysis of chitin nanofibers integrated bulk acoustic wave humidity sensor with asymmetric electrode configuration. *Nanomaterials*, 12(17):3035, 2022.

[42] Qiao Chen, Kun-lei Mao, Yao Yao, Xian-he Huang, and Zhen Zhang. Nanodiamond/cellulose nanocrystals composite-based acoustic humidity sensor. *Sensors and Actuators B: Chemical*, 373:132748, 2022.

[43] Wei Chen, Haodong Tang, Yulong Chen, Julian E Heger, Nian Li, Lucas P Kreuzer, Yue Xie, Depeng Li, Carl Anthony, Zoe Pikramenou, et al. Spray-deposited pbs colloidal quantum dot solid for near-infrared photodetectors. *Nano Energy*, 78:105254, 2020.

[44] Marie C Cheynet, Simone Pokrant, Frans D Tichelaar, and Jean-Luc Rouvière. Crystal structure and band gap determination of hfo2 thin films. *Journal of Applied Physics*, 101(5), 2007.

[45] Matthew L Chin, Prakash Periasamy, Terrance P O'Regan, Matin Amani, Cheng Tan, Ryan P O'Hayre, Joseph J Berry, Richard M Osgood, Philip A Parilla, David S Ginley, et al. Planar metal–insulator–metal diodes based on the nb/nb2o5/x material system. *Journal of Vacuum Science & Technology B*, 31(5), 2013.

[46] Lay-Lay Chua, Peter KH Ho, Henning Sirringhaus, and Richard H Friend. High-stability ultrathin spin-on benzocyclobutene gate dielectric for polymer field-effect transistors. *Applied Physics Letters*, 84(17):3400–3402, 2004.

[47] COMSOL. *AC/DC Module User's Guide*. COMSOL Multiphysics.

[48] COMSOL. *Structural Mechanics Module User's Guide*. COMSOL Multiphysics.

[49] Supriyo Datta. *Quantum transport: atom to transistor*. Cambridge university press, 2005.

[50] Chong-An Di, Yunqi Liu, GUI Yu, and Daoben Zhu. Interface engineering: an effective approach toward high-performance organic field-effect transistors. *Accounts of chemical research*, 42(10):1573–1583, 2009.

[51] Zaihua Duan, Juan Li, Zhen Yuan, Yadong Jiang, and Huiling Tai. Capacitive humidity sensor based on zirconium phosphate nanoplates film with wide sensing range and high response. *Sensors and Actuators B: Chemical*, 394:134445, 2023.

[52] Zaihua Duan, Boyu Zhang, Mingxiang Zhang, Zhen Yuan, Yadong Jiang, and Huiling Tai. High-performance electrochemical power generation humidity sensor based on nacl/sodium alginate humidity sensing electrolyte and cu/zn electrodes for visual humidity indication and respiratory patterns detection. *Sensors and Actuators B: Chemical*, page 135585, 2024.

[53] Zaihua Duan, Mingxiang Zhang, Yadong Jiang, Zhen Yuan, and Huiling Tai. Emerging electrochemical humidity sensor for zero power consumption and self-powered humidity detection: a perspective. *Journal of Materials Chemistry A*, 2024.

[54] Caglar Elbuken. *Magnetic levitation of polymeric photo-thermal microgrippers*. PhD thesis, University of Waterloo, 2008.

[55] Alaa Elhady and Eihab Abdel-Rahman. Measurement of the electric permittivity using bleustein–gulyaev wave sensor. *Journal of Micromechanics and Microengineering*, 32(3):034004, 2022.

[56] Sabrina Engel, Eva-Corinna Fritz, and Bart Jan Ravoo. New trends in the functionalization of metallic gold: from organosulfur ligands to n-heterocyclic carbenes. *Chemical Society Reviews*, 46(8):2057–2075, 2017.

[57] Pashang Esfandiari, G Bernstein, P Fay, W Porod, B Rakos, A Zarandy, B Berland, L Boloni, G Boreman, B Lail, et al. Tunable antenna-coupled metal-oxide-metal (mom) uncooled ir detector. In *Infrared Technology and Applications XXXI*, volume 5783, pages 470–482. SPIE, 2005.

[58] JC Fisher and Ivar Giaever. Tunneling through thin insulating layers. *Journal of Applied Physics*, 32(2):172–177, 1961.

[59] JA Floro, SJ Hearne, JA Hunter, P Kotula, E Chason, SC Seel, and CV Thompson. The dynamic competition between stress generation and relaxation mechanisms during coalescence of volmer–weber thin films. *Journal of Applied Physics*, 89(9):4886–4897, 2001.

[60] William E Ford, Deqing Gao, Nikolaus Knorr, Rene Wirtz, Frank Scholz, Zoi Karipidou, Kodo Ogasawara, Silvia Rosselli, Vadim Rodin, Gabriele Nelles, et al. Organic dipole layers for ultralow work function electrodes. *ACS nano*, 8(9):9173–9180, 2014.

[61] Ada Fort, Enza Panzardi, Valerio Vignoli, Elia Landi, Carlo Trigona, and Marco Mugnaini. Performance analysis of a humidity sensor based on a microresonator functionalized with tio 2 nanoparticles. *IEEE Transactions on Instrumentation and Measurement*, 69(10):7999–8008, 2020.

[62] Shao-Wei Fu and Chin C Lee. A study on intermetallic compound formation in ag–al system and evaluation of its mechanical properties by micro-indentation. *Journal of Materials Science: Materials in Electronics*, 29:3985–3991, 2018.

[63] Chong Leong Gan, Classe Francis, Bak Lee Chan, and Uda Hashim. Extended reliability of gold and copper ball bonds in microelectronic packaging. *gold Bulletin*, 46:103–115, 2013.

[64] F Pelayo García de Arquer, Dmitri V Talapin, Victor I Klimov, Yasuhiko Arakawa, Manfred Bayer, and Edward H Sargent. Semiconductor quantum dots: Technological progress and future challenges. *Science*, 373(6555):eaaz8541, 2021.

[65] Qiang Geng, Dien Wang, Pengfei Chen, and Shih-Chi Chen. Ultrafast multi-focus 3-d nano-fabrication based on two-photon polymerization. *Nature communications*, 10(1):2179, 2019.

[66] Chwee Sim Goh, Wee Ling Eddy Chong, Teck Kheng Lee, and Christopher Breach. Corrosion study and intermetallics formation in gold and copper wire bonding in microelectronics packaging. *Crystals*, 3(3):391–404, 2013.

[67] Peter G Gordon, Goran Bačić, Gregory P Lopinski, and Seán T Barry. Work function of doped zinc oxide films deposited by ald. *Journal of Materials Research*, 35(7):756–761, 2020.

[68] Christopher Gregory, Allan Hilton, Katherine Violette, and Ethan JD Klem. 66-3: invited paper: colloidal quantum dot photodetectors for large format nir, swir, and

eswir imaging arrays. In *SID Symposium Digest of Technical Papers*, volume 52, pages 982–986. Wiley Online Library, 2021.

[69] MD Groner, JW Elam, FH Fabreguette, and Sm M George. Electrical characterization of thin al2o3 films grown by atomic layer deposition on silicon and various metal substrates. *Thin solid films*, 413(1-2):186–197, 2002.

[70] Sachit Grover and Garret Moddel. Applicability of metal/insulator/metal (mim) diodes to solar rectennas. *IEEE journal of photovoltaics*, 1(1):78–83, 2011.

[71] Yangyang Guan, Xianhao Le, MingZhe Hu, Weixin Liu, and Jin Xie. A noninvasive method for monitoring respiratory rate of rats based on a microcantilever resonant humidity sensor. *Journal of micromechanics and microengineering*, 29(12):125001, 2019.

[72] Ahmet Gulsaran, Bersu Bastug Azer, Resul Saritas, Samed Kocer, Yasser S Shama, Sasan Rahmanian, Hamza Mouharrar, Rana Abdelrahman, Eihab Abdel-Rahman, and Mustafa Yavuz. High sensitivity, thermal noise-driven aluminum-based resonant mems humidity sensor. *Sensors and Actuators A: Physical*, 378:115844, 2024.

[73] Ahmet Gulsaran, Bersu Bastug Azer, Samed Kocer, Sasan Rahmanian, Resul Saritas, Eihab M Abdel-Rahman, and Mustafa Yavuz. Built-in packaging for single terminal devices. *Sensors*, 22(14):5264, 2022.

[74] Ahmet Gulsaran, Bersu Bastug Azer, Dogu Ozyigit, Resul Saritas, Samed Kocer, Eihab Abdel-Rahman, and Mustafa Yavuz. Built-in packaging for two-terminal devices. *Micromachines*, 14(7):1473, 2023.

[75] Yihao Guo, Jian Zhou, Zhangbin Ji, Yanghui Liu, Rongtao Cao, Fengling Zhuo, Kaitao Tan, Huigao Duan, and Yongqing Fu. A new strategy to minimize humidity influences on acoustic wave ultraviolet sensors using zno nanowires wrapped with hydrophobic silica nanoparticles. *Microsystems & Nanoengineering*, 8(1):121, 2022.

[76] Lisa P Hackett, Abid Ameen, Wenyue Li, Faiza Khawar Dar, Lynford L Goddard, and Gang Logan Liu. Spectrometer-free plasmonic biosensing with metal–insulator–metal nanocup arrays. *ACS sensors*, 3(2):290–298, 2018.

[77] Claudia Haensch, Stephanie Hoeppener, and Ulrich S Schubert. Chemical modification of self-assembled silane based monolayers by surface reactions. *Chemical Society Reviews*, 39(6):2323–2334, 2010.

[78] E Hagen and H Rubens. Über beziehungen des reflexions-und emissionsvermögens der metalle zu ihrem elektrischen leitvermögen. *Annalen der Physik*, 316(8):873–901, 1903.

[79] Mohammad H Hasan, Fadi M Alsaleem, and Hassen M Ouakad. Novel threshold pressure sensors based on nonlinear dynamics of mems resonators. *Journal of Micromechanics and Microengineering*, 28(6):065007, 2018.

[80] BD Hauer, C Doolin, KSD Beach, and JP Davis. A general procedure for thermomechanical calibration of nano/micro-mechanical resonators. *Annals of Physics*, 339:181–207, 2013.

[81] William M Haynes. *CRC handbook of chemistry and physics*. CRC press, 2016.

[82] Wenqiang He, Wenchao Xu, Qiang Peng, Chuan Liu, Guofu Zhou, Sujuan Wu, Min Zeng, Zhang Zhang, Jinwei Gao, Xingsen Gao, et al. Surface modification on solution processable zro2 high-k dielectrics for low voltage operations of organic thin film transistors. *The Journal of Physical Chemistry C*, 120(18):9949–9957, 2016.

[83] Mahsa Keshavarz Hedayati, Abdolali Abdipour, Reza Sarraf Shirazi, Max J Ammann, Matthias John, Cagri Cetintepe, and Robert Bogdan Staszewski. Challenges in on-chip antenna design and integration with rf receiver front-end circuitry in nanoscale cmos for 5g communication systems. *IEEE Access*, 7:43190–43204, 2019.

[84] WK Hiebert, D Vick, V Sauer, and MR Freeman. Optical interferometric displacement calibration and thermomechanical noise detection in bulk focused ion beam-fabricated nanoelectromechanical systems. *Journal of Micromechanics and Microengineering*, 20(11):115038, 2010.

[85] D Hiller, R Zierold, J Bachmann, M Alexe, Y Yang, JW Gerlach, Andre Stesmans, Mihaela Jivanescu, U Müller, J Vogt, et al. Low temperature silicon dioxide by thermal atomic layer deposition: Investigation of material properties. *Journal of Applied Physics*, 107(6), 2010.

[86] A Hocini, N Melouki, D Khedrouche, et al. Design and analysis of near infrared high sensitive metal-insulator-metal plasmonic bio-sensor. In *IOP Conference Series: Materials Science and Engineering*, volume 1046, page 012003. IOP Publishing, 2021.

[87] Xingwang Hu, Li Liu, Sheng Liu, Meng Ruan, and Zhiwen Chen. Effects of voids on thermal fatigue reliability of solder joints on inner rings in ball grid array packaging by finite element analysis. *Micromachines*, 14(3):588, 2023.

[88] Yaoqiao Hu, Huaxing Jiang, Kei May Lau, and Qiang Li. Chemical vapor deposited monolayer mos2 top-gate mosfet with atomic-layer-deposited zro2 as gate dielectric. *Semiconductor Science and Technology*, 33(4):045004, 2018.

[89] Yue Huang, Chun Lin, Zhen-Hua Ye, and Rui-Jun Ding. Reflow flip-chip bonding technology for infrared detectors. *Journal of Micromechanics and Microengineering*, 25(8):085009, 2015.

[90] Robert R Hughes and Steve Dixon. Analysis of electrical resonance distortion for inductive sensing applications. *IEEE Sensors Journal*, 18(14):5818–5825, 2018.

[91] Robert Hull and John C Bean. Misfit dislocations in lattice-mismatched epitaxial films. *Critical Reviews in Solid State and Material Sciences*, 17(6):507–546, 1992.

[92] Tony G Ivanov, James Weil, Pankaj B Shah, A Glen Birdwell, Khamsouk Kingkeo, and Edward A Viveiros. Diamond rf transistor technology with f t= 41 ghz and fmax= 44 ghz. In *2018 IEEE/MTT-S International Microwave Symposium-IMS*, pages 1461–1463. IEEE, 2018.

[93] Mohammad Tariq Jan, Farooq Ahmad, Nor Hisham B Hamid, Mohd Haris B Md Khir, Muhammad Shoaib, and Khalid Ashraf. Experimental investigation of temperature and relative humidity effects on resonance frequency and quality factor of cmos-mems paddle resonator. *Microelectronics Reliability*, 63:82–89, 2016.

[94] Kwang S Jeong, Jiang Tang, Huan Liu, Jihye Kim, Andrew W Schaefer, Kyle Kemp, Larissa Levina, Xihua Wang, Sjoerd Hoogland, Ratan Debnath, et al. Enhanced mobility-lifetime products in pbs colloidal quantum dot photovoltaics. *ACS nano*, 6(1):89–99, 2012.

[95] S-W Jeong, HJ Lee, KS Kim, MT You, Y Roh, T Noguchi, W Xianyu, and J Jung. Effects of annealing temperature on the characteristics of ald-deposited hfo2 in mim capacitors. *Thin solid films*, 515(2):526–530, 2006.

[96] Bing Ji, Volker Pickert, Wenping Cao, and Bashar Zahawi. In situ diagnostics and prognostics of wire bonding faults in igbt modules for electric vehicle drives. *IEEE Transactions on Power Electronics*, 28(12):5568–5577, 2013.

[97] Cunjie Jia, Jie Huang, Linglong Fu, Yuhan Xiang, Yukang Chen, Hongtao Yue, Qian Zhao, Wenwen Gu, Yongfeng Wu, and Jilong Zhang. A novel differential capacitive humidity sensor on siw re-entrant cavity microwave resonators with pedot: Pss film. *IEEE Sensors Journal*, 22(7):6576–6585, 2022.

[98] Huaxing Jiang, Chao Liu, Kar Wei Ng, Chak Wah Tang, and Kei May Lau. High-performance algan/gan/si power moshemts with zro 2 gate dielectric. *IEEE Transactions on Electron Devices*, 65(12):5337–5342, 2018.

[99] John Bertrand Johnson. Thermal agitation of electricity in conductors. *Physical review*, 32(1):97, 1928.

[100] Aline Jolivet, Christophe Labbé, Cédric Frilay, Olivier Debieu, Philippe Marie, Bryan Horcholle, Franck Lemarié, Xavier Portier, Clara Grygiel, Sylvain Duprey, et al. Structural, optical, and electrical properties of tio2 thin films deposited by ald: Impact of the substrate, the deposited thickness and the deposition temperature. *Applied Surface Science*, 608:155214, 2023.

[101] Amr Kamel, Samed Kocer, Lyazzat Mukhangaliyeva, Resul Saritas, Ahmet Gulsaran, Alaa Elhady, Mohamed Basha, Parsin Hajireza, Mustafa Yavuz, and Eihab Abdel-Rahman. Resonant adaptive mems mirror. In *Actuators*, volume 11, page 224. MDPI, 2022.

[102] Devrez M Karabacak, Sywert H Brongersma, and Mercedes Crego-Calama. Enhanced sensitivity volatile detection with low power integrated micromechanical resonators. *Lab on a Chip*, 10(15):1976–1982, 2010.

[103] Danny A Kassie and David Elata. Harmonic biasing in a double-sided comb-drive resonator, for resolving feed-through issues in low-power driving. *Sensors and Actuators A: Physical*, 332:113031, 2021.

[104] NL Kazanskiy, SN Khonina, and MA Butt. Plasmonic sensors based on metal-insulator-metal waveguides for refractive index sensing applications: A brief review. *Physica E: Low-dimensional systems and nanostructures*, 117:113798, 2020.

[105] Ariadne P Kerasidou, Martha A Botzakaki, Nikolaos Xanthopoulos, Stella Kennou, Spyridon Ladas, Stavroula N Georga, and Christoforos A Krontiras. Probing the properties of atomic layer deposited zro2 films on p-germanium substrates. *Journal of Vacuum Science & Technology A*, 31(1), 2013.

[106] AA Khan, Gaurav Jayaswal, FA Gahaffar, and Atif Shamim. Metal-insulator-metal diodes with sub-nanometre surface roughness for energy-harvesting applications. *Microelectronic Engineering*, 181:34–42, 2017.

[107] Dongyoon Khim, Kang-Jun Baeg, Juhwan Kim, Jun-Seok Yeo, Minji Kang, Paul SK Amegadzea, Mu-Gyeom Kim, Joonhyuk Cho, Jung Hun Lee, Dong-Yu Kim, et al.

Electron injection enhancement by a cs-salt interlayer in ambipolar organic field-effect transistors and complementary circuits. *Journal of Materials Chemistry*, 22(33):16979–16985, 2012.

[108] David K Kim, Yuming Lai, Benjamin T Diroll, Christopher B Murray, and Cherie R Kagan. Flexible and low-voltage integrated circuits constructed from high-performance nanocrystal transistors. *Nature communications*, 3(1):1216, 2012.

[109] Seokbeom Kim, Bora Lee, Yeowon Yoon, Thomas Thundat, and Jungchul Lee. Static and dynamic operation of metal-coated hydrogel cantilever humidity sensors based on hygroscopic mismatch. In *2017 19th International Conference on Solid-State Sensors, Actuators and Microsystems (TRANSDUCERS)*, pages 300–302. IEEE, 2017.

[110] Edward C Kinzel, Robert L Brown, James C Ginn, Brian A Lail, Brian A Slovick, and Glenn D Boreman. Design of an mom diode-coupled frequency-selective surface. *Microwave and Optical Technology Letters*, 55(3):489–493, 2013.

[111] Casey J Kirkpatrick, Bongmook Lee, Rahul Suri, Xiangyu Yang, and Veena Misra. Atomic layer deposition of SiO_2 for algan/gan mos-hfets. *IEEE electron device letters*, 33(9):1240–1242, 2012.

[112] LP Kiss, G Szeidl, and A Messaoudi. Vibration of an axially loaded heterogeneous fixed–fixed beam with an intermediate roller support. *Journal of the Brazilian Society of Mechanical Sciences and Engineering*, 44(10):461, 2022.

[113] Ethan JD Klem, Harnik Shukla, Sean Hinds, Dean D MacNeil, Larissa Levina, and Edward H Sargent. Impact of dithiol treatment and air annealing on the conductivity, mobility, and hole density in pbs colloidal quantum dot solids. *Applied Physics Letters*, 92(21), 2008.

[114] Samed Kocer, Lyazzat Mukhangaliyeva, Resul Saritas, Ahmet Gulsaran, Alaa Elhady, Kevan Bell, Amr Kamel, Mohamed Basha, Taylan Das, Muhammed Kayaharman, et al. Resonant varifocal mems mirror. In *2022 IEEE 35th International Conference on Micro Electro Mechanical Systems Conference (MEMS)*, pages 963–966. IEEE, 2022.

[115] Roope Kokkoniemi, J-P Girard, Dibyendu Hazra, Antti Laitinen, Joonas Govenius, RE Lake, Iiro Sallinen, Visa Vesterinen, Matti Partanen, JY Tan, et al. Bolometer operating at the threshold for circuit quantum electrodynamics. *Nature*, 586(7827):47–51, 2020.

[116] S Komiyama, O Astafiev, V Antonov, T Kutsuwa, and H Hirai. A single-photon detector in the far-infrared range. *Nature*, 403(6768):405–407, 2000.

[117] Gerasimos Konstantatos and Edward H Sargent. Solution-processed quantum dot photodetectors. *Proceedings of the IEEE*, 97(10):1666–1683, 2009.

[118] MA Korhonen and Christine A Paszkiet. X-ray determination of the residual stresses in thin aluminum films deposited on silicon substrates. *Scripta metallurgica*, 23(8):1449–1453, 1989.

[119] Ghenadii Korotcenkov. *Handbook of Humidity Measurement, Volume 3: Sensing Materials and Technologies*. CRC Press, 2020.

[120] Herbert Kroemer. Nobel lecture: Quasielectric fields and band offsets: teaching electrons new tricks. *Reviews of modern physics*, 73(3):783, 2001.

[121] Gwang Mo Ku, Eunho Lee, Boseok Kang, Jung Hun Lee, Kilwon Cho, and Wi Hyoung Lee. Relationship between the dipole moment of self-assembled monolayers incorporated in graphene transistors and device electrical stabilities. *RSC advances*, 7(43):27100–27104, 2017.

[122] Xianhao Le, Yihan Liu, Li Peng, Jintao Pang, Zhen Xu, Chao Gao, and Jin Xie. Surface acoustic wave humidity sensors based on uniform and thickness controllable graphene oxide thin films formed by surface tension. *Microsystems & nanoengineering*, 5(1):36, 2019.

[123] Xianhao Le, Jintao Pang, Xuying Chen, Dongsheng Li, Zhen Xu, Chao Gao, and Jin Xie. Highly sensitive ain surface acoustic wave humidity sensor based on uniform graphene oxide thin film formed by surface tension. In *2018 IEEE 13th Annual International Conference on Nano/Micro Engineered and Molecular Systems (NEMS)*, pages 173–176. IEEE, 2018.

[124] Xianhao Le, Li Peng, Jintao Pang, Zhen Xu, Chao Gao, and Jin Xie. Humidity sensors based on aln microcantilevers excited at high-order resonant modes and sensing layers of uniform graphene oxide. *Sensors and Actuators B: Chemical*, 283:198–206, 2019.

[125] Xuan-Luc Le, Xuan-Bach Le, Yuhwan Hwangbo, Jiho Joo, Gwang-Mun Choi, Yong-Sung Eom, Kwang-Seong Choi, and Sung-Hoon Choa. Mechanical reliability assessment of a flexible package fabricated using laser-assisted bonding. *Micromachines*, 14(3):601, 2023.

[126] Bongmook Lee, Casey Kirkpatrick, Young-Hwan Choi, Xiangyu Yang, Yalin Wang, Xingchen Yang, Alex Huang, and Veena Misra. Impact of ald gate dielectrics (sio2, hfo2, and sio2/hah) on device electrical characteristics and reliability of algan/gan moshfet devices. *ECS Transactions*, 41(3):445, 2011.

[127] Han-Sheng Lee. Metal-oxide-semiconductor instability produced by electron-beam evaporation of aluminum gates. *IEEE Transactions on Electron Devices*, 25(7):795–799, 1978.

[128] Dongsheng Li, Xianhao Le, Jintao Pang, and Jin Xie. An aln resonant microcantilever humidity sensor by activating specific sets of top electrodes based on graphene oxide. In *2019 20th International Conference on Solid-State Sensors, Actuators and Microsystems & Eurosensors XXXIII (TRANSDUCERS & EUROSENSORS XXXIII)*, pages 1337–1340. IEEE, 2019.

[129] Huijin Li, Dedong Han, Zhuang Yi, Junchen Dong, Shengdong Zhang, Xing Zhang, and Yi Wang. High-performance zno thin-film transistors prepared by atomic layer deposition. *IEEE Transactions on Electron Devices*, 66(7):2965–2970, 2019.

[130] Jing Li, Yong Zhou, Yanjie Wang, Sen Zhou, Ruijie Zhang, Yuhang Wang, and Zhigang Zang. Improving humidity sensing of black phosphorus nanosheets by co-doping benzyl viologen and au nanoparticles. *Journal of The Electrochemical Society*, 169(1):017513, 2022.

[131] Mengqi Li and Dongqing Li. Microvalve using electrokinetic motion of electrically induced janus droplet. *Analytica Chimica Acta*, 1021:85–94, 2018.

[132] Xiangrong Li, Qiulin Tan, Li Qin, Lei Zhang, Xiaorui Liang, and Xiawen Yan. A high-sensitivity mos2/graphene oxide nanocomposite humidity sensor based on surface acoustic wave. *Sensors and Actuators A: Physical*, 341:113573, 2022.

[133] Xueqin Li, Linchun Gao, Tao Ni, Jingnan Zhou, Xiaojing Li, Yifan Li, Lida Xu, Runjian Wang, Chuanbin Zeng, Bo Li, et al. Analysis of degradation of electromigration reliability of au-al and opm wire bonded contacts at 250° c using resistance monitoring method. *Micromachines*, 14(3):640, 2023.

[134] Zhijia Li, Muzhou Teng, Ronghua Yang, Feiyan Lin, Yu Fu, Weiqiang Lin, Judun Zheng, Xiaoping Zhong, Xiaodong Chen, Bin Yang, et al. Sb-doped wo3 based qcm humidity sensor with self-recovery ability for real-time monitoring of respiration and wound. *Sensors and Actuators B: Chemical*, 361:131691, 2022.

[135] Zhaokang Liang, Yao Wen, Zhi Zhang, Zihao Liang, Zefeng Xu, and Yu-Sheng Lin. Plasmonic metamaterial using metal-insulator-metal nanogratings for high-sensitive refraction index sensor. *Results in Physics*, 15:102602, 2019.

[136] Sang Chul Lim, Seong Hyun Kim, Jung Hun Lee, Mi Kyung Kim, Taehyoung Zyung, et al. Surface-treatment effects on organic thin-film transistors. *Synthetic Metals*, 148(1):75–79, 2005.

[137] Jianbin Lin, Naibo Gao, Jiamin Liu, Zhixiang Hu, Han Fang, Xianhua Tan, Huayao Li, Hao Jiang, Huan Liu, Tielin Shi, et al. Superhydrophilic cu (oh) 2 nanowire-based qcm transducer with self-healing ability for humidity detection. *Journal of Materials Chemistry A*, 7(15):9068–9077, 2019.

[138] Huan Liu, Min Li, Oleksandr Voznyy, Long Hu, Qiuyun Fu, Dongxiang Zhou, Zhe Xia, Edward H Sargent, and Jiang Tang. Physically flexible, rapid-response gas sensor based on colloidal quantum dot solids. *Advanced Materials*, 26(17):2718–2724, 2014.

[139] Jihang Liu, Zhan Zhao, Zhen Fang, Zhenyu Liu, Yusi Zhu, and Lidong Du. High-performance fbar humidity sensor based on the pi film as the multifunctional layer. *Sensors and Actuators B: Chemical*, 308:127694, 2020.

[140] Jing Liu, Peilin Liu, Dengyang Chen, Tailong Shi, Xixi Qu, Long Chen, Tong Wu, Jiangping Ke, Kao Xiong, Mingyu Li, et al. A near-infrared colloidal quantum dot imager with monolithically integrated readout circuitry. *Nature Electronics*, 5(7):443–451, 2022.

[141] Junqing Liu, Junpeng Li, Jianzhuo Wu, and Jiaming Sun. Structure and dielectric property of high-k zro 2 films grown by atomic layer deposition using tetrakis (dimethylamido) zirconium and ozone. *Nanoscale Research Letters*, 14:1–12, 2019.

[142] Mengxia Liu, Nuri Yazdani, Maksym Yarema, Maximilian Jansen, Vanessa Wood, and Edward H Sargent. Colloidal quantum dot electronics. *Nature Electronics*, 4(8):548–558, 2021.

[143] Yuan Liu, Hui Huang, Lingling Wang, Daoping Cai, Bin Liu, Dandan Wang, Qiuhong Li, and Taihong Wang. Electrospun ceo2 nanoparticles/pvp nanofibers based high-frequency surface acoustic wave humidity sensor. *Sensors and Actuators B: Chemical*, 223:730–737, 2016.

[144] Priyanka Londhe, Nandu B Chaure, and Anjali Athawale. Interface engineering of gate dielectrics with multifunctional self-assembled monolayers in copper phthalocyanine based organic field-effect transistors. *Materials Science and Engineering: B*, 273:115397, 2021.

[145] Qianbo Lu, Weidong Fang, Chen Wang, Jian Bai, Yuan Yao, Jiaxiao Chen, Xiang Xu, and Wei Huang. Investigation of a complete squeeze-film damping model for mems devices. *Microsystems & Nanoengineering*, 7(1):54, 2021.

[146] Yin-Fen Ma, You-Mei Wang, Jia Wen, Ao Li, Xiao-Liang Li, Mei Leng, Yong-Biao Zhao, and Zheng-Hong Lu. Review of roll-to-roll fabrication techniques for colloidal quantum dot solar cells. *Journal of Electronic Science and Technology*, 21(1):100189, 2023.

[147] Ravi Mahajan, Zhiguo Qian, Ram S Viswanath, Sriram Srinivasan, Kemal Aygün, Wei-Lun Jen, Sujit Sharan, and Ashish Dhall. Embedded multidie interconnect bridge—a localized, high-density multichip packaging interconnect. *IEEE transactions on components, packaging and manufacturing technology*, 9(10):1952–1962, 2019.

[148] LA Majewski, Martin Grell, SD Ogier, and Janos Veres. A novel gate insulator for flexible electronics. *Organic Electronics*, 4(1):27–32, 2003.

[149] Leszek Artur Majewski, Raoul Schroeder, and Martin Grell. Low-voltage, high-performance organic field-effect transistors with an ultra-thin tio2 layer as gate insulator. *Advanced functional materials*, 15(6):1017–1022, 2005.

[150] Kayaku Advanced Materials. *LOR/PMGI Technical Data Sheet, Rev. B*. Kayaku Advanced Materials.

[151] Sofiane Ben Mbarek, Nouha Alcheikh, Hassen M Ouakad, and Mohammad I Younis. Highly sensitive low field lorentz-force mems magnetometer. *Scientific Reports*, 11(1):21634, 2021.

[152] SA McDonald, PW Cyr, L Levina, and EH Sargent. Photoconductivity from pbsnanocrystal/ semiconducting polymer composites for solution-processible, quantum-size tunableinfrared photodetectors. *Applied physics letters*, 85(11):2089–2091, 2004.

[153] Vamsi C Meesala, Muhammad R Hajj, and Eihab Abdel-Rahman. Bifurcation-based mems mass sensors. *International Journal of Mechanical Sciences*, 180:105705, 2020.

[154] Shengli Mi, Haitao Pu, Shengyue Xia, and Wei Sun. A minimized valveless electromagnetic micropump for microfluidic actuation on organ chips. *sensors and actuators A: Physical*, 301:111704, 2020.

[155] Herbert B Michaelson. The work function of the elements and its periodicity. *Journal of applied physics*, 48(11):4729–4733, 1977.

[156] Elisa M Miller, Daniel M Kroupa, Jianbing Zhang, Philip Schulz, Ashley R Marshall, Antoine Kahn, Stephan Lany, Joseph M Luther, Matthew C Beard, Craig L Perkins, et al. Revisiting the valence and conduction band size dependence of pbs quantum dot thin films. *ACS nano*, 10(3):3302–3311, 2016.

[157] Kissan Mistry, Viet Huong Nguyen, Mohamed Arabi, Khaled H Ibrahim, Hatameh Asgarimoghaddam, Mustafa Yavuz, David Muñoz-Rojas, Eihab Abdel-Rahman, and Kevin P Musselman. Highly sensitive self-actuated zinc oxide resonant microcantilever humidity sensor. *Nano Letters*, 22(8):3196–3203, 2022.

[158] Kissan Mistry, Viet Huong Nguyen, Mohamed Arabi, Khaled H Ibrahim, Hatameh Asgarimoghaddam, Mustafa Yavuz, David Muñoz-Rojas, Eihab Abdel-Rahman, and Kevin P Musselman. Highly sensitive self-actuated zinc oxide resonant microcantilever humidity sensor. *Nano letters*, 22(8):3196–3203, 2022.

[159] Gordon E Moore et al. Cramming more components onto integrated circuits, 1965.

[160] Akshay Moudgil, Sanjay Singh, Nishant Mishra, Prashant Mishra, and Samaresh Das. Mos2/tio2 hybrid nanostructure-based field-effect transistor for highly sensitive, selective, and rapid detection of gram-positive bacteria. *Advanced Materials Technologies*, 5(1):1900615, 2020.

[161] Ali H Nayfeh, Mohammad I Younis, and Eihab M Abdel-Rahman. Dynamic pull-in phenomenon in mems resonators. *Nonlinear dynamics*, 48:153–163, 2007.

[162] I Novodchuk, M Kayaharman, I Prassas, A Soosaipillai, R Karimi, IA Goldthorpe, E Abdel-Rahman, J Sanderson, EP Diamandis, M Bajcsy, et al. Electronic field effect detection of sars-cov-2 n-protein before the onset of symptoms. *Biosensors and Bioelectronics*, 210:114331, 2022.

[163] Shinji Okazaki. Resolution limits of optical lithography. *Journal of Vacuum Science & Technology B: Microelectronics and Nanometer Structures Processing, Measurement, and Phenomena*, 9(6):2829–2833, 1991.

[164] Rocio Ponce Ortiz, Antonio Facchetti, and Tobin J Marks. High-k organic, inorganic, and hybrid dielectrics for low-voltage organic field-effect transistors. *Chemical reviews*, 110(1):205–239, 2010.

[165] Dilek Nur Ozen, Bora Timurkutluk, and Kemal Altinisik. Effects of operation temperature and reactant gas humidity levels on performance of pem fuel cells. *Renewable and Sustainable Energy Reviews*, 59:1298–1306, 2016.

[166] Dogu Ozyigit, Farman Ullah, Ahmet Gulsaran, Bersu Bastug Azer, Ahmed Shahin, Kevin Musselman, Michal Bajcsy, and Mustafa Yavuz. Manufacturing of quantum-tunneling mim nanodiodes via rapid atmospheric cvd in terahertz band. *Scientific Reports*, 13(1):20733, 2023.

[167] Hyun Hee Park, Pil Soo Kang, Gyu Tae Kim, and Jeong Sook Ha. Effect of gate dielectrics on the device performance of sno2 nanowire field effect transistors. *Applied Physics Letters*, 96(10), 2010.

[168] Sangtak Park and Eihab Abdel-Rahman. Low voltage electrostatic actuation and displacement measurement through resonant drive circuit. In *International Design Engineering Technical Conferences and Computers and Information in Engineering Conference*, volume 45042, pages 119–126. American Society of Mechanical Engineers, 2012.

[169] Yongsup Park, V Choong, Yongli Gao, Bing R Hsieh, and Ching Wan Tang. Work function of indium tin oxide transparent conductor measured by photoelectron spectroscopy. *Applied physics letters*, 68(19):2699–2701, 1996.

[170] VM Paviot, JJ Vlassak, and WD Nix. Measuring the mechanical properties of thin metal films by means of bulge testing of micromachined windows. *MRS Online Proceedings Library (OPL)*, 356:579, 1994.

[171] Vladimir Pejović, Epimitheas Georgitzikis, Jiwon Lee, Itai Lieberman, David Cheyns, Paul Heremans, and Paweł E Malinowski. Infrared colloidal quantum dot image sensors. *IEEE Transactions on Electron Devices*, 69(6):2840–2850, 2021.

[172] B Pelz and G Moddel. Demonstration of distributed capacitance compensation in a metal-insulator-metal infrared rectenna incorporating a traveling-wave diode. *Journal of Applied Physics*, 125(23):234502, 2019.

[173] Prakash Periasamy, Joseph J Berry, Arrelaine A Dameron, Jeremy D Bergeson, David S Ginley, Ryan P O'Hayre, and Philip A Parilla. Fabrication and characterization of mim diodes based on nb/nb2o5 via a rapid screening technique. *Advanced Materials*, 23(27):3080–3085, 2011.

[174] Vitaly Podzorov. Organic single crystals: Addressing the fundamentals of organic electronics. *MRS bulletin*, 38(1):15–24, 2013.

[175] Marcel W Pruessner, Todd H Stievater, Mike S Ferraro, William S Rabinovich, Jennifer L Stepnowski, and R Andrew McGill. Waveguide micro-opto-electro-mechanical resonant chemical sensors. *Lab on a Chip*, 10(6):762–768, 2010.

[176] Pengjia Qi, Tong Zhang, Jieren Shao, Bai Yang, Teng Fei, and Rui Wang. A qcm humidity sensor constructed by graphene quantum dots and chitosan composites. *Sensors and Actuators A: Physical*, 287:93–101, 2019.

[177] Yan Qiao, Alaaeldin Elhady, Mohamed Arabi, Eihab Abdel-Rahman, and Wenming Zhang. Thermal noise-driven resonant sensors. *Microsystems & Nanoengineering*, 10(1):90, 2024.

[178] Tianling Qin, Ge Mu, Pengfei Zhao, Yimei Tan, Yanfei Liu, Shuo Zhang, Yuning Luo, Qun Hao, Menglu Chen, and Xin Tang. Mercury telluride colloidal quantum-dot focal plane array with planar pn junctions enabled by in situ electric field–activated doping. *Science advances*, 9(28):eadg7827, 2023.

[179] Xiaotun Qiu, Rui Tang, Jie Zhu, Jonathon Oiler, Cunjiang Yu, Ziyu Wang, and Hongyu Yu. Experiment and theoretical analysis of relative humidity sensor based on film bulk acoustic-wave resonator. *Sensors and Actuators B: Chemical*, 147(2):381–384, 2010.

[180] Sasan Rahmanian, Shahrokh Hosseini-Hashemi, and Masoud Rezaei. Out-of-plane motion detection in encapsulated electrostatic mems gyroscopes: Principal parametric resonance. *International Journal of Mechanical Sciences*, 190:106022, 2021.

[181] Ehsan Ranjbar, Mostafa Yaghoubi, and Amir Abolfazl Suratgar. Adaptive sliding mode controller design for a tunable capacitor susceptible to unknown upper-bounded uncertainties and disturbance. *Iranian Journal of Science and Technology, Transactions of Electrical Engineering*, 44:327–346, 2020.

[182] Singiresu S Rao. *Vibration of continuous systems*. John Wiley & Sons, 2019.

[183] Tobias Rauch, Michaela Böberl, Sandro F Tedde, Jens Fürst, Maksym V Kovalenko, Günter Hesser, Uli Lemmer, Wolfgang Heiss, and Oliver Hayden. Near-infrared imaging with quantum-dot-sensitized organic photodiodes. *nature photonics*, 3(6):332–336, 2009.

[184] Zeyang Ren, Dandan Lv, Jiamin Xu, Jinfeng Zhang, Jincheng Zhang, Kai Su, Chunfu Zhang, and Yue Hao. High temperature (300° c) ald grown al2o3 on hydrogen terminated diamond: Band offset and electrical properties of the mosfets. *Applied Physics Letters*, 116(1), 2020.

[185] Antoni Rogalski. Progress in quantum dot infrared photodetectors. *Quantum Dot Photodetectors*, pages 1–74, 2021.

[186] Antoni Rogalski. Scaling infrared detectors—status and outlook. *Reports on Progress in Physics*, 85(12):126501, 2022.

[187] Michael J Sailor. *Porous silicon in practice: preparation, characterization and applications*. John Wiley & Sons, 2012.

[188] Muhammad Mubasher Saleem, Shayaan Saghir, Syed Ali Raza Bukhari, Amir Hamza, Rana Iqtidar Shakoor, and Shafaat Ahmed Bazaz. A low-g mems accelerometer with high sensitivity, low nonlinearity and large dynamic range based on mode-localization of 3-dof weakly coupled resonators. *Micromachines*, 12(3):310, 2021.

[189] Resul Saritas, Majed Al-Ghamdi, Taylan Memik Das, Omar Rasheed, Samed Kocer, Ahmet Gulsaran, Asif Abdullah Khan, Md Masud Rana, Mahmoud Khater, Muhammed Kayaharman, et al. Nano groove and prism-structured triboelectric nanogenerators. *Micromachines*, 14(9):1707, 2023.

[190] Günter Sauerbrey. Verwendung von schwingquarzen zur wägung dünner schichten und zur mikrowägung. *Zeitschrift für physik*, 155:206–222, 1959.

[191] Abraham Savitzky and Marcel JE Golay. Smoothing and differentiation of data by simplified least squares procedures. *Analytical chemistry*, 36(8):1627–1639, 1964.

[192] Silvan Schmid, Luis Guillermo Villanueva, and Michael Lee Roukes. *Responsivity and Sensitivity*, chapter 6, pages 175–203. Springer International Publishing, Cham, 2023.

[193] Steven C Seel and Carl V Thompson. Tensile stress generation during island coalescence for variable island-substrate contact angle. *Journal of applied physics*, 93(11):9038–9042, 2003.

[194] Andi Setiono, Michael Fahrbach, Alexander Deutschinger, Ernest J Fantner, Christian H Schwalb, Iqbal Syamsu, Hutomo Suryo Wasisto, and Erwin Peiner. Performance of an electrothermal mems cantilever resonator with fano-resonance annoyance under cigarette smoke exposure. *Sensors*, 21(12):4088, 2021.

[195] Li Shan, Mingyang Cui, and J Mark Meacham. Spray characteristics of an ultrasonic microdroplet generator with a continuously variable operating frequency. *The Journal of the Acoustical Society of America*, 150(2):1300–1310, 2021.

[196] Peng-Zhi Shao, Hai-Ming Zhao, Hui-Wen Cao, Xue-Feng Wang, Yu Pang, Yu-Xing Li, Ning-Qin Deng, Jing Zhang, Guang-Yu Zhang, Yi Yang, et al. Enhancement of carrier mobility in mos2 field effect transistors by a sio2 protective layer. *Applied Physics Letters*, 108(20), 2016.

[197] Lei Sheng, Chen Dajing, and Chen Yuquan. A surface acoustic wave humidity sensor with high sensitivity based on electrospun mwcnt/nafion nanofiber films. *Nanotechnology*, 22(26):265504, 2011.

[198] CJR Sheppard. Microscopy overview. *Encyclopedia of Modern Optics*, 3:61–68, 2004.

[199] Naoki Shinohara. Trends in wireless power transfer: Wpt technology for energy harvesting, mllimeter-wave/thz rectennas, mimo-wpt, and advances in near-field wpt applications. *IEEE microwave magazine*, 22(1):46–59, 2020.

[200] Shilpi Shriwastava and CC Tripathi. Metal–insulator–metal diodes: A potential high frequency rectifier for rectenna application. *Journal of Electronic Materials*, 48:2635–2652, 2019.

[201] Tejinder Singh, Navjot K Khaira, and Raafat R Mansour. Thermally actuated soi rf mems-based fully integrated passive reflective-type analog phase shifter for mmwave applications. *IEEE Transactions on Microwave Theory and Techniques*, 69(1):119–131, 2020.

[202] Rafal Sliz, Marc Lejay, James Z Fan, Min-Jae Choi, Sachin Kinge, Sjoerd Hoogland, Tapio Fabritius, F Pelayo García de Arquer, and Edward H Sargent. Stable colloidal quantum dot inks enable inkjet-printed high-sensitivity infrared photodetectors. *ACS nano*, 13(10):11988–11995, 2019.

[203] Pingyue Song and Hossein Hashemi. Rf filter synthesis based on passively coupled n-path resonators. *IEEE Journal of Solid-State Circuits*, 54(9):2475–2486, 2019.

[204] DR Southworth, LM Bellan, Y Linzon, Harold G Craighead, and JM Parpia. Stress-based vapor sensing using resonant microbridges. *Applied physics letters*, 96(16), 2010.

[205] HP Stabler. Gallium-indium eutectic. *American Journal of Physics*, 28(8):x–x, 1960.

[206] Stefano Stassi, Valentina Cauda, Sonia Fiorilli, and Carlo Ricciardi. Surface area enhancement by mesoporous silica deposition on microcantilever sensors for small molecule detection. *Journal of Materials Chemistry C*, 3(48):12507–12513, 2015.

[207] Brian R Strohmeier. An esca method for determining the oxide thickness on aluminum alloys. *Surface and interface analysis*, 15(1):51–56, 1990.

[208] Yunpeng Su, Cuiping Li, Mingji Li, Hongji Li, Sheng Xu, Lirong Qian, and Baohe Yang. Surface acoustic wave humidity sensor based on three-dimensional architecture graphene/pva/sio2 and its application for respiration monitoring. *Sensors and Actuators B: Chemical*, 308:127693, 2020.

[209] Chi Sun, Tingting Hao, Junjie Li, Haitao Ye, and Changzhi Gu. The design and performance of hydrogen-terminated diamond metal-oxide-semiconductor field-effect transistors with high k oxide hfo2. *Micro and Nano Engineering*, 6:100046, 2020.

[210] Ata Taghipour and Hamid Heidarzadeh. Design and analysis of highly sensitive lspr-based metal–insulator–metal nano-discs as a biosensor for fast detection of sars-cov-2. In *Photonics*, volume 9, page 542. MDPI, 2022.

[211] Xin Tang, Matthew M Ackerman, Menglu Chen, and Philippe Guyot-Sionnest. Dual-band infrared imaging using stacked colloidal quantum dot photodiodes. *Nature photonics*, 13(4):277–282, 2019.

[212] NM Tashtoush, JDN Cheeke, and N Eddy. Surface acoustic wave humidity sensor based on a thin polyxio film. *Sensors and Actuators B: Chemical*, 49(3):218–225, 1998.

[213] Serdar B Tekin, AD Weerakkody, N Sedghi, Stephen Hall, M Werner, JS Wrench, PR Chalker, and IZ Mitrovic. Single and triple insulator metal-insulator-metal diodes for infrared rectennas. *Solid-State Electronics*, 185:108096, 2021.

[214] Stuart R Thomas, Pichaya Pattanasattayavong, and Thomas D Anthopoulos. Solution-processable metal oxide semiconductors for thin-film transistor applications. *Chemical Society Reviews*, 42(16):6910–6923, 2013.

[215] John A Thornton. Influence of substrate temperature and deposition rate on structure of thick sputtered cu coatings. *Journal of Vacuum Science and Technology*, 12(4):830–835, 1975.

[216] Stephen P. Timoshenko and James M. Gere. *Theory of elastic stability*. Dover Civil and Mechanical Engineering. Dover Publications, Inc., Mineola, New York, 2009.

[217] Badri Tiwari, Jeffrey A Bean, Gergő Szakmány, Gary H Bernstein, Patrick Fay, and Wolfgang Porod. Controlled etching and regrowth of tunnel oxide for antenna-coupled metal-oxide-metal diodes. *Journal of Vacuum Science & Technology B: Microelectronics and Nanometer Structures Processing, Measurement, and Phenomena*, 27(5):2153–2160, 2009.

[218] Le-Giang Tran, Hyouk-Kyu Cha, and Woo-Tae Park. Rf power harvesting: a review on designing methodologies and applications. *Micro and Nano Systems Letters*, 5:1–16, 2017.

[219] Toshihiro Tsuji, Toru Oizumi, Hideyuki Fukushi, Nobuo Takeda, Shingo Akao, Yusuke Tsukahara, and Kazushi Yamanaka. Development of ball surface acoustic wave trace moisture analyzer using burst waveform undersampling circuit. *Review of Scientific Instruments*, 89(5), 2018.

[220] JR Tucker and MF Millea. Photon detection in nonlinear tunneling devices. *Applied Physics Letters*, 33(7):611–613, 1978.

[221] W Merlijn Van Spengen. Mems reliability from a failure mechanisms perspective. *Microelectronics Reliability*, 43(7):1049–1060, 2003.

[222] BJ Van Wees, H Van Houten, CWJ Beenakker, J Gr Williamson, LP Kouwenhoven, D Van der Marel, and CT Foxon. Quantized conductance of point contacts in a two-dimensional electron gas. *Physical Review Letters*, 60(9):848, 1988.

[223] Suresh Vasimalla, Nimmakayala VV Subbarao, Murali Gedda, Dipak K Goswami, and Parameswar Krishnan Iyer. Effects of dielectric material, hmds layer, and channel length on the performance of the perylenediimide-based organic field-effect transistors. *ACS omega*, 2(6):2552–2560, 2017.

[224] J Verd, M Sansa, A Uranga, F Perez-Murano, J Segura, and N Barniol. Metal microelectromechanical oscillator exhibiting ultra-high water vapor resolution. *Lab on a Chip*, 11(16):2670–2672, 2011.

[225] Denis V Vertyanov, Igor A Belyakov, Sergey P Timoshenkov, Anna V Borisova, and Vitaly N Sidorenko. Effects of gold-aluminum intermetallic compounds on chip wire bonding interconnections reliability. In *2020 IEEE Conference of Russian Young Researchers in Electrical and Electronic Engineering (EIConRus)*, pages 2216–2220. IEEE, 2020.

[226] Annie Wang, Ioannis Kymissis, Vladimir Bulovic, and Akintunde Ibitayo Akinwande. Engineering density of semiconductor-dielectric interface states to modulate threshold voltage in ofets. *IEEE Transactions on Electron Devices*, 53(1):9–13, 2005.

[227] Gaoqiang Wang, Andreas Rühling, Saeed Amirjalayer, Marek Knor, Johannes Bruno Ernst, Christian Richter, Hong-Jun Gao, Alexander Timmer, Hong-Ying Gao, Nikos L Doltsinis, et al. Ballbot-type motion of n-heterocyclic carbenes on gold surfaces. *Nature Chemistry*, 9(2):152–156, 2017.

[228] Kun-Lun Wang, Yan-Qing Xin, Ji-Feng Zhao, Shu-Mei Song, Sheng-Chi Chen, Ying-Bo Lu, and Hui Sun. High transmittance in ir region of conductive ito/azo multilayers deposited by rf magnetron sputtering. *Ceramics International*, 44(6):6769–6774, 2018.

[229] Yanjie Wang, Yong Zhou, Guangzhong Xie, Jing Li, Yuhang Wang, Xiaoyu Liu, and Zhigang Zang. Dual resistance and impedance investigation: ultrasensitive and stable humidity detection of molybdenum disulfide nanosheet-polyethylene oxide hybrids. *ACS Applied Materials & Interfaces*, 13(21):25250–25259, 2021.

[230] Chenyang Wu, Junqiang Wang, Xiaofei Liu, Mengwei Li, Zehua Zhu, and Yue Qi. Au wire ball welding and its reliability test for high-temperature environment. *Micromachines*, 13(10):1603, 2022.

[231] Pan Xia, Sasa Wang, Yiqing Chen, Ahmet Gulsaran, Yangning Zhang, Maral Vafaie, Muhammad Imran, Amin Morteza Najarian, Yanjiang Liu, Hyeongwoo Ban, et al. Improved facet and edge passivation in near-infrared iii-v colloidal quantum dot photodetectors. *Advanced Materials*, 37(18):2419020, 2025.

[232] Jiushuai Xu, Maik Bertke, Xiaojing Li, Haibo Mu, Hao Zhou, Feng Yu, Gerry Hamdana, Angelika Schmidt, Heiko Bremers, and Erwin Peiner. Fabrication of zno nanorods and chitosan@ zno nanorods on mems piezoresistive self-actuating silicon microcantilever for humidity sensing. *Sensors and Actuators B: Chemical*, 273:276–287, 2018.

[233] Jiushuai Xu, Maik Bertke, Xiaojing Li, Haibo Mu, Hao Zhou, Feng Yu, Gerry Hamdana, Angelika Schmidt, Heiko Bremers, and Erwin Peiner. Fabrication of zno nanorods and chitosan@ zno nanorods on mems piezoresistive self-actuating silicon microcantilever for humidity sensing. *Sensors and Actuators B: Chemical*, 273:276–287, 2018.

[234] Yanping Xu, Xian Zhao, Yongfu Li, Zengguang Qin, Yuxi Pang, and Zhaojun Liu. Simultaneous measurement of relative humidity and temperature based on forward brillouin scattering in polyimide-overlaid fiber. *Sensors and Actuators B: Chemical*, 348:130702, 2021.

[235] Yongqing Xu, Ying Tian, Binzhen Zhang, Junping Duan, and Li Yan. A novel rf mems switch on frequency reconfigurable antenna application. *Microsystem Technologies*, 24:3833–3841, 2018.

[236] Yuanjie Xu and Joshua E-Y Lee. Single-device and on-chip feedthrough cancellation for hybrid mems resonators. *IEEE transactions on industrial electronics*, 59(12):4930–4937, 2011.

[237] Weipeng Xuan, Marina Cole, Julian W Gardner, Sanju Thomas, Farah-Helúe Villa-López, Xiaozhi Wang, Shurong Dong, and Jikui Luo. A film bulk acoustic resonator oscillator based humidity sensor with graphene oxide as the sensitive layer. *Journal of Micromechanics and Microengineering*, 27(5):055017, 2017.

[238] Xiaomeng Xue, Qun Hao, and Menglu Chen. Very long wave infrared quantum dot photodetector up to 18 μm. *Light: Science & Applications*, 13(1):89, 2024.

[239] Hao Yang, Qixiang Cheng, Rui Chen, and Keren Bergman. Polarization-diversity microring-based optical switch fabric in a switch-and-select architecture. In *2020 Optical Fiber Communications Conference and Exhibition (OFC)*, pages 1–3. IEEE, 2020.

[240] YT Yeow, DR Lamb, and SD Brotherton. An investigation of the influence of low-temperature annealing treatments on the interface state density at the si-sio2. *Journal of Physics D: Applied Physics*, 8(13):1495, 1975.

[241] Mohammad I Younis, Eihab M Abdel-Rahman, and Ali Nayfeh. A reduced-order model for electrically actuated microbeam-based mems. *Journal of Microelectromechanical systems*, 12(5):672–680, 2003.

[242] Chang Zhang and Raphael St-Gelais. Demonstration of frequency stability limited by thermal fluctuation noise in silicon nitride nanomechanical resonators. *Applied Physics Letters*, 122(19), 2023.

[243] Haozhi Zhang, John C Peterson, and Philippe Guyot-Sionnest. Intraband transition of hgte nanocrystals for long-wave infrared detection at 12 μm. *ACS nano*, 17(8):7530–7538, 2023.

[244] Mingxiang Zhang, Zaihua Duan, Boyu Zhang, Zhen Yuan, Qiuni Zhao, Yadong Jiang, and Huiling Tai. Electrochemical humidity sensor enabled self-powered wireless humidity detection system. *Nano Energy*, 115:108745, 2023.

[245] Xiaoli Zhang, Xingguo Zhang, Xiaochen Lai, Ridong Wang, Haixia Yu, and Dachao Li. Pressure self-compensation for humidity sensing using graphene-oxide-modified dual-frequency cmut. *Sensors and Actuators B: Chemical*, 314:128074, 2020.

[246] Xiaosheng Zhang, Kyungmok Kwon, Johannes Henriksson, Jianheng Luo, and Ming C Wu. A large-scale microelectromechanical-systems-based silicon photonics lidar. *Nature*, 603(7900):253–258, 2022.

[247] Yangning Zhang, Muhammad Imran, Pan Xia, Yiqing Chen, Ahmet Gulsaran, Yanjiang Liu, Ehsan Nikbin, Benjamin Rehl, Lizhou Fan, Filip Dinic, et al. Nucleophilic covalent ligands enable simultaneous surface reconstruction and passivation of colloidal insb quantum dots for stable short-wave infrared photodetectors. *Angewandte Chemie International Edition*, page e202505179, 2025.

[248] Dong-Hui Zhao, Zi-Liang Tian, Hao Liu, Zheng-Hao Gu, Hao Zhu, Lin Chen, Qing-Qing Sun, and David Wei Zhang. realizing an omega-shaped gate mos2 field-effect transistor based on a sio2/mos2 core–shell heterostructure. *ACS applied materials & interfaces*, 12(12):14308–14314, 2020.

[249] Yunong Zhao, Jianjun Chen, Zhixiang Hu, Yan Chen, Yanbing Tao, Le Wang, Long Li, Ping Wang, Hua-Yao Li, Jianbing Zhang, et al. All-solid-state sars-cov-2 protein biosensor employing colloidal quantum dots-modified electrode. *Biosensors and Bioelectronics*, 202:113974, 2022.

[250] Zhou Zheng, Naeun Kim, William S Wong, and John TW Yeow. Inkjet-printed cmut humidity sensors with high sensitivity and low hysteresis. *Sensors and Actuators B: Chemical*, 327:128920, 2021.

[251] Zhou Zheng, Chunxia Tang, and John TW Yeow. A high-performance cmut humidity sensor based on cellulose nanocrystal sensing film. *Sensors and Actuators B: Chemical*, 320:128596, 2020.

[252] Zhou Zheng, Guodong Zhang, Xiaomin Wang, and Xu Kong. Comparative study of gravimetric humidity sensor platforms based on cmut and qcm. *Micromachines*, 13(10):1651, 2022.

[253] Zhou Zheng, Guodong Zhang, Xiaomin Wang, and Xu Kong. Comparative study of gravimetric humidity sensor platforms based on cmut and qcm. *Micromachines*, 13(10):1651, 2022.

[254] Yongzhi Zu, Jingrui Hu, Min Yang, Zaihua Duan, Mingxiang Zhang, Zhen Yuan, Yadong Jiang, and Huiling Tai. Electrochemical power generation humidity sensor based on ws2 nanoflakes. *Sensors and Actuators B: Chemical*, 405:135325, 2024.

APPENDICES

Appendix A

Fabrication of N/MEMS Resonators

The profilometer measurement result showing the thickness of the MEMS resonator sensor is given below.

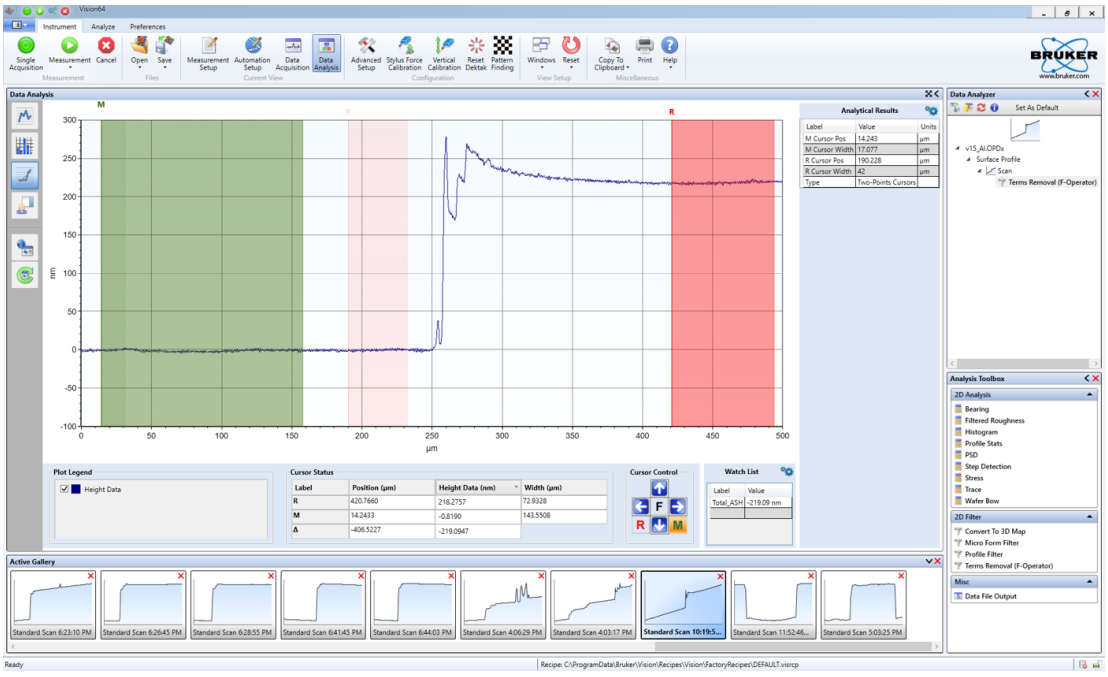


Figure A.1: The surface profile of Al obtained from mechanical surface profilometer. Reproduced with permission from Elsevier [72].

Appendix B

Python Code for Extracting Diode Performance Parameters

The Python code used to extract the diode performance parameters is given below.

```
import pandas as pd
import numpy as np
from scipy.signal import savgol_filter
import tkinter as tk
from tkinter import filedialog
import matplotlib.pyplot as plt


# Create a simple GUI for file selection
root = tk.Tk()
root.withdraw()

# Ask the user to provide an Excel file
file_path = filedialog.askopenfilename()

# Load the data from the Excel file
data = pd.read_excel(file_path)

# Apply the Savitzky-Golay filter to the I data
filtered_I = savgol_filter(data['I'], 2, 1)
```

```
# Calculate the first and second derivatives of the filtered I wrt. V
first_derivative = np.gradient(filtered_I, data['V'])
second_derivative = np.gradient(first_derivative, data['V'])

# Calculate the responsivity
responsivity = 2 * second_derivative / first_derivative

# Apply the Savitzky-Golay filter to the responsivity
filtered_responsivity = savgol_filter(responsivity, 499, 3)

# Calculate non-linearity
non_linearity = first_derivative / (filtered_I / data['V'])

# Apply the Savitzky-Golay filter to the non-linearity
filtered_non_linearity = savgol_filter(non_linearity, 499, 3)

# Calculate asymmetry
asymmetry = np.abs(filtered_I / np.flip(filtered_I))

# Apply the Savitzky-Golay filter to the asymmetry
filtered_asymmetry = savgol_filter(asymmetry, 499, 3)

# Calculate resistance
resistance = np.gradient(data['V'], filtered_I)
filtered_resistance = savgol_filter(resistance, 51, 1)
filtered_resistance = np.abs(filtered_resistance)

# Add calculated data to dataframe
data['filtered_I'] = filtered_I
data['dI/dV'] = first_derivative
data['d2I/dV2'] = second_derivative
data['responsivity'] = responsivity
data['filtered_responsivity'] = filtered_responsivity
data['non_linearity'] = non_linearity
data['filtered_non_linearity'] = filtered_non_linearity
data['asymmetry'] = asymmetry
data['filtered_asymmetry'] = filtered_asymmetry
```

```
data['Resistance'] = resistance
data['Filtered_Resistance'] = filtered_resistance

# Define indices for the plots
marker_indices = np.arange(0, len(data['V']), len(data['V']) // 10)

# Start building the plots
plt.figure(figsize=(20, 15))

# Current plot
plt.subplot(2, 3, 1)
plt.plot(data['V'], np.log10(np.abs(data['filtered_I'])), marker='o',
markevery=marker_indices)
plt.xlabel('Voltage(V)')
plt.ylabel('Current(I)')
plt.grid(True)

# Responsivity plot
plt.subplot(2, 3, 2)
plt.plot(data['V'], data['filtered_responsivity'], marker='o',
markevery=marker_indices)
plt.xlabel('Voltage(V)')
plt.ylabel('Responsivity(A/W)')
plt.xlim(left=0, right=1)
plt.grid(True)

# Non-linearity plot
plt.subplot(2, 3, 3)
plt.plot(data['V'], data['filtered_non_linearity'], marker='o',
markevery=marker_indices)
plt.xlabel('Voltage(V)')
plt.ylabel('Non-linearity')
plt.xlim(left=0, right=1)
plt.grid(True)

# Asymmetry plot
plt.subplot(2, 3, 4)
plt.plot(data['V'], data['filtered_asymmetry'], marker='o',
```

```
markevery=marker_indices)
plt.xlabel('Voltage(V)')
plt.ylabel('Asymmetry')
plt.xlim(left=0, right=1)
plt.grid(True)

# Resistance plot
plt.subplot(2, 3, 5)
plt.semilogy(data['V'], data['Filtered_Resistance'], marker='o',
markevery=marker_indices)
plt.xlabel('Voltage(V)')
plt.ylabel('Resistance(Ohm)')
plt.grid(True)  # add grid lines
plt.xlim(left=0)  # start x-axis at 0

# Save the figure
plt.savefig(file_path.replace('.xlsx', '-graph.png'))

# Write the filtered data to a new Excel file
data.to_excel(file_path.replace('.xlsx', '-filtered.xlsx'), index=False)
```

Appendix C

Preleminary Results from Dielectric Interface Testing

The preleminary results from the dielectric interface testing are presented below.

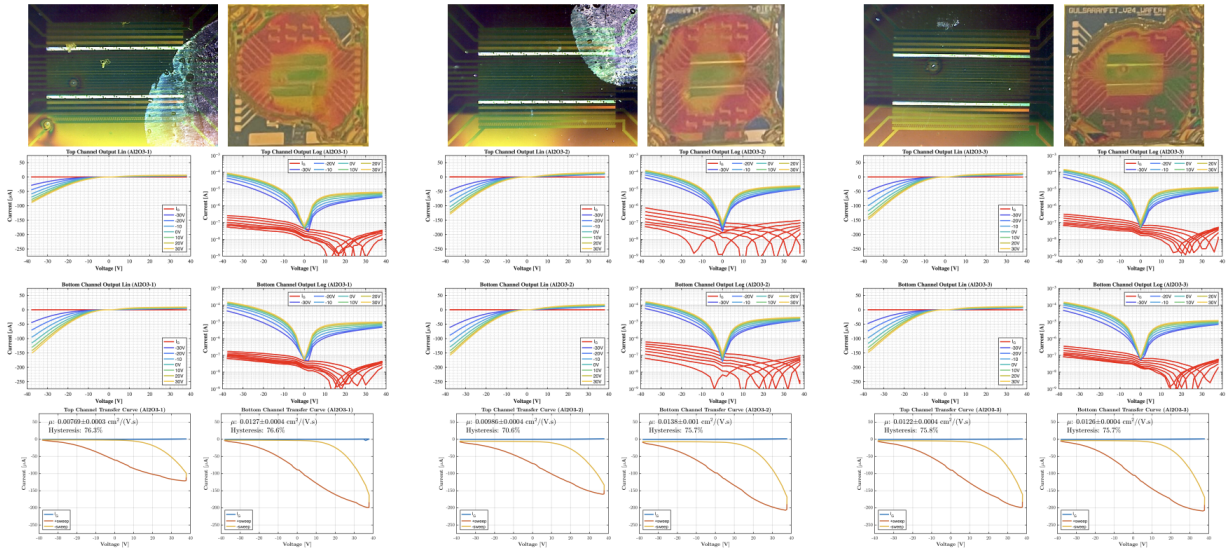


Figure C.1: FET performance with Al_2O_3 dielectric interface.

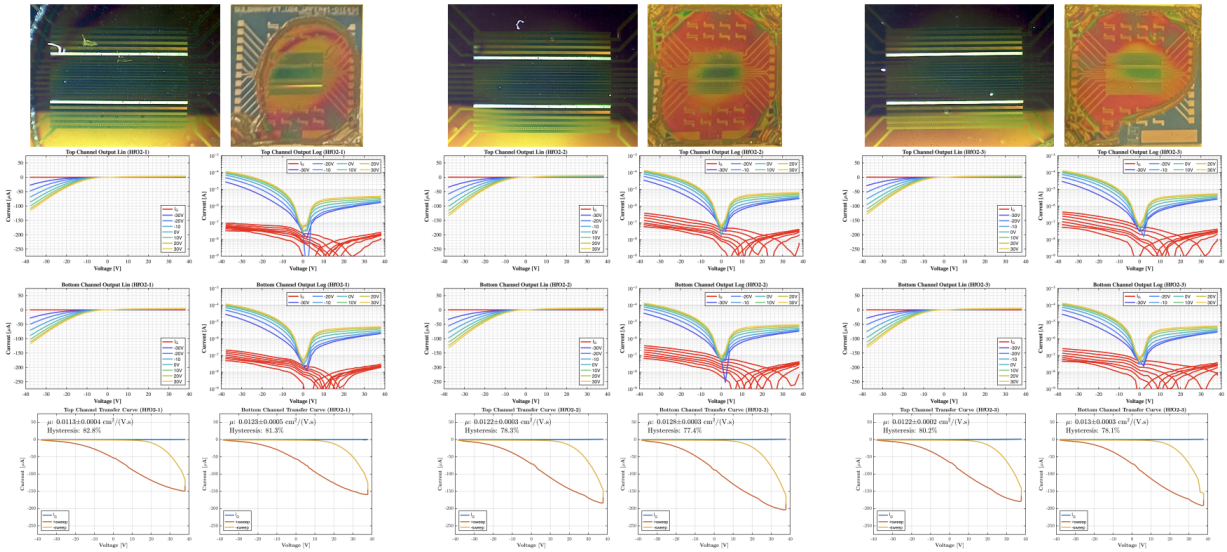


Figure C.2: FET performance with HfO_2 dielectric interface.

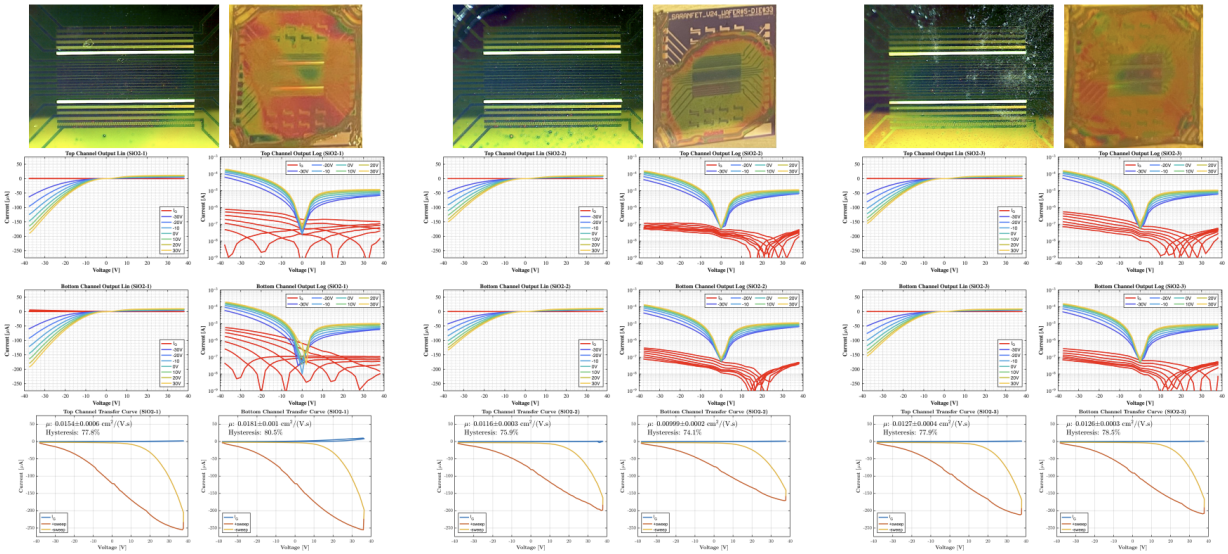


Figure C.3: FET performance with SiO_2 dielectric interface.

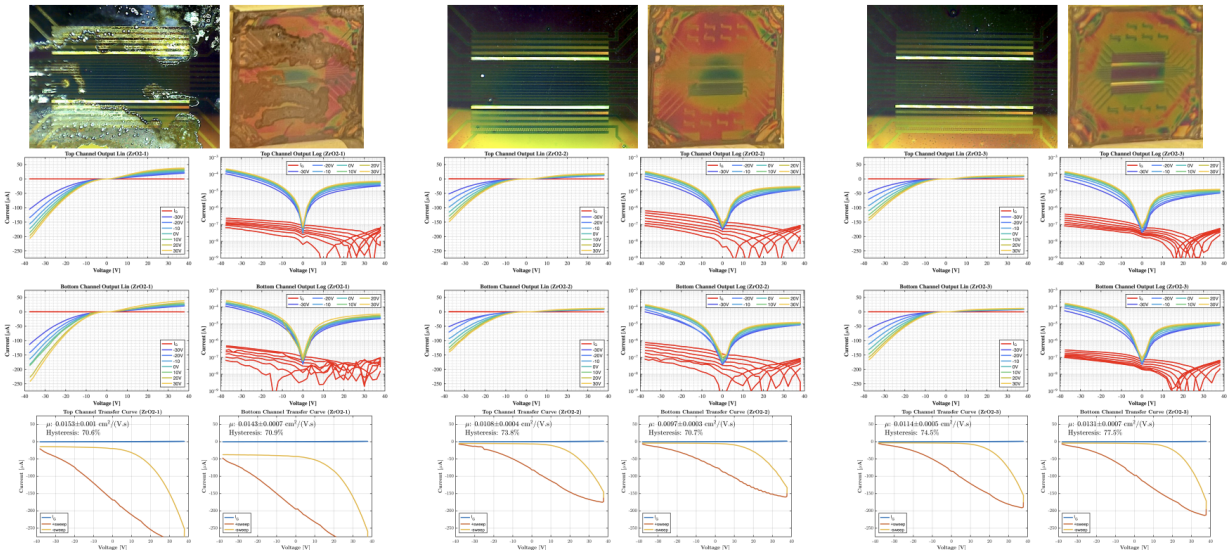


Figure C.4: FET performance with ZrO_2 dielectric interface.